ÉCOLE POLYTECHNIQUE DE BRUXELLES

UNIVERSITÉ LIBRE DE BRUXELLES

Towards the predictive FE analysis of a metal/composite booster casing's thermomechanical integrity

Thèse présentée par Adélie CAPRON

en vue de l'obtention du grade académique de docteure en Sciences de l'Ingénieur et Technologie

Année académique 2020-2021

Sous la direction du Professeur Stéphane GODET,
promoteur

et du Professeur Thierry J. MASSART,
co-promoteur

SAFRAN

SAFRAN AERO BOOSTERS

Université libre de Bruxelles
École polytechnique de Bruxelles
Département 4MAT

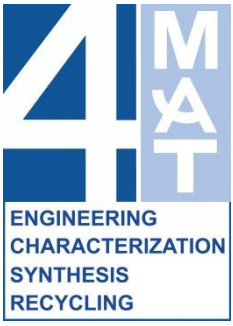

Towards the predictive FE analysis of a metal/composite booster casing's thermomechanical integrity

Adélie Capron

Composition du jury:

Prof. Stéphane Godet (Promoteur)	Université libre de Bruxelles
Prof. Thierry J. Massart (Co-promoteur)	Université libre de Bruxelles
Prof. Marie-Paule Delplancke (Présidente)	Université libre de Bruxelles
Prof. Peter Berke (Secrétaire)	Université libre de Bruxelles
Prof. Thomas Pardoen	Université catholique de Louvain
Prof. Danny Van Hemelrijck	Vrije Universiteit Brussel
Dr. Ir. Johann Pancrace	Safran Aero Boosters

Bruxelles, le 30 novembre 2020

À mon bien-aimé Maxime.

Si haute que soit la montagne,
on y trouve un sentier.
- proverbe afghan

Remerciements

Le nombre de personnes que je souhaite remercier en préambule de cette thèse semble être proportionnel au nombre d'années que j'ai passées à y travailler. De très nombreux noms me viennent à l'esprit au moment de rédiger ces lignes, que j'avais d'ailleurs consignés au fur et à mesure pour m'assurer de ne pas les oublier.

Je commencerai par mes promoteurs, Stéphane et Thierry. Merci de m'avoir emboîté le pas au départ de cette thèse, d'avoir monté ce projet et permis qu'il se réalise. À toi Stéphane, merci pour toutes ces portes que tu m'as ouvertes grâce aux excellentes relations que tu entretiens à l'intérieur comme à l'extérieur de l'ULB. À toi Thierry, merci de m'avoir initiée à la modélisation et simulation par éléments finis. Merci aussi pour l'enthousiasme bienveillant avec lequel tu accueillais chacune de mes petites victoires.

Cette thèse, je la dois aussi à Safran Aero Boosters qui a proposé et financé ce projet de recherche doctoral. Merci notamment à Laurent Schuster et Alain Derclaye, qui ont été à l'origine de notre collaboration avec cette entreprise renommée.

Aux membres de mon jury ensuite, merci d'avoir accepté la charge d'en faire partie. Cela a d'autant plus d'importance pour moi que chacun de vous a, d'une manière ou d'une autre, contribué à la réalisation de ce travail. Marie-Paule, grâce à votre gestion du service 4MAT j'ai eu la chance de travailler avec des techniciens et des équippements de qualité, et de profiter de moments conviviaux au sein de cette grande famille. Peter, merci d'avoir tou-

jours répondu présent lorsque je faisais appel à ta grande connaissance du logiciel SAMCEF. Thomas, un immense merci de m'avoir donné l'accès à votre laboratoire. On peut dire que sans les machines et les techniciens de l'iMMC il manquerait une bonne centaine de pages à ce manuscrit. Merci aussi pour votre présence stimulante et encourageante à nos réunions de suivi. Professor Danny Van Hemelrijck, I have been lucky to benefit from the expertise of the MEMC department in tensile testing and digital image correlation. Thank you very much for that ! Johann, merci pour le temps que tu as investi dans le suivi SAB de ma thèse lorsque tu en as pris la relève à mi-parcours.

Merci en outre pour votre participation bienveillante à ma soutenance privée (dont je garde en fait un agréable souvenir !), et pour toutes les améliorations que j'aurai pu apporter à mon manuscrit grâce à la lecture attentive que vous en avez fait.

Chez Safran Aero Boosters, je remercie aussi Philippe Bérot pour son soutien et son engagement dans le processus de fabrication de mes plaques RTM, Simon Rémy et Hugues Bolsée pour leurs réponses au millier de questions qui me sont venues en rédigeant le Chapitre 1 –votre aide a été inestimable–, et Boris Colson pour son support technique à diverses occasions. Élodie et Martin, vous avez quitté SAB pour d'autres horizons mais je n'oublie pas votre sympathie et votre assistance dans les premières années de ma thèse.

À quelques reprises, j'ai eu l'impression d'« envoyer une bouteille à la mer », à destination d'un auteur ou d'un expert. Tous n'ont pas répondu, mais j'ai ainsi eu la chance de pouvoir compter sur les conseils précieux des professeurs John Hutchinson et Anthony J. Kinloch, et plus récemment, sur les explications de Stéphane Hiernaux, senior engineer chez Safran Aero Boosters. It meant a lot to me, thank you.

J'ai souvent été accueillie dans plusieurs départements extérieurs à mon université, où j'ai eu la chance de bénéficier d'un accompagnement scientifique et technique pour la réalisation de mes mesures.

Dans le département iMMC (UCL), je remercie du fond du cœur Marc Sinnaeve, Jonathan, Alban et Quentin pour le support qu'ils m'ont apporté lors de mes nombreuses journées d'essais mécaniques. Merci en plus à toi et ton équipe, Marc, pour la fabrication de mon dispositif d'essai de pelage. À l'iMMC il y a aussi Vincent Destoop, que je remercie pour m'avoir assistée lors de mes premiers essais DCB et généreusement prêté ses « end blocks » sur une période plus longue que prévu. Et enfin, merci à Alex Bertholet de m'avoir patiemment appris à coller des jauges de déformation lorsque je pensais en avoir besoin.

From the MEMC department (VUB), I am very thankful to Professor Hugo Sol who accepted with enthusiasm to apply his Resonalyser procedure to my thin metal sheet, and Artemis Kalteremidou for her kindness and investment in the realisation of my DIC measurements.

From the FYSC departement (VUB), I would like to thank Professor Guy Van Assche and Professor Bruno Van Mele who kindly welcomed me in their laboratory and let me use diverse characterisation tools. In particular, thank you Guy for having guided me in the realisation of my first TMA measurements. Merci aussi à Audrey Cuvelier et Maxime Defour pour le précieux support qu'ils m'ont apporté lors de ces longues journées de mesures.

Dans le service BATir de l'ULB, Guy Paulus m'a apporté un support informatique dont je n'aurais jamais osé rêver, et toujours avec le sourire ;-) Merci pour tout, Guy! Sans toi, il n'y aurait probablement pas de solution EF 3D à la fin de ce manuscrit.

Dans mon propre département, le service 4MAT, j'ai aussi reçu un soutien précieux. Merci à toi Tiriana pour ta gentillesse et ta disponibilité, notamment lors de notre campagne de mesures par XRD. Merci Colin pour le joyeux usinage de mes éprouvettes époxy avec ta super fraiseuse numérique ! Merci Suzanne pour ton aide dans le polissage de mes échantillons multicouches. Merci Didier pour m'avoir spontanément aidée à préparer certaines éprouvettes, et enfin merci René pour la fabrication de mes systèmes de chargement.

Je pense aussi bien sûr à mes chouettes collègues. Céline, Charlotte, Ève-Line, Gaëlle, Loïc, Pierre, Shain, Sylvain, Solange, Jenny,... Je n'étais souvent que de passage et je partirai avec le regret de ne pas avoir passé plus de temps avec vous ! Un merci tout particulier à Gaëlle pour ses innombrables attentions et son soutien inconditionnel, et à Sylvain, avec qui j'ai apprécié de partager mon bureau et de pouvoir discuter de SAMCEF.

Après ces 7 années de thèse lors desquelles je me suis progressivement laissée envahir par mon travail, il me reste heureusement encore quelques amitiés précieuses et sincères. Gaëlle, Nancy, Gamze, merci les filles d'avoir été présentes pour moi jusqu'au bout !

Un grand merci à toute ma famille, et plus particulièrement à vous, Maman et Oobaachan. Repas, vaisselles, lessives, nettoyages, gardes d'enfants,... vous nous avez soutenus par tous les moyens sur le long terme et dans les périodes difficiles. Merci aussi à toi Odile pour la lecture et la critique constructive de certains de mes chapitres.

Merci à mes beaux-parents, qui m'ont bien aidée en prenant soin de leurs petits-enfants, et qui ont mis au monde et élevé l'homme formidable qui partage ma vie.

Maxime, tu mérites à toi seul un manuscrit de remerciements. Comme je ne l'ai pas encore écrit, je te dédie au moins celui-ci, c'est déjà ça… Calme, patient, rassurant, ouvert, attentionné et serviable, tu m'auras aidée et soutenue de la première année à la dernière minute de ce parcours, à travers toutes mes difficultés. Maintenant qu'on en est venus à bout, une nouvelle vie va commencer pour nous -une vie dont on a déjà tant rêvé !- et je suis sûre qu'avec toi, elle sera fantastique !

Éric et Soline, mes amours… Je n'avais pas prévu de tout mélanger, et pourtant c'est arrivé. La vie n'a pas attendu la fin de cette thèse pour nous donner, à Papa et moi, les plus beaux des cadeaux, deux enfants merveilleux. Vous m'avez donc rejointe dans mon parcours, d'abord embryons puis magnifiques et joyeuses petites personnes, et votre présence a grandement contribué à mon équilibre et à mon bonheur. Je vais m'occuper de vous de tout mon être à présent, comme je le souhaite depuis longtemps.

Je voudrais en tous les cas vous dire, à tous les trois et du fond du cœur, désolée et merci pour votre patience.

Éric et Soline, accompagnant leur maman dans son travail.
Ces photos ne sauraient trouver de meilleure place qu'ici.

Je me réjouis de pouvoir être plus présente pour vous tous maintenant.

Abstract

In response to serious environmental and economic concerns, the design and production of aircrafts have been changing profoundly over the past decades with the nose-to-tail switch from metallic materials to lightweight composite materials such as carbon fibre reinforced plastic (CFRP). In this context, the present doctoral research work aimed to contribute to the development of a CFRP booster casing, a real innovation in the field initiated and conducted by Safran Aero Boosters. More specifically, this thesis addresses the matter of joining metal/CFRP hybrid structures, which are prone to possibly detrimental residual stresses.

The issue is treated with an approach combining experimental characterisation and finite element (FE) simulations. The multi-layered system's state of damage was systematically examined on hundreds of micrographs, and the outcome of this study is presented under the form of a statistical analysis. Further, the defects' 3D morphology is investigated by incremental polishing. A number of thermal and mechanical properties are measured by diverse physical tests on part of the constituent materials, i.e. the aerospace grade RTM6 epoxy resin, the structural Redux 322 epoxy film adhesive, and AISI 316L stainless steel. They are used as input data in a FE model of the multilayer that is developed and progressively refined to obtain detailed residual stress fields after thermal loading. These results are compared to experimental data acquired by X-ray diffraction stress analysis and with the curvature-based Stoney formula. Cohesive elements are placed at specific locations within the FE model to allow simulating progressive damage. Peel tests,

mode I, mode II and mixed mode I/II fracture tests are thus performed in view of measuring the joint toughness. The results of these tests are discussed and the presence of residual stress in the fracture specimens is highlighted. Key information for the calibration of the cohesive law is finally identified via inverse FE analysis of the mode I test, this being a significant step in the process of building a damage predictive FE model of the multilayered system.

Contents

1. Introduction 25

1.1 General context 25

1.2 A composite low-pressure compressor at Safran Aero Boosters 29

1.3 Close-up on the composite casing 30

1.3.1 Design characteristics 31

1.3.2 Manufacturing process 35

1.3.3 Constituent materials 39

1.3.4 A damaged end product 48

1.4 Motivation, objective and outline of the thesis 50

2. Scientific background 53

2.1 Introduction 53

2.2 About residual stress 53

2.2.1 Origin of residual stresses in multilayers 53

2.2.2 Analytical method for the evaluation of thermally induced residual stresses in multilayers 57

2.3 Fracture mechanics of multilayers 61

2.3.1 Introduction 61

2.3.2 Small-scale yielding 62

2.3.3 Stress intensity factor 63

2.3.4 Strain energy release rate 65

2.3.5 Relationship between $\boldsymbol{G}$ and $\boldsymbol{K}$ 67

2.3.6 Fracture toughness 68

2.3.7 *Mixed mode fracture* 70
2.4 Fracture toughness testing of adhesively bonded joints 75
2.4.1 *Introduction* 75
2.4.2 *Beam-bending LEFM tests* 77
2.4.3 *Peel tests* 87
2.5 Simulation of progressive damage with cohesive finite elements 91
2.5.1 *Introduction* 91
2.5.2 *Cohesive zone and cohesive zone models* 92
2.5.3 *Definition of a cohesive zone length and implication* 94
2.5.4 *Approaches for modelling with cohesive elements* 95
2.5.5 *Description of the CZM used in this work* 97

3. Experimental investigation of the multilayer's damage state 101

3.1 Introduction 101
3.2 Damaged zones and types of damage 102
3.3 Statistical analysis of the multilayer's damage state 107
3.3.1 *Methodology* 107
3.3.2 *Statistical analysis* 109
3.3.3 *Global review* 118
3.4 Investigation of the 3D configuration and damage morphology at the inter-segments gap 120
3.5 Conclusion 128

4. Thermo-mechanical characterisation of the constituent materials 129

4.1 Introduction 129
4.2 Effective properties of the CFRP composite laminate 130
4.2.1 *Thermoelastic properties of the constituent laminae* 131

4.2.2 *Effective thermoelastic properties of the laminate* 132
4.3 Properties of the RTM6 resin and the Redux 322 structural film adhesive 134
4.3.1 *Materials* 134
4.3.2 *Thermal stability* 136
4.3.3 *Glass transition temperature* 137
4.3.4 *Mechanical and thermal properties* 143
4.4 Properties of the as-rolled and micro-perforated 316L SS strips 156
4.4.1 *Materials* 156
4.4.2 *Mechanical and thermal properties* 156
4.5 Conclusion 168

5. Evaluation of the thermally induced residual stresses in the multilayer 173

5.1 Introduction 173
5.2 Experimental evaluation of the residual stress state 174
5.2.1 *X-ray stress analysis of free-standing and co-cured 316L SS strips* 174
5.2.2 *Curvature-based experimental evaluation of the residual stress with an extension of the Stoney formula* 184
5.2.3 *Conclusion* 189
5.3 Analytical prediction of the through-thickness profile of thermally induced residual stress 189
5.3.1 *Introduction* 189
5.3.2 *Through-thickness residual stress profiles thermally induced in the three-layered systems* 189
5.4 FE prediction of the thermally induced residual stresses 192
5.4.1 *Basic prediction of the residual stresses with model A* 192
5.4.2 *Refined prediction of the residual stress fields with model B* .. 197

5.5 Conclusion 220

6. Measurement of the critical SERRs of the co-cured joint 222

6.1 Introduction 222

6.2 Materials 223

6.2.1 *Peel test specimens* 223

6.2.2 *Beam-type LEFM tests specimens* 226

6.3 Adhesive fracture energy of the co-cured bond measured with the Fixed Arm Peel test 229

6.4 Mode I critical SERR of the co-cured joint measured with the Double Cantilever Beam test 241

6.4.1 *Experimental procedure* 242

6.4.2 *Load-displacement curves and fracture surfaces* 244

6.4.3 *Curvature of the DCB specimen* 251

6.4.4 *Data reduction schemes* 252

6.4.5 *R-curves and mode I critical SERRs* 255

6.4.6 G_{Ic} compared to G_A 257

6.5 Mode II and mixed mode I/II critical SERR of the co-cured joint measured with the End-Loaded Split test and the Fixed Ratio Mixed Mode test 257

6.5.1 *Experimental procedures* 258

6.5.2 *Load-displacement curves* 260

6.5.3 *R-curves* 260

6.5.4 *Mode II and mixed mode I/II critical SERRs* 264

6.6 Conclusion 265

7. Identification of the mode I cohesive law parameters by inverse FE analysis of the DCB test 269

7.1 Introduction ... 269
7.2 Presentation of the FE models ... 271
7.2.1 *2D and 3D geometries* ... 272
7.2.2 *Mesh* ... 272
7.2.3 *Materials* ... 274
7.2.4 *Loads and boundary conditions* ... 276
7.3 Parametric study and inverse analysis of the DCB test ... 279
7.3.1 *Influence and selection of the penalty stiffness value* ... 279
7.3.2 *Influence of the spatial discretisation of the cohesive zone and selection of a criterion for mesh convergence* ... 282
7.3.3 *Identification of a value for the mode I critical SERR* ... 285
7.3.4 *Identification of a value for the mode I peak stress* ... 287
7.4 Validation of the 2D approach with the 3D model ... 289
7.5 Preliminary identification of the fracture envelope and the mode coupling coefficient ... 291
7.6 Conclusion ... 293

8. Conclusion and perspectives ... 295

8.1 Conclusion ... 295
8.2 Perspectives ... 299

A. Dundurs' parameters ... 303

B. Kinking, penetration, and deflection of an interface crack ... 304

B.1 Crack kinking ... 304
B.2 Crack penetration/deflection ... 305

C. Derivation of the analytical expression of G_{II} for the ELS test 306

D. Derivation of the analytical expression of $G_{I/II}$ for the FRMM test 307

E. Derivation of the analytical expression of Gdb , the total energy dissipated in bending of the peel arm 308

F. Classical Lamination Theory for the prediction of the effective thermoelastic properties of laminated media 310

F.1 Introduction 310

F.2 Model by Gudmundson and Zang 312

F.2.1 Constitutive relation of the lamina 313

F.2.2 Transformation from the lamina (principal) to the laminate (global) coordinate system 315

F.2.3 Constitutive relation of the laminate 316

G. Experimental methods 321

G.1 Thermogravimetric Analysis 321

G.2 Thermomechanical Analysis 322

G.2.1 Thermomechanical analysis of RTM6 and Redux 322 324

G.2.2 Thermomechanical analysis of the as-rolled AISI 316L SS strip 325

G.3.1 Dynamic Mechanical Analysis of RTM6 and Redux 322 327

G.4 Quasi-static macroscopic tensile testing 329

G.4.1 Quasi-static macroscopic tensile testing of RTM6 and Redux 322 330

G.4.2 Quasi-static macroscopic tensile testing of as-rolled and micro-perforated AISI 316L SS 331
G.5 Resonant-based identification of elastic constants 335
G.5.1 Resonant-based identification of as-rolled and micro-perforated AISI 316L SS elastic constants 338

H. Global analysis of the TMA curves 340

I. Comment on the DMA curves 342

J. Polynomial fits and discrete values of E-modulus and CTE 343

K. X-ray stress analysis 346

K.1 Introduction 346
K.2 Fundamental principles of X-ray diffraction 346
K.3 XRD applied to stress analysis 349
K.3.1 Why stress can be quantified 349
K.3.2 How stress is quantified 353
K.3.3 Measurement procedure 359

L. Bi-linear fit parameters of the steel strips' nominal tensile curves 363

List of acronyms

2D	Two-Dimensional
3D	Three-Dimensional
APS	Atmospheric (or Air) Plasma Spray
A-R	As-Rolled
B-K	Benzeggagh-Kenane
CBT	Corrected Beam Theory
CFRP	Carbon Fiber Reinforced Plastic/Polymer
CLT	Classical Lamination Theory
CPU	Central Processing Unit
CTE	Coefficient of linear Thermal Expansion
CZM	Cohesive Zone Model
DCB	Double Cantilever Beam
DIC	Digital Image Correlation
DMA	Dynamic Mechanical Analysis
DOF	Degree(s) of Freedom
DRF	Data Rejection Factor
ECM	Experimental Compliance Method
EDM	Electrical Discharge Machining
ELS	End-Loaded Split
ENF	End Notched Flexure
ERR	Energy Release Rate
ESIS TC4	European Structural Integrity Society Technical Committee 4
FE(M)	Finite Element (Method)
FPZ	Fracture Process Zone

FRMM	Fixed Ratio Mixed Mode
FWHM	Full Width at Half Maximum
ISG	Inter-Segments Gap
LEFM	Linear Elastic Fracture Mechanics
MBT	Modified Beam Theory
MMB	Mixed-Mode Bending
MMF	Mixed-Mode Flexure
MNET	Mixed Numerical-Experimental Technique
M-P	Micro-Perforated
PL	Power Law
RD	Rolling Direction
RTM	Resin Transfer Moulding
SAB	Safran Aero Boosters
SBT	Simple Beam Theory
SEM	Scanning Electron Microscope/Microscopy
SERR	Strain Energy Release Rate
SIF	Stress Intensity Factor
SS	Stainless Steel
SSY	Small-Scale Yielding
TD	Transverse Direction
TDCB	Tapered Double Cantilever Beam
TGA	Thermogravimetric Analysis
TMA	Thermomechanical Analysis
TTT	Time-Temperature-Transformation
UD	Uni-Directional
WT	Wedge Test
XEC	X-ray Elastic Constant
XRD	X-Ray Diffraction
XSA	X-ray Stress Analysis

1. Introduction

1.1 General context

16 billion. This is the number of air passengers forecasted for 2050 [1]; that is to say a massive growth compared to the 4.2 billion passengers counted in 2018 [2]. CO_2 emissions from international civil aviation would then approximately triple [3], while this sector of activity is already responsible for 2.4 % of global CO_2 emissions from fossil fuel use today, a share comparable to that of Germany [4]. Yet, while it is now impossible to ignore the effects of global warming, such increase in greenhouse gas emissions should be avoided at all costs.

The aviation industry has fortunately committed in 2016 to start assuming its share of responsibility towards climate change, and targets a 50 % reduction in net aviation CO_2 emissions by 2050 relative to 2005 levels [5][6][7]. Furthermore, besides environmental considerations, fuel saving is at the centre of airlines' concerns for economic reasons, as fuel represents a significant part of their operating costs [8]. Environmental and economic interests would thus go hand in hand, since for every ton of aviation fuel that is not burn, both 3.16 tonnes of CO_2 and 1120 US$[1] are saved [9].

In 2009 already, Boeing executed the first flight of its 787 Dreamliner [10]. Its competitor, the Airbus A350 XWB, took off for the first time less than four

[1] Average price of kerosene in Belgium from October 7, 2019 to January 13, 2020 [233].

years later [11]. These new generation long-haul wide-body airliners embody the efforts undertaken by aircraft manufacturers to improve the fuel efficiency of their fleet: with a typical capacity of 242 (B787-8) and 366 (A350-900) seats, they are respectively able of saving 20 % and 25 % of fuel burn compared with their predecessors of equivalent capacity and range [12][13][14]. This remarkable progress results from the combination of "the very latest aerodynamics, new generation engines, and lightweight materials", according to Airbus [14]. Weight reduction is indeed the supreme way towards better fuel efficiency; in both planes it was achieved through the use of approximately 50 weight percent of composite materials, a large majority of which being Carbon Fibre Reinforced Plastic (CFRP) particularly appreciated for its high specific strength [14][15]. Cockpit, fuselage, wings, nacelles, empennage… CFRP is basically everywhere in the structure and outer shell of these aircrafts (Figure 1-1).

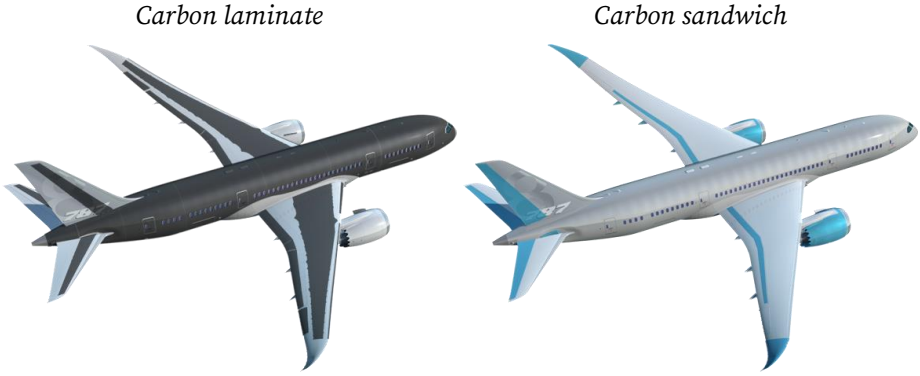

Figure 1-1. Distribution of carbon laminate (left) and carbon sandwich (right) composites in the Boeing 787' structure [15]

In addition to weight savings, use of composite materials offers new time- and cost-effective design opportunities. The B787's fuselage, for instance, is made of four one-piece CFRP barrels, a totally innovative solution that eliminates the need of about 150.000 mechanical fasteners as compared

with the standard aluminium panels solution [12]. Besides, adhesive bonding with structural adhesives should continue replacing traditional joining methods such as bolting and riveting. It indeed presents a number of advantages, among which the fact that it preserves the structural integrity of the adherends: fibre reinforcements are not cut, the load is uniformly distributed along the bonded joint and the fatigue life of the assembly is significantly improved. Adhesive bonding also brings additional design freedom and participates to the weight reduction objective [16][17].

As opposed to the airframe, the engines still are mostly metallic. Carbon fibre composite is indeed at best used for the fan blades and the fan case at General Electric and Rolls Royce -the two top turbofan manufacturers- in their GEnx and Advance engine, respectively [18][19]. Use of lightweight composite material for the fan system allows these companies to follow the demand for ever larger jet engines without impacting their weight. This actually is a technical feat already, given the shape and size of the blades (Figure 1-2), and the stress they must resist for instance upon bird strike or fan blade-out [20].

Figure 1-2. General Electric GEnx engine with carbon fibre composite fan blades and fan case. Visitors set the scale. [21]

The pressure and temperature levels reached everywhere else in the engine explain the prolonged reliance on advanced metal alloys. The huge amount of air continuously sucked in by the rotating fan divides into two flows inside the engine (Figure 1-3). The major part (external or secondary flow) bypasses the core of the engine and goes directly into the exhaust stream where it provides much of the thrust that makes the aircraft move forward. The other part (internal or primary flow) undergoes an extreme thermodynamic cycle which provides the energy to drive the engine. It is first squeezed through the low-pressure compressor, or *booster*, where it is compressed to about 2 atm. It is then forced into the high-pressure compressor where its pressure is further increased to several tens of atmospheres [22].

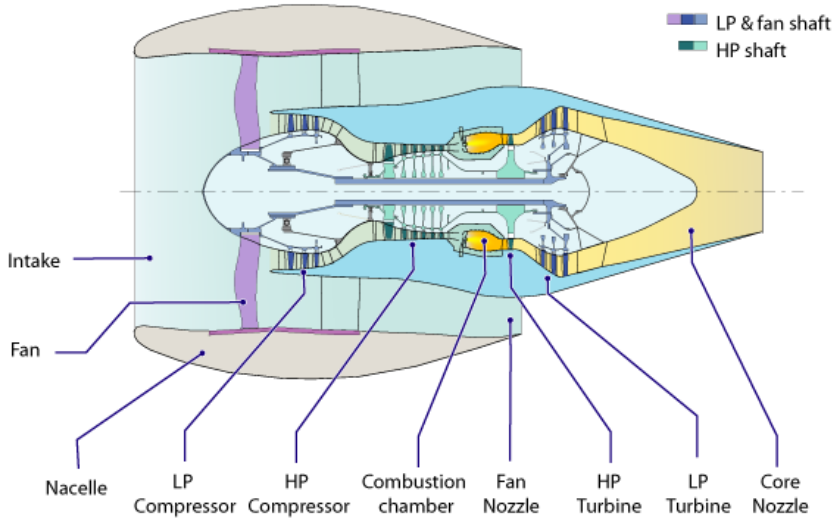

Figure 1-3. Schematic cross-section of a two-spool turbofan engine [23].

Next, this very dense, hot air is mixed with atomised fuel and ignited in the combustion chamber where its temperature can reach 2100 °C [24]! The resulting explosion produces a high-energy gas flow that, while escaping downstream of the engine, transfers most of its energy to the turbines in charge of the fan and compressors rotation. The turbine blades must there-

fore survive service temperatures above 1600 °C and high levels of centrifugal force [24]. The exhaust gas flow is finally conveyed towards the exit through a nozzle designed to maximise the thrust it can still provide.

Although its compression ratio may seem low compared to that of the high-pressure compressor, the booster is a key component of many turbofan engines. By pre-compressing air, it allows increasing the airflow into the high-pressure compressor and the combustor, which, as a result, increases the thrust. Boosters thus make it possible to design a series of different engines spanning a given thrust range, without having to change the high-pressure compressor (which is a more complex and delicate part to develop).

1.2 A composite low-pressure compressor at Safran Aero Boosters

The present thesis has been proposed and funded by Safran Aero Boosters, often referred to as *SAB* or *industrial partner* in this manuscript. With 60 years of experience in propulsion, the company is the world leader in design, manufacture and assembly of low-pressure compressors (boosters) for turbofan engines. Its products cover the whole thrust range and, working in close partnership with engine manufacturers, are found in most civil aviation engines [25].

SAB invests approximately 15 % of its revenue in research, technologies and development, thereby sustaining its status of cutting edge technological partner. Hence, in 2007, the company started developing what could be the "booster of the future", designed to be 20 % lighter than the current equivalent model [26]. It comprises a lightweight carbon fibre-based composite casing with three stages of bolted stationary stator blades surrounding a titanium alloy drum with three stages of friction-welded rotor blades (Figure 1-4). The composite casing is completed with two titanium alloy elements:

one stage of stators and rotors upstream, and a part that makes the connection with the high pressure compressor downstream. These parts are not shown in the figure.

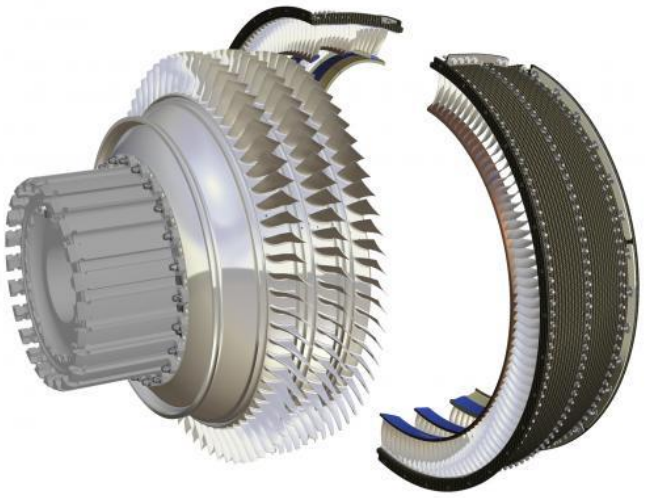

Figure 1-4. Computer-generated image of the lightweight booster, with an exploded view of the composite casing. Courtesy of Safran Aero Boosters.

With a mean outer diameter of about one metre, this booster would equip small turbofan engines such as the CFM International LEAP which does already rely on carbon fibre composite for its fan blades and fan case [27].

1.3 Close-up on the composite casing

Among all components forming the booster, the present thesis did more specifically deal with the composite casing. It does hence deserve being presented in detail: one will start with an overview of its design characteristics before studying its manufacturing process and main constituent materials. Given the complexity of this piece of engineering, the content of these topics can hardly be dissociated. One will thus receive complementary information throughout the reading of the following sections.

1.3.1 Design characteristics

The composite booster casing is made of *two half pieces* of about 30 cm in height. As shown in Figure 1-4 and Figure 1-5, these are manufactured separately then assembled by means of axial *flanges*, while circumferential flanges ensure the connection with the upstream and downstream titanium alloy elements.

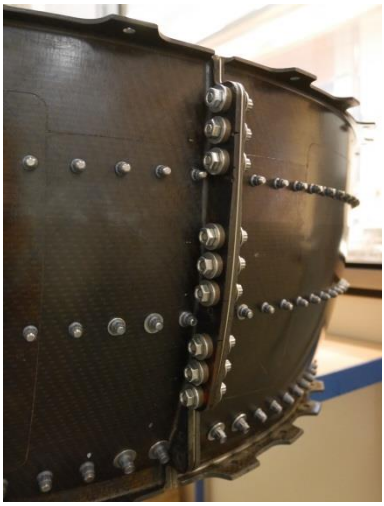

Figure 1-5. Close-up view of two half composite casings bolted together at the axial flanges.

The casing is a structural part; its fibre reinforcement has therefore been engineered to carry the service loads. It is a *laminate* of woven glass and carbon fabrics.

In a compressor, stages of stators and rotors follow one another. In service, this system creates a significant pressure gradient towards the rear of the engine, from which the airflow would naturally tend to escape by any opening. Therefore, on the inner surface of the casing, the stators stages do alternate with annular *abradable seals* facing the tip of rotor blades. These are are sacrificial coatings playing two important roles: they allow controlling (minimising) the clearance between blades tips and casing surface while protect-

ing both of them against wear and mechanical damage upon contact [22]. In particular, the composite booster casing comprises two of these abradable tracks, called RM3 track (upstream) and RM4 track (downstream), as shown in Figure 1-6. The abradable coating is conventionally *plasma sprayed* on the bare inner surface of metallic casings. Yet, this practice resulted in severe lack of adhesion when simply transferred to the composite casing. The solution implemented consists in plasma spraying the abradable coating on thin strips of *micro-perforated stainless steel* that are integrated into the composite casing surface, by *co-curing*, in the early stage of its manufacturing.

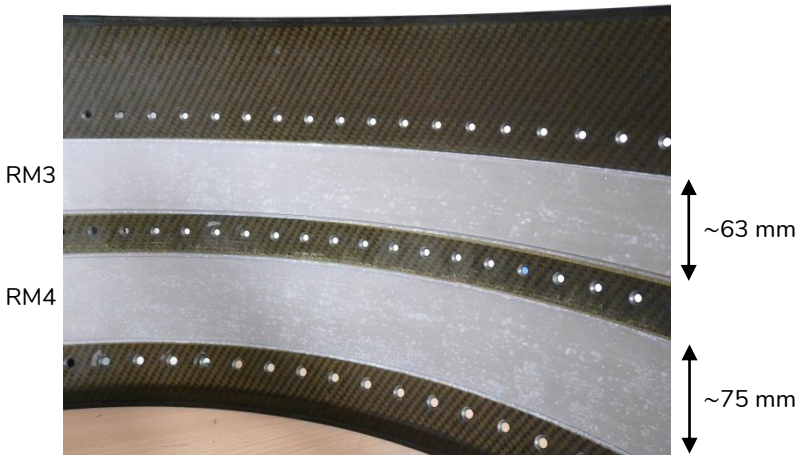

Figure 1-6. Close-up view of the plasma sprayed abradable seal tracks on the composite casing, with their designation RM3 and RM4.

Rather than a single piece, three segments of stainless steel strip are used to cover the half circumference of the casing. The small space left between two segments is called the *inter-segments gap* (*ISG*); two of them are thus found on each abradable track (Figure 1-7). Longitudinal *slits* cut into the segments do further improve their ability to match the complex curvature of the casing; they too are pointed out in Figure 1-7. Finally, in addition to its primary role,

the steel strip is also expected to act as a shield protecting the composite surface in case of powerful impact.

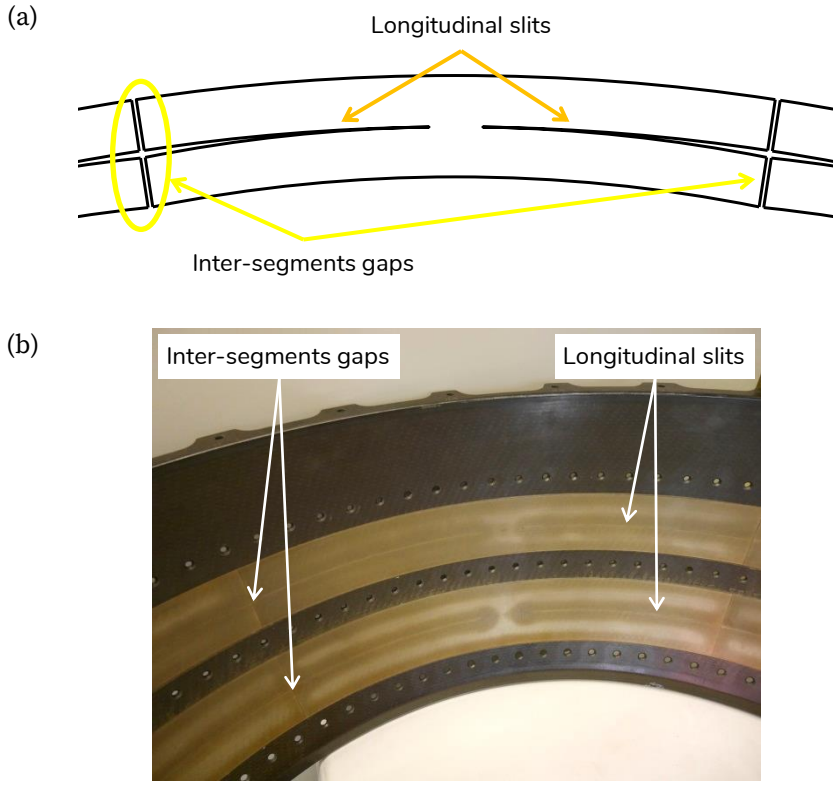

Figure 1-7. Examples of inter-segments gaps and longitudinal slits highlighted on (a) a schematic of the steel strip's contour, and (b) a close-up view of the steel strip segments co-cured with the composite casing.

This whole engineering solution yields a multi-layered, multi-material system of which an optical micrograph is shown in Figure 1-8.

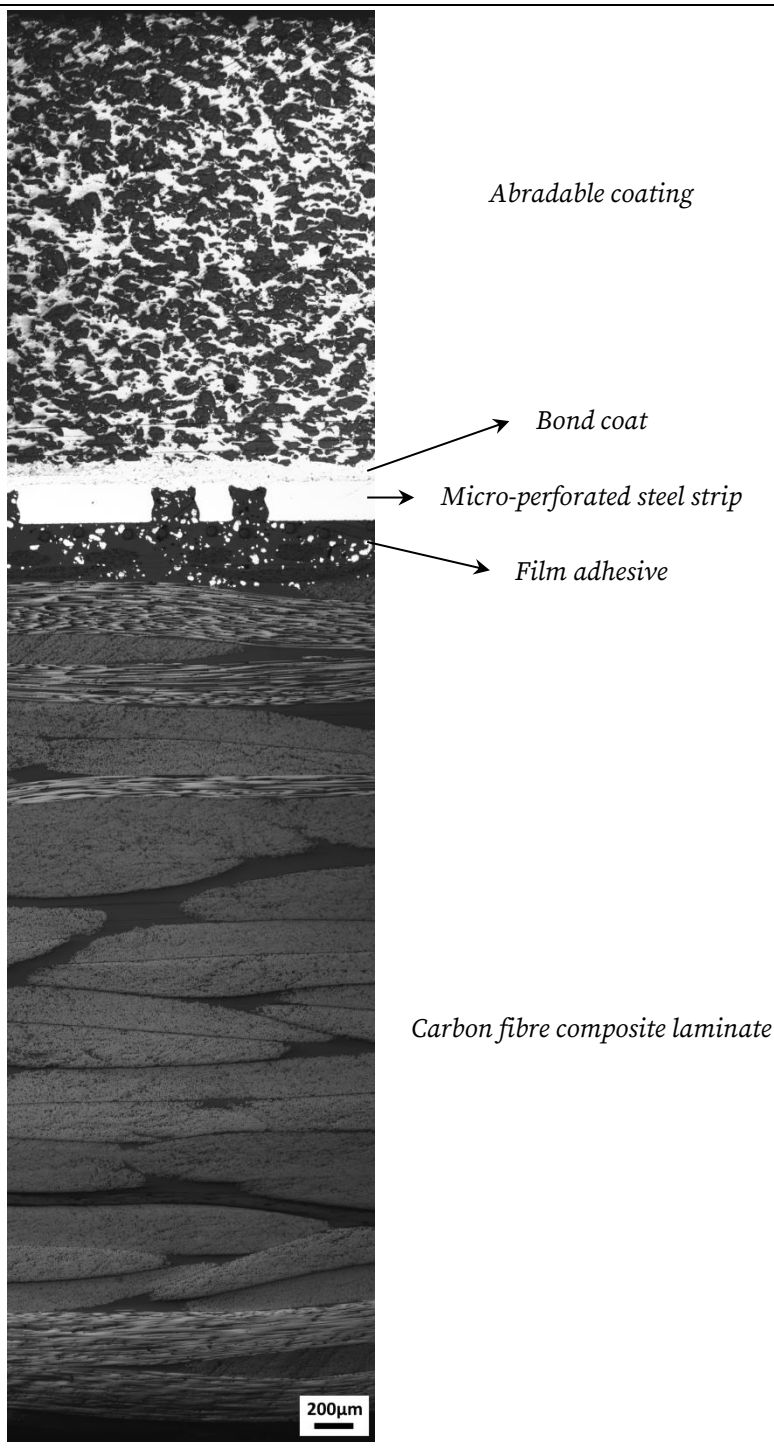

Figure 1-8. Optical micrograph of the multi-layered system found within the abradable seal tracks.

1.3.2 Manufacturing process

The manufacturing process developed at SAB is outlined below and illustrated in Figure 1-9 and Figure 1-10.

The half casing is produced by Resin Transfer Moulding (RTM), a technology by which a composite part is formed by impregnation of reinforcement material (the *preform*) with low viscosity resin in a rigid, closed mould. This process is used for the production of small to medium composite parts; it is appreciated for its numerous qualities, among which the control it offers on the dimensions, fibre volume fraction and surface finish of the final part [28].

The preform is prepared with woven carbon and glass fabrics draped on a male mould according to a defined stacking sequence. The segments of stainless steel strip, sandblasted and degreased, are precisely placed on the surface of the male part of the injection mould and held by means of a few solder points. Segments of *film adhesive* are then applied on the stainless steel strips surface in order to improve their adhesion to the casing. Profiled pre-impregnated strands are placed in the fillets of the mould to form the sharp edges of the casing. Next, the preform is transferred to the injection mould using a specially designed vacuum lifting tool. Finally, before closing the mould, inserts are placed on the preform to shape the flanges.

Once the mould is closed, its internal temperature is set to 80 °C for about 85 minutes during which the preform is allowed to dry. Meanwhile, the resin placed in the resin pot is brought to 60 °C and 0.5 mbar for maximum 60 minutes and stirred to let it liquefy and degas. Then, it is injected in the mould with a pressure of 7 bars via two inlet ports found upstream of the half casing. The advancing resin *flow front* wets the fibre preform and expels the air which escapes through a vent valve at the opposite side of the mould. Vacuum assistance is performed through the vent during the whole injection

step, which is known to reduce the voidage content of the final part [29]. After a few minutes, when all air has escaped through the vent, the latter is closed and the injection pressure is brought to 9 bars. Since the mould internal temperature is continuously and slowly increased from the start of injection, the *polymerisation reaction* (*cure*) progressively takes place and the resin both hardens and shrinks. Injection is stopped when a pressure drop is recorded at the vent, which is a sign that the reaction progresses. The rest of the reaction takes place in the closed mould upon heating to 180 °C and during a 120 minutes long *isotherm* at that temperature. Then, controlled cooling of the mould is performed and the half casing is demoulded at about 100 °C.

Several conditioning, control and cleaning operations are performed during this whole process, which participate to its smooth running and ensure the lasting quality of the equipment.

After visual inspection and three-dimensional measurement, two half casings are assembled and machined. The casing is then brought to the plasma spray shop where the abradable coating is deposited on the annular tracks.

The next and final steps of the manufacturing process are dedicated to the installation of the stators stages and will not be covered in this text, considering that these elements are external to the composite casing.

A completed composite booster is shown in Figure 1-11, standing on the clamping tool used for the final manufacturing operation.

Preparation of the preform

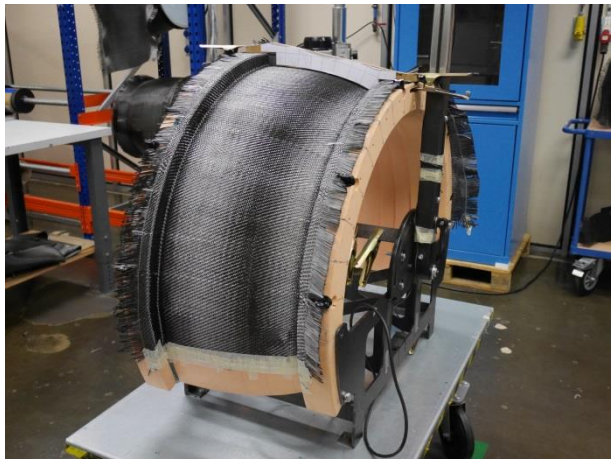

Installation of the steel strip segments

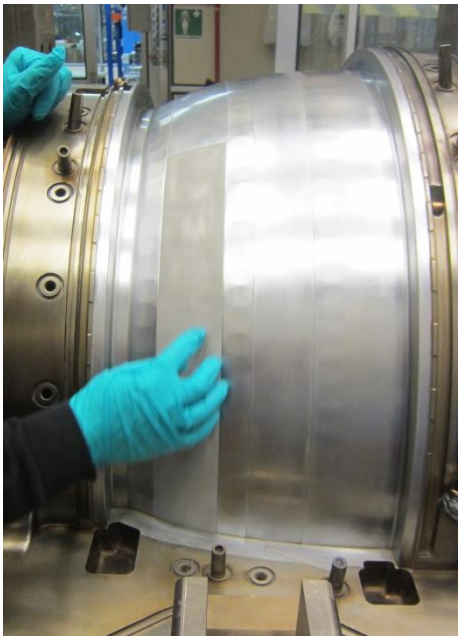

Application of the adhesive film

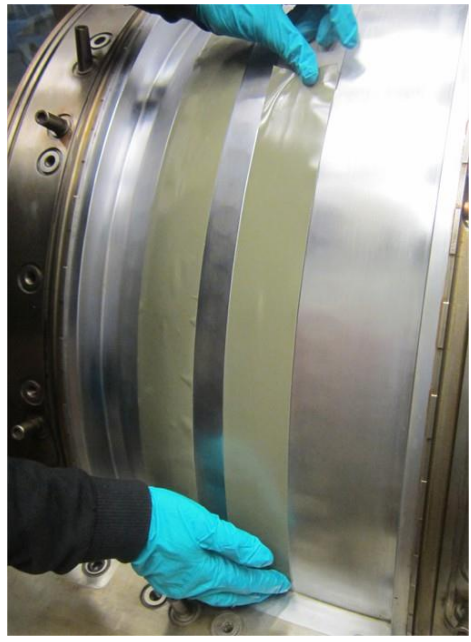

Figure 1-9. Manufacturing of the composite booster casing (part 1). Courtesy of Safran Aero Boosters.

Preform transferred to the injection mould

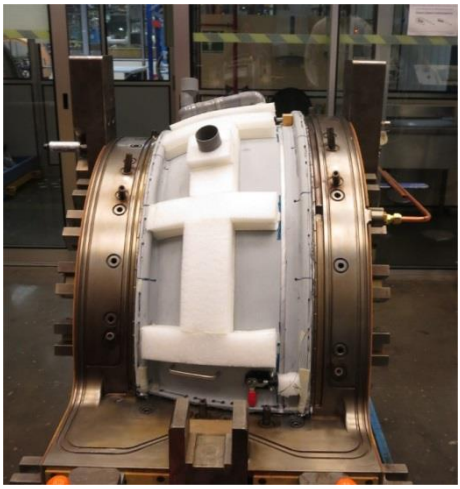

Inserts installed at the flanges

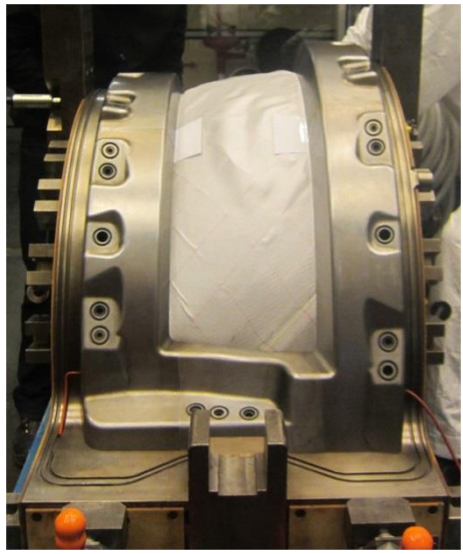

Mould closure

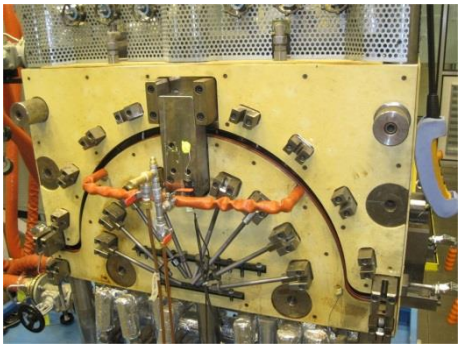

Part demoulded and machined

Casing at the plasma spray shop

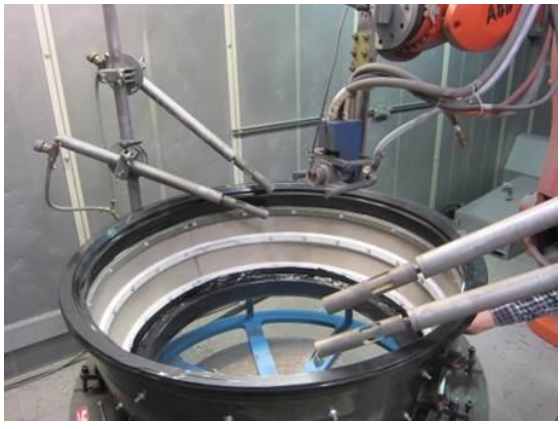

Figure 1-10. Manufacturing of the composite booster casing (part 2). Courtesy of Safran Aero Boosters.

Figure 1-11. Finalised composite booster (standing on a clamping tool). Courtesy of Safran Aero Boosters.

1.3.3 Constituent materials

The materials forming the multi-layered system shown in Figure 1-8 will now be briefly described one after the other.

1.3.3.1 Composite laminate

The casing structural material is a composite laminate, i.e. a series of *laminae* superimposed with a given orientation. These laminae can be thought of as orthogonal 2D woven carbon or glass fabrics embedded in a polymer matrix. The fabrics are made of *tows* (bundles of thousands of fibres) arranged in two mutually perpendicular directions: the *warp* direction (along the fabric length) and the *weft* direction[2]. The tows are interlaced following pre-defined weaving patterns in which weft tows pass over and under warp tows. Various fabrics can hence be obtained such as plain weave, twill weave and satin weave, which exhibit different properties. They generally offer a better drapability than unidirectional (UD) fabrics, which allows wrapping around complex shapes [30].

[2] Respectivement chaîne et trame, en français.

Four types of laminae are used in the present application: the *warp heavy* and *weft heavy* carbon laminae (the adjective "heavy" indicating which of the warp or weft tows have the largest diameter), the *balanced* carbon lamina (the adjective "balanced" indicating that warp and weft tows have the same diameter) and the *glass* lamina. The first two are 2x2 twill weaves where each weft tow passes over and under two warp tows (Figure 1-12). The balanced lamina is an 8HS satin weave where each weft tow passes over seven warp tows and under the eighth. Finally, the glass lamina is a 4HS satin weave where each weft tow passes over three warp tows and under the fourth. The weave pattern of these fabric types is illustrated in Figure 1-12. Note that these data concerning the weave patterns are provided for introductory purposes only; they will not be used in the rest of this manuscript since the laminae have been considered as homogenised layers with effective properties in the present work.

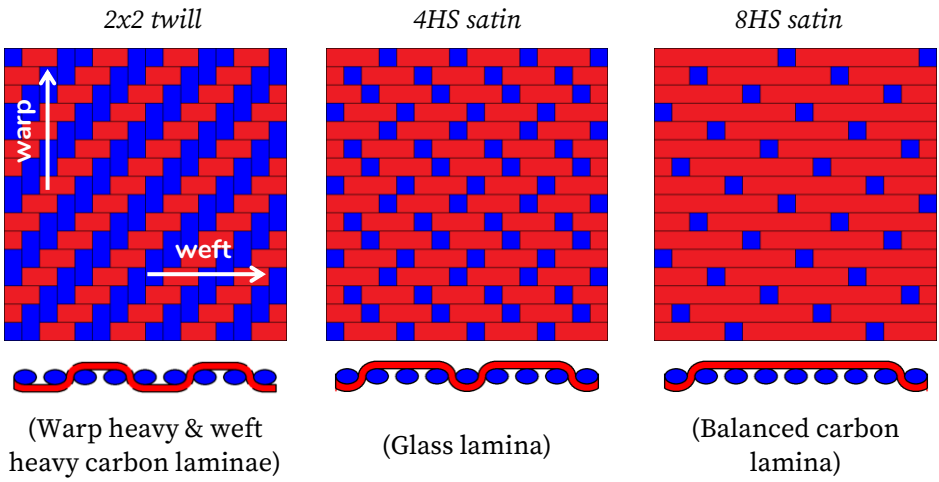

Figure 1-12. Top row: weave patterns of the carbon and glass fabrics used in the manufacturing of the composite booster casing (warp direction is vertical and warp tows are shown in blue). Illustrations adapted from [31]. *Bottom row: schematic cross-sections of these weave patterns showing the undulation of a weft tow around warp tows.*

The stacking sequence (or *layup*) followed for the preparation of the laminate is sketched in Figure 1-13 and detailed in Table 1-1.

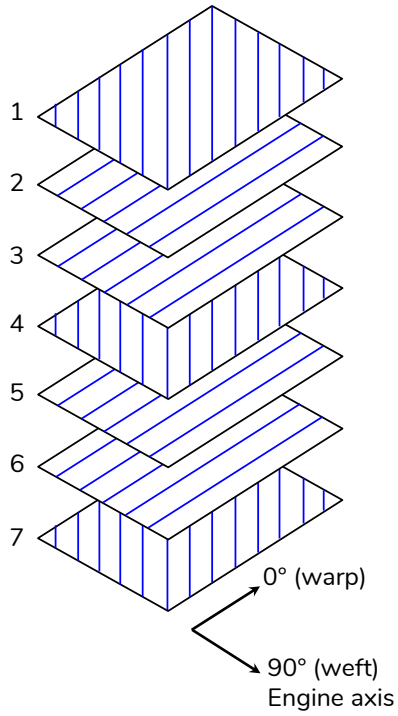

Figure 1-13. Exploded sketch of the top half of the laminate, showing its layup and the reference directions. The lines indicate the direction of the warp tows in the laminae.

Table 1-1. Layup of the laminate.

	Type of lamina	Orientation angle
1	Glass	45°
2	Weft heavy	0°
3	Weft heavy	0°
4	Balanced	45°
5	Warp heavy	0°
6	Warp heavy	0°
7	Balanced	45°
8	Balanced	45°
9	Warp heavy	0°
10	Warp heavy	0°
11	Balanced	45°
12	Weft heavy	0°
13	Weft heavy	0°
14	Glass	45°

It contains 14 laminae and is mirror symmetrical with respect to its mid-plane. Glass laminae are found at the top and bottom surfaces; they are laid up with an orientation angle of 45° meaning that their warp tows form an angle of 45° with the reference *0° direction*, i.e. the *circumferential direction* of the casing in this application. They are followed by two weft heavy laminae whose warp tows are aligned with the circumferential direction

(0° direction). One balanced lamina appears next with an orientation angle of 45°, followed by two warp heavy laminae whose warp tows are aligned with the 0° direction. Finally, one balanced lamina is found on either side of the mid-plane, with a 45° orientation angle.

As explained earlier, the fibre reinforcement laminate (the *preform*) is impregnated with a polymer matrix during the RTM process. This matrix is described below.

1.3.3.2 Resin and film adhesive

Two polymers are used in the composite booster casing: one is a resin that forms the continuous matrix phase of the composite laminate, the other is an adhesive intended to secure the adhesion of the steel strip to the casing.

The resin is HexFlow® RTM6 (Hexcel, USA), a one-part (i.e. premixed) epoxy system specifically designed for RTM processes and qualified for aerospace applications with service temperatures from -60 °C to 120 °C [32].

The adhesive is Redux® 322 300 gsm (Hexcel, USA), a high performance modified epoxy *film adhesive* with very low volatile content and suitable for bonding metal-to-metal or sandwich structures with service temperatures up to 200-220 °C [33]. The qualifier “modified” is given due to the presence of 10-30 % of aluminium flakes, a type of filler used to modify physical properties such as thermal conductivity and viscosity [16][34]. Besides, the film adhesive is supported on a woven nylon carrier that facilitates handling and delivers a constant bond line thickness.

Both of these materials are *epoxy resins*, a broad class of *thermosetting* polymers extensively used in structural and specialty composite applications for its multiple desirable properties such as high strength, high modulus, low shrinkage, excellent adhesion to various substrates, effective electrical insu-

lation, chemical and solvent resistance, thermal stability... [35]. The general formulation of an epoxy resin contains (i) at least one *base epoxy resin (*which bears the *epoxy groups),* (ii) at least one *curing agent* (also called *hardener* or *curative*) and, possibly, (iii) one *modifier* or more (used to provide specific physical and mechanical performance in both the unreacted and reacted system); it can be tailored at will to fit a wide range of applications [35].

RTM6 and Redux 322 are respectively based on TGMDA[3] and DGEBA[4], two of the most widely used aromatic base resins. In the course of an exothermic chemical reaction (called "*cure reaction*") with aromatic amine curing agents, crosslinks establish at the epoxy groups and an *infinite three-dimensional network* forms (Figure 1-14). This yields a glassy (i.e. *amorphous*), infusible and insoluble material [35][36] where crosslinks provide load transfer capacity since one molecule can pull on another [37].

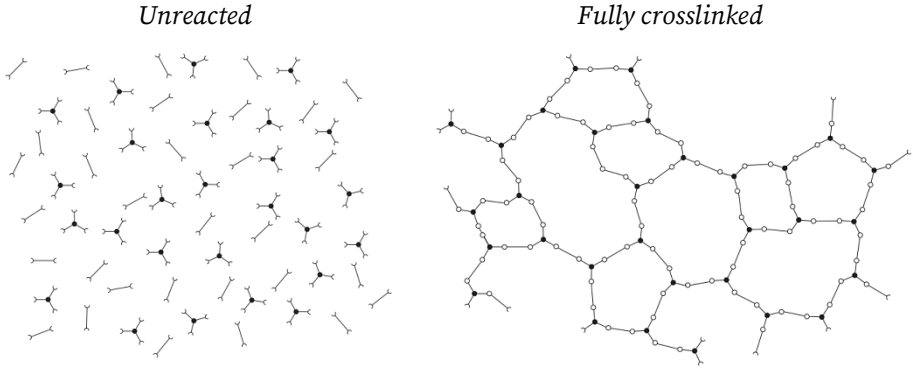

Figure 1-14. First step and final product of a cure polymerisation reaction: unreacted system (left) and fully crosslinked thermoset network (right) [36].

The cure reaction is thermally driven for both of these epoxy systems, therefore they are stored at -18 °C and cured at about 180 °C following the manufacturer's recommendations [32][33]. The flux of RTM6 resin crosses the film

[3] Tetraglycidil methylene dianiline.
[4] Diglycidil ether of bisphenol-A.

adhesive during co-curing, whereupon these epoxies form a heterogeneous, immiscible polymer blend. It has been observed by scanning electron microscopy (SEM) and an example of SEM micrograph is shown in Figure 1-15. This nodular morphology has sometimes been observed as deep as the first carbon lamina. Obviously, the blend microstructure varies on short distances (depending on the local relative concentration of the epoxies), with the change in nodules size, and the switch between matrix phase and secondary phase (nodules).

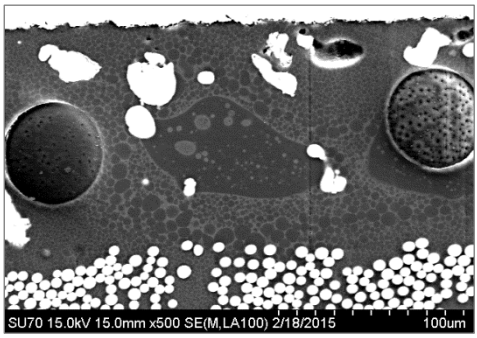

Figure 1-15. Scanning electron micrograph of the immiscible blend of RTM6 (dark grey) and Redux 322 (light grey) found in the co-cured joint.

Such nodular blend morphology might contribute to the toughening of the matrix phase, through several types of mechanisms involving the interaction of the growing crack with the dispersed phase (see e.g. [38] for a general overview, [39] and [40] for rubber toughening of epoxy polymers, and [41] for an example of thermoplastic toughening of RTM6). Yet, in the present case, some concerns exist about the dilution of Redux 322 with RTM6, which may result in some loss of its adhesive properties. This specific topic has not been further investigated in this work, though, and the question is still open.

1.3.3.3 Micro-perforated stainless steel sheet

The micro-perforated sheet metal is made of type AISI 316 L austenitic stainless steel, the composition of which is reported in Table 1-2.

Table 1-2. Chemical composition of type AISI 316 L austenitic stainless steel in wt.% (balance is Fe).

C	Cr	Ni	Mo	Mn	Si	N	S	P	Cu
0.019	16.72	10.13	2.17	1.44	0.38	0.052	0.0022	0.031	0.44

This alloy is an important technological material due to its excellent corrosion resistance and good mechanical properties [42][43]. Still, its yield strength and hardness need often be improved by work hardening [44]. The present sheet is cold rolled to its final thickness of 0.2 mm; this forming process modifies the steel microstructure, which becomes *anisotropic*. One therefore distinguishes two reference directions in the plane of the sheet: the rolling direction (RD) and the transverse direction (TD), perpendicular thereto. Microscopically, the grains are elongated in the rolling direction; macroscopically, this direction is indicated by the rolling stripes on the sheet surface (Figure 1-16-a). Furthermore, the large strains to which the material is submitted in the process of sheet forming by cold rolling may cause the transformation of some of the austenite phase (γ, FCC lattice) into hard martensite phase (α', BCC lattice) [44][45].

The sheet is used in a *micro-perforated* (M-P) form with 26.5 % open area, as opposed to its original *as-rolled* (A-R, solid, continuous) form (Figure 1-16-a). This provides an effect of *mechanical anchorage* or *interlocking* which improves its adhesion to the casing [46][47][48]. Besides, during the injection process micro-perforations are as many escape routes for the air initially trapped in the dry preform, and they also contribute to the overall weight reduction objctive.

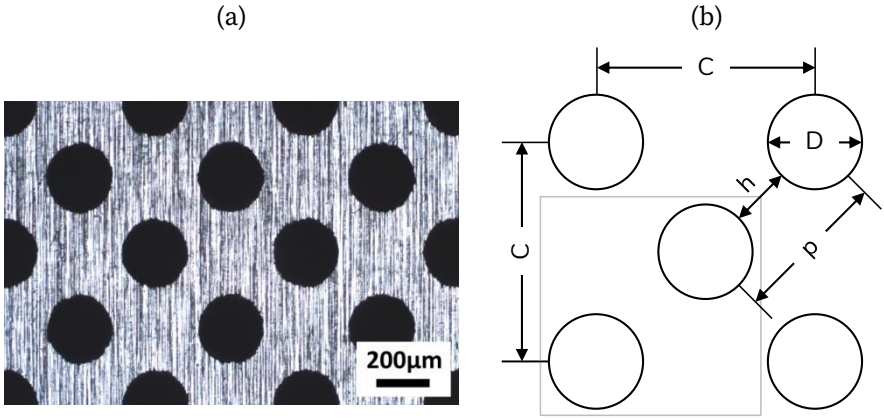

Figure 1-16. (a) Optical micrograph of the micro-perforated stainless steel sheet surface; (b) schematic penetration pattern with geometrical parameters and a square unit cell.

The present micro-perforation pattern (or *penetration pattern*) is a periodic arrangement of holes obtained by chemical etching, a process that does not strain the material. In the scientific literature dedicated to perforated plates (e.g. [49]), it would be referred to as *45° rotated square* and would be described by its *pitch* p -minimum centre-to-centre distance- and its *minimum ligament width* h -minimum distance separating neighbouring holes. The hole diameter D and the maximum centre-to-centre distance C are other important features. These quantities are shown on the schematic penetration pattern in Figure 1-16-b and their numerical values are given in Table 1-3.

Table 1-3. Values of the parameters describing the present penetration pattern.

Hole diameter	D	0.229	mm
Maximum centre-to-centre distance	C	0.557	mm
Minimum centre-to-centre distance (pitch)	p	0.394	mm
Minimum ligament width	h	0.165	mm

1.3.3.5 Abradable coating and bond coat

A good abradable material combines abradability and resistance to erosion by solid particles and gas. Some porous materials are likely to fulfil these requirements, as they wear away when they are rubbed by the blades. In particular, hybrid materials made of a low shear strength *metallic matrix* with a soft second phase (*solid lubricant*) are well established materials for low to medium-temperature abradable seals [22][50].

The abradable coating used in the present application is an aluminium-silicon based matrix with 40 wt.% polyester as second phase (AlSi-Po, Figure 1-17). It is produced by atmospheric plasma spray, a thermal spray process using plasma-generated thermal energy to melt fine particles and accelerate them towards the substrate surface [51]. The feedstock therefore is Metco 601NS *powder*.

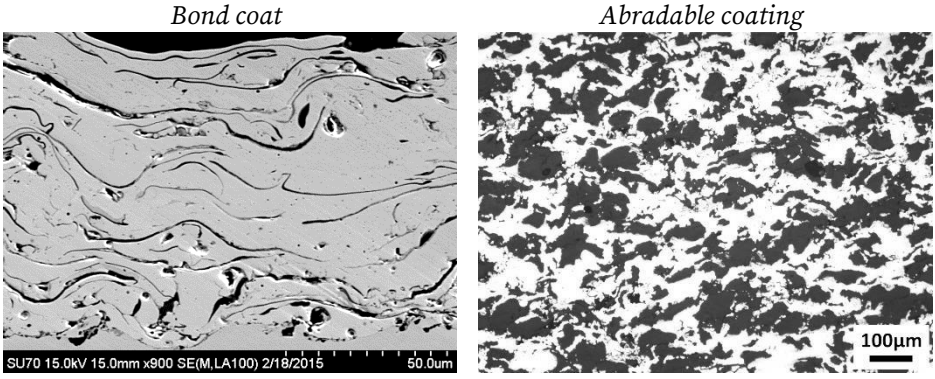

Figure 1-17. SEM micrograph of a cross-section of the bond coat (left) and optical micrograph of a cross-section of the abradable coating with polyester in dark grey (right).

Upon impact at the substrate surface, the molten spherical powder particles undergo significant deformation and freeze in the form of flat lamellae also known as “splats” [51]. The abradable coating is constructed incrementally onto the rotating casing, by superposition of continuous splats layers until a thickness of about 3 mm is attained. Note that a 0.1 mm thick nick-

el-aluminium bond coat is actually sprayed first (Metco 450NS powder) as an adhesion promoter.

The plasma spray process forms a characteristic lamellar structure, well identifiable in the bond coat cross-section (Figure 1-17). A very fine columnar microstructure furthermore exists within the splats due to their huge solidification rate. Such plasma sprayed abradable material is therefore *transversely isotropic*, with the plane of isotropy lying parallel to the surface [51].

1.3.4 A damaged end product

As a means of product quality assessment, the casing prototypes are frequently cut into small cross-section samples that are polished and observed with the optical microscope. Furthermore, some of the manufactured composite casings are subjected to *thermal shock* tests consisting in 1000 transfers between a cold chamber at -40 °C and a hot chamber at 135 °C. This treatment aims to approach, in an accelerated manner, the state of thermal ageing of a booster casing with 30 years of service.

It thus appeared quite early in the development process that the composite booster casing contains internal damage. In the regions covered by the abradable seal tracks, different forms of damage affect the composite substrate and the co-cured joint:

- *microcracks* in the co-cured joint
- *transverse* (or *intralaminar*) microcracks in the tows of the woven laminae
- *longitudinal* microcracks (or *meta-delaminations*) at the interface between warp and weft tows [52]
- vertical and horizontal *disbonds* of the steel strip segments

An example of each of these damage modes is given in Figure 1-18. Clearly, they are a manifestation of the thermally induced *residual stresses* that build up in the multi-layered system due to the *constrained differential thermal shrinkage* of its constituent materials.

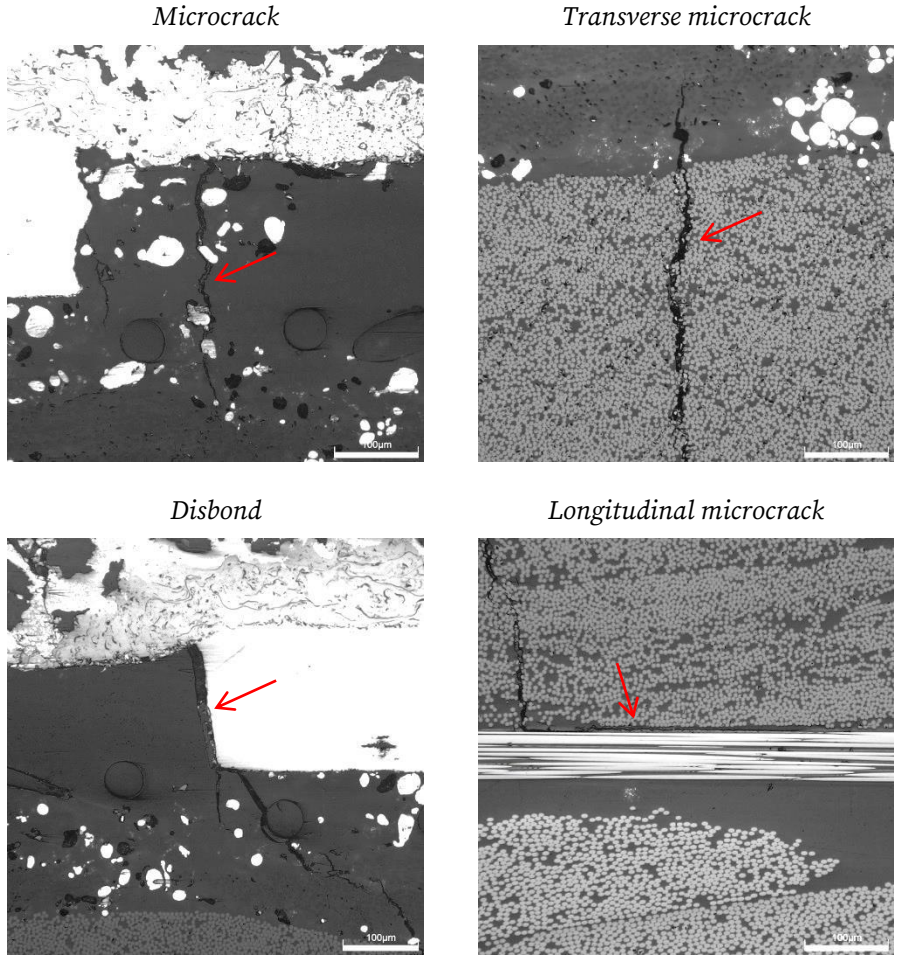

Figure 1-18. Optical micrographs showing examples of damage modes observed in cross-section of the composite casing, in the regions covered by the abradable seal tracks.

Although the extent of damage generally remains in the sub-millimetre range, obvious safety concerns call for a comprehensive study of their cause and the possible consequences.

1.4 Motivation, objective and outline of the thesis

Of course, the industrial partner addressed this thermo-mechanical damage issue internally in the first place. SAB's engineers developed an advanced 3D finite element (FE) model of the casing, which did unfortunately not converge towards realistic estimates of the damage state after thermal loading. It was changed for a more successful experimental approach in which intuitive solutions were tried and tested on real scale prototypes subjected to thermal cycles. At that time, given the cost and uncertainty of such a trial-and-error approach, SAB expressed the need for a new look at this multifaceted issue and its parallel comprehensive treatment through three research axes:

1) Understand the causes of the defects found at the multilayer's interfaces.
2) Propose solutions.
3) Evaluate and validate the solutions based on a reliable FE model capable of predicting the damage phenomena.

A long-term scientific methodology clearly needed to be established to accomplish these tasks, and the company turned to the academic community. This is how this doctoral research project was born, as well as the collaboration between Safran Aero Boosters and the Université libre de Bruxelles on this project. Several questions initially arose, some of which have found an answer in this work. *What is the relative importance of the different damage modes?, Is there a weak spot in the multi-layered system or casing?, What is the level of residual stresses and what does it trigger?, What change in materials or manufacturing operation could mitigate or eliminate damage?,* (and therefore)

What are the thermal, mechanical and fracture properties of the materials involved?,...

It is practically impossible to analytically determine the stress level present in such a complex system. This thesis therefore contributes to the elaboration of an advanced finite element model capable of predicting the residual stress level and its consequences at the multilayer scale. As a matter of fact, such a predictive numerical model is a valuable engineering tool that reduces the need for full-scale production and testing.

The development path to this model is multidisciplinary and features a strong coupling between computational and experimental work. Reliable experimental data had indeed to be obtained to feed the FE model and validate the results of the simulations. The research methodology developed and followed in this regard is summarised in Figure 1-19, and the corresponding work and achievements are presented in the six next chapters of this manuscript.

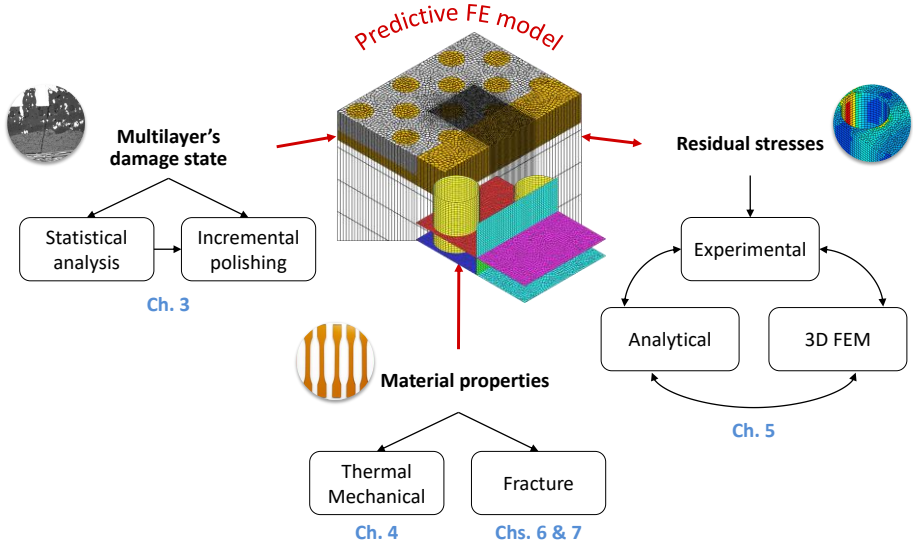

Figure 1-19. Methodology developed and applied in this doctoral research work.

After the present introduction which is coming to an end, **Chapter 2** revises the scientific background pertaining to thermomechanical damage in multilayers subject to residual stresses. **Chapter 3** presents the results of the experimental study of the damage state of several composite casings, while Chapter 4 contains the results of the experimental characterisation of the constituent materials in terms of thermal and mechanical properties. **Chapter 5** focuses on the evaluation of the thermally induced residual stress level by experimental, analytical and numerical methods. The experimental work performed for the characterisation of fracture in the co-cured joint is presented in **Chapter 6**. Finally, **Chapter 7** exposes the numerical work carried out for the FE modelling and inverse FE analysis of a double cantilever beam (DCB, mode I) test on a specimen with thermally induced residual stresses. In **Chapter 8**, we summarize the contributions of this research work and suggest some further work directions.

2. Scientific background

2.1 Introduction

The theoretical background exposed in this chapter contains some theory about residual stress in multilayers, fundamental concepts of linear elastic fracture mechanics, the description of several physical tests for the measurement of the fracture toughness of adhesively bonded joints, and, finally an introduction to progressive damage analysis with cohesive finite elements.

2.2 About residual stress

2.2.1 Origin of residual stresses in multilayers

A material body is seldom stress-free: even in the absence of applied loading, it can contain *residual stresses* [53], that is, *misfit* stresses caused by *incompatible* elastic or plastic strains generated thermally, chemically, or by (non-uniform) plastic deformation [54]. In essence, any permanent and non-uniform change in dimensions gives rise to residual stresses [53]. They are therefore found virtually everywhere: in single-phase as well as multi-phase bodies, in layered systems and in multipart components [54].

Residual stresses do *self-equilibrate* over a range that goes from the scale of the microstructure to the scale of the whole body, and can be classified accordingly. On the one hand, type I *macrostresses* are long range residual

stresses typical of thin films, welds, and engineering structures; type II and type III *microstresses*, on the other hand, are short range residual stresses typical of composite materials and phase transformations (type II) or dislocations and point defects (type III) [54].

Type I residual stresses are particularly relevant in the context of this thesis. By analogy with the thin films theory, they may also be categorised as *intrinsic* and *extrinsic* stresses [54][55]. The former are those stresses arising by different mechanisms *during* the growth of a film on a substrate, an example of which is the tensile stresses generated in the splats upon cooling during plasma spraying of bond coats and abradable coatings [54]. The latter are residual stresses arising from changes in the physical environment of a material system *after* it has been formed, an example of which is the distribution of thermal stresses in a bilayer due to the constrained differential thermal shrinkage of the film/substrate system cooled down from its temperature of assembly [54].

Indeed, thermal strains are proportional to the coefficient of linear thermal expansion (CTE, noted α) of the material (Eq. (2-1)) and, when constrained, give rise to thermal stresses whose magnitude scales with the Young's modulus of the material.

$$\varepsilon_{th} = \alpha \Delta T \tag{2-1}$$

The material property chart reproduced in Figure 2-1 shows the relation between the CTE and the Young's modulus for many materials of different families. Clearly, since different materials have different thermoelastic properties they experience different thermal strains for the same temperature change ΔT.

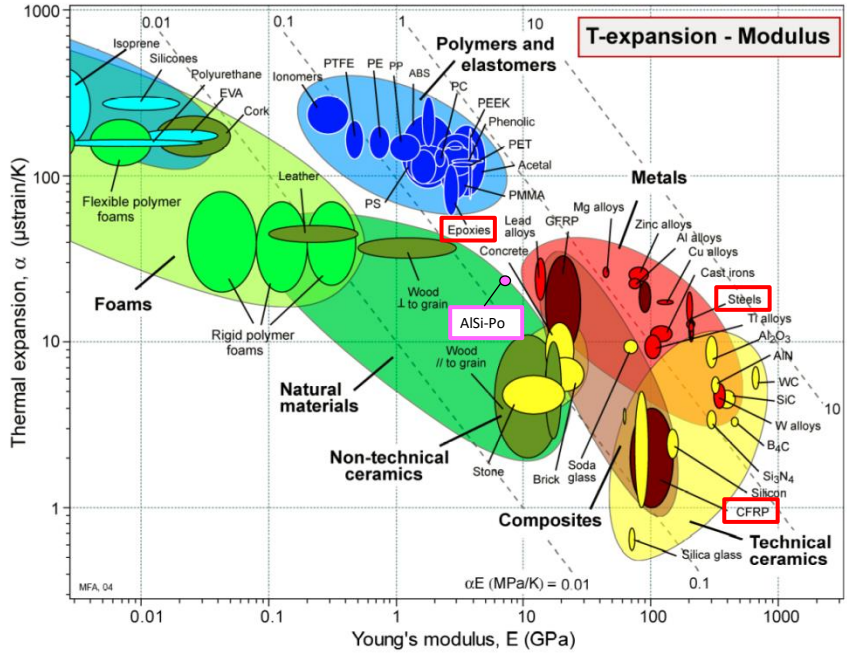

Figure 2-1. Material property chart showing the variation of the coefficient of linear thermal expansion with the Young's modulus for a wide variety of materials from different families [56]. *The materials involved in the multi-layered system studied in this thesis have either been highlighted with a red box or added to the chart in a pink box).*

The mental experiment illustrated in Figure 2-2 helps understanding the mechanism underlying the generation of thermal residual stresses, in particular for a film/substrate system with $\alpha_{film} > \alpha_{substrate}$ [53][57]. As long as the bilayer is at the assembly temperature, the film and substrate have the same lateral dimensions (Figure 2-2-a). If they were then separated and cooled to room temperature, their relaxed lengths would differ by an amount proportional to the difference between their thermal expansion coefficients (Figure 2-2-b). Reassembling the bilayer would thus require a biaxial extension of the film and a biaxial contraction of the substrate, to retrieve the compatibility of the dimensions at the interface (Figure 2-2-c). The residual stresses in the reconstituted bilayer can be represented as tensile forces along the mid-

plane of the film, and compressive forces along the mid-plane of the substrate (Figure 2-2-d) [53]. Because they are not symmetrically distributed about the mid-plane of the bilayer, these forces create a bending moment that is balanced by a change in the curvature of the system (Figure 2-2-e). A self-balanced residual stress field however still remains in the bilayer [53].

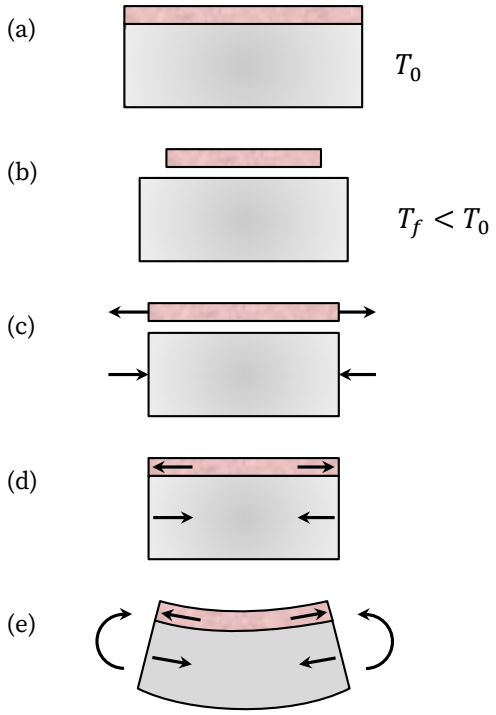

Figure 2-2. Imaginary deconstruction of a film/substrate system subject to thermal residual stresses. Inspired from [53] *and* [57].

Residual stresses may be beneficial as well as detrimental. On the one hand, positive (tensile) stresses are generally detrimental because they provide the driving force for crack growth. Negative (compressive) stresses, on the other hand, are generally beneficial as they keep the crack surfaces closed and thereby oppose crack growth. They may however also be detrimental as when they drive the delamination of thin films [58]. In any case, residual

stresses combine to the service stresses; their sign and magnitude must therefore be taken into account in the design of critical engineering components and structures to avoid premature, possibly catastrophic, failure [53][59].

Numerical methods may be required to compute the residual stress field. For thermally induced residual stresses in multi-layered systems, however, closed-form analytical solutions are available, such as that published in [60] and described below.

2.2.2 Analytical method for the evaluation of thermally induced residual stresses in multilayers

One considers a multilayer, without limitation on the number n of layers attached to the substrate [60]. The system is depicted in Figure 2-3, where the substrate is denoted by the subscript s, and the layers are denoted by the subscript i, with $i = 1$ to n.

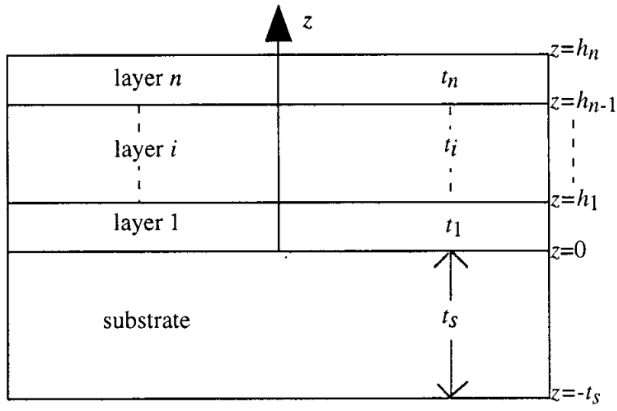

Figure 2-3. Multilayer with associated notations and coordinate system [60].

The substrate thickness is t_s and the thickness of layer i is t_i. The origin of the coordinate system ($z = 0$) is located at the interface between the sub-

strate and layer 1; the coordinate of the interface between layer i and layer $i+1$ is therefore noted h_i, which is related to the thicknesses t_i through

$$h_i = \sum_{j=1}^{i} t_j \tag{2-2}$$

The materials are isotropic and follow a linear elastic behaviour; the Young's modulus is E_s for the substrate and E_i for layer i in a one-dimensional geometry. In a two-dimensional geometry, they should be replaced by the corresponding biaxial modulus, $E/(1-\nu)$, where ν is Poisson's ratio. The coefficients of thermal expansion of the substrate and layers are noted α_s and α_i, respectively. The layers are deposited at an elevated temperature, T_0, after which the multilayer is allowed to cool down to temperature T_f. Again, bending results from the asymmetric distribution of thermal stresses in the system; the radius of curvature of the multilayer is noted r, and the bending axis is defined as the line with zero bending strain situated at $z = t_b$.

Following the logic described in Figure 2-2, the strain distribution in the system, ε, can be decomposed into a uniform component, c (Figure 2-2-c), and a bending component (Figure 2-2-e). The latter is proportional to the distance from the bending axis and to the curvature of the multi-layered system, $\kappa = 1/r$. This is expressed in Eq. (2-3) for z comprised between $-t_s$ and h_n [60].

$$\varepsilon = c + \kappa(z - t_b) \tag{2-3}$$

The distributions of stress in the thickness of the substrate and layers, σ_s and σ_i, are in turn related to the strain by Eq. (2-4) (for z comprised between $-t_s$ and 0) and Eq. (2-5), where $\Delta T = T_f - T_0$ [60].

$$\sigma_s = E_s(\varepsilon - \alpha_s \Delta T) \tag{2-4}$$

$$\sigma_i = E_i(\varepsilon - \alpha_i \Delta T) \tag{2-5}$$

The expressions for stresses and strains in the multilayer thus involve three unknowns, i.e. parameters c, t_b and κ. These can be determined by solving three equations inferred from the boundary conditions. First, the uniform strain component is given by Eq. (2-7), which derives from the condition of equilibrium of the forces caused by that strain component (Eq. (2-6)) [60].

$$E_s(c - \alpha_s \Delta T)t_s + \sum_{i=1}^{n} E_i(c - \alpha_i \Delta T)t_i = 0 \tag{2-6}$$

$$c = \frac{(E_s t_s \alpha_s + \sum_{i=1}^{n} E_i t_i \alpha_i)\Delta T}{E_s t_s + \sum_{i=1}^{n} E_i t_i} \tag{2-7}$$

Second, the coordinate of the bending axis is given by Eq. (2-9), which derives from the condition of equilibrium of the forces corresponding to the bending strain component (Eq. (2-8), with $h_{i-1} = 0$ when $i = 1$) [60].

$$\int_{-t_s}^{0} E_s \kappa (z - t_b) dz + \sum_{i=1}^{n} \int_{h_{i-1}}^{h_i} E_i \kappa (z - t_b) dz = 0 \tag{2-8}$$

$$t_b = \frac{-E_s t_s^2 + \sum_{i=1}^{n} E_i t_i (2h_{i-1} + t_i)}{2\left(E_s t_s + \sum_{i=1}^{n} E_i t_i\right)} \tag{2-9}$$

Third, the curvature is given by Eq. (2-11), which derives from the condition of equilibrium of the bending moments (Eq. (2-10)) [60].

$$\int_{-t_s}^{0} \sigma_s (z - t_b) dz + \sum_{i=1}^{n} \int_{h_{i-1}}^{h_i} \sigma_i (z - t_b) dz = 0 \tag{2-10}$$

$$\kappa = \frac{3[E_s(c - \alpha_s \Delta T)t_s^2 - \sum_{i=1}^{n} E_i t_i (c - \alpha_i \Delta T)(2h_{i-1} + t_i)]}{E_s t_s^2 (2t_s + 3t_b) + \sum_{i=1}^{n} E_i t_i [6h_{i-1}^2 + 6h_{i-1} t_i + 2t_i^2 - 3t_b(2h_{i-1} + t_i)]} \tag{2-11}$$

With the above solutions for parameters c, t_b and κ, one can determine the exact distribution of elastic stresses and strains in the multilayer.

Furthermore, for the particular case of a bilayer made of a single film (subscript f) on a substrate, it is possible to express the average residual stress in the film either in terms of the (radius of) curvature of the system (Eq. (2-12)) or in terms of the thermal mismatch (Eq. (2-13)) [60].

$$\overline{\sigma_f} = \frac{-\left(E_s t_s^3 + E_f t_f^3\right)}{6t_f\left(t_s + t_f\right)r} \tag{2-12}$$

$$\overline{\sigma_f} = \frac{E_s E_f t_s\left(E_s t_s^3 + E_f t_f^3\right)\left(\alpha_s - \alpha_f\right)\Delta T}{E_s^2 t_s^4 + E_f^2 t_f^4 + 2E_s E_f t_s t_f\left(2t_s^2 + 2t_f^2 + 3t_s t_f\right)} \tag{2-13}$$

Assuming that the film is much thinner than the substrate ($t_f \ll t_s$), these equations respectively reduce to Eq. (2-14) and Eq. (2-15) [60]. Remarkably, the former equation is the same as the classical Stoney formula that relates the stress in a thin film to the uniform curvature of its substrate [61][55]. The latter equation, on the other hand, yields the average residual stress level in the film when the substrate is so stiff that it imposes its thermal strain to the film.

$$\sigma_0 = -\frac{E_s t_s^2}{6t_f r} \tag{2-14}$$

$$\sigma_0 = E_f\left(\alpha_s - \alpha_f\right)\Delta T \tag{2-15}$$

2.3 Fracture mechanics of multilayers

2.3.1 Introduction

The field of science pertaining to the development of cracks in materials is named *fracture mechanics*. It involves methods of analytical and computational solid mechanics to calculate the driving force on a crack, and methods of experimental solid mechanics to characterise the material's resistance to fracture [62]. Historically, fracture mechanics was born in the context of straight sharp cracks in *brittle* materials[5]; one such crack is illustrated in Figure 2-4 with two of its important features, namely the *crack faces* and the *crack front* (or *crack tip*, in 2D).

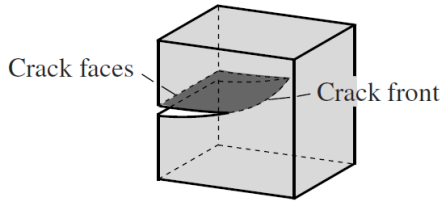

Figure 2-4. Example of cracked body [63].

Fracture mechanics, however, has evolved over the years to account for other types and shapes of flaws and other material behaviours. One therefore distinguishes two branches of fracture mechanics: *linear elastic* fracture mechanics (LEFM) and *nonlinear* fracture mechanics; whichever is used depends on the material behaviour of the cracked body [64]. The former applies to the fracture of materials and structures whose global behaviour is linear elastic; in this case, plastic deformation (if any) is confined to a region that is negligibly small compared with the macroscopic dimensions of the body [63]. The latter, on the contrary, applies to materials and structures that undergo

[5] Whose failure strain is small, with little or no plastic deformation before failure (as opposed to *ductile* materials).

significant plastic deformation before failure, and to time-dependent materials [64]. Some fundamental concepts of LEFM are exposed in what follows.

2.3.2 Small-scale yielding

Cracks, as a geometrical discontinuity, do locally alter the otherwise uniform spatial distribution of stresses and strains in a loaded body: stress tends to concentrate in the vicinity of the discontinuity, where a local stress-strain field thus exists. The intensity of that stress field gives rise to the formation of a small region called *plastic zone* or *fracture process zone* (FPZ) at the crack tip, where inelastic (i.e. irreversible) processes, such as plastic deformation, take place in addition to atomic bond breaking [63]. This region is schematically illustrated in Figure 2-5.

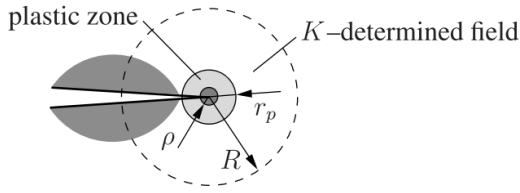

Figure 2-5. Plastic zone (radius r_p) and zone of K-dominance (outer radius R) at the tip of a crack, adapted from [63]. *A zone of radius ρ where bond breaking occurs is also represented.*

The fundamental assumption of linear elastic fracture mechanics is that inelastic processes are confined to the plastic zone or FPZ, which, in addition, is very small compared to the macroscopic dimensions of the cracked body. This is called the *small-scale yielding* (SSY) condition [64][65].

When it is satisfied, an annular region exists at the crack tip where the stress-displacement field is completely characterised by a single parameter: the stress intensity factor (noted K), which will be properly introduced in the next section. This region is thus called the zone of *K-dominance* [65]; it is illustrated in Figure 2-5.

The size of the plastic zone increases during crack growth until it reaches the steady-state. In front of the crack tip, this size can be estimated with Eq. (2-16), where M is a factor that depends on the model hypotheses, K_I is the (mode I) stress intensity factor, and σ_y is the yield stress of the material [64].

$$r_p = M\left(\frac{K_I}{\sigma_y}\right)^2 \tag{2-16}$$

As already mentioned, SSY is valid only as long as the plastic zone size is small relative to key dimensions of the body, such as the crack size. In practice, it therefore takes very large specimens to test low strength, high toughness materials in the context of LEFM [64].

2.3.3 Stress intensity factor

A crack in a loaded body may experience one of the basic loading modes illustrated in Figure 2-6, or a combination thereof.

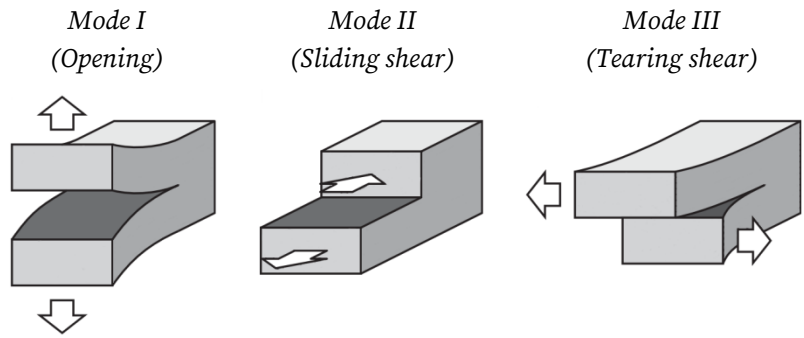

Figure 2-6. The three fundamental modes of crack loading, adapted from [66].

Mode I is characterised by the symmetric displacement of the crack faces in the direction perpendicular to the plane of the crack. Mode II is characterised by the antisymmetric displacement of the crack faces in the plane of the crack, in the direction normal to the crack front. Finally, Mode III is charac-

terised by the displacement of the crack faces in the plane of the crack, in the direction parallel to the crack front. Mode I problems prevail while mode III problems are the least commonly encountered [62].

With the origin of a polar coordinate system defined at the crack tip (Figure 2-7), the local stress field produced by a pure mode of crack loading is described by Eq. (2-17) for an isotropic linear elastic body [64].

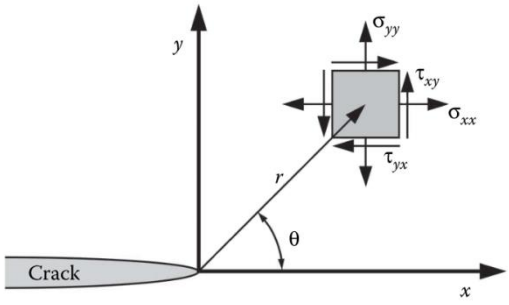

Figure 2-7. Definition of the polar and Cartesian coordinate systems at a crack tip [64]. *Components of the stress tensor are shown on a material particle close to the crack tip.*

$$\sigma_{ij} = \frac{K}{\sqrt{2\pi r}} f_{ij}(\theta) \tag{2-17}$$

In this expression, σ_{ij} is a component of the stress tensor, r and θ are the polar coordinates defined in Figure 2-7, and f_{ij} is a dimensionless trigonometric function of θ that is mode-dependent and can be found in reference books on fracture mechanics such as [62] and [64], for instance. Parameter K, on the other hand, is the *stress intensity factor* (SIF) expressed in $\mathrm{MPa}\sqrt{\mathrm{m}}$.

For a given loading mode, the *distribution* of the stress field at the crack tip is thus clearly independent of the loading and geometry. Besides, because the right-hand-side term is proportional to $1/\sqrt{r}$, stress is asymptotic to $r = 0$ and the stress field is square-root singular. In contrast, the *amplitude* of this singularity is set by the SIF that depends on the applied load, the crack size,

and the geometry of the cracked body. Hence, the parameter K is the only "messenger" between the boundary conditions and the crack tip fields [67]; it does play an extremely important role in the mechanics of brittle fracture as it completely characterises the crack tip conditions in a linear elastic body [62][64][65]. Closed-form solutions for K have been derived for a number of simple configurations. As an example, the SIF of the so-called *Griffith crack*[6] is given by Eq. (2-18), where the subscript I refers to pure mode I loading [64].

$$K_I = \sigma_\infty \sqrt{\pi a} \tag{2-18}$$

K can otherwise be estimated experimentally or numerically. Several handbooks (e.g. [68]) gather the stress intensity solutions that have been published so far.

2.3.4 Strain energy release rate

A continuum body subjected to external quasi-static loading undergoes a change in internal energy. Potential energy accumulated in that material body can be released in the process of extension of an existing crack if it is larger than the energy to be spent in the fracture of the material.

The law of conservation of energy dictates the global energy balance during crack growth for such a system containing a crack of area A. This reads

$$\frac{\partial W}{\partial A} = \frac{\partial E}{\partial A} + \frac{\partial \Gamma}{\partial A} \tag{2-19}$$

that is, the rate of work supplied to the continuum by the applied loads ($\partial W/\partial A$) distributes into the rate of internal energy ($\partial E/\partial A$) and the rate of energy dissipated in crack propagation ($\partial \Gamma/\partial A$) [65]. Note that in this context,

[6] A central, through-thickness, crack of length $2a$ in an infinite plate subject to a remote tensile stress σ_∞ applied perpendicular to the crack plane.

the term rate does not refer to a derivative with respect to time; instead, it refers to the rate of change of the quantity with the crack area.

The internal energy can be developed as the sum of the elastic strain energy U^e and the plastic work U^p:

$$E = U^e + U^p \tag{2-20}$$

In the linear elastic case, the plastic work is negligible and one can thus recast the energy balance as

$$\frac{\partial W}{\partial A} = \frac{\partial U^e}{\partial A} + \frac{\partial \Gamma}{\partial A} \tag{2-21}$$

Further, Eq. (2-21) can be written in terms of the potential energy of the system, $\Pi = U^e - W$. This yields

$$\frac{\partial \Gamma}{\partial A} = -\frac{\partial \Pi}{\partial A} \tag{2-22}$$

Hence, the rate of increase in energy dissipated in the crack extension process is equal to the rate of decrease in potential energy of the system [65]. Potential energy is thus irreversibly released during crack growth [62].

Eq. (2-22) is actually most generally known under the form given in Eq. (2-23), where G is the *strain energy release rate* (SERR).

$$G = -\frac{\partial \Pi}{\partial A} \tag{2-23}$$

So, G is a measure of the energy available for an increment of extension of the crack surface and is therefore expressed in Jm^{-2}. Given that these units can reduce to Nm^{-1}, G is sometimes also called the *crack extension force* or *crack driving force* [63].

It can be shown that the SERR is related to the compliance of a linear elastic body subjected to an arbitrary loading through Eq. (2-24), where P is the applied load (or the reaction force) and C is the compliance, which is an increasing function of the crack area. This relation is known as the *Irwin-Kies equation*. It offers a means of determining G experimentally; examples of application of this definition will be given in section 2.4.2 for several test configurations.

$$G = \frac{P^2}{2}\frac{\partial C}{\partial A} \tag{2-24}$$

Eq. (2-24) also allows deriving closed-form solutions for K. The strain energy release rate and the stress intensity factor are indeed univocally related, as developed below.

2.3.5 Relationship between G and K

Two parameters have been introduced so far that describe the behaviour of cracks from a global (G) or local (K) point of view. It can be shown that the release of strain energy associated with the extension of a crack can be calculated from the crack tip stress-displacement field. A unique relation thus exists between G and K, which is described by

$$\begin{cases} G_{I,II} = \dfrac{{K_{I,II}}^2}{\bar{E}} \\ G_{III} = \dfrac{{K_{III}}^2}{2\mu} \end{cases} \tag{2-25}$$

where subscripts I, II and III denote the mode of loading, $\bar{E} = E/(1-\nu^2)$ under plane strain conditions and $\bar{E} = E$ under plane stress conditions (with E the Young's modulus and ν Poisson's ratio) and $\mu = E/2(1+\nu)$ is the shear modulus [62][63].

2.3.6 Fracture toughness

In the traditional strength of materials approach to structural design, the expected stress level is kept below the material tensile or yield strength through appropriate design and material selection. Similarly, in the fracture mechanics approach, the quantity K or G is compared with the *fracture toughness* of the material noted K_c or G_c [64]. Hence, the onset of fracture occurs if Eq. (2-26) (or, equally, Eq. (2-27)) is satisfied.

$$K = K_c \tag{2-26}$$

$$G = G_c \tag{2-27}$$

Indeed, assuming that the material fails locally at some critical stress implies that fracture must occur at a *critical value* of stress intensity, K_c. Equivalently, fracture occurs when the energy available for crack extension reaches a critical value sufficient to overcome the material resistance, G_c [64].

Fracture toughness is a material property representative of the amount of energy needed to advance a crack by a unit area. Except for ideally brittle materials, this amount is much larger than the surface energy alone owing to the presence of the plastic zone at the crack tip. Fracture toughness can thus be expressed in terms of its different contributions as in Eq. (2-28), where γ_s is the surface energy density, that is, the energy required to form a unit of new material surface, and w_p represents the energy dissipated in the plastic zone per unit area of the fracture formed [55].

$$G_c = 2\gamma_s + w_p \tag{2-28}$$

Plastic work generally increases during crack growth along with the size of the plastic zone, and eventually reaches a constant value as the plastic zone attains its steady-state size. Consequently, a material's resistance to crack extension is most often described by a function $G_R(\Delta a)$ known as *crack growth*

resistance curve or *R-curve*, rather than by a single G_c value [63][64]. One such curve is illustrated in bold in Figure 2-8, where G_R does monotonously increase with crack advance (noted Δa). The R-curve is a characteristic of the material for a given thickness, temperature and strain rate [65].

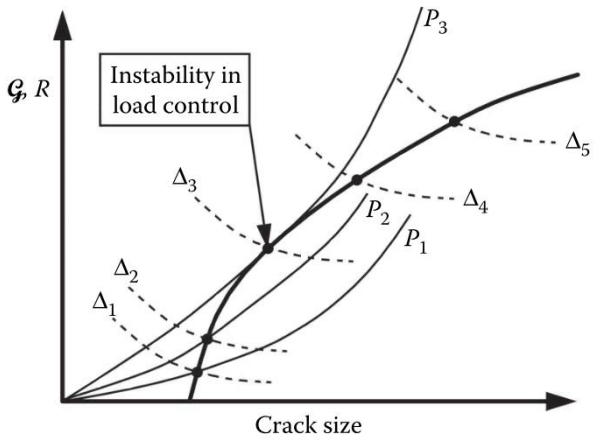

Figure 2-8. Schematic representation of a "rising" R-curve (in bold), adapted from [64]*. The crack driving force curves are typical of a test on a DCB specimen performed under displacement control (dashed,* Δ*) or load control (continuous,* P*).*

As already mentioned, the onset of fracture occurs when Eq. (2-26) (or Eq. (2-27)) is satisfied. Furthermore, crack growth can be *stable* or *unstable*, the former meaning that a loading increment must be supplied to obtain a crack extension increment. Stability depends on how the crack driving force, G, and the crack resistance force, G_R, vary with crack size [64]. Indeed, a crack grows stably when, at the point where the criterion for fracture (Eq. (2-26)) is satisfied, the rate of change of the crack driving force curve is slower than that of the R-curve. Stated another way, the crack resistance force must increase more rapidly with increasing crack length than the crack driving force [63]. The conditions for stable crack growth are thus expressed by [64]:

$$G = G_R \tag{2-29}$$

$$\frac{\partial G}{\partial a} < \frac{\partial G_R}{\partial a} \tag{2-30}$$

Finally, note that the rate of change of G depends on how the structure is loaded; displacement control tends to be more stable than load control, as illustrated schematically in Figure 2-8.

2.3.7 Mixed mode fracture

2.3.7.1 Mixed mode loading: local and global descriptions

The concepts introduced so far have been presented in the context of crack loading in pure mode. Yet, in practice, the loads are not necessarily aligned with the orientation of the crack, so that an actual crack generally grows under a combination of mode I and mode II (mode III is seldom active and will thus be ignored). In such a *mixed mode* problem, following the principle of linear superposition, the individual contributions to a given stress component can be summed, and Eq. (2-17) takes the general form [58]:

$$\sigma_{ij} = \frac{K_I}{\sqrt{2\pi r}} f_{ij}^{I}(\theta) + \frac{K_{II}}{\sqrt{2\pi r}} f_{ij}^{II}(\theta) \tag{2-31}$$

The G-K relationship defined by Eq. (2-25) in pure mode becomes Eq. (2-32) in mixed mode, where it appears that the SERR relates to the two pure mode SIFs [58]. By application of Eq. (2-25), the latter relation becomes Eq. (2-33), which highlights the additivity of the pure mode energy release rates.

$$G = \frac{K_I^2}{\bar{E}} + \frac{K_{II}^2}{\bar{E}} \tag{2-32}$$

$$G = G_I + G_{II} \tag{2-33}$$

Mixed mode loading is commonly described through G and ψ rather than K_I and K_{II}. The energy release rate represents the amplitude of the loads, while ψ, the *mode mixity angle*, is a measure of the relative proportion of mode II to mode I. It is defined by Eq. (2-34), from which it can be inferred that the limiting cases of pure mode I and pure mode II loading are described by $\psi = 0°$ and $\psi = \pm 90°$, respectively [67].

$$\psi = \tan^{-1}\left(\frac{K_{II}}{K_I}\right) \tag{2-34}$$

2.3.7.2 Fracture envelope and mixed mode fracture criteria

Fracture toughness depends on the mode of loading, which is usually emphasised by the notation $G_c(\psi)$. The critical condition for crack growth can thus be represented by a *fracture envelope*, i.e. a curve in the (K_{Ic}, K_{IIc})-plane or, alternatively, in the (G_c, ψ)-plane. As it is definitely impractical to measure G_c for all mixed mode combinations, many different fracture criteria have been proposed to extrapolate a mixed mode fracture behaviour from just a few experimental fracture toughness data [69]. These criteria model the fracture envelope by means of some set of parameters that generally comprises physical parameters such as the pure mode fracture toughnesses, and fit parameters. 2D mixed mode fracture criteria define the value of G_c for all combinations of crack loading modes from pure mode I to pure mode II; they have been reviewed in [70] and [71]. Extensions to 3D mixed mode criteria incorporating the effect of the mode III component of crack loading have been investigated in [69]. The equations of two 3D fracture criteria, namely the 3D power law (PL) criterion (Eq. (2-35)) and the 3D adaptation of the Benzeggagh-Kenane (B-K) criterion (Eq. (2-36)), are given in this introductory chapter for that they are implemented in the commercial FE packages SAMCEF and ABAQUS, respectively. Once introduced, the B-K criterion

(whose original 2D form was proposed in [72]) has superseded the power law criterion in many publications [69].

$$\left(\frac{G_I}{G_{Ic}}\right)^{\alpha} + \left(\frac{G_{II}}{G_{IIc}}\right)^{\beta} + \left(\frac{G_{III}}{G_{IIIc}}\right)^{\chi} \geq 1 \tag{2-35}$$

$$\frac{G_T}{G_{Ic} + \left((G_{IIc} - G_{Ic})\frac{G_{II}}{G_T} + (G_{IIIc} - G_{Ic})\frac{G_{III}}{G_T}\right)\left(\frac{G_{II} + G_{III}}{G_T}\right)^{\eta-1}} \geq 1 \tag{2-36}$$

Note that $G_c(0°)$ is always the lowest and it is well established that, in a homogeneous isotropic solid, crack growth therefore follows a trajectory that provides mode I conditions at the crack tip [67][71]. Hence, Eq. (2-27) with mode I fracture toughness often provides an acceptable, conservative, fracture criterion. Nevertheless, the concept of mixed mode cracking is central to another field of fracture mechanics, which is concerned with interface fracture.

2.3.7.3 Interface fracture

A crack found in the interface between two dissimilar materials has an intrinsically mixed mode crack tip stress field due to the mismatch in elastic properties of the adjacent materials. The latter is described by the Dundurs' parameters, α and β [58], whose exact expression is given in Appendix A. Furthermore, the crack may not be able to deviate into either of the neighbouring solids to find a local mode I path [58]. Such *interface crack* is sketched in Figure 2-9, where material 1 is stiffer than material 2.

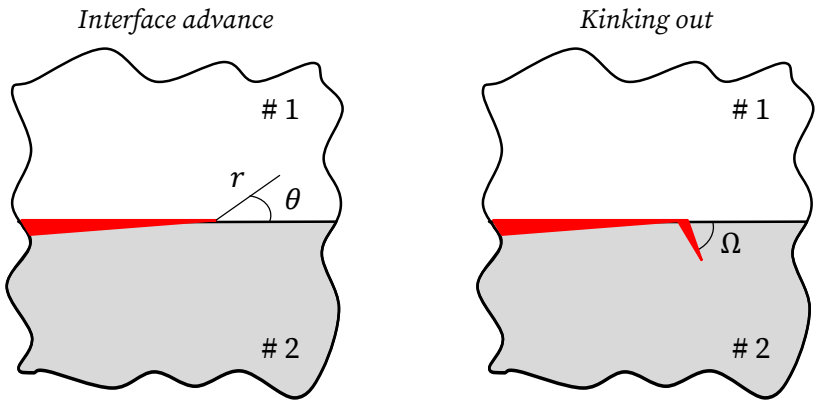

Figure 2-9. Schematic of (left) a crack propagating straight ahead at a bimaterial interface and (right) kinking out of that interface.

In addition to being mixed mode, the stress field at the tip of an interface crack presents the *oscillatory singularity* described by Eq. (2-37), where $i = \sqrt{-1}$ and $r^{i\varepsilon} = \cos(\varepsilon \ln r) + i \sin(\varepsilon \ln r)$ [58].

$$\sigma_{ij} = \frac{\mathrm{Re}\left[K r^{i\varepsilon}\right]}{\sqrt{2\pi r}} f_{ij}^{I}(\theta, \varepsilon) + \frac{\mathrm{Im}\left[K r^{i\varepsilon}\right]}{\sqrt{2\pi r}} f_{ij}^{II}(\theta, \varepsilon) \tag{2-37}$$

In this equation, ε is the dimensionless *bimaterial constant*; it is defined in Eq. (2-38) where its dependence on the elastic properties of the materials appears through the Dundurs' parameter β.

$$\varepsilon = \frac{1}{2\pi} \ln\left(\frac{1-\beta}{1+\beta}\right) \tag{2-38}$$

Besides, K is now the *complex interface stress intensity factor* defined in Eq. (2-39), with real and imaginary parts K_1 and K_2.

$$K = K_1 + iK_2 \tag{2-39}$$

The angular functions $f_{ij}^{I}(\theta, \varepsilon)$ and $f_{ij}^{II}(\theta, \varepsilon)$ are normalised, so that the stresses on the interface ahead of the crack tip are given by Eq. (2-40) [58].

$$\sigma_{xx} + i\tau_{xy} = \frac{(K_1 + iK_2)}{\sqrt{2\pi r}} r^{i\varepsilon} \tag{2-40}$$

It can be shown that K_1 and K_2 are both associated with the normal *and* shear components of stress acting on the interface, so that they cannot be simply related to either K_I or K_{II}. Moreover, the displacement field oscillates as well, which dictates the interpenetration -or more exactly, the contact- of the crack faces at some distances behind the crack tip. These difficulties are commonly overcome by letting $\beta = 0$ (and thereby $\varepsilon = 0$), which is an acceptable approximation for most bimaterial systems [58]. In this case, Eq. (2-37) reduces to Eq. (2-31), so that the crack tip stress field is again correctly described by the square-root singularity, and K_I and K_{II} respectively set the amplitude of the normal and shear stresses on the interface [58]. Given its mixed mode nature, loading of an interface crack can also be defined by the pair (G, ψ). Besides, the *interface toughness* is mode-dependent, as illustrated in Figure 2-10 for a Plexiglas/epoxy interface; it is thus again noted $G_c(\psi)$ and can be modelled with mixed mode criteria [58].

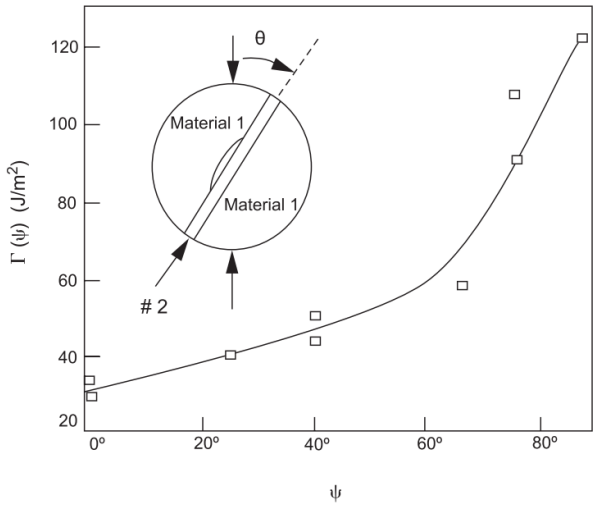

Figure 2-10. Fracture envelope of a Plexiglas/epoxy (material 1/material 2) interface [58]. *The caption illustrates the Brazil nut test specimen used to obtain these data.*

Interface cracks face some competition between the propagation modes illustrated in Figure 2-9: the crack may grow *straight-ahead in the interface* or it may *kink out of the interface*, with an angle Ω that usually minimises the mode II contribution to the SERR [58]. This has been studied in [73] and is briefly addressed in Appendix B. The competition between crack *penetration through an interface* and crack *deflection into an interface* has also received attention [74][75]. It is illustrated in Figure 2-11, where the parent crack impinges the interface at right angle and is stressed symmetrically with respect to its plane. This case is also briefly addressed in the same appendix.

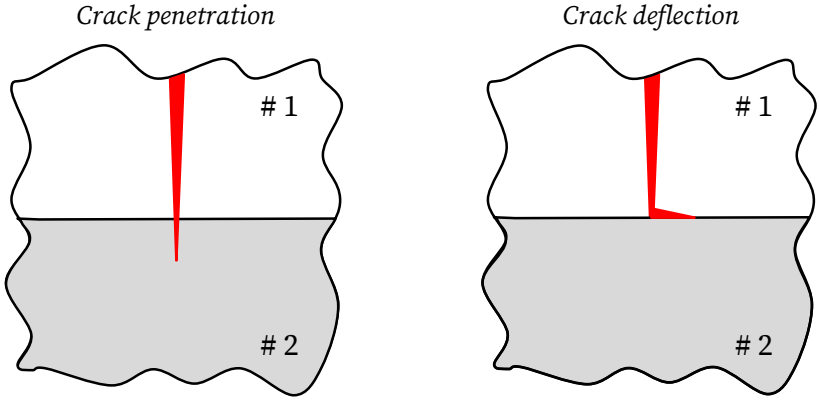

Figure 2-11. Schematic of a crack that, upon impinging a bimaterial interface, (left) penetrates through that interface or (right) is deflected into that interface.

2.4 Fracture toughness testing of adhesively bonded joints

2.4.1 Introduction

The fracture mechanics approach to design fundamentally relies on the knowledge of fracture toughness [64]. This property of a material or an interface is usually measured experimentally; a wide panel of mechanical tests exists, among which a natural distinction is made between those that satisfy

the LEFM assumption and those that do not. The present section focuses on a sample of tests used to measure the fracture toughness of *adhesively bonded joints*; the topic has otherwise been comprehensively covered in [76], [77] and [78], for instance.

Adhesives can either be tested as bulk specimens or as part of adhesively bonded joints. The latter configuration has the merit of placing the adhesive in conditions similar to those under which it is generally used. Indeed, applying adhesive as a thin layer between substrates has several consequences that differentiate its fracture toughness from that of bulk adhesive [78]. Among them, one can cite (i) the influence of the bond line thickness on the steady-state size of the crack tip plastic zone, (ii) the different possible locations of the failure path (cohesive at the centreline, cohesive near the interface, interfacial,...), (iii) the constraint effect of the substrates, which contain the crack path within the adhesive layer even under mixed mode or mode II loading conditions.

An important class of fracture tests is based on the *beam-type* specimen geometry [58]. It falls in the category of tests that satisfy the LEFM assumption, meaning that the specimen undergoes no permanent deformation during the test. This presents the advantage of providing a firm theoretical basis for the *data reduction* process, i.e. the conversion of the experimental data into a value of the fracture toughness of the adhesively bonded joint.

Another important class of mechanical tests used for the characterisation of adhesively bonded assemblies is based on the controlled peeling of a flexible adherend off a flexible or rigid substrate. Peel tests fall in the category of tests that do not satisfy the LEFM assumption, as the peel arm often undergoes extensive plastic deformation during the test. The data reduction scheme takes this energy loss into account and provides a value of a material parameter called *adhesive fracture energy*, which, similarly to the fracture

toughness, encompasses the energy required to break the atomic bonds, and the energy dissipated locally ahead of the peel front [79].

Both families of tests are introduced in the next sub-sections, starting with that based on the elastic bending of beam-type specimens.

2.4.2 Beam-bending LEFM tests

2.4.2.1 General overview

The beam-type test specimen is a beam of thickness $2h$ which separates at one end into two beams of thickness h, called the *cantilever arms*. Basically, two symmetric beam adherends are joined with an adhesive bond line of constant thickness, leaving an unbonded area at one end. The test specimen is loaded under displacement control so as to initiate and drive the propagation of a pre-crack in the adhesive layer. The load-displacement curve is recorded, and the crack advance is monitored throughout the test and plotted regularly on this curve. Then, the fracture toughness (or R-curve) is derived using a data reduction scheme based on the Irwin-Kies equation (Eq. (2-24)) and beam theory.

A variety of mode mixity angles can be accessed through proper control of the loading configuration and/or the specimen geometry, allowing to explore the *fracture envelope* (i.e. $G_c(\psi)$) from mode I to mode II. Pure mode I crack loading is universally achieved with the Double Cantilever Beam (DCB) test sketched in Figure 2-12 or the tapered version of it (TDCB), and pure mode II is most popularly achieved with the End-Notched Flexure (ENF) test, the End-Loaded Split (ELS) test sketched in Figure 2-12, or the 4-point loaded End Notched Flexure (4-ENF) test. A fixed ratio of mode I to mode II can be achieved with the Fixed Ratio Mixed Mode (FRMM) test sketched in Figure 2-12 or the Mixed-Mode Flexure (MMF) test, while the Mixed-Mode Bending (MMB) test allows achieving virtually any degree of mode mixity via loading

with a lever arrangement. Besides, the Asymmetric Double Cantilever Beam (ADCB) test allows for modest changes of the mode mixity by introducing some asymmetry in the specimen, either with dissimilar beam materials or with different beam thicknesses [76][80].

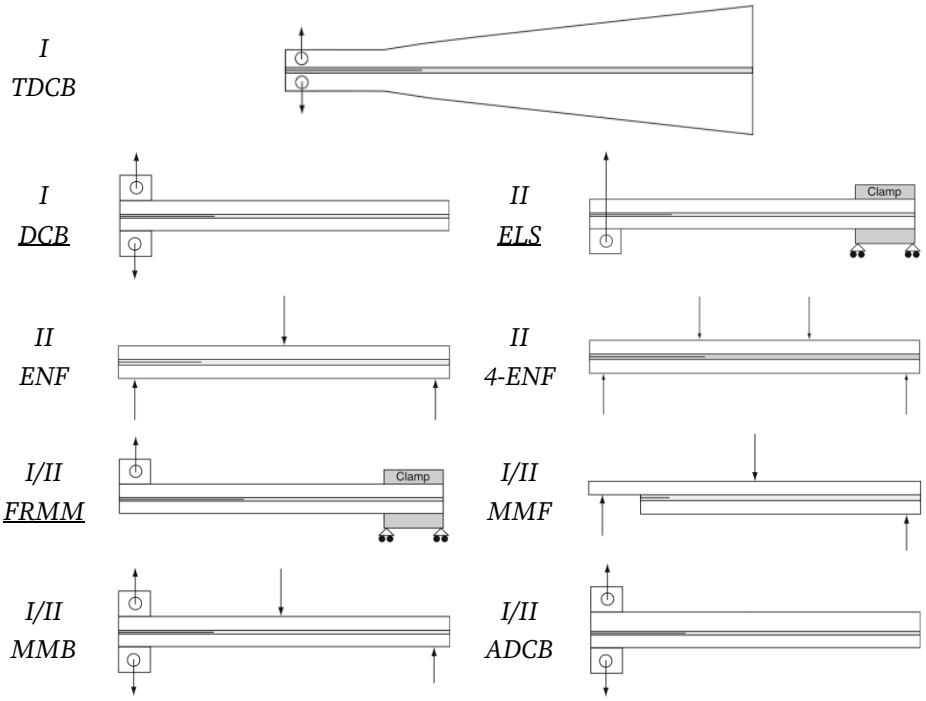

Figure 2-12. Standard beam-bending tests used for measuring an adhesively bonded joint's fracture toughness under, pure mode I, pure mode II, or mixed mode I/II crack loading conditions. Adapted from [78]. *The acronyms of the tests used in this thesis are underlined.*

Finally, the wedge test (WT) in Figure 2-13 is an alternative method for measuring the mode I fracture toughness of an adhesively bonded joint, this time under constant displacement [80]. In the aircraft industry where ageing is a major concern for safety, the wedge test is extensively used as preferred method for evaluating the environmental durability of adhesive bonds (following ASTM D3762, [81]), e.g. in view of assessing and comparing the performance of different adhesives or different adherend surface preparations

under various hygrothermal conditions [77]. The severe combination of stress and moisture at the crack tip of a wedge test specimen indeed makes it possible to obtain useful ageing information in realistic time lapses, whereas the generally slow moisture diffusion through the free edges of a soaked specimen may require unpractical conditioning times before testing [78].

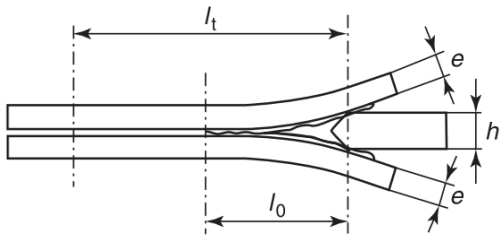

Figure 2-13. The wedge test, used for the evaluation of the environmental durability of adhesive bonds under constant displacement. On insertion of a wedge of thickness h*, the adhesive cracks over the length* l_0*. If any perturbation occurs (e.g. ageing of the adhesive at the current crack tip), the crack extends to another position (here given by the length* l_t*)* [80].

The set formed by the DCB, ELS and FRMM tests constitutes a reasonable choice for the characterisation of an adhesive's fracture toughness. They are briefly described in the following sub-sections.

2.4.2.2 Double cantilever beam test

The DCB test is a standardised [82][83][84] mechanical test method for measuring the mode I fracture toughness of adhesively bonded joints. It is actually one of the most popular LEFM tests used to this aim, and it has been applied for years to the characterisation of mode I fracture of a quite broad range of materials and systems such as adhesive joints (e.g. [66][85][86]), CFRP and composite laminates (e.g. [87][88][89][90]), wood (e.g. [91][92]), cortical bone tissue (e.g. [93]), etc.

For this test, both adherends are symmetrically pulled apart at a slow, controlled rate by a universal tensile testing machine via bonded load blocks (as in Figure 2-12)or piano hinges, or via drilled holes.

Both the DCB and TDCB tests generally allow for stable crack propagation. The latter offers several advantages among which a linear change of the compliance with crack length, which eliminates the need of monitoring the crack advance during the test [94]. However, tapered adherends are more complicate to manufacture than regular beam-shaped adherends. Furthermore, CFRP substrates are flat by essence, and would require the use of backing beams to provide the tapered contour.

The schematic of a loaded DCB test specimen and the associated free body diagram are drawn in Figure 2-14, with the length a of the pre-crack, the height h of the beams, and the force P corresponding to the displacement $u/2$ of one cantilever arm. The specimen width is noted B, so that the crack area is given by $A = Ba$.

The SERR is related to the rate of change of the specimen compliance upon crack growth through the Irwin-Kies equation, which, as a reminder, is given by Eq. (2-41).

$$G = \frac{P^2}{2B}\frac{\partial C}{\partial a} \tag{2-41}$$

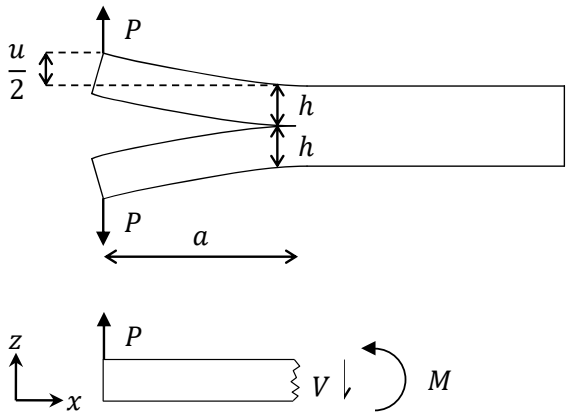

Figure 2-14. Schematic and free body diagram of a loaded DCB test specimen.

Knowing that the compliance defines as $C = u/P$, one must derive an expression for the total opening u, which is twice the load point deflection, $u/2$. The latter is given by Eq. (2-42) that derives from Castigliano's second theorem, where U is the elastic strain energy of the beam given by Eq. (2-43), with $I = Bh^3/12$ the moment of inertia of the beam and E the modulus of elasticity.

$$\frac{u}{2} = \frac{\partial \mathrm{U}}{\partial P} \tag{2-42}$$

$$\mathrm{U} = \int \frac{M^2}{2EI} dx \tag{2-43}$$

Introducing the expression of U into Eq. (2-42), one obtains Eq. (2-44). Besides, a glance at the beam model shown in Figure 2-14 indicates that, from the condition of equilibrium of moments, $M = Px$.

$$\frac{u}{2} = \int_0^a \frac{M}{EI} \frac{\partial M}{\partial P} dx \tag{2-44}$$

Replacing M and I by their respective expression in Eq. (2-44) and solving yields the expression for u given in Eq. (2-45), with which one arrives at Eq. (2-46) for the compliance.

$$u = \frac{8Pa^3}{EBh^3} \tag{2-45}$$

$$C = \frac{8a^3}{EBh^3} \tag{2-46}$$

Finally, replacing C and A by their respective expression in Eq. (2-41) and solving yields the analytical expression for the mode I SERR given in Eq. (2-47). Alternatively, the term EBh^3 can be replaced by $8Pa^3/u$ (Eq. (2-45)), so that another expression for G_I is obtained (Eq. (2-48)), independent of the possibly unknown modulus of the beams.

$$G_I = \frac{12P^2a^2}{EB^2h^3} \tag{2-47}$$

$$G_I = \frac{3Pu}{2Ba} \tag{2-48}$$

In practice, the cantilever beams are not perfectly built-in at the crack front as presupposed in the beam model of Figure 2-14. As a result, simple beam theory (SBT) underestimates the beam compliance and the value of G_{Ic}. This can be corrected by assuming a slightly longer crack, $a + |\Delta_I|$, as exposed in the standards in the section concerned with the data reduction scheme based on the *corrected* beam theory (CBT) also known as the *modified* beam theory (MBT).

An alternative method to determine the SERR is the *experimental compliance method* (ECM), in which $\partial C/\partial a$ is directly extracted from the experimental results. Indeed, Eq. (2-46) is generalised into $C = Fa^n$ so that Eq. (2-48) be-

comes Eq. (2-49) where the value of the exponent n is obtained from the slope of the straight line plot of $\log C$ vs. $\log a$ [83].

$$G_I = \frac{nPu}{2Ba} \tag{2-49}$$

Mode I critical strain energy release rates determined with the CBT and the ECM data reduction schemes usually agree closely, while, as already mentioned, the SBT analysis yields a lower, conservative value of G_{Ic} [80].

2.4.2.3 End-loaded split test

The ELS test is a standardised [95] mechanical test method for measuring the mode II interlaminar fracture toughness of composite laminates, which can be transferred to the characterisation of low to medium toughness structural adhesive joints [96].

For this test, the *lower* adherend of the specimen is lifted at a slow, controlled rate so that both arms deform in a compatible manner. Besides, the bonded end of the specimen is clamped on a linear bearing trolley that naturally translates horizontally during the test, as sketched in Figure 2-12.

Unlike the ENF test, the ELS test offers the advantage of stable crack growth so that the full R-curve can be deduced, in contrast to only the initiation value of G_{IIc} when crack propagation is unstable. Besides, although the choice between the ELS test and the 4-ENF test primarily depends on the availability of the equipment, the ELS test is preferred when testing tough material systems as it is more likely to guarantee the elastic deformation of the substrate beams [97].

The diagram and beam model of a loaded ELS test specimen are drawn in Figure 2-15, with the length a of the pre-crack, the free length L_F from the load point to the clamp, the height h of the beams, and the force P corre-

sponding to the deflection u of the beams. The specimen width is noted B, so that the crack surface area is given by $A = Ba$.

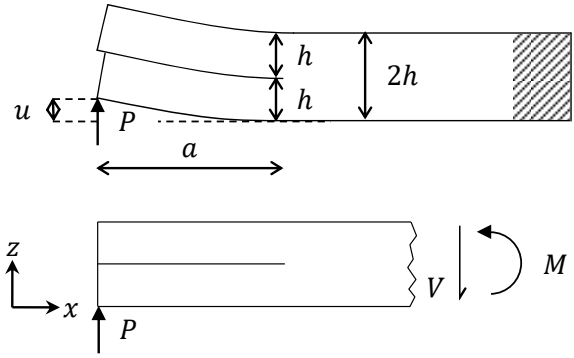

Figure 2-15. Schematic and free body diagram of a loaded ELS test specimen.

The derivation of an analytical expression for G_{II} follows the same logic as that detailed for G_I. The development is given in Appendix C and yields the analytical expression for the mode II SERR given in Eq. (2-50). Again, it can be transformed so that the expression for G_{II} becomes independent of the modulus E (Eq. (2-51)).

$$G_{II} = \frac{9P^2a^2}{4EB^2h^3} \tag{2-50}$$

$$G_{II} = \frac{9Pa^2u}{2B(3a^3 + L_F^3)} \tag{2-51}$$

A CBT analysis method does again take into account the deviation of the real cantilever arms from the simple beam theory via the definition of a slightly extended crack length, $a + |\Delta_{II}|$. The ECM analysis exists as well; the generalised form of the ELS specimen compliance writes $C = C_0 + ma^3$, and the mode II SERR is thus given by Eq. (2-52) where m is the slope of the plot of C vs. a^3 [95].

$$G_{II} = \frac{3P^2a^2m}{2B} \tag{2-52}$$

Finally, an *effective crack length* approach is also proposed in the standard where it is called the CBTE method. It allows circumventing the generally difficult reading of the mode II crack length, and accounting for the variability in clamping conditions [80][97].

2.4.2.4 Fixed ratio mixed mode test

The FRMM test is an established mechanical test method for measuring the mixed mode fracture toughness of adhesively bonded joints with a fixed ratio of $G_I/G_{II} = 4/3$ ($\psi = 41°$). It has long been described in a test protocol [98] and is now being examined by the Technical Committee 4 of the European Structural Integrity Society as a potential standard test method for mixed mode delamination in fibre-reinforced polymer composites [96].

For this test, only the upper (resp. lower) adherend of the specimen is lifted (resp. pushed down) at a slow, controlled rate so that the end of the lower adherend can deform freely. As for the ELS test, the bonded end of the specimen is clamped on a linear bearing trolley that allows horizontal translation to take place during the test (Figure 2-12).

The FRMM test usually provides stable crack growth. Although it is restrictive in terms of mode mixity as opposed to the standardised MMB test, this test is still an interesting choice when combined to the ELS test as they share a common loading fixture, and a common specimen can be designed that satisfies the requirements for both tests [96].

The diagram and beam model of a loaded FRMM test specimen are drawn in Figure 2-16, the length a of the pre-crack, the free length L_F from the load point to the clamp, the height h of the beams, and the force P corresponding

to the deflection u of the top beam. The crack surface area is still given by $A = Ba$, with B the specimen width.

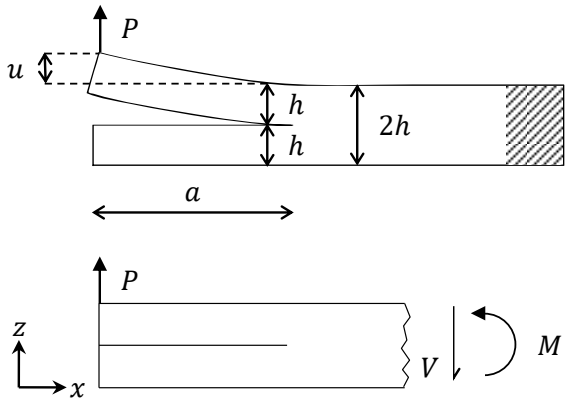

Figure 2-16. Schematic and free body diagram of a loaded FRMM test specimen.

One derives analytical expressions for the mixed mode I/II SERR with the same logic as before. The development is given in Appendix D and yields the analytical expression for $G_{I/II}$ given in Eq. (2-53).

$$G_{I/II} = \frac{21P^2a^2}{4EB^2h^3} \tag{2-53}$$

It can be partitioned into the opening and sliding contributions, G_I^{mixed} and G_{II}^{mixed} (Eq. (2-54)). The crack length corrections $|\Delta_I|$ and $|\Delta_{II}|$ determined for the DCB and ELS tests may hence be respectively applied to the mode I and mode II components, as detailed in Eq. (2-55).

$$G_{I/II} = G_I^{\text{mixed}} + G_{II}^{\text{mixed}} \tag{2-54}$$

$$G_{I/II} = \frac{3P^2(a + |\Delta_I|)^2}{EB^2h^3} + \frac{9P^2(a + |\Delta_{II}|)^2}{4EB^2h^3} \tag{2-55}$$

Finally, the mixed mode critical SERR can also be determined with the ECM analysis method, which relies on Eq. (2-52), as for the ELS test.

2.4.3 Peel tests

2.4.3.1 Introduction

Peel tests are frequently used in the industry for the characterisation of adhesively bonded assemblies including at least one flexible adherend, as in food packaging laminates, electronic components or metallic structural joints for e.g. automotive and aerospace applications [78]. They take diverse forms such as Floating Roller Peel, Climbing Drum Peel, Mandrel Peel, T-Peel, Wedge Peel, Fixed Arm Peel (Figure 2-17), which allow for a quite straightforward measurement of the *peel strength*, i.e. the average peel force per unit width of the test specimen [99].

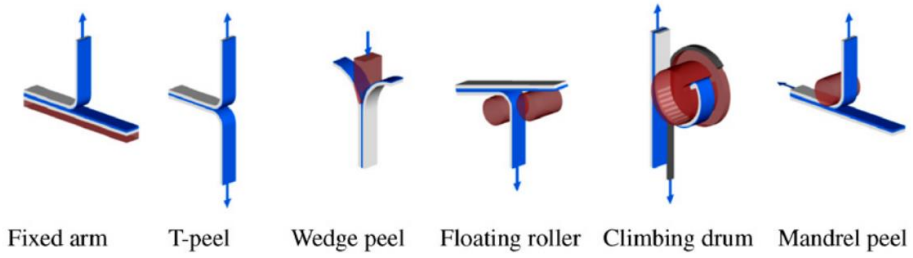

Figure 2-17. Various configurations for peel testing of flexible laminates [99].

2.4.3.2 Deformation in the peel test and implication

A peel test is schematised in Figure 2-18, where a flexible peel arm is peeled off a rigid substrate under the action of a peel force P applied at an angle θ to the horizontal. The peel arm has a width B and thickness h, and its constituent material has a Young's modulus E and a yield strain ε_y. Its root (point A) is not perfectly built-in and is therefore rotated to an angle θ_0 with respect to the horizontal. The curvature at that same location is denoted k_0.

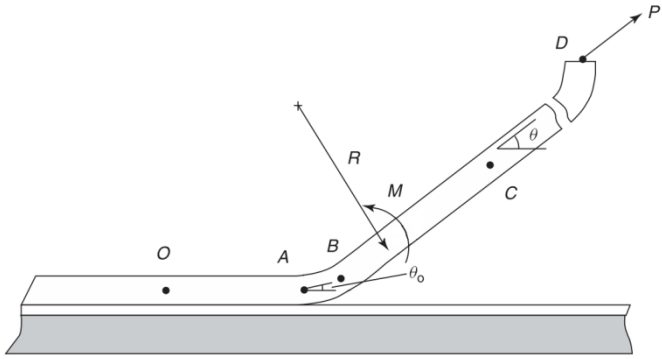

Figure 2-18. Basic peel test, adapted from [100].

The peel test can impose large plastic strains on the peel arm, which are predominantly due to bending [79]. In the steady-state, each segment of the flexible arm being peeled off goes through a definite loading-unloading sequence whereby it bends then unbends, as illustrated in Figure 2-18 [77][100]. The sequence comprises *elastic loading* ahead of the peel front, *plastic bending* in the vicinity of the peel root (point A), *elastic unloading* passed the peel front (point B), and, eventually, *reverse plastic bending* (point C).

These deformation phenomena contribute to the measured peel force, as does the adhesive fracture energy, G_a. Hence, the peel strength is not a reliable indicator of the adhesive fracture energy: it is influenced by the amount of energy stored or dissipated in the peel arm(s) during the test, and is thus dependent on parameters such as the peel arm material or thickness, the adhesive toughness and the peel angle [78]. Determining a value of G_a that is *geometry-independent* and truly representative of the energy intrinsically required for fracturing the bond material or the interface thus requires successfully partitioning the above-cited contributions to the external work done by the peel force [101]. A number of authors have addressed this issue and developed some advanced analytical (e.g. [79][102]) or numerical (e.g.

[101][103]) methods for the analysis of peel tests. An introduction to the former approach is given in what follows.

2.4.3.3 Calculation of the adhesive fracture energy

First, the adhesive fracture energy is expressed from a global balance of the energy terms accompanying an increment of peeled surface area $dA = Bda$. This writes

$$G_a = \frac{1}{B}\left(\frac{dU_{\text{ext}}}{da} - \frac{dU_{\text{s}}}{da} - \frac{dU_{\text{dt}}}{da} - \frac{dU_{\text{db}}}{da}\right) \tag{2-56}$$

where dU_{ext} is the external work, $dU_{\text{s}}$is the change in elastic strain energy stored in the peel arm, and dU_{dt} and dU_{db} represent the energy dissipated in tensile and bending deformation of the peel arm, respectively [79]. Eq. (2-56) can also conveniently be written as

$$G_a = G_{\text{tot}} - G_{\text{s}} - G_{\text{dt}} - G_{\text{db}} \tag{2-57}$$

where each of the G terms thus represent an energy per unit crack area. The increment of external work writes $dU_{\text{ext}} = Pd\delta$, where $d\delta$ is the increment of displacement in the direction of application of the load. In the hypothetical case of a flexible but inextensible peel arm, $d\delta = da(1 - \cos\theta)$, and $G_{\text{s}} = G_{\text{dt}} = G_{\text{db}} = 0$. So, one can express G_{tot} as [79]

$$G_{\text{tot}} = \frac{P}{B}(1 - \cos\theta) \tag{2-58}$$

When the peel arm is extensible but still bends elastically, the steady-state axial tensile strain ε_a is taken into account, while G_{db} still equals zero. In this case, the adhesive fracture energy is noted G_a^{eb} and becomes [79]

$$G_a^{\text{eb}} = G_{\text{tot}} - (G_{\text{s}} + G_{\text{dt}}) = \frac{P}{B}(1 + \varepsilon_{\text{a}} - \cos\theta) - h\int_0^{\varepsilon_{\text{a}}} \sigma d\varepsilon \tag{2-59}$$

In the most general case, however, plastic bending-unbending of the peel arm represents a significant energy sink, so that G_{db}, the total energy dissipated in this process, has to be taken into account in the computation of the adhesive fracture energy [79]. As shortly exposed in Appendix E, this term is evaluated with the large displacement beam theory [100]. Then, G_a is obtained by solving

$$G_a = G_a^{\mathrm{eb}} - G_{\mathrm{db}} \tag{2-60}$$

A macro-enabled Microsoft Excel spreadsheet called "*ICPeel*" has been developed at the Mechanical Engineering Department of Imperial College, London for the automatized conversion of the experimental data into adhesive fracture energy. It is freely available to download[7], along with the ESIS TC4 Peel Test Protocol that provides guidance for the measurement of the peel strength with the fixed arm peel and the T-peel test configurations [104]. Furthermore, this research group recognised that "*the extent to which the external energy is corrected for plastic bending energy is an inherent source of error in the determination of adhesive fracture toughness*" [105]. Hence, two quantities are calculated in addition to the adhesive fracture energy, namely the *Data Rejection Factor* (DRF) and the *Maximum Bending Strain in the Arm* ($\varepsilon_{\max}$) which write as in Eq. (2-61) [106]. They allow verifying that the energy dissipated in plastic bending of the peel arm is not too large as compared to the total energy involved during the test: the value obtained for G_a is accepted if both criteria are satisfied and is rejected otherwise.

$$\begin{cases} \mathrm{DRF} = 100\dfrac{G_p}{G} \leq 85\ \% \\ \varepsilon_{\max} \leq 4\ \% \end{cases} \tag{2-61}$$

[7] From the Imperial College website:
https://www.imperial.ac.uk/mechanical-engineering/research/mechanics-of-materials/composites-adhesives-and-soft-solids/adhesion/test-protocols

2.5 Simulation of progressive damage with cohesive finite elements

2.5.1 Introduction

Finite element modelling is an important tool in fracture analysis [64]. In particular, simulation of crack nucleation and growth is conveniently achieved with *cohesive elements* placed along the potential crack paths [107][108]. These are zero-thickness finite elements (Figure 2-19) generated at interfaces between two-dimensional or three-dimensional solid elements. They are governed by a *cohesive zone model* (CZM), i.e. a constitutive law derived from the *continuum damage mechanics* theory (Figure 2-19), and allow for jumps in the displacement field along the pre-defined interface. This advanced FE modelling technique enables the simulation of progressive damage up to complete structural failure; it also gives access to the interface stress components before and during crack growth [107]. The necessity of defining the crack path in advance is not really a constraint as regards adhesively bonded systems, since damage propagation is generally restricted to well defined planes of the bond line [107][109].

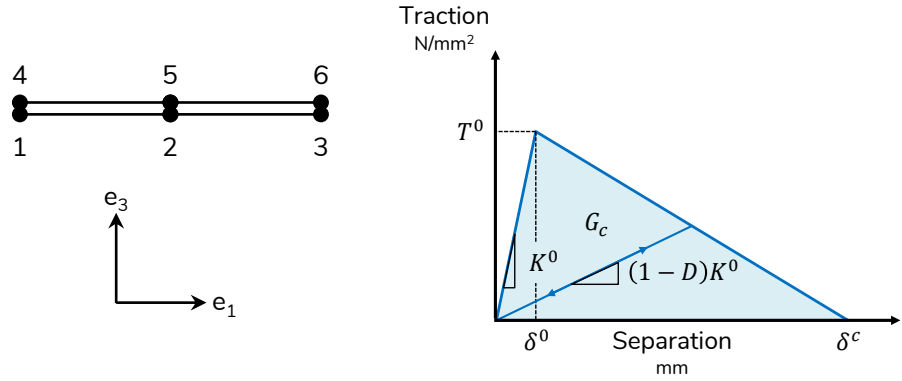

Figure 2-19. (Left) 2D example of 6-node cohesive element, showing the pairs of coincident nodes; (right) example of cohesive law, here of the triangular (or bi-linear) type.

2.5.2 Cohesive zone and cohesive zone models

A macroscopic crack results from micro-failure mechanisms taking place in a region of the material called the *fracture process zone* (FPZ). In the cohesive zone approach, these damage phenomena are condensed onto a very thin band ahead of the crack tip, also known as the *cohesive zone*, which is held closed by *cohesive surface tractions* or *closure tractions* [65]. These concepts are illustrated in Figure 2-20.

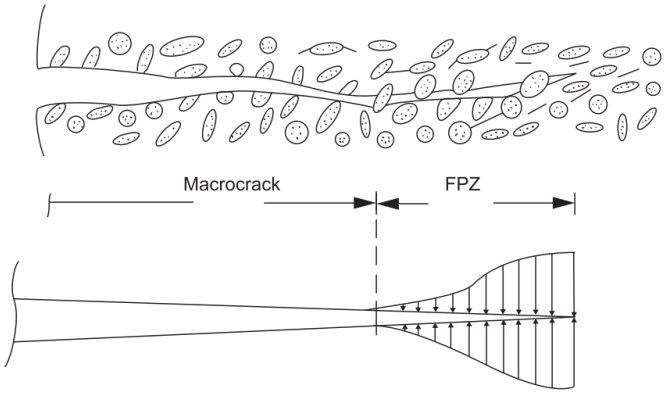

Figure 2-20. Fracture process zone ahead of a macrocrack (here in concrete) and associated closure tractions [65].

A cohesive zone model describes the relationship between the closure traction T (also written σ for pure mode I and τ for pure mode II) and the relative displacement δ of the initially coincident interface nodes through all phases of the loading and damage process. The cohesive zone eventually separates into two crack faces once the *displacement jump* (δ) has reached a critical value. Although it is possible to access the exact constitutive cohesive law of a given material system experimentally, its shape is most often assumed and is defined with one of the several idealised shapes, e.g. the trapezoidal, triangular, polynomial, linear-parabolic and exponential traction-separation laws [107][110]. The effect of the cohesive law shape on the numerical result has

been studied in [111], [112] and [113], for instance. These laws comprise different levels of complexity and differently influence the convergence of the iterative solving procedure. However, the selection of the cohesive law should primarily be guided by the material or interfacial behaviour under consideration. As far as adhesive bonds are concerned, the trapezoidal law is preferred for ductile adhesives, while for brittle and moderately ductile adhesives the triangular law is chosen instead [107][112]. The latter shape is still the most widely used for its small set of defining parameters, and is used as basis for the following description of a cohesive zone model's major features.

Under the influence of the surrounding displacement field, paired cohesive nodes progressively separate. In the first loading stage of the triangular traction-separation law (see Figure 2-19), increasing separation δ generates some linearly increasing closure traction T, i.e. $T = K^0\delta$. There is no damage yet: upon unloading, traction and separation would return to their initial state following the unchanged slope K^0. Beyond a threshold value of separation δ^0, however, damage starts developing in the cohesive element: the material stiffness degrades gradually and irreversibly according to $T = (1 - D)K^0\delta$, where D is a scalar damage variable whose value progresses from 0 (no damage) to 1 (total damage) during the damage process. The traction T^0 corresponding to δ^0 is known as the *peak stress* or *cohesive strength*; it also writes σ^0 for pure mode I and τ^0 for pure mode II loading. Strain softening thus proceeds in the second loading stage of the triangular cohesive law until the separation between paired nodes of a cohesive element reaches a critical value δ^c at which the element fails completely. Cohesive tractions vanish on that element, the crack advances to the next element in the cohesive zone and stress redistributes in the material body [107]. The area under the traction-separation curve has units of energy per unit area and corresponds to the fracture toughness of the material, G_c.

Cohesive zone models hence incorporate two key ingredients, namely a strength criterion for the onset of damage, and a mixed mode energy criterion ruling damage propagation [107][114]. The triangular cohesive law is thus defined by parameters K^0, T^0 and G_c, the last two being linked to separation values by the simple relations given in Eq. (2-62) and (2-63).

$$\delta^0 = \frac{T^0}{K^0} \tag{2-62}$$

$$\delta^c = \frac{2G_c}{T^0} \tag{2-63}$$

2.5.3 Definition of a cohesive zone length and implication

In the FEM framework, the FPZ is the region over which the cohesive elements response is described by the softening part of their traction-displacement curve (Figure 2-21). It thus extends from the crack tip (where $T = 0$ and $D = 1$) to the point of maximum closure traction ($T = T^0$ and $D = 0$) ahead of the crack tip [115][116]. Its length l_{cz} (also called *process zone length* or *cohesive zone length*) can be estimated with Eq. (2-16), which, in this context, rather writes [117]

$$l_{cz} = ME\frac{G_c}{(T^0)^2} \tag{2-64}$$

where M is a factor found between 0.21 and 1 depending on the model hypotheses, and E is the Young's modulus of the material.

The cohesive zone length must incorporate a sufficient number of cohesive elements for the closure tractions to be correctly evaluated. This requirement must be met to hedge against mesh-dependency of the numerical solution. The exact number of elements is not well defined in the literature but is often seen to be at least equal to 3 [117][115].

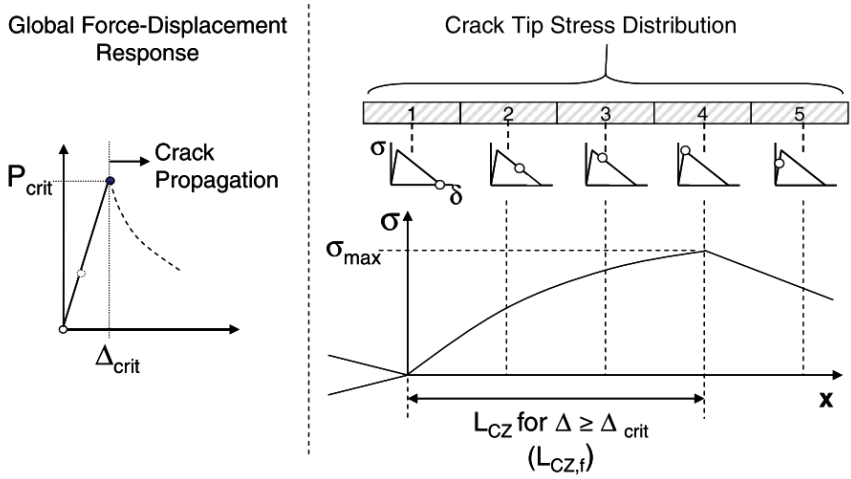

Figure 2-21. Development of the numerical cohesive zone (here in relation to a simulated DCB test, which global force-displacement curve is shown at left) [115].

2.5.4 Approaches for modelling with cohesive elements

For the modelling of adhesively bonded assemblies, the entire bond line is sometimes replaced by a single row of cohesive elements (e.g. [118][119]). In this case, they are expected to reproduce the mechanical behaviour of the adhesive bond material, and the stiffness K^0 thus takes the value of the material's modulus of elasticity. K^0 is set to a much higher value otherwise, i.e. when the use of cohesive elements is restricted to damage growth simulation while the representation of the material behaviour is supported by continuum finite elements surrounding the cohesive zone (e.g. [120][118][121]). With such penalty stiffness one ensures that the cohesive elements do not interfere with the structure deformation before the onset of damage [107][117]. On the other hand, for the delamination analysis of laminated composites, a hybrid approach is followed: interfaces between laminae are exclusively modelled with cohesive elements whose initial stiffness still takes a high penalty value (e.g. [117][122][123]).

The other parameters, T^0 and G_c, are most often quantitatively identified using the *inverse method* that is based on the trial and error, iterative fitting of a simulated result (such as the load-displacement curve) to the corresponding experimental result. The laboratory value of the material's fracture strength and fracture toughness is then generally taken as initial guess for T^0 and G_c, respectively [107]. The effect of these parameters on the cohesive law shape is schematised in Figure 2-22.

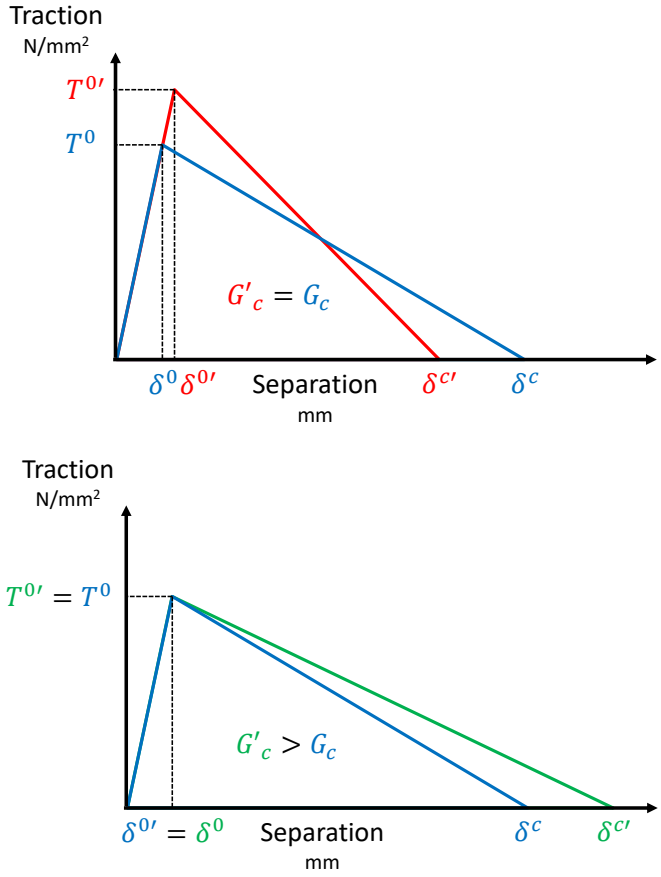

Figure 2-22. Effect of a change in peak stress (T^0) or fracture toughness (G_c) on the shape of the triangular cohesive law.

2.5.5 Description of the CZM used in this work

The present CZM has been developed in the context of delamination in composite laminates, see e.g. [124] and [125]. It is included in the commercial FE package SAMCEF under the name of "damage interface material" (DAMINT).

The model describes the mechanical behaviour of a *damageable interface*, which is defined as a mechanical surface that initially ensures stress and displacement transfer between the adjoining solids. Its elastic strain energy per unit area writes

$$E_d = \frac{1}{2}(1-D_1)K_1^0[u_1]^2 + \frac{1}{2}(1-D_2)K_2^0[u_2]^2 + \frac{1}{2}(1-D_3)K_3^0\langle[u_3]\rangle_+^2 + \frac{1}{2}K_3^0\langle[u_3]\rangle_-^2 \tag{2-65}$$

where subscripts 1, 2, 3 respectively refer to two mutually orthogonal directions in the interface plane, and to the direction normal to that plane. $[u_i] = u_i^+ - u_i^-$, is the displacement jump, i.e. the difference in displacement between the upper and lower surfaces of the zero-thickness interface; for the sake of consistency with the notation adopted earlier in this section, one will replace $[u_i]$ by δ_i in the next equations. K_i^0 represents the initial stiffness of the interface in each of the three directions of loading, and D_i is an internal damage indicator that evolves from 0 to 1 and accounts for the deterioration of the interfacial mechanical connection. Subscripts 1, 2 and 3 of K_i^0 and D_i could equally be replaced by the corresponding Fracture Mechanics modes II, III and I. The model considers a different damageable behaviour in tension and compression in direction 3, assuming that compression does not actually generate damage in the interface. This is indicated with Macaulay brackets $\langle x\rangle_+$ and $\langle x\rangle_-$, which designate the positive and negative part of x.

Partial derivatives of the strain energy yield the tractions t_i (Eq. (2-66)) and the thermodynamic forces Y_i, called *damage energy release rates* (Eq. (2-67)).

$$t_i = \left.\frac{\partial E_d}{\partial \delta_i}\right|_{D_i} \tag{2-66}$$

$$Y_i = -\left.\frac{\partial E_d}{\partial D_i}\right|_{\delta_i} \geq 0 \tag{2-67}$$

Energetic considerations impose that damage variables do only increase in time (i.e. $\dot{D}_i \geq 0$), which implies that the degradation is irreversible. Further, the present cohesive zone model assumes that damage under mixed mode loading conditions is driven by a unique *equivalent damage energy release rate* of the form

$$\underline{Y}(t) = \sup|_{\tau \leq t} \left[G_{Ic} \left(\left(\frac{Y_3}{G_{Ic}}\right)^{\alpha} + \left(\frac{Y_1}{G_{IIc}}\right)^{\alpha} + \left(\frac{Y_2}{G_{IIIc}}\right)^{\alpha} \right) \Big|_{t=\tau}^{1/\alpha} \right] \tag{2-68}$$

where t is the current time instant while τ stands for elapsed times, and α governs the shape of the fracture envelope since it is related to the 3D power law criterion for mixed mode fracture (Eq. (2-35)) with $\alpha = \beta = \chi$.

Besides, the model considers *isotropic damage*, meaning that all three damage variables follow the same evolution law and are thus identical. This writes

$$D_1 = D_2 = D_3 = D = \begin{cases} \omega(\underline{Y}) & D < 1 \\ 1 & \text{otherwise} \end{cases} \tag{2-69}$$

where $\omega(\underline{Y})$ is a material function that sets the shape of the traction-separation curve. It is considered confidential information at SAMTECH for the triangular cohesive law; however, it probably takes a form similar to that of Eq. (2-70) [126][127], with Y_0 the threshold value of damage ERR from which damage arises and Y_c the critical value of damage ERR at which the interface is damaged completely.

$$\omega(\underline{Y}) = \frac{\langle\sqrt{\underline{Y}} - \sqrt{Y_0}\rangle_+}{\sqrt{Y_c} - \sqrt{Y_0}} \tag{2-70}$$

It can be shown that $Y_c = G_{Ic}$. Y_0, on the other hand, represents the area under the traction-separation curve before the onset of strain softening. It is thus related to some threshold level of traction T_i^0 or displacement discontinuity δ_i^0 at the beginning of the damage process. These can be known if the initiation point is clearly identified in a fracture mechanics test, e.g. by acoustic emission. For the triangular law shape, Y_0 simply reads

$$Y_0 = \frac{(T^0)^2}{2K^0} \tag{2-71}$$

In SAMCEF, Y_0 is identical in mode I and mode II, so that the shear and normal interface strengths a related by [128]

$$\tau^0 = \sigma^0 \sqrt{\frac{G_{IIc} K_{II}^0}{G_{Ic} K_I^0}} \tag{2-72}$$

Finally, a viscous regularisation technique can be used to overcome the divergence issues frequently arising in the softening regime when damage growth is unstable [107][127]. A delay effect is introduced by substituting the following damage evolution law (Eq. (2-73)) for the previous one (Eq. (2-69)) [129][130]. In this equation, τ_c is a characteristic time constant and parameter a sets the brittleness of the interface.

$$\begin{cases} \dot{D} = \dfrac{1}{\tau_c}\left[1 - \exp\left(-a\langle\omega(\underline{Y}) - D\rangle_+\right)\right] & D < 1 \\ \dot{D} = 0 \quad (D = 1) & \text{otherwise} \end{cases} \tag{2-73}$$

As a result, an increase in $\underline{Y}$ does not lead to an instantaneous increase of the damage variable; moreover, the damage rate is finite and bounded by $\dot{D} \leq 1/\tau_c$ [129]. The cohesive tractions can thus exceed their limiting value τ_{0i}

[107] and the otherwise sudden release of elastic energy stored in the material is delayed [127]. The optimal value of parameter τ_c is that which allows converging without altering the overall structural response [131].

3. Experimental investigation of the multilayer's damage state

3.1 Introduction

A *multi-layered, multi-material* system has been presented in Chapter 4, which constitutes the innovative composite booster casing. Its state of thermo-mechanical damage calls for a thorough study, for instance by FE progressive damage analysis. Yet, modelling such system is not straightforward, and the accuracy of the results directly depends not only on the modelling hypotheses, but also on the quality of the input data defining the material properties. The geometry of the region of interest and the type, number, morphology and location of defects to be modelled must also be sufficiently well known.

Therefore, the experimental characterisation of the multilayer's materials and damage state was undertaken in this thesis. The present chapter covers the work carried out to investigate the multilayer's damage state, namely:

- A synthesis of the damaged zones and types of damage
- A statistical analysis of the multilayer's damage state based on the examination of several hundreds of micrographs
- An approach of the 3D geometry and damage morphology of the region found at the inter-segments gap.

3.2 Damaged zones and types of damage

The industrial partner accumulated over the years a wealth of information on the damage state of its composite booster casings, at different production stages and with different degrees of thermal ageing. It took the form of hundreds of micrographs showing cross-sections of the multilayer at different characteristic locations of the abradable tracks. During this thesis, numerous optical microscope sessions were also performed on a number of samples extracted from two casings, with a particular emphasis on the region of the multilayer enclosing the (bi-material) interfaces between the different layers.

Different forms of damage were observed in the multilayer, as announced in Chapter 1 and illustrated in Figure 1-18. As a reminder, besides occasional voids in resin-rich zones of the laminate, defects of the following types were seen in the composite substrate and the co-cured joint:

- *microcracks* in the co-cured joint
- *transverse* (or *intralaminar*) matrix microcracks in the tows of the woven laminae
- *longitudinal* microcracks (or *meta-delaminations*) at the interface between warp and weft tows [52]
- vertical and horizontal *disbonds* of the steel strip segments

In particular, transverse and longitudinal microcracks are symptomatic of tensile loading[8] of woven fabric composites in the on-axis direction[9] [52]; they develop following the scheme reproduced in Figure 3-1. Their presence in booster casings well before the application of any mechanical load thus indeed indicates the existence of tensile residual stresses in the laminate.

[8] The cited work more precisely focuses on the effect of tensile-tensile *mechanical fatigue* loading, but it is assumed here that this type of tensile loading of the matrix can result from *thermal fatigue* loading as well.
[9] Warp or weft direction

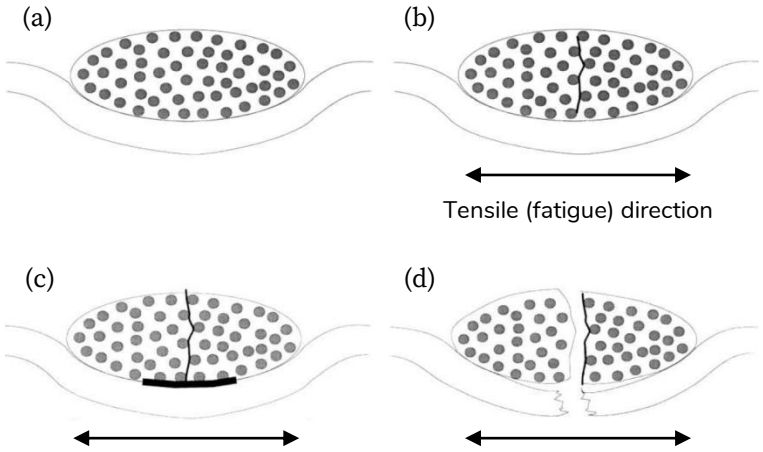

Figure 3-1. Scheme of the tensile (fatigue) damage development in woven fabric composites loaded in the on-axis direction, adapted from [52]. *(a) Initial undamaged state of a transverse tow and a longitudinal tow, (b) Transverse matrix crack in the transverse tow, (c) Transverse matrix crack deflected into the longitudinal tow within the same lamina (meta-delamination), (d) Failure of the longitudinal tow by fiber fracture.*

For all that, it rapidly emerged that the region of the multilayer enclosing the bi-material interfaces was generally undamaged. Such sound area is presented in Figure 3-2, where the adhesion is visibly good at all interfaces and the layers are free of microcracks.

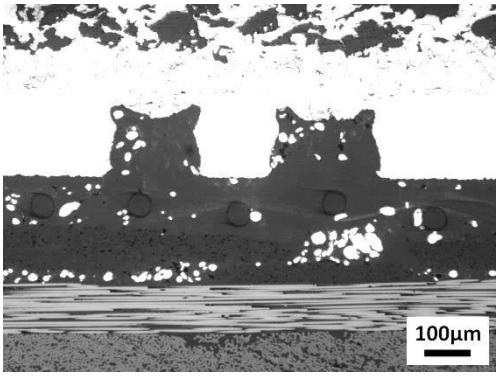

Figure 3-2. Sound interfaces of the multilayer as they typically appear in cross-sections of the booster casings.

Damage actually concentrated at a few specific locations of the abradable tracks, starting with the inter-segments gap (defined in Figure 1-7). A great deal of variability in gap width and levelling of the segments ends was observed, which testifies to the difficulty of controlling the positioning of the steel strips during resin transfer moulding. The gap width would indeed range from a few microns to a few millimetres within the same booster casing, while the ends of the steel strip segments would either be aligned, collapsed (i.e. found at different heights) or superimposed. Some examples are gathered in Figure 3-4. Interestingly, the loss of positioning control in the form of collapsed and superimposed segments ends did not seem to cause severe damage. Instead, the largest number and variety of defects was observed at ISGs with aligned segments ends and large gap width, as shown in Figure 3-5. A similar region of damage was found at the slits that, as a reminder, are cut into the steel strips to improve their match to the casing's curvatures (recall Figure 1-7).

Damage was also repeatedly observed along the horizontal edges of the abradable tracks, some examples of which are given in Figure 3-3. In this zone, it expressed as microcracks in the co-cured joint, and vertical as well as horizontal disbonds at the end of the steel strip segment.

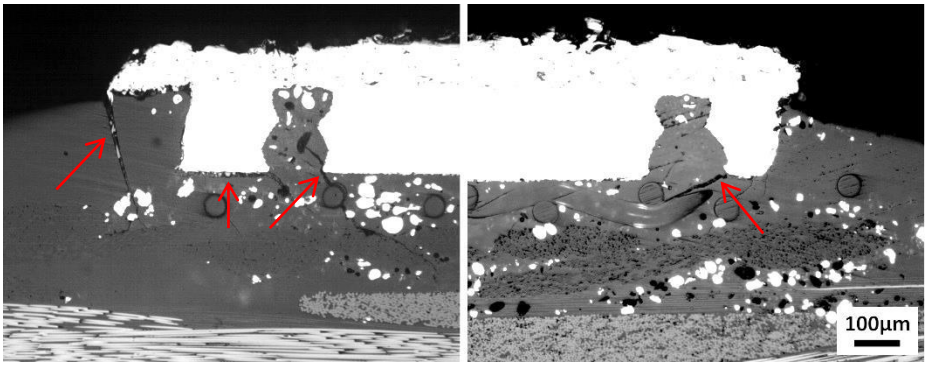

Figure 3-3. Selection of optical micrographs showing the zone found at the horizontal edges of the steel strip segments. Red arrows point to the observed defects.

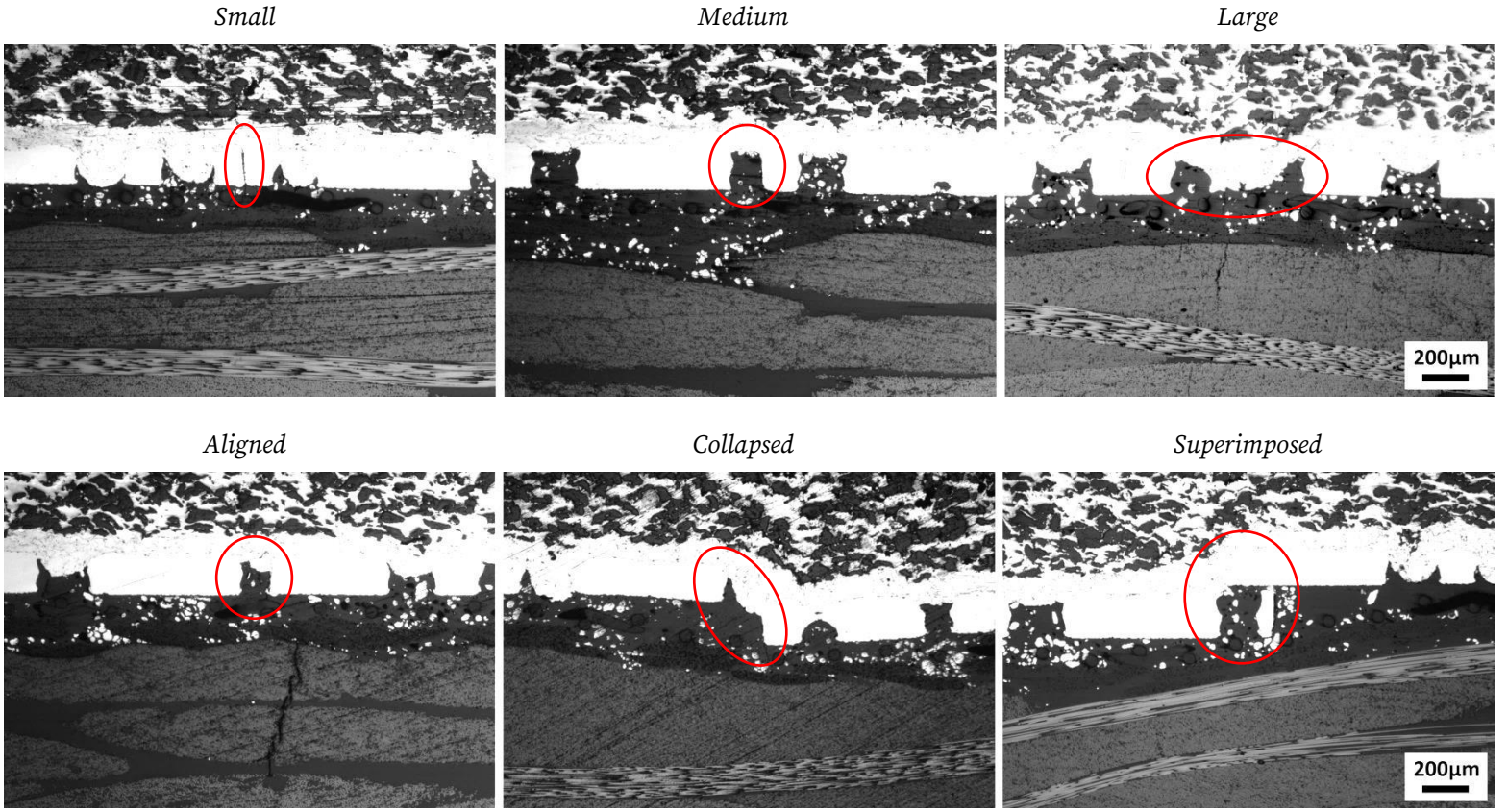

Figure 3-4. Selection of optical micrographs showing inter-segments gaps with (top) different gap widths and (bottom) different positionings of the ends of the steel strip segments. All views are centred on the inter-segments gap, which is furthermore circled in red.

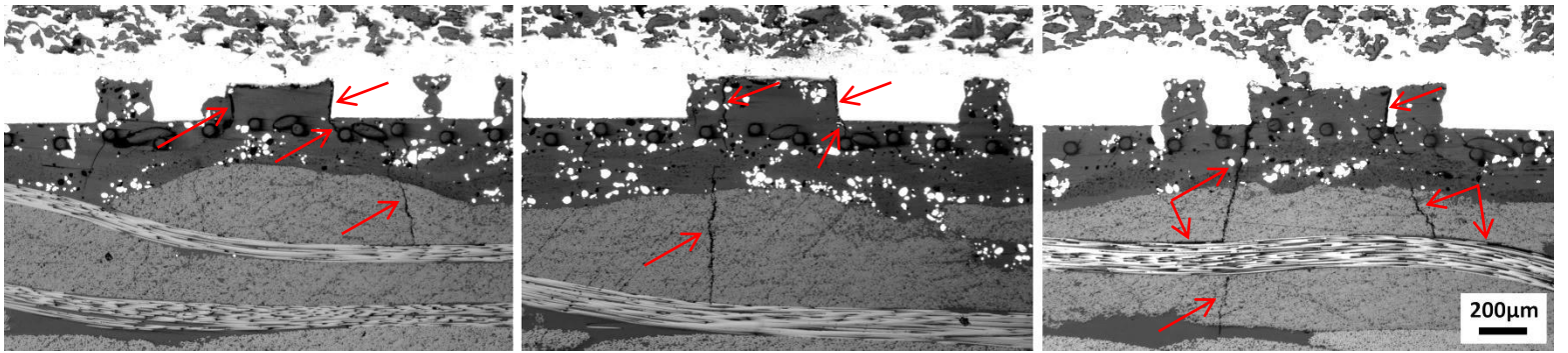

Figure 3-5. Selection of optical micrographs showing the type of damage typically observed at inter-segments gaps with aligned segments ends and large gap width.

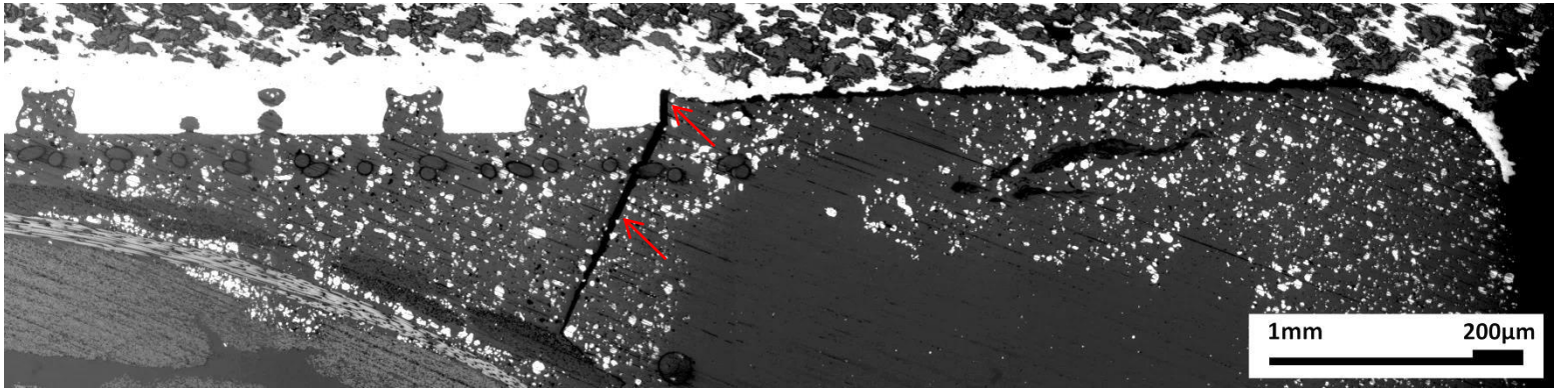

Figure 3-6. Example of damage occasionally observed at the booster casings flanges.

The last specific damage zone was encountered at the booster casing's flanges, which also coincide with ends of steel strip segments. This zone was occasionnally affected by long cracks starting in the co-cured joint from the end of the steel strip segment and propagating diagonally towards the composite laminate, as can be seen in Figure 3-6.

Outside these specific zones, microcracks were sometimes encountered in the co-cured joint, where they remained confined. These microcracks started from the bottom circumference of the micro-perforations and from the mesh of the nylon carrier of the film adhesive, as illustrated in Figure 3-7. Although less serious than previously, they still indicate the presence of tensile residual stresses large enough to cause their onset and growth.

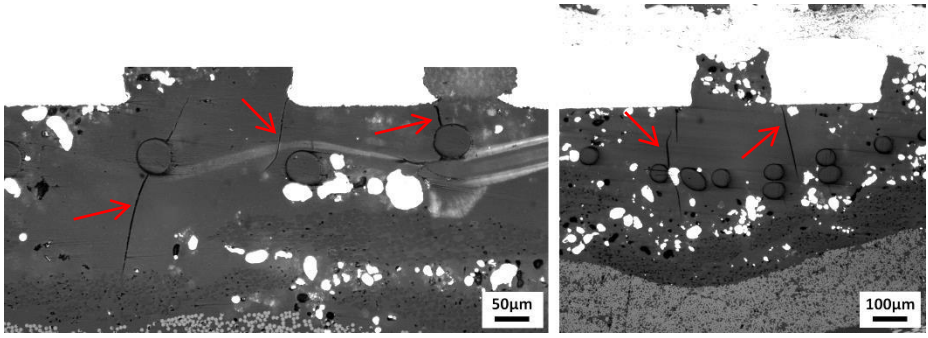

Figure 3-7. Minor microcracks confined in the polymer blend, initiating at the bottom circumference of the micro-perforations and at the mesh of the nylon carrier.

3.3 Statistical analysis of the multilayer's damage state

3.3.1 Methodology

The organisation of SAB's data in a multitude of independent image folders did clearly not provide the readability necessary for their analysis. Therefore, at the beginning of this thesis, 268 micrographs showing the bi-material

interfaces area of 15 booster casings were selected for their interest and listed in an Excel spreadsheet, the columns of which inventoried a large amount of qualitative and quantitative information about the casing (e.g. abradable, thermal shock), the zone (e.g. track, location, type, width of the ISG, leveling of the steel segments ends) and the damage observed (e.g. type, quantity, size, spacing). The *damage types* were defined as: Micro-crack, (Meta-)delamination, (Meta-)delamination + micro-crack, Horizontal disbond, Horizontal disbond + micro-crack, None. Indeed, when observed on the same micrograph, micro-cracks and (meta-)delaminations –as well as micro-cracks and horizontal disbonds– were labelled together. Besides, vertical disbonds were, at the time, treated as micro-cracks running along the steel/joint interface. The *types of damage zones* were as previsouly identified: Inter-segments gap, Slit, Track edge, Flange edge, Other.

This spreadsheet became the starting point for the creation of several Excel pivot tables that allowed performing a statistical analysis and perceiving causal links between the above-cited information. All micrographs featuring damage were taken into account. In addition, damage-free micrographs were listed as well if captured at inter-segments gaps and slits, as they contributed to enrich the library of information about the gap or slit width and the positioning of the ends of the steel strip segments.

For the sake of the analysis, the booster casings were divided into three categories based on their projection status and their thermal history. These are identified in Table 3-1.

Table 3-1. Classification of the booster casings into three categories based on their projection status (abradable) and their thermal history (thermal shock).

	No thermal shock	Thermal shock
No abradable	Cat. 1	Cat. 2
Abradable	-	Cat. 3

The statistical analysis was performed in detail for the three individual casings categories. This is presented first, followed by a global review of these results.

3.3.2 Statistical analysis

3.3.2.1 Casings without abradable nor thermal shock (category 1)

The analysis was based on 78 micrographs evenly distributed between the RM3 track (47 %) and the RM4 track (53 %) of three booster casings, and featuring inter-segments gaps, slits and track edges. The distribution of the 65 micrographs with damage over these zones of the casing is shown in the pie chart of Figure 3-8, for both tracks combined.

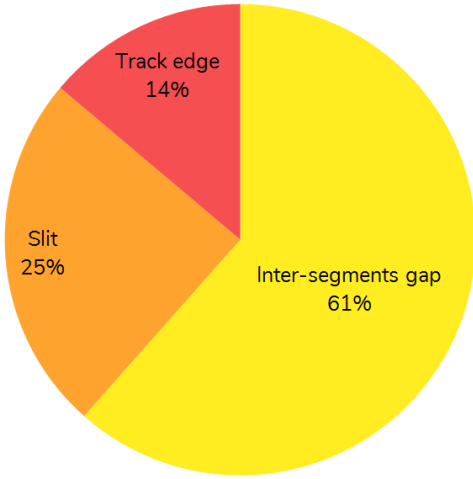

Figure 3-8. Distribution of the 65 micrographs with damage over the specific zones of the booster casings without abradable nor thermal shock (cat. 1), for both tracks combined.

A total of 70 damage occurrences were observed in these micrographs, of which 41 % on the RM3 track and 59 % on the RM4 track. All of them were microcracks, predominantly found at the ISGs (64 % for both tracks combined, or 69 % for RM3 and 61 % for RM4), as can be seen from the distribu-

tion of observed defects shown in the pie charts of Figure 3-9 (top) for both tracks combined. This result can be put into perspective, considering that the different zones of the casings were looked at in different proportions (remind Figure 3-8). This is the purpose of the bar graph in Figure 3-10 that presents the distribution of damage over the different zones of the casings relatively to the number of micrographs examined for each zone (in this graph, a value of 1 indicates that there is in average one defect per micrograph, while a value of e.g. 2.53 indicates that there is in average 2.53 defects per micrograph, etc.). It reveals that the distribution of damage over the three zones is not as contrasted as suggested in Figure 3-9 (top), damage being actually found in approximately the same ammount at ISGs, slits and track edges.

At the ISGs of both tracks, the ends of the steel strip segments were mostly aligned (94 %) with a mean gap width of 0.51 mm, or collapsed (6 %) with a mean gap width of 0.41 mm. The first type of segments positioning counted 60 % of all observed microcracks, while 4 % were found at inter-segments gaps presenting the second type of positioning. When the segments ends were aligned, 60 % of the microcracks were interfacial, running at the steel strip/gap vertical interface with a mean length of 0.30 mm; the other 40 % were cohesive in the polymer blend filling the gap, with a mean length of 0.18 mm. Besides, 14 % of these gaps contained a maximum of two concurrent microcracks, while the other 86 % contained only single microcracks, as detailed in the pie charts of Figure 3-11 (first column). In case of collapsed segments ends, the microcracks were exclusively cohesive in the gap, with a mean length of 0.36 mm. Only single microcracks were then observed.

Finally, for all zones combined, only two microcracks out of 70 (i.e. 3 %) reached the composite laminate, with a length of 0.9 mm and 1.16 mm.

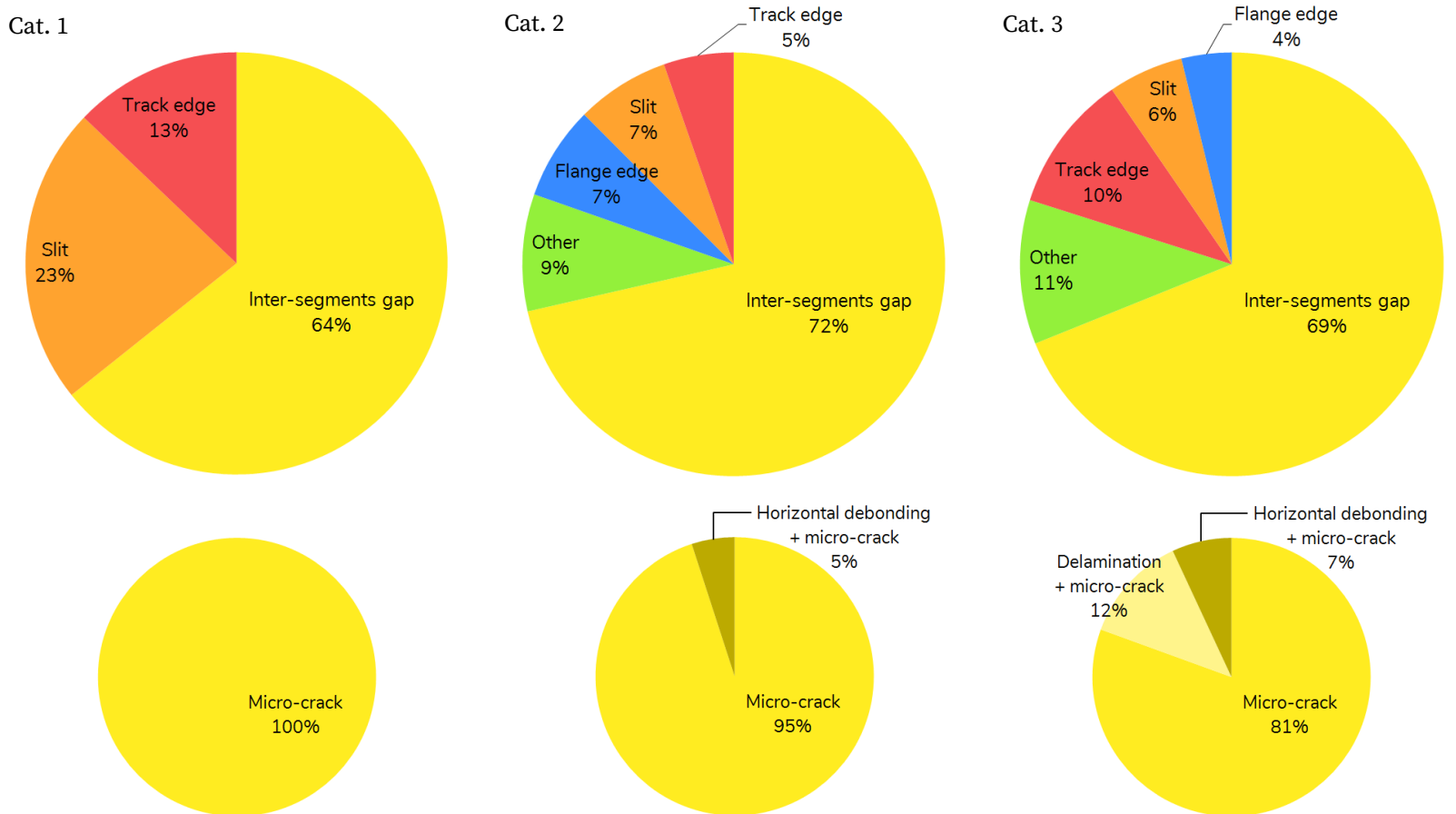

Figure 3-9. Diversification (top) of the distribution of observed defects over the different zones of the booster casing and (bottom) of their type at the inter-segments gaps, for booster casings (left to right) without abradable nor thermal shock, with abradable without thermal shock, with abradable and thermal shock.

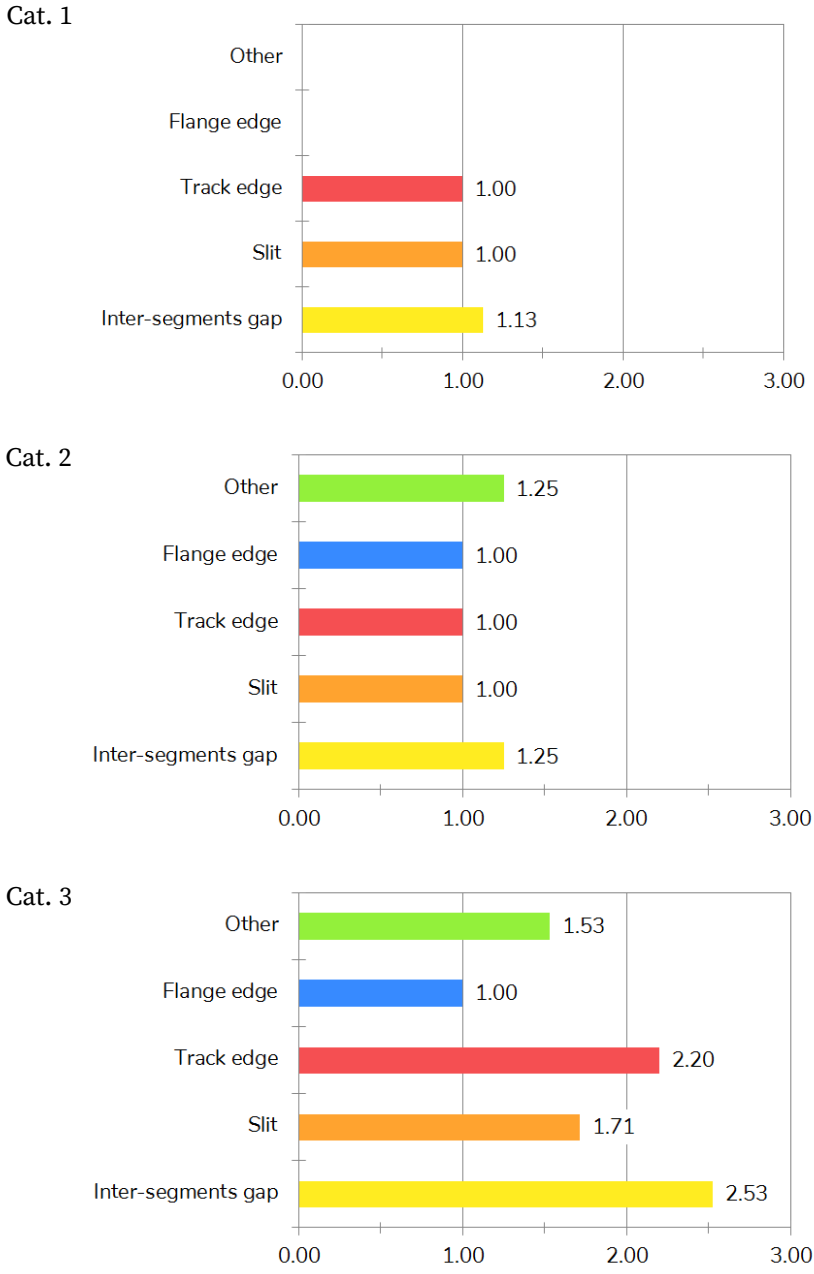

Figure 3-10. Ratio of the number of defects of all types observed in a zone to the number of micrographs captured in this zone (for the different zones of booster casings of the three categories). A value of e.g. 2.53 indicates that there is in average 2.53 defects per micrograph.

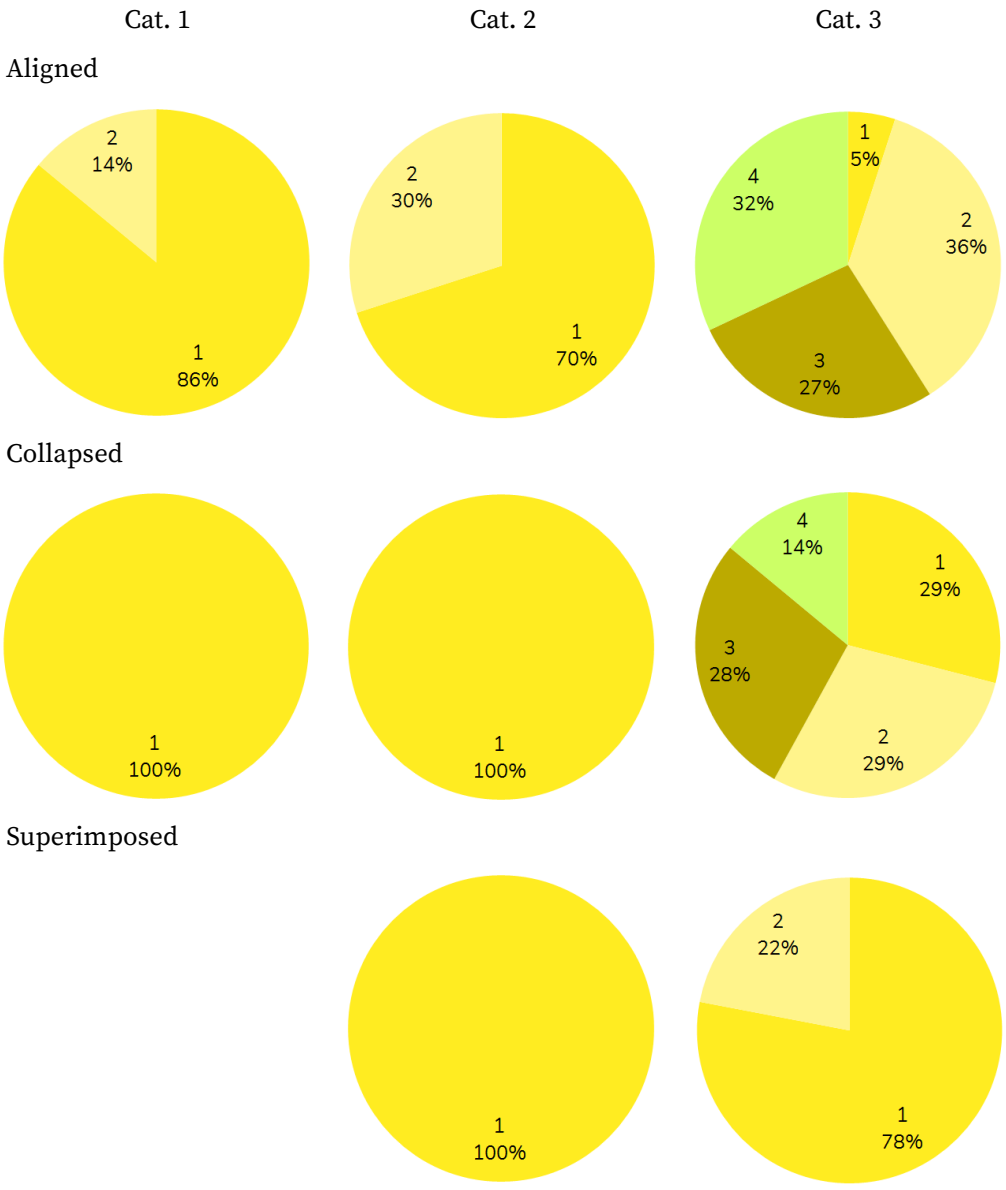

Figure 3-11. Number of concurrent microcracks (from 1 to 4 and more) observed at inter-segments gaps with ends of segments (top to bottom) aligned, collapsed or superimposed, for booster casings (left to right) without abradable nor thermal shock, with abradable without thermal shock, with abradable and thermal shock.

3.3.2.2 Casings with abradable without thermal shock (category 2)

The analysis was this time based on 88 micrographs captured on five booster casings. 42 % of them showed cross-sections of the RM3 track while the other 58 % showed cross-sections of the RM4 track. These views featured all types of zones, i.e. inter-segments gaps, slits, track edges, flange edges and other less specific zones. The distribution of the 47 micrographs with defects over these zones is shown in the pie chart of Figure 3-12, for both tracks combined.

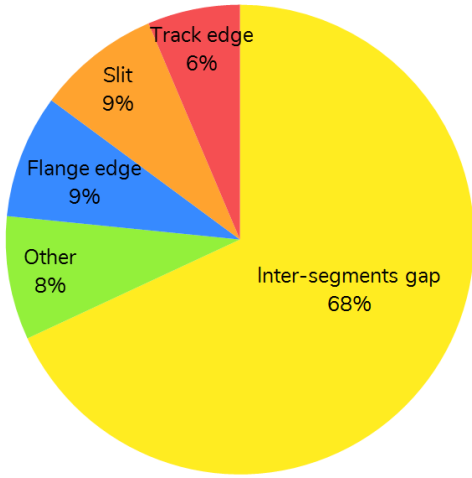

Figure 3-12. Distribution of the 47 micrographs with defects over the specific zones of the booster casing with abradable without thermal shock (cat. 2), for both tracks combined.

The 56 defects observed in these micrographs were equally shared between the RM3 track and the RM4 track. They were still predominantly found at the inter-segments gaps (72 % for both tracks combined, or 86 % for RM3 and 57 % for RM4), as can be seen from the distribution of defects shown in the pie charts of Figure 3-9 (top) for both tracks combined. Nevertheless, the results in Figure 3-9 (top) are again put into perspective with the bar graph in Figure 3-10 showing the distribution of defects observed over the different zones of the casings relatively to the number of micrographs examined for

each zone. The distribution of defects over these zones is indeed not as contrasted as suggested in Figure 3-9 (top). They were actually found in the same percentage (100 %) at slits, track edges and flange edges, and in a larger percentage (125 %) at inter-segments gaps and other less specific zones.

Three types of defects were encountered, namely microcracks, horizontal disbonds and a combination thereof. Most of them were microcracks (79 % for both tracks combined, or 96 % for RM3 and 61 % for RM4), although on the RM4 track horizontal disbonds still counted for 32 % of the observations. The defects at ISGs were 95 % of microcracks and 5 % of horizontal disbond combined with microcrack, as detailed in Figure 3-9 (bottom). Track edges and flange edges exclusively contained horizontal disbonds (respectively 5 % and 7 % of the observed defects), while slits exclusively contained microcracks (7 % of the observed defects).

At the ISGs of both tracks, the ends of the steel strip segments were again mostly aligned (83 %) with a mean gap width of 0.41 mm. They were otherwise collapsed (11 %) with a mean gap width of 0.17 mm, or superimposed for the 6 % remaining. The first type of segments positioning counted 63 % of all observed defects, while 5 % and 4 % of the defects were respectively found at inter-segments gaps presenting the second and third types of positioning. More specifically, 88 % of the microcracks observed at ISGs were found where segments edges were aligned. This type of segments positioning presented slightly more cohesive microcracks than interfacial ones. 54 % of the microcracks were cohesive in the polymer blend, most often starting at the level of the steel strip and arresting in the co-cured joint beneath the steel strip, with a mean length of 0.34 mm; the other 46 % were interfacial, running at the steel strip/gap vertical interface with a mean length of 0.28 mm and extending to the co-cured joint. Besides, in these gaps, microcracks were again at most going by pair, with 30 % of gaps with paired microcracks versus

70 % of gaps with isolated microcracks, as detailed in the pie charts of Figure 3-11 (second column). When the ends of the steel strip segments were collapsed, 67 % of the microcracks were cohesive in the polymer blend filling the gap with a mean length of 0.25 mm; the other 33 % were interfacial, running at the strip/gap vertical interface with a mean length of 0.19 mm. The microcracks were then exclusively isolated. In case of superimposed segments ends, the microcracks started from the steel strip/gap vertical interface and presented a mean length of 0.31 mm. They were exclusively isolated, too. Finally, for all zones combined, only five microcracks out of 46 (i.e. 11 %) were either totally or partly found in the composite laminate, with a length ranging from 0.36 mm to 0.87 mm.

3.3.2.3 Casings with abradable and thermal shock (category 3)

This last analysis was based on 101 micrographs captured on seven booster casings, with 45 % of cross-sections of the RM3 track and 55 % of cross-sections of the RM4 track. These views again featured all types of damage zones. The distribution of the 97 micrographs with defects over these zones is shown in the pie chart of Figure 3-13, for both tracks combined.

The 209 defects observed in these micrographs were almost equally distributed between the RM3 track and the RM4 track. They were still predominantly found at the inter-segments gaps (69 % for both tracks combined, or 78 % for RM3 and 60 % for RM4), as can be seen from the distribution of defects shown in the pie charts of Figure 3-9 (top) for both tracks combined. Again, the results in Figure 3-9 (top) are put into perspective with the corresponding bar graph in Figure 3-10. Although the proportions largely differ, the scheme of defects distribution over the different zones does relatively well correspond to that suggested in Figure 3-9 (top). The largest percentage of defects (253 %, i.e. 253 defects for 100 micrographs, or 2.53 defects per micrograph) was found at ISGs, followed by track edges (220 %) and slits (171 %).

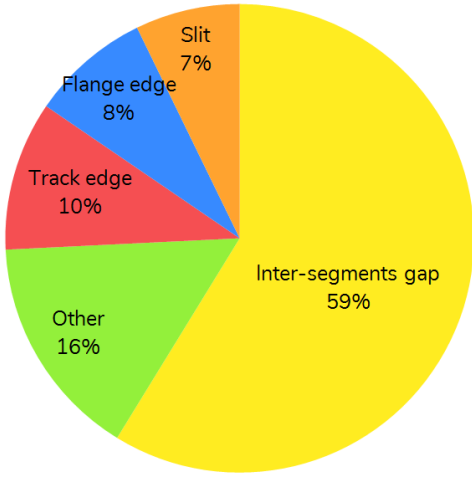

Figure 3-13. Distribution of the 97 micrographs with defects over the specific zones of the booster casing with abradable and thermal shock, for both tracks combined.

The whole panel of damage types was this time encountered. Most defects were microcracks (75 % for both tracks combined, or 79 % for RM3 and 70 % for RM4) while the second major type of defect was the combination of horizontal disbond and microcrack, which counted for 11 % of the observations on each track. In particular, the damage at ISGs was 81 % of microcracks, 12 % of (meta-)delamination combined with microcrack, and 7 % of horizontal disbond combined with microcrack, as detailed in Figure 3-9 (bottom).

At the inter-segments gaps of both tracks, the ends of the steel strip segments were still mostly aligned (71 %) with a mean gap width of 1 mm. The rest was either collapsed (14 %) with a mean gap width of 0.29 mm, or superimposed (15 %). 56 % of all observed defects were found at ISGs with aligned segments ends, while 8 % and 5 % of the defects were respectively found at inter-segments gaps presenting collapsed or superimposed segments ends. More specifically, ISGs with aligned segments ends counted 81 % of the microcracks observed in this type of damage zone. All types of segments positioning presented much more cohesive microcracks than interfacial ones.

When the segments ends were aligned, 77 % of the microcracks were cohesive in the polymer blend, most often starting in the co-cured joint and reaching the first carbon lamina (with a mean length of 0.48 mm) or the second carbon lamina (with a mean length of 0.72 mm); the other 23 % were interfacial, running at the strip/gap vertical interface with a mean length of 0.82 mm and reaching the third carbon lamina, at most. Not less than 32 % of these gaps were now affected by four (or more) concurrent microcracks, as detailed in Figure 3-11 (third column). When the ends of the steel strip segments were collapsed, 75 % of the microcracks were cohesive in the polymer blend filling the gap with a mean length of 0.46 mm; the other 25 % were interfacial, running at the strip/gap vertical interface with a mean length of 0.79 mm. 14 % of these gaps were still affected by four microcracks or more. In case of superimposed segments ends, 73 % of the microcracks were cohesive and essentially started from the corner of the bottom steel strip segment, with a mean length of 0.37 mm. Besides, microcracks at this type of inter-segments gap were at most going by pair (22 % versus 78 % of superimposed gaps with isolated microcracks). Finally, for this category of casings, microcracks were much more often (actually 83 % of the time) totally or partly found in the composite laminate for all zones combined, with 167 cases out of the 201 existing microcracks.

3.3.3 Global review

One may capture the main outcomes of the three detailed individual studies with the following list of statements.

- *Both abradable tracks are about equally damaged*

The RM3 and RM4 abradable tracks were found to be damaged in approximately the same proportion, for all three categories of casings. The position of the track on the casing did not seem to influence the multilayer's damage state.

- *The quantity, size and diversification of defects increase with plasma spray and thermal shock.*

Overall, one noted the increase in the quantity and size of defects as well as their diversification from the first to the third category of casings, as a result of the complexification of the multi-layered system (abradable) and the thermal history of the casing (thermal shock).

- *Inter-segments gaps are the most damaged zones.*

While the different zones of the abradable tracks were about equally affected by defects in the absence of abradable and thermal shock (cat. 1), inter-segments gaps progressively stood out as the most damaged zone in casings with abradable (cat. 2) and in casings with abradable and thermal shock (cat. 3).

- *Damage most often occurs as matrix microcracking.*

Microcracks formed the large majority of defects found in all categories of casings, distantly followed by the combination of horizontal disbond and microcrack.

- *The number of concurrent microcracks increases with plasma spray and thermal shock, especially at ISGs with aligned segments ends and large gap width.*

The maximum number of concurrent microcracks increased in every damage zone with the introduction of abradable and thermal shock in the system. At ISGs, it jumped from two (cat. 1 and 2) to four and more (cat. 3) and was most often found where the ends of the steel strip segments were aligned. In this case, the number of concurrent microcracks did furthermore clearly increase with the width of the gap. This type of positioning was the most frequently observed in all casings categories and the measured gap width ranged from 0.00 mm to 2.79 mm, with a mean value of 0.66 mm. In contrast,

superimposed segments end –the least frequently observed type of positioning– always presented the smallest number of concurrent microcracks.

- *Microcracks at ISGs are generally cohesive in the polymer material of the co-cured joint, but propagate to the composite laminate under the effect of thermal shock.*

At inter-segments gaps, microcracks were most often cohesive in the polymer blend filling the gap and/or in the co-cured joint. They otherwise ran along the strip/gap vertical interface. The number of microcracks touching the composite laminate dramatically increased with thermal shock (cat. 3), after which microcracks regularly reached the second lamina and –to a lesser extent– the third lamina.

This statistical analysis of defects reinforced the interest in the inter-segments gap and demonstrated that this zone of the abradable tracks deserves further investigation. It could for instance be the focus of a study of damage initiation and propagation with the finite element method. This would preferably be performed in 3D, yet the defects contained in this region have until now appeared as two-dimensional features lying in the plane of the observed cross-sections. By common sense, it was assumed that they extend further than this plane, in the sample width. An experimental method was developed in order to reveal the defects morphology in the volume of the multilayer. It was called *fine incremental polishing*, as explained in the following section.

3.4 Investigation of the 3D configuration and damage morphology at the inter-segments gap

For the aforementioned reasons, one selected four interesting samples featuring damaged ISGs. Fine layers of material were removed from their visible cross-section by grinding and polishing with SiC paper 1200 and diamond

pastes down to the granulometry of 1 µm. Optical micrographs of the exposed surface were captured after each step of layer removal so as to keep trace of the damage appearance along this destructive process.

Although small, the curvatures of the samples cut from booster casings made it impossible to measure their width with a micrometer, least of all for determining the thickness of the layer removed by a polishing step. This layer thickness was thus rather evaluated using the radius R of the steel strip's micro-perforations (a steady characteristic of the multilayer), and the chord length C of a reference micro-perforation close to the ISG. These measures are illustrated in Figure 3-14 and related through Eq. (3-1).

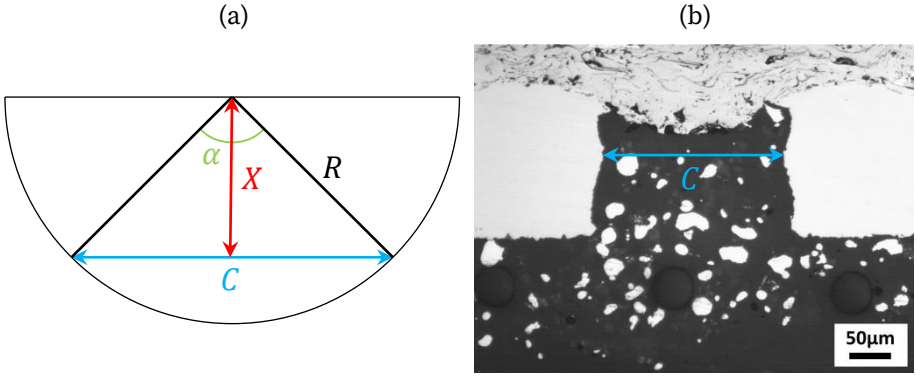

Figure 3-14. (a) Schematic top view of half a micro-perforation, as basis for the trigonometric calculation of the layer thickness removed by fine incremental polishing. (b) Chord length of a micro-perforation as seen in optical micrographs.

$$C = 2R \sin\left(\frac{\alpha}{2}\right) \tag{3-1}$$

It was then possible, with simple trigonometry, to express the distance X separating the centre of that chord and the centre of the micro-perforation (Eq. (3-2)). Calculating X for consecutive polishing steps enabled determining the distance by which one had moved towards (if the chord length increased) or away (otherwise) from the centre of the micro-perforation, or in other

words, the thickness of the layer removed in the course of each polishing step.

$$X = R\cos\left(\frac{\alpha}{2}\right) \tag{3-2}$$

At least two reference micro-perforations were followed through the incremental polishing process, as it allowed overcoming the disappearance of a micro-perforation during a polishing step. Moreover, as extra precaution, the reference micro-perforations were usually chosen close to their longest chord, thereby ensuring that about a whole radius could be crossed before they disappear.

The sequences of optical micrographs obtained with this method definitely gave food for thought and triggered significant progress in the understanding of features seen in this particular region of the booster casing. The sets of micrographs shown in Figure 3-15 and Figure 3-18 were selected out of the eleven polishing steps performed on a sample that presented an interesting combination of damage types, namely a microcrack in the polymer blend filling the inter-segments gap, and a transverse microcrack in the composite. They do perfectly illustrate the announced elements of discovery and form a good support for their explanation

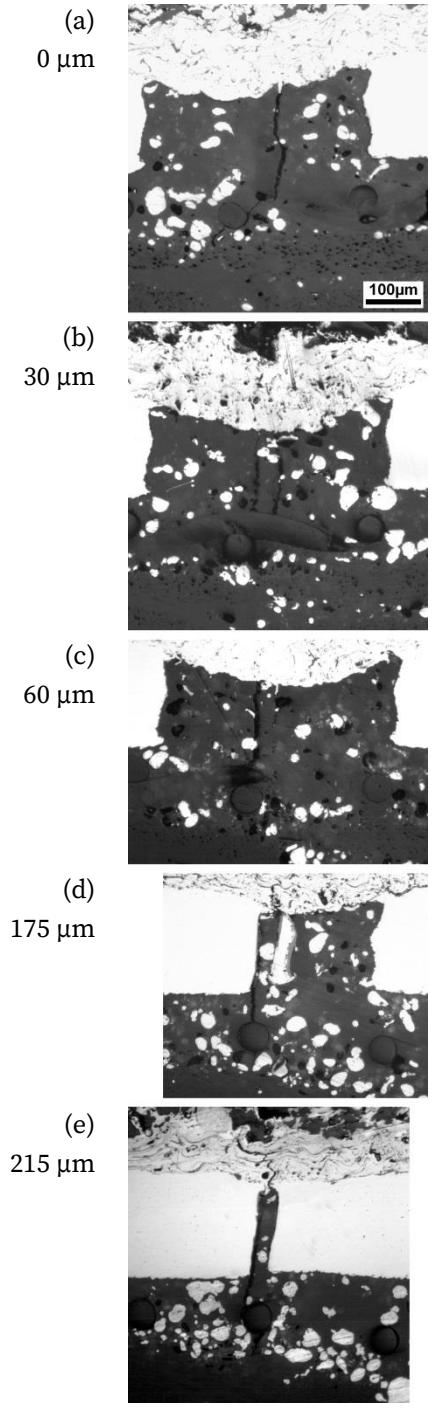

Figure 3-15. Simultaneous evolution of the morphology of a microcrack and an inter-segments gap revealed by fine incremental polishing. The distance indicated at left of each micrograph is that separating the current cross-section from the initial view.

- *Micro-perforations do modify the gap width locally*

The inter-segments gap width was seen to change considerably within this set of optical micrographs. While it was approximately constant over the first 60 µm (Figure 3-15-(a) to (c)), it surprisingly appeared to be dramatically reduced in the two last micrographs. Furthermore, the morphology of the gap varied together with its width. More specifically, the edges of the steel strip segments changed from the typical hourglass shape of micro-perforations to a straight shape recalling the neat cutting of as-rolled steel strips. This helped realising that micro-perforations play a role in defining the width of the ISG. In fact, the distance between the strip segments in Figure 3-15-(e) is the gap width intended by the manufacturer, namely about 35 µm here. Yet, this gap width was obviously regularly modified by the presence of cut micro-perforations, in a way that is schematically illustrated in Figure 3-16.

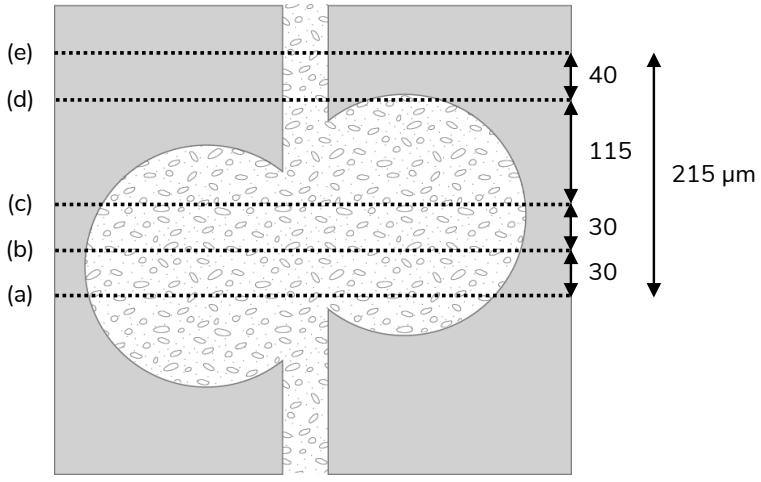

Figure 3-16. Modification of the inter-segments gap width by cut micro-perforations (with reference to the location of the micrographs along the inter-segments gap in Figure 3-15).

Although this modification may seem anecdotal at the scale of the booster casing, it has its importance at the scale of the ISG: cut micro-perforations do not only alter the gap width, they also introduce geometric singularities

which are as many stress concentrators. This must be taken into account in the finite element modelling.

- *Microcracks arise from vertical disbonds at the segments edges*

Figure 3-15-(b) shows two microcracks in the gap. The left microcrack is still present and well recognisable in Figure 3-15-(c), after a 30 µm thick layer was removed. At the next polishing step however, it was unexpectedly replaced by a disbond along the end of the left steel strip segment (Figure 3-15-(d)). This change in nature of the defect was elucidated with the measurement of the distance separating the cracks in Figure 3-15-(b): it indeed turned out to be precisely equal to the gap width seen in the two last micrographs. The only valid explanation of this equality was that these microcracks actually arose from former disbonds at the straight edges of the steel segments ends. One can then understand that a disbond does not follow the contour of the cut micro-perforations lying along its path, it rather propagates straight ahead and fractures the material in the co-cured joint, as shown schematically in Figure 3-17 with disbonds in green and microcracks in red.

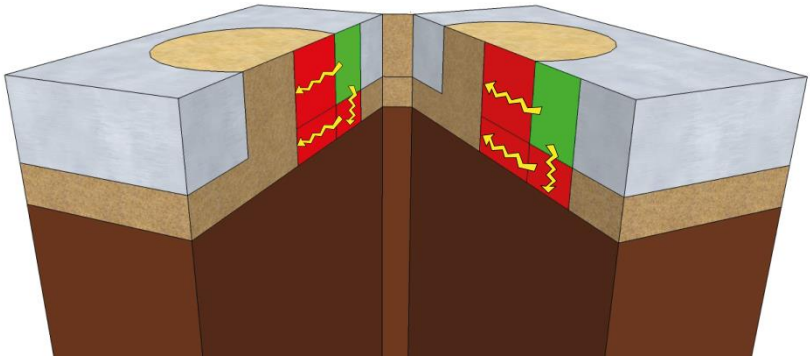

Figure 3-17. Exploded view of an ISG for the schematic illustration of the hypothesis on the origin and evolution of the microcracks at this location. The green areas are disbonded and the red areas are fractured. The arrows show the directions of damage propagation.

A microcrack in the inter-segments gap and a disbond along the straight edge of a steel segment are thus one and the same defect, or more exactly, one is the continuation of the other. Finally, one can note that, whatever its nature, damage always extended to the co-cured joint.

- *Shielding occurs at the inter-segments gap*

From the two microcracks seen in Figure 3-15-(b), the right-hand microcrack is the only one visible on the initial cross-section in Figure 3-15-(a), while the left-hand microcrack is the only one remaining in Figure 3-15-(c). In terms of propagation, it means that these microcracks did run in parallel over a few microns only. Their arrest is due to energetic reasons: a microcrack grows by consuming the elastic strain energy stored in the surrounding material; yet, when the amount of energy becomes too low to sustain its propagation, the crack stops. Thus, from the moment the microcracks crossed each other, they were both evolving in regions where the elastic strain energy had already been consumed by the other crack, and they were hence visibly forced to stop. This phenomenon is known as *crack shielding*, since each of the two cracks protects the material behind its tip from being damaged by the opposite crack.

The same sample provided the opportunity of observing the evolution of a microcrack situated at 3.1 mm of the ISG. This is illustrated in Figure 3-18 where the micrographs have been selected for their quality and do not necessarily correspond to the same polishing steps as those in Figure 3-15.

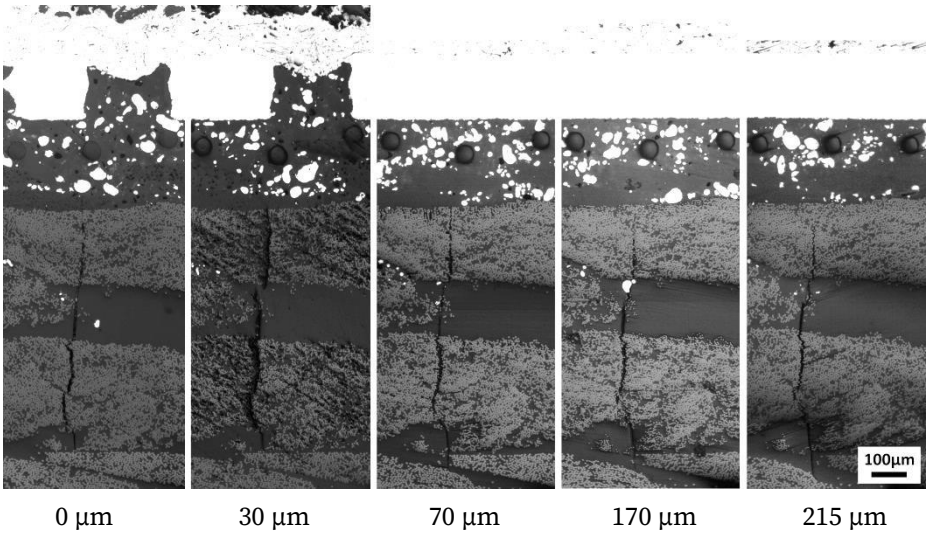

Figure 3-18. Evolution of a microcrack in the composite revealed by fine incremental polishing. The distance indicated below each micrograph is that separating the current cross-section from the initial view.

- *Microcracks have a steady morphology in the laminate*

This microcrack was seen to have a constant length (~700 µm) and a stable morphology over the 215 µm of material removed. This information is valuable for the FE simulation of crack growth with cohesive elements where the crack path must be assumed in advance. The set of micrographs did unfortunately not reveal the cause of this microcrack, and the root of the defect might actually not even lie in this sample cut from the booster casing. However, by continuing the fine incremental polishing experiment on this sample, one could at least interestingly reach an area where the crack meets a longitudinal tow and arrests or deviates from its original trajectory.

3.5 Conclusion

The study presented in this chapter yielded clear information about the multilayer's damage state in the areas covered by the abradable tracks. One demonstrated that damage preferentially develops in several specific zones (ISGs, longitudinal slits, track edges, flange edges) and most often takes the form of microcracks in the co-cured joint and/or in the composite laminate. Moreover, one highlighted that booster casings with abradable contain a larger quantity and diversity of defects than those which had not been thermal sprayed, while subsequent ageing by thermal shock further increases the quantity of defects and their size all over the abradable tracks. As it was shown that inter-segments gaps concentrate the largest quantity of defects in all casings categories, this damage zone received particular attention with a fine incremental polishing study. Its 3D configuration and damage morphology were thereby revealed, and it was understood that (i) cut microperforations at the ends of the steel strip segments do modify the gap width, (ii) cohesive microcracks in the gap do derive from vertical disbonds at the ends of the steel strip segments, (iii) concurrent microcracks do arrest by the crack shielding phenomenon, and (iv) transverse matrix microcracks seem to propagate with a steady shape in the composite laminate.

4. Thermo-mechanical characterisation of the constituent materials

The results presented in this chapter were obtained using various experimental and analytical methods. Yet, to improve the readability of this text, the complete description of these methods was transferred to Appendix F and Appendix G to which the reader is kindly invited to refer complementarily to the present chapter.

4.1 Introduction

This chapter reviews the efforts made to characterise the mechanical and thermal behaviour of the multi-layered system's constituent materials in view of obtaining reliable input data for the analytical calculations and FE analyses. Data acquired by the industrial partner prior to the beginning of the thesis were collected and used, when available. Some important ones were missing, however, especially regarding the mechanical and thermal behaviour of the resin, the adhesive and the steel sheet.

Many of these gaps were filled in this work, using a variety of experimental techniques. Sometimes, under the influence of intellectual curiosity (or scientific enthusiasm!), two techniques were used to measure the same material

property. Comparison of the obtained results allowed identifying the most suitable technique, which has already proved useful for subsequent work of characterisation by SAB. In general, the results were critically analysed and discussed as far as possible in light of relevant theories and literature data.

4.2 Effective properties of the CFRP composite laminate

Layered media such as composite laminates are *inhomogeneous* and most often *anisotropic*. Many applications require modelling such type of material which can then either be considered *discontinuous* and modelled in a ply-by-ply approach (Discrete Ply Modelling, e.g. [132]), or be considered *continuous* and modelled as a *homogeneous* material. The second modelling option is often conveniently used in analytical calculations, and is sometimes preferred in FE analyses when it is not necessary to model the constituent layers explicitly. The *equivalent* homogeneous solid is then defined with *effective* thermoelastic properties such that its thermal and mechanical behaviour is equivalent to that of the layered solid. However, these properties are a complex combination of those of the constituent layers; they have been determined analytically in this work by means of the Classical Lamination Theory (CLT), which allows calculating the *macroscopic effective* properties of anisotropic layered media based on their layup and the properties of the individual layers. More specifically, the three-dimensional semi-analytical model developed by Gudmundson and Zang [133] (described in Appendix F) was used in this work.

4.2.1 Thermoelastic properties of the constituent laminae

The layup of the laminate of interest has already been defined (Table 1-1). It is used for the manufacturing of the composite booster casing, and was also used in this work for the manufacturing of fracture test specimens. As a reminder, this laminate can be virtually decomposed into 14 laminae as it results from the stacking and resin impregnation of 14 pieces of 2D woven fabric of four types (warp heavy, weft heavy, balanced, glass). It is symmetric about the plane situated between the seventh and eighth laminae.

The heterogeneous laminae (fabric + resin) are assumed orthotropic. Their effective thermoelastic properties at room temperature and under ambient humidity conditions were predicted by SAB engineers based on the properties of the resin and fibres, using a mean-field homogenisation procedure. They calibrated their model with an inverse method consisting of an abatement factor applied to the Young's modulus of the fibres until the predicted properties matched those measured with tensile and compression tests performed in the warp and weft directions of the plane of physical laminae. This approach is thought to take the effect of the actual woven nature of the laminae into account. The effective thermoelastic properties are reported in Table 4-1 for each type of lamina, and are expressed in the principal material coordinate system with subscripts 1, 2, 3 respectively referring to the warp direction, the weft direction and the normal direction. In a multi-scale approach, these properties can be used to determine the effective thermoelastic properties of the homogeneous equivalent laminate. Alternatively, they can be used as such to define the behaviour of the individual laminae in a ply-by-ply modelling approach of the laminate.

Table 4-1. Effective thermal and mechanical properties provided by SAB for the four types of laminae constituting the composite laminate.

Lamina	Balanced	Warp heavy	Weft heavy	Glass
Thickness [mm]				
t	0.378	0.342	0.342	0.080
Young's moduli [GPa]				
E_1	73.3	116	34.1	23.2
E_2	73.3	34.1	116	23.2
E_3	8.70	11.1	11.1	8.76
Poisson's ratios [-]				
ν_{12}	0.06	0.10	0.03	0.10
ν_{13}	0.40	0.36	0.36	0.37
ν_{23}	0.40	0.37	0.37	0.37
Shear moduli [GPa]				
G_{12}	5.10	5.40	4.40	3.08
G_{13}	2.50	2.70	2.70	2.90
G_{23}	2.50	3.70	3.70	2.90
Coefficients of linear thermal expansion [µm/m/°C]				
α_1	2.12	1.44	7.36	15.8
α_2	2.12	7.36	1.44	15.8
α_3	55.6	46.6	46.6	56.9

4.2.2 Effective thermoelastic properties of the laminate

The laminate layup and the properties of the individual laminae were used to determine the effective thermoelastic properties of the composite laminate at room temperature with the model of Gudmundson and Zang [133]. The predicted data expressed in the global coordinate system (defined in Appendix F, Figure F-2) are reported in Table 4-2 together with experimental data provided by SAB.

The predicted values compare relatively well with the experimental ones provided by SAB. The effective Young's modulus and the effective coefficient of thermal expansion (CTE) in both reference directions of the layers' plane (xy-plane) appear to be identical, yet their value in the direction normal to this plane (z-direction) differs significantly from the in-plane values. These properties are indeed influenced by the duality of materials constituting the laminae: the low stiffness and large thermal expansion in the out-of-plane direction are dictated by the polymer matrix, while their values in the plane of the laminae are rather dictated by the carbon fibres (the axial CTE of which is known to be slightly negative [134]). In the end, the equivalent homogenised material may be considered orthotropic, with three planes of symmetry passing by the geometric centre of the laminate and parallel to the axes of the global coordinate system.

Table 4-2. Thermoelastic properties of the laminate at room temperature predicted with the selected CLT model. The last column contains experimental data provided by SAB (only the out-of-plane Young's modulus -marked with an asterisk- was determined analytically).

Source	Gudmundson & Zang	SAB
Thickness [mm]		
t	4.408	-
Young's moduli [GPa]		
E_x	59.2	57.1 ± 10 %
E_y	59.2	69.4 ± 10 %
E_z	10.2	9.40*
Poisson's ratios [-]		
ν_{xy}	0.23	-
ν_{xz}	0.31	-
ν_{yz}	0.32	-

Source	Gudmundson & Zang	SAB
Shear moduli [GPa]		
G_{xy}	15.3	-
G_{xz}	2.63	-
G_{yz}	3.15	-
Coefficients of linear thermal expansion [µm/m/°C]		
α_x	2.75	2.31
α_y	2.76	2.71
α_z	51.0	53.1

4.3 Properties of the RTM6 resin and the Redux 322 structural film adhesive

4.3.1 Materials

The material samples used for the characterisation of RTM6 and Redux 322 come from plates casted in a 300 mm x 300 mm x 4 mm stainless steel mould. Two RTM6 plates were readily prepared by pouring the slightly heated pre-mixed epoxy system in the mould prepared with release agent (Watershield, Zyvax). The Redux 322 plate, on the other hand, necessitated more preparation work since 20 pieces of film adhesive had to be stacked to fill the plate thickness. The filled mould was then closed and placed in a laboratory oven at ambient pressure, as illustrated in Figure 4-1-a. Following recommendations received from SAB, the temperature programs defined in Figure 4-1-b with isotherms and a 1 °C/min heating rate were applied to perform the cure reaction. Finally, the plates were left for relatively slow cooling in the oven at the end of the temperature program.

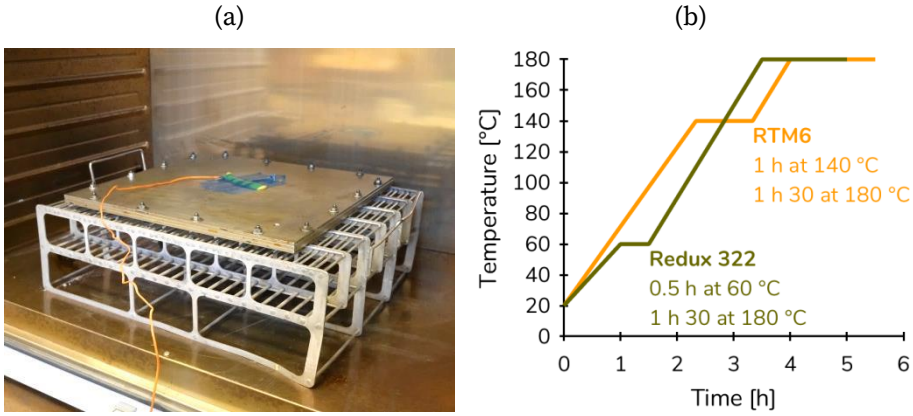

Figure 4-1. (a) Stainless steel mould in the laboratory oven for ambient pressure curing of the RTM6 resin. (b) Cure cycles of the RTM6 resin and the Redux 322 adhesive, with a 1 °C/min heating rate.

Note that a seal joint was placed along the mould contour to avoid leakage of RTM6 whose viscosity decreases by several orders of magnitude upon heating. Pictures of the resulting plates are shown in Figure 4-2.

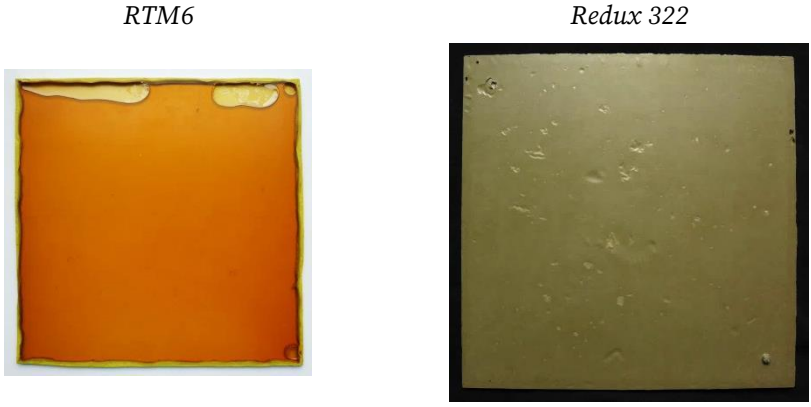

Figure 4-2. Examples of plates produced in this work.

The quality of the RTM6 plates was excellent, as voids exclusively concentrated at the edges. Unfortunately, the production of the Redux 322 plate was not that successful: a multitude of voids were discovered in the plate thick-

ness where small air pockets were trapped between the successive layers of film adhesive, despite the care taken during assembly.

4.3.2 Thermal stability

It is important to study the thermal stability of polymer materials prior to performing other thermal analyses. Indeed, from a laboratory practice point of view, it reveals the temperature window within which the materials can be analysed without risk of thermal degradation and contamination of the test equipment. Besides, from the point of view of the present application, it allows verifying that the polymers are thermally stable up to the maximum temperature to which they will be exposed, i.e. the 180 °C isothermal cure temperature (T_{cure}).

Two samples of each thermoset were studied by ThermoGravimetric Analysis (TGA). After an initial isotherm of 30 minutes at 60 °C, the sample weight (in percent of its initial value) and its time derivative were monitored throughout heating from 60 °C to 500 °C at a rate of 10 °C/min. One set of data curves by material is presented in the graphs of Figure 4-3.

The extrapolated onset temperature[10] T_0 was graphically determined with the TA Universal Analysis software. For both thermosets, the values given in Table 4-3 are clearly above 180 °C and should hence never be met during manufacturing or normal operation of the booster casing.

[10] I.e. the temperature at which thermal degradation begins, as defined in Appendix G.

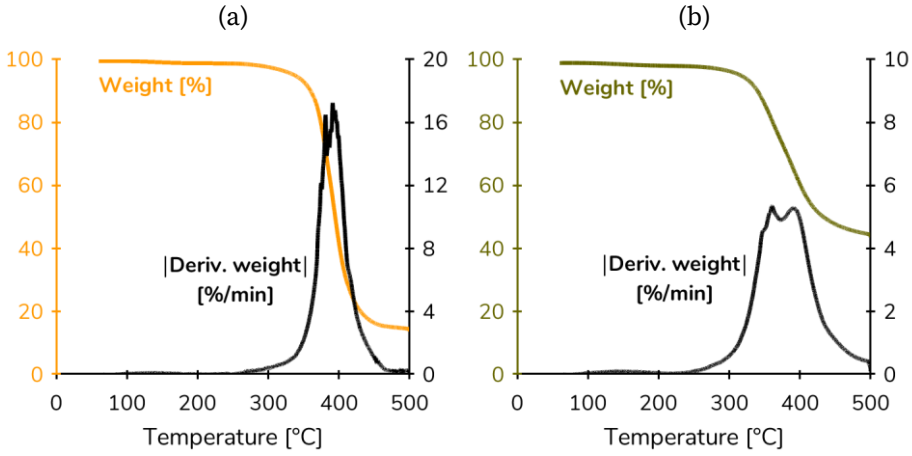

Figure 4-3. Evolution of the weight and absolute time derivative of the weight of (a) RTM6 and (b) Redux 322 samples, as a function of temperature.

Table 4-3. Onset degradation temperature of RTM6 and Redux 322.

Material	T_0 [°C]
RTM6	365 ± 19
Redux 322	331 ± 6

4.3.3 Glass transition temperature

Glass transition is a thermally-driven physical phenomenon that modifies the state of the amorphous fraction of materials, causing remarkable changes in their mechanical behaviour and physical properties (volume, heat capacity, coefficient of linear thermal expansion, modulus of elasticity, etc) [135][136]. The temperature at which this transition takes place is noted T_g and called the *glass transition temperature*; the amorphous material is liquid or rubbery above its T_g and glassy (solid) below its T_g [135]. The glass transition temperatures of RTM6 and Redux 322 have been determined by Thermomechanical Analysis (TMA) and Dynamic Mechanical Analysis (DMA) in this work, based on the change in CTE and modulus, respectively. This is reported in the two following sub-sections.

4.3.3.1 Glass transition temperatures determined by TMA

Glass transition presents the characteristics of a second-order thermodynamic transition as it is marked by the *discontinuity* in second partial derivatives of the Gibbs free energy (e.g. CTE, heat capacity) and the *continuity* of the free energy and its first partial derivatives (e.g. volume, enthalpy) [136]. The schematic plots in Figure 4-4 illustrate the effect of glass transition on volume V and CTE α, namely a *change in slope* for the first and a *step change* or *jump* for the latter.

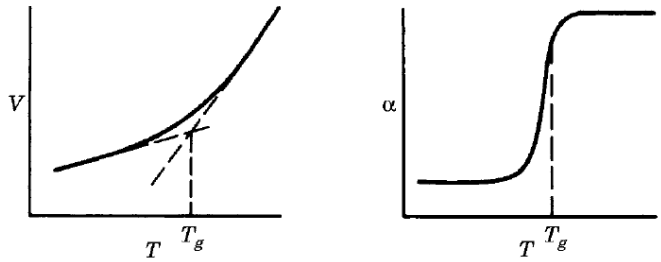

Figure 4-4. Theoretical change in volume (left) and coefficient of thermal expansion (right) in the glass transition region [135].

These changes usually occur over an interval of 10 to 30 °C, so that the elbow and step shown in Figure 4-4 are not sharp [135]. Nevertheless, the abscissa of the elbow in volume-temperature studies constitutes a fundamental measure of the glass transition temperature [135]. According to the prevailing standard (ASTM E 1545-11, [137]), the elbow in the plot of sample length versus temperature obtained by TMA can be used as well.

In practice, the length of two samples of each material was monitored while they were exposed to a heat-cool-heat temperature program defined on a temperature range going from -75 °C to 210 °C (RTM6) or 235 °C (Redux 322), with 10 minutes long isotherms at these temperatures and a heating/cooling

rate of 2 °C/min. Figure 4-5 shows the original data for a sample of RTM6 and a sample of Redux 322.

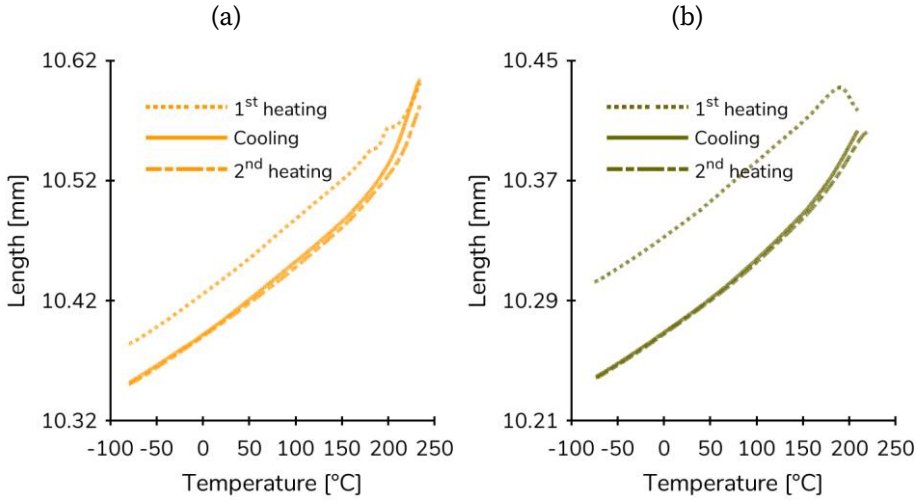

Figure 4-5. Evolution of the sample length with temperature throughout a full heat-cool-heat cycle of thermomechanical analysis on a sample of (a) RTM6 and (b) Redux 322.

A global analysis of the evolution of the sample length with temperature has been performed and can be found in Appendix H. Indeed, these curves present interesting features indicating the occurrence of phenomena typical of the thermal behaviour of (thermosetting) polymers, and their interpretation provides an insight of the manufactured plates' quality.

Glass transition temperatures were determined from the change in sample length *on cooling*, as these curves appeared to be virtually unaffected by the aforementioned phenomena. The change in slope is well visible on these curves -especially for RTM6 (Figure 4-5-a). This allowed locating T_g from the intersect of tangents to the curve drawn before and after the elbow[11], as illustrated in Figure 4-4-left. The values resulting from this graphical determina-

[11] In practice, tangents to the curve were taken between 100 °C and 120 °C, and between the maximum temperature T_{max} and $(T_{max} - 20)$ °C.

tion are reported in Table 4-4; they are close to the temperature of 180 °C at which the final isotherm was performed during cure.

Table 4-4. Glass transition temperature of RTM6 and Redux 322 as graphically determined from the change in sample length with temperature measured on cooling in the TMA experiments (mean of two and 95 % confidence interval).

Material	T_g [°C]
RTM6	194 ± 13
Redux 322	168 ± 0

4.3.3.2 Glass transition temperatures determined by DMA

With Dynamic Mechanical Analysis, one followed the evolution of the real and imaginary parts of the thermosets' complex modulus[12] over a large range of temperatures. Three samples of each material were successively subjected to a sinusoidal strain of 0.08 % applied in tensile mode with a 1 Hz frequency. Their temperature was meanwhile increased from -50 °C to 250 °C at a constant rate of 2 °C/min, starting with an initial isotherm of 10 minutes at -50 °C. Although the main purpose of these measurements was to record the temperature-dependent evolution of the storage modulus (E') of RTM6 and Redux 322 (see Section 4.3.4.2), the results were also used for the determination of their T_g.

Figure 4-6 shows a complete set of evolution curves obtained for one sample of each thermoset. The prevailing ASTM standard (ASTM E1640-09, [138]) recommends the determination of the glass transition temperature from the extrapolated onset of the sigmoidal change in E-modulus (E'). Alternatively, damping being particularly strong at glass transition [136], T_g can easily be located from the position of the peak in S-modulus (E'') or in loss tangent ($\tan(\delta)$) [139][135]. The values obtained by these means may commonly differ

[12] $E^* = E' + iE''$, as detailed in Appendix G.

from each other by some 5 to 25 °C, and the use of the S-modulus signal is then generally preferred [140].

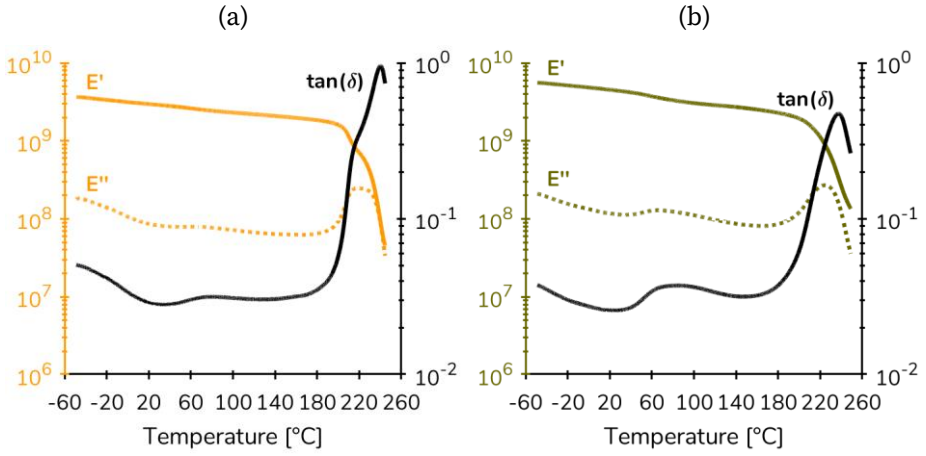

*Figure 4-6. Evolution of the E-modulus (**E'**, in Pa), S-modulus (**E''**, in Pa) and loss gent ($tan(\delta)$) with temperature, as measured by dynamic mechanical analysis in tensile mode on a sample of (a) RTM6 and (b) Redux 322.*

The glass transition temperatures derived from the three signals are reported in Table 4-5 for RTM6 and Redux 322. The thermosets obviously vitrify in the same region of temperature, with all T_g values exceeding the 180 °C isothermal cure temperature of the original plates.

Table 4-5. Glass transition temperatures of RTM6 and Redux 322 as graphically determined from the evolution of the different signals recorded in the DMA experiments (mean of three and 95 % confidence interval).

Material	T_g from E' [°C]	T_g from E'' [°C]	T_g from tan(δ) [°C]
RTM6	202 ± 5	216 ± 10	216 ± 2 (shoulder) 240 ± 1 (peak)
Redux 322	201 ± 1	224 ± 1	237 ± 1

4.3.3.3 Discussion and conclusion

According to TMA results, glass transition temperatures of RTM6 and Redux 322 are close to 180 °C, which corresponds to the isothermal cure temperature of the plates produced in this work. On the contrary, DMA results suggest that the T_g of these thermosets is quite markedly superior to T_{cure}. The latter trend has also been reported for RTM6 in the scientific literature [141], and in the RTM6 product data sheet for a quasi-equivalent cure cycle, where glass transition derived from the three signals equals 194 °C, 206 °C and 211 °C [32].

This discrepancy may be examined from the point of view of the time-temperature-transformation (TTT) isothermal cure diagram of thermosetting systems. This diagram indeed indicates that the T_g of a cured thermoset theoretically corresponds to T_{cure} if the latter temperature was below the glass transition temperature of the fully cured thermoset (noted $T_{g\infty}$) [142]. However, in practice, T_g is generally 30 °C to 50 °C higher than T_{cure} for two reasons: (i) the cure reaction can (slowly) continue proceeding in the glassy state at T_{cure}, and (ii) the cure reaction can resume during the heating scan employed for the measurement of T_g[13] [142].

Besides, T_g is kinetically determined and its value increases with increasing cooling rate (e.g. [140]). It is thus conceivable that the DMA values exceed the TMA values, since DMA values derive from the first controlled heating curve only preceded by the oven cooling of the original plates, while TMA values derive from the controlled cooling curve preceded by controlled heating both performed at a lower rate than that seen in oven cooling.

Glass transition does anyway seem to be found outside the temperature ranges of interest defined in the present work, i.e. [23 °C; 180 °C] for pro-

[13] Residual cure during the DMA measurement is commented in Appendix I.

cessing and [-40 °C; 135 °C] for operation. This has the important consequence that RTM6 and Redux 322 will not show dramatic change in mechanical behaviour during normal operation of the booster casing. They will on the contrary quite constantly behave as glassy elastic solids, the physical properties of which may nevertheless still be moderately influenced by temperature.

4.3.4 Mechanical and thermal properties

4.3.4.1 Mechanical properties measured by quasi-static tensile tests

The thermosets' mechanical properties were measured at 23 °C and 125 °C in quasi-static uniaxial tension. At least three dog bone-shaped specimens of each thermoset were therefore loaded up to fracture at a constant crosshead speed of 2 mm/min. For RTM6, the tensile tests were additionally performed at 135 °C. At room temperature, the strain was simultaneously measured in the axial and transverse directions thanks to a double side-to-side extensometer, allowing for the determination of the Poisson's ratio. The resulting tensile stress-strain curves are shown in Figure 4-7 for RTM6 and Redux 322.

The Young's modulus was determined on an interval of 0.05 % to 0.25 % axial strain, as prescribed by the standard (EN ISO 527-1, [143]). Poisson's ratio was determined on the same interval but only at room temperature where the evolution of the transverse strain had been recorded. A representative pair of axial and transverse strain evolution curves is presented in Figure 4-8 for each thermoset, for it served as basis to the determination of the Poisson's ratio. All mechanical properties determined from the tensile curves are given in Table 4-6 and Table 4-7 respectively for RTM6 and Redux 322, along with relevant literature data.

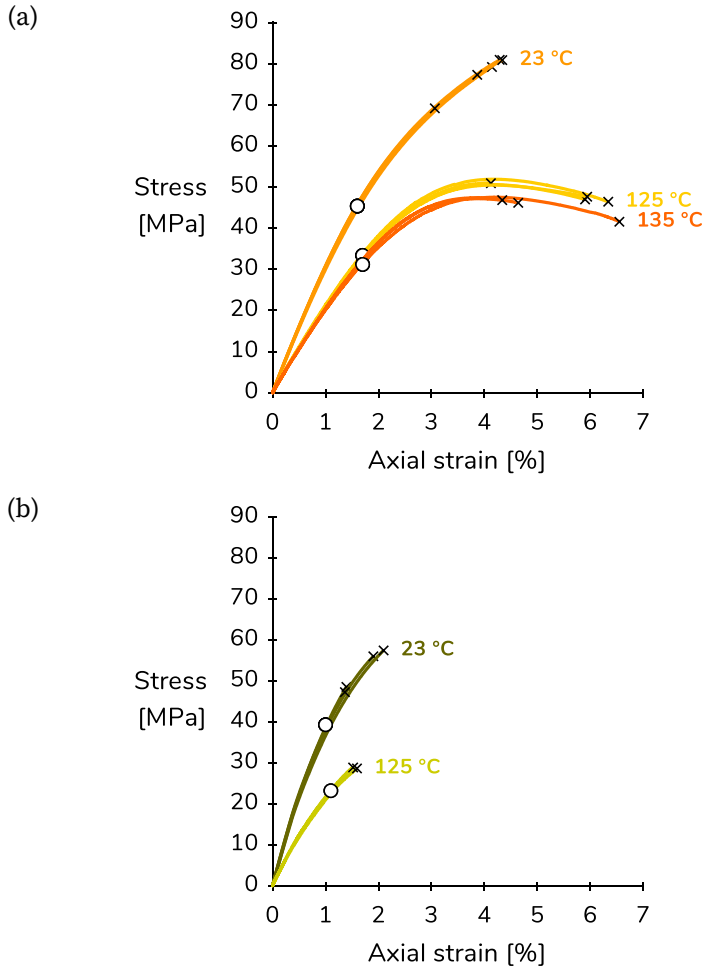

Figure 4-7. Stress-strain curves of (a) RTM6 and (b) Redux 322 obtained by quasi-static uniaxial tensile tests at several temperatures. The open circle indicates the mean 0.2 % offset yield stress (a property determined from the intersection of the curve with a straight line whose slope is given by the Young's modulus and which intersects the x-axis at 0.2 % axial strain), and the cross indicates the fracture point of the test specimen.

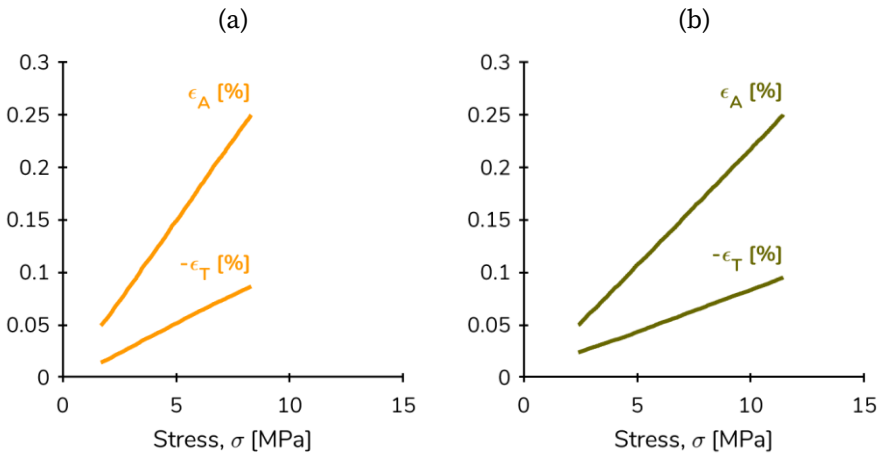

Figure 4-8. Representative pair of axial and transverse strain evolution curves obtained by quasi-static uniaxial tensile test on (a) RTM6 and (b) Redux 322.

Clearly, temperature strongly influenced the mechanical behaviour of both thermosets, as already demonstrated for RTM6 [144][145]. They presented a marked decrease in stiffness, yield stress and fracture strength with temperature. Moreover, while RTM6 was brittle at room temperature, its ductility increased with temperature so that larger strains were achieved before fracture. Plastic flow initiated after the *elastic-viscoelastic deformation* stage at small strain, and a region of *yield drop* or *intrinsic strain softening* followed the onset of yielding at 125 °C and 135 °C, showing (true) stress decreasing with increasing strain [146][147]. Intrinsic softening is known to eventually cause *geometric strain softening* or *necking* (localisation of plastic deformation), but this was not observed in this case. Finally, all specimens failed before the occurrence of *strain hardening* (increasing stress with increasing strain), a last stage of deformation typically observed in the *compression* stress-strain response of RTM6 but not in the tensile one [145].

Table 4-6. Mechanical properties of RTM6 derived from quasi-static uniaxial tensile tests results at three temperatures (this work) and compared to literature data.

Source	This work	Product data sheet [32]	Hobbiebrunken et al. [144]	Generic for epoxies [140]
# specimens	≥ 3	-	5	-
Young's modulus [GPa]				
$E_{23°C}$	3.27 ± 0.07	2.89	2.76	2.4
$E_{125°C}$	2.18 ± 0.03	-	-	-
$E_{135°C}$	2.13 ± 0.02	-	-	-
Poisson's ratio [-]				
$\nu_{23°C}$	0.38 ± 0.04	-	0.38	0.37
0.2 % offset yield stress [MPa]				
$\sigma_{0.2,23°C}$	48.3 ± 0.6	-	-	-
$\sigma_{0.2,125°C}$	35.9 ± 2.0	-	-	-
$\sigma_{0.2,135°C}$	33.4 ± 4.0	-	-	-
Tensile strength [MPa]				
$\sigma_{M,23°C}$	80.7 ± 6.7	-	-	-
$\sigma_{M,125°C}$	53.2 ± 1.0	-	-	-
$\sigma_{M,135°C}$	49.3 ± 0.7	-	-	-
Tensile stress at break [MPa]				
$\sigma_{B,23°C}$	80.6 ± 6.8	75	87.5	55
$\sigma_{B,125°C}$	50.7 ± 2.6	-	57.6	-
$\sigma_{B,135°C}$	47.2 ± 6.3	-	-	-
Tensile strain at break [%]				
$\varepsilon_{B,23°C}$	3.9 ± 0.6	3.4	-	5
$\varepsilon_{B,125°C}$	5.4 ± 1.5	-	-	-
$\varepsilon_{B,135°C}$	5.0 ± 2.8	-	-	-

Table 4-7. Mechanical properties of Redux 322 derived from quasi-static uniaxial tensile tests results at two temperatures (this work) and compared to literature data.

Source	This work	Jeandrau [148][149]	Generic for epoxies [140]
# specimens	≥ 3	5	-
Young's modulus [GPa]			
$E_{23°C}$	4.64 ± 0.20	4.50 ± 0.10	2.4
$E_{125°C}$	2.52 ± 0.15		-
Poisson's ratio [-]			
$\nu_{23°C}$	0.39 ± 0.02	0.38	0.37
0.2 % offset yield stress [MPa]			
$\sigma_{0.2,23°C}$	40.4 ± 2.1	-	-
$\sigma_{0.2,125°C}$	24.1 ± 2.2	-	-
Tensile strength [MPa]			
$\sigma_{M,23°C}$	53.3 ± 8.5	-	-
$\sigma_{M,125°C}$	29.4 ± 0.6	-	-
Tensile stress at break [MPa]			
$\sigma_{B,23°C}$	53.2 ± 8.6	61.5 ± 0.5	55
$\sigma_{B,125°C}$	29.1 ± 0.0	-	-
Tensile strain at break [%]			
$\varepsilon_{B,23°C}$	1.7 ± 0.6	1.79 ± 0.05	5
$\varepsilon_{B,125°C}$	1.6 ± 0.6	-	-

Redux 322 did not present the same trend and rather seemed to retain its original brittleness, with small failure strains and little plastic strain even at high temperature. However, the measurement may have been biased by the presence of voids in the test specimens. Indeed, the fracture strength and tensile strain at break of Redux 322 are somewhat lower than the available room temperature data published by Jeandrau [148], whereas these properties are known to be impaired by the presence of defects in the material (which are as many loci of stress concentration). While the theoretical frac-

ture strength of most solids is estimated to be about 10 % of their Young's modulus, measured fracture strengths rarely exceed half of this value [150] and decrease with the test specimen size owing to a statistical increase of the quantity and size of defects in larger gauge volumes [151]. According to the measured values of Young's modulus, the theoretical fracture strength of RTM6 at room temperature is about 330 MPa and that of Redux 322 is about 460 MPa. Chevalier *et al.* hence developed a two-parameter fracture criterion for RTM6, based on the attainment of a 300 MPa principal stress at the tip of an internal spheroidal defect of prescribed aspect ratio. Their work demonstrated the ability of this criterion to accurately predict fracture of macroscopic specimens for a wide range of stress states and test conditions [152][153].

The fact that fracture strengths measured in this work only represent 11 % (Redux 322) to 25 % (RTM6) of their theoretical counterpart –even though the RTM6 specimens did not feature apparent defects– illustrates the incidence of microscopic as well as macroscopic defects on the macroscopic fracture strength. Besides, Hobbiebrunken *et al.* reported a value of 135 MPa as a result of an experimental study on the tensile fracture strength of RTM6 fibres [154]. This value is about 65 % larger than that obtained with macroscopic dog bone-shaped specimens, and this in turn illustrates the influence of the scale effect on fracture strength. In a more recent study, Misumi *et al.* [155] noted a significant increase in yield stress, ultimate stress and failure strain for several epoxy resin systems tested in the form of micro-scaled epoxy fibre specimens as compared to macroscopic dog bone specimens[14]. Their results emphasise the role of specimen gauge volume and surface roughness on the measured mechanical properties, and show that although epoxy res-

[14] With e.g.an increase of the failure strain from about 5 % (macroscopic specimen) to about 50 % (microscopic specimen) for the DGEBA-based resin system !

ins are macroscopically brittle, they are stronger and ductile *at lower length scales*.

The tensile mechanical properties determined in the present work otherwise generally correlate well with the available literature data.

4.3.4.2 Tensile modulus measured by DMA

The storage modulus of RTM6 and Redux 322 was measured by Dynamic Mechanical Analysis over a large range of temperatures. This set of measurements has already been introduced in the section dedicated to the glass transition temperature. As a reminder, three samples of each material were successively subjected to a sinusoidal strain of 0.08 % applied in tensile mode with a 1 Hz frequency. Their temperature was meanwhile increased from -50 °C to 250 °C at a constant rate of 2 °C/min, starting with an initial isotherm of 10 minutes at -50 °C.

The evolution of the storage modulus with temperature is presented in Figure 4-9 for both thermosets. Interestingly, the curves related to RTM6 are in excellent agreement with that published in [144]. Temperature generally has such a huge influence on the E-modulus of polymers that it is vital to have a good knowledge of their modulus-temperature relation for the successful processing and use of these materials [156]. The present thermosets are visibly no exception, with a 50 % decrease in E-modulus for RTM6 and a 56 % decrease in E-modulus for Redux 322 when the temperature is increased from -40 °C to 180 °C.

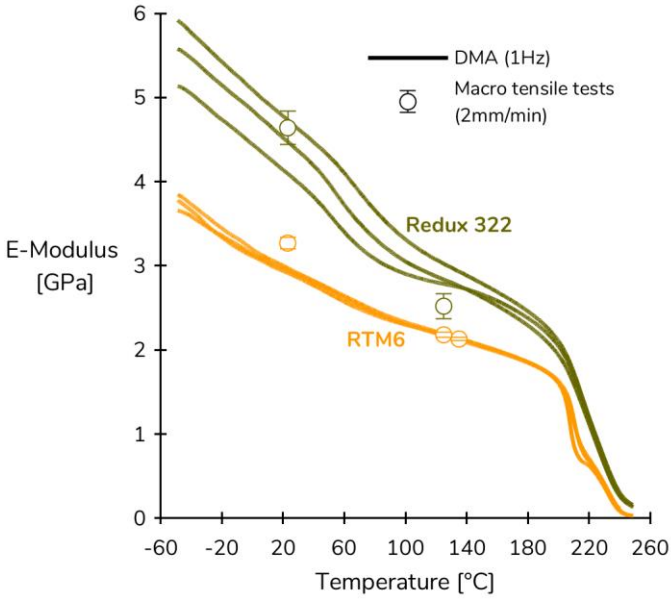

Figure 4-9. Evolution of the E-modulus with temperature as measured by dynamic mechanical analysis in tensile mode on three samples of RTM6 and three samples of Redux 322.

Although it occurs outside the temperature range of interest defined in the present work, it is worth noting the substantial E-modulus drop in the glass transition region for both thermosets in Figure 4-9. It is followed by the start of a rubbery plateau, which is the last region of viscoelastic behaviour before thermal degradation. Some stiffness is indeed retained after T_g as the three-dimensional network of thermosets does prevent macromolecules from slipping and flowing, contrarily to other polymers whose macromolecules are entangled but not crosslinked [157][139]. Finally, as pointed out in Appendix I, the shoulder appearing in the glass transition region of the RTM6 curves may indicate the inhomogeneous conversion of the resin. A heat-cool-heat cycle performed on one RTM6 sample however indicated that while some residual cure indeed took place during the measurement, it left the E-modulus virtually unchanged.

Strictly speaking, the E-modulus E' is not equivalent to the Young's modulus E. Indeed, E' does only represent the real part of the complex dynamic modulus E^*, the absolute value of which *is* equal to the Young's modulus, as recalled in Eq. (4-1) [135].

$$E^* = E' + iE''$$
$$E = |E^*| = \sqrt{(E')^2 + (E'')^2} \tag{4-1}$$

Nevertheless, when the contribution of the loss modulus E'' is small[15], the storage modulus is just slightly smaller than the Young's modulus [135]. This is the case of the present thermosets, whose E-modulus was seen to exceed the S-modulus by almost two orders of magnitude in the glassy state (Figure 4-6). Figure 4-9 confirms the good correlation of the E-modulus curves with the Young's modulus values measured by quasi-static macroscopic tensile tests at 23 °C and 125 °C for both thermosets. Similar correlations exist for RTM6 in the literature [144][158].

Such consistency motivated the selection of the E-modulus as input for the definition of the temperature-dependent polymers stiffness in the FE simulations. For this purpose, the mean E-modulus of each thermoset was fitted with bi-linear and bi-polynomial functions of temperature computed on the intervals [-40 °C; 70°C] and [70 °C; 180°C][16], as shown in Figure 4-10. Discrete values of the mean E-modulus were also extracted at several temperatures of interest distributed between -40 °C and 180 °C, as alternative input data for the definition of the temperature-dependent polymers stiffness in the FE simulations. The polynomial fits coefficients and the discrete numerical values are provided in Appendix J.

[15] I.e. when the material is predominantly elastic
[16] The temperature range of interest was splitted so as to best accommodate the non-linearity of the E-modulus curves, especially observed for Redux 322.

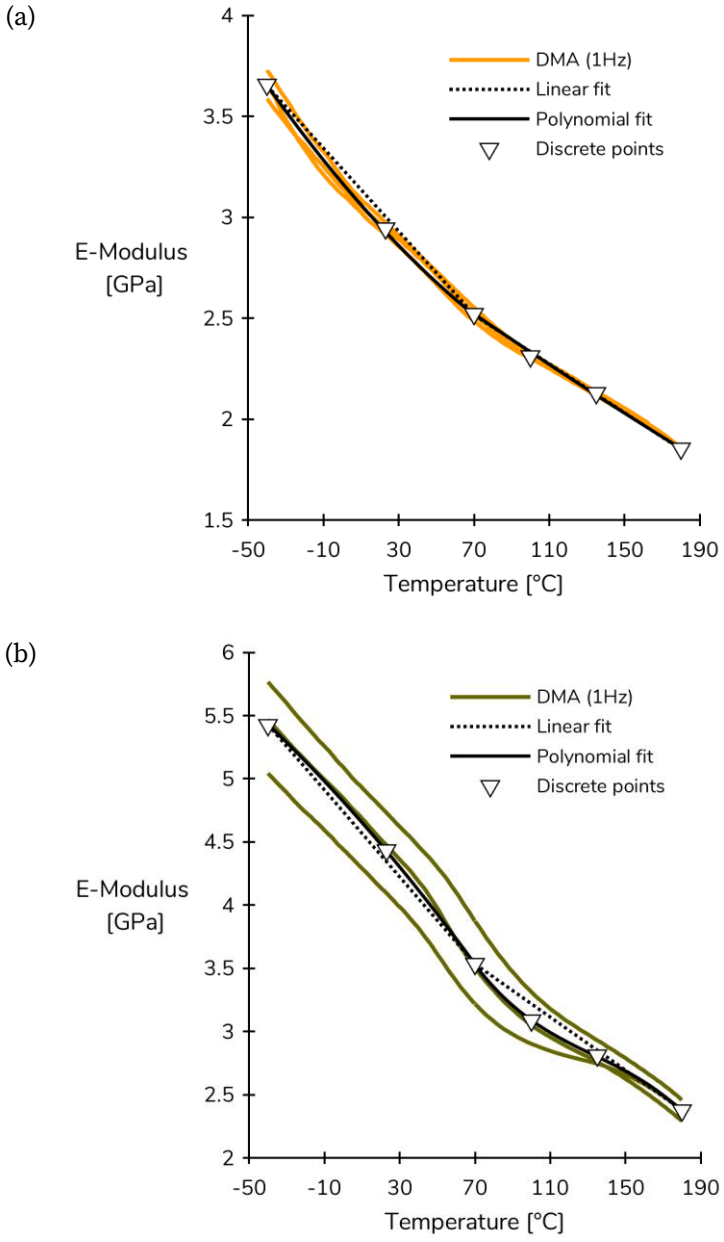

Figure 4-10. Close view of the evolution of the E-modulus of (a) RTM6 and (b) Redux 322 with temperature between -40 °C and 180 °C, as measured by dynamic mechanical analysis on three samples. Bi-linear and bi-polynomial fits are drawn as well, along with discrete mean E-modulus values calculated at -40 °C, 23 °C, 70 °C, 100 °C, 135 °C and 180 °C.

4.3.4.3 Coefficients of linear thermal expansion

The coefficient of linear thermal expansion of RTM6 and Redux 322 was derived from the evolution of sample length with temperature recorded by TMA. This set of measurements has already been introduced in the section dedicated to the glass transition temperature. As a reminder, the length of two samples of each thermoset was monitored while they were exposed to a heat-cool-heat temperature program defined on a temperature range going from -75 °C to 210 °C (RTM6) or 235 °C (Redux 322), with 10 minutes long isotherms at these temperatures and a heating/cooling rate of 2 °C/min.

Figure 4-11 shows the evolution of the CTE of RTM6 and Redux 322 with temperature, as determined at each data point of the original curves previously presented in Figure 4-5.

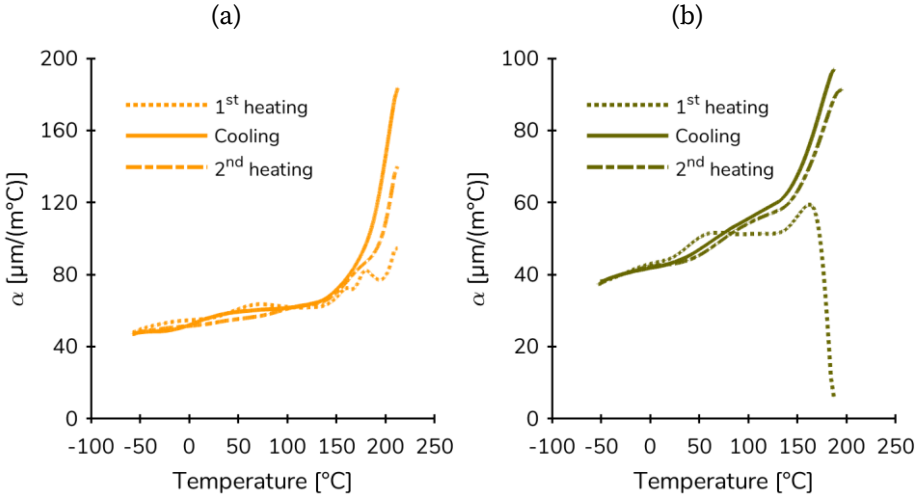

Figure 4-11. Evolution of the coefficient of linear thermal expansion with temperature of a sample of (a) RTM6 and (b) Redux 322, as determined from the change in sample length measured throughout a full heat-cool-heat cycle of thermomechanical analysis.

Among all curves recorded during the full temperature cycle, the cooling curve best represented the evolution of the thermosets' CTE, with the least

influence of residual cure and free volume relaxation[17]. The CTEs derived from the cooling curves were thus selected as input for the definition of the temperature-dependent thermal expansion of the polymers in the FE simulations. For this purpose, the mean CTE of each thermoset[18] was fitted with bi-polynomial functions of temperature computed on the intervals previously defined for the E-modulus ([-40 °C; 70 °C] and [70 °C; 180 °C][19]), as shown in Figure 4-12. Discrete values of the mean CTE were also extracted at several temperatures of interest distributed across the whole interval, as alternative input data for the definition of the temperature-dependent thermal expansion of polymers in the FE simulations. The coefficients of the polynomial fits and the discrete numerical values are provided in Appendix J. The value of 56.4 µm/(m°C) determined for the CTE of RTM6 at room temperature is pretty close to that of 52.7 µm/(m°C) given by the manufacturer in the product data sheet [32]. Besides, the continuous evolution of the CTE of RTM6 with temperature is in good agreement with that published in [144], especially between -40 °C and 135 °C.

Finally, note that the expected step change in CTE at T_g is visible on the cooling and second heating curves of both materials in Figure 4-11, although scanning to higher temperatures would have allowed the upper plateau to develop and appear more clearly.

[17] See Appendix H for more information.
[18] A technical issue encountered during the cooling step for one RTM6 sample made it impossible to continue the measurement below 10 °C. The bi-polynomial fit is thus based on the only curve available for the whole interval, and the shorter curve is displayed on the graph to testify to its closeness with the other result and fit.
[19] As for the E-modulus, the temperature range of interest was splitted so as to best accommodate the non-linearity of the evolution of the CTE with temperature.

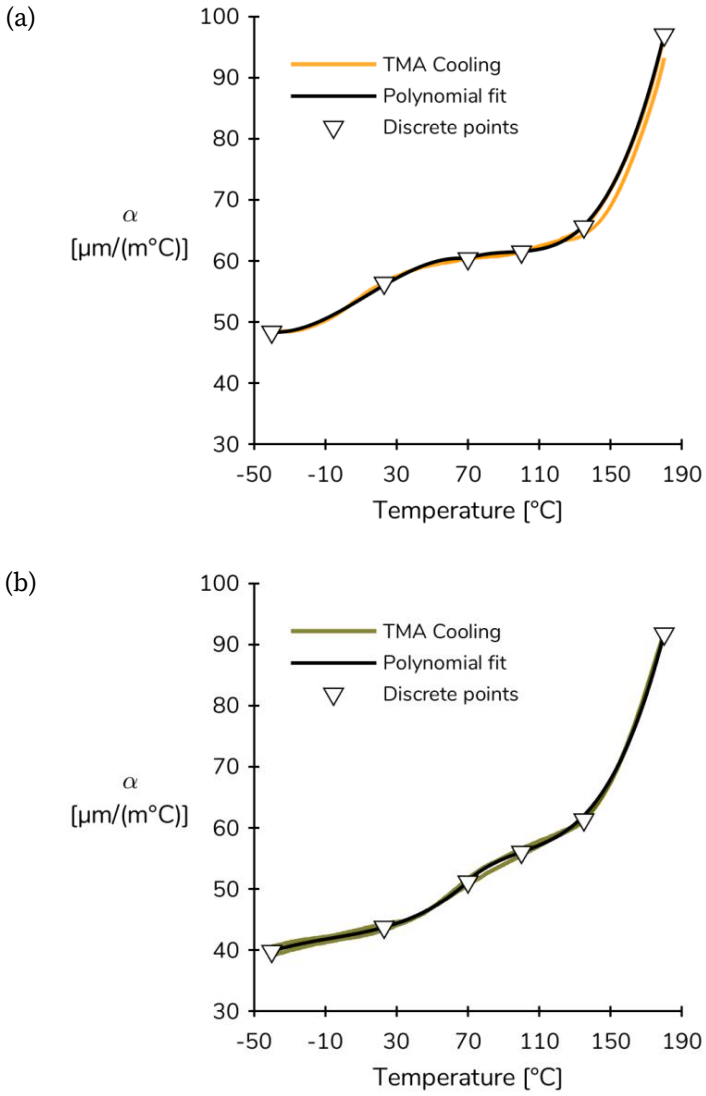

Figure 4-12. Close view of the evolution of the CTE with temperature on cooling from 180 °C to -40 °C, as measured by thermomechanical analysis on (a) one sample of RTM6 and (b) two samples of Redux 322. The bi-polynomial fits are drawn as well, along with discrete mean CTE values calculated at -40 °C, 23 °C, 70 °C, 100 °C, 135 °C and 180 °C.

4.4 Properties of the as-rolled and micro-perforated 316L SS strips

4.4.1 Materials

The material samples used throughout the characterisation process of the steel strip in its as-rolled and micro-perforated versions respectively come from a coil of 0.2 mm thick as-rolled steel sheet and from 0.2 mm thick micro-perforated sheets.

4.4.2 Mechanical and thermal properties

4.4.2.1 Room temperature mechanical properties measured by quasi-static macroscopic tensile tests

Uniaxial tensile tests were performed at room temperature on at least 8 dog bone-shaped specimens machined in the *rolling* (RD) and *transverse* (TD) reference directions of the as-rolled and micro-perforated steel sheets. The specimens were loaded at a constant crosshead speed of 1 mm/min. One representative tensile stress-strain curve is drawn in Figure 4-13 for each combination of sheet type and axial direction. Several tensile mechanical properties were extracted from the stress-strain curves, whose numerical values are reported in Table 4-8 for both types of sheet. General mechanical properties of AISI 316L collected from some bibliographical references are included in the same table for comparison purposes.

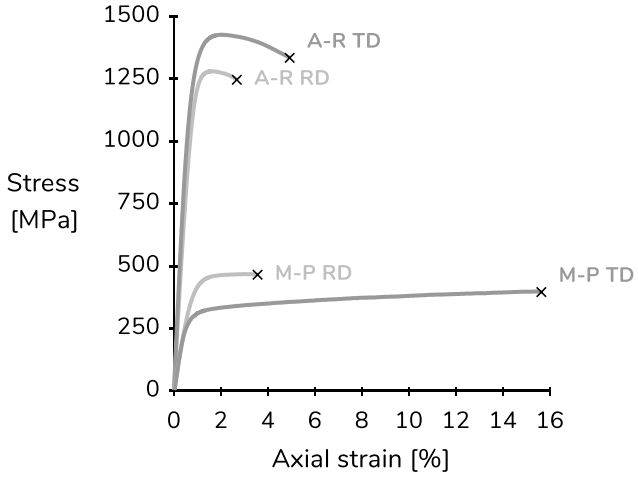

Figure 4-13. Representative stress-strain curves obtained as a result of quasi-static uniaxial tensile testing of as-rolled and micro-perforated AISI 316L SS sheet specimens aligned with the reference directions of the cold rolled sheet.

Micro-perforations obviously caused the decrease of the sheet's modulus, yield stress and tensile strength, combined to the increase of the sheet's ductility.

As regards the modulus of elasticity, the micro-perforated steel sheet can actually be considered a steel/air composite, whose effective properties are found in between those of its constituent materials. Its effective stiffness is thus logically lower than that of a 100 % steel sheet as the air stiffness is zero. The present 26.5 % open area contributes here, in both material directions, to a reduction of the sheet's modulus of elasticity by a factor of three. This value agrees quite well with that of 2.4 semi-analytically computed by Bailey and Hicks for a similar diagonal penetration pattern [159], and that of 2.6 obtained with another analytical method published in a more recent study by Zhang *et al.* [160].

Further, micro-perforations modify the distribution of the applied stress as they reduce the material section. They actually are *stress raisers*, which *concentrate* the tensile stress at some points of their circumference. For instance, let us take the specific case of a single circular hole in an infinite plate. Under equibiaxial tensile loading, the tensile stress in the plate is known to *locally* reach twice the remote stress value, at four points situated at $-\pi/2$ and $\pi/2$ with respect to both loading directions. When the same perforated plate is rather subjected to uniaxial tensile loading, the *stress concentration factor* equals 3 instead of 2, at two points situated at $-\pi/2$ and $\pi/2$ with respect to the single loading direction [161][162]. The effective uniaxial tensile yield stress of that perforated plate can therefore be as much as three times lower than that of the corresponding solid plate; not because of any modification of the intrinsic yield stress of the plate material, but because that yield stress is reached locally at the hole for a three times lower remote stress. Stress concentration factors in plates containing more than one hole take increasingly complex forms involving, among others, the hole diameter and the pitch of the penetration pattern. Plastic flow in perforated plates is the topic of numerous specialised studies (e.g. [163],[164]) which go far beyond the scope of this thesis. Nevertheless, the simple stress concentration factor of 3 was particularly well verified in the present work when the micro-perforated steel sheet was stretched in its rolling direction. The effective offset yield stress was indeed reduced by a factor of 3 compared to the offset yield stress of the as-rolled steel sheet stretched in that same direction. In the transverse direction, the effective offset yield stress was reduced by a factor of 4.3 while, given the symmetry of the penetration pattern, one expected to measure an equal influence of the micro-perforations in both directions of traction[20].

[20] The reason of this difference has not been investigated but could be due to some misorientation of the penetration pattern with respect to the reference material directions, or to a different interaction of the material with the micro-perforations when stretched in the transverse direction.

The reference material direction clearly played an important role, with the transverse direction being at the same time *stiffer*, *stronger* and *more ductile* than the rolling direction. This reflects the transversely isotropic nature of the steel sheet caused by its forming process.

Besides, the comparison of the mechanical properties of the as-rolled steel sheet with the general mechanical properties of AISI 316L in Table 4-8 gives a good overview of the influence of cold rolling. A spectacular increase in yield stress and tensile strength arose due to cold rolling, with a dramatic decrease in ductility of the cold-rolled material. Cold working is indeed known to trigger the formation of strain-induced martensite and to be responsible for the large increase in dislocations density [44]. Both of these consequences can contribute to an increase in the yield stress and tensile strength of the cold-worked metal since (i) martensite has a larger yield stress than austenite [45], and (ii) the motion of dislocations underlying plastic deformation is more difficult as their density increases. The work hardening action obtained by cold working is therefore often used as a means to enhance the initially rather low yield stress of austenitic stainless steels [44]. The Young's modulus meanwhile appeared to be least modified by this forming process, notwithstanding the fact that it became anisotropic in the plane of the sheet.

Table 4-8. Room temperature mechanical properties of the as-rolled and micro-perforated AISI 316L SS sheets derived from quasi-static uniaxial tensile tests results (this work) and compared to relevant data from the literature.

Source	This work A-R	This work M-P	1 mm thick [44]	Specification ASTM A240 [165]	General [166]
# specimens	9	≥ 8	-	-	-
Young's moduli [GPa]					
$E_1 = E_{RD}$	164 ± 0	55.1 ± 1.6	-	-	189 – 210
$E_2 = E_{TD}$	202 ± 1	64.8 ± 0.8			
Poisson's ratios [-]					
ν_{12}	0.28 ± 0.02	0.50 ± 0.01	-	-	-
ν_{21}	0.37 ± 0.01	0.45 ± 0.01			
0.2 % offset yield stress [MPa]					
$\sigma_{0.2,RD}$	1203 ± 5	389 ± 8	265	≥ 170	170 - 1000
$\sigma_{0.2,TD}$	1238 ± 6	289 ± 6			
Tensile strength [MPa]					
$\sigma_{M,RD}$	1310 ± 5	467 ± 9	577	≥ 485	480 – 2240
$\sigma_{M,TD}$	1454 ± 4	457 ± 16			
Tensile stress at break [MPa]					
$\sigma_{B,RD}$	1250 ± 9	451 ± 9	≅ σ_M	-	-
$\sigma_{B,TD}$	1323 ± 12	400 ± 8			
Tensile strain at break [%]					
$\varepsilon_{B,RD}$	2.8 ± 0.1	3.5 ± 0.3	100.4	≥ 40	-
$\varepsilon_{B,TD}$	5.0 ± 0.3	14 ± 2		-	-

Finally, it is worth noting that the micro-perforations and the anisotropic nature of the steel sheet affected the Poisson's ratio as well. This is graphically summarized in Figure 4-14. Poisson's ratio increased with the presence of micro-perforations by a factor of 1.8 in the rolling direction and 1.2 in the transverse direction. This is quite similar to the increase by a factor of 1.4 computed by Bailey and Hicks in their semi-analytical work on perforated plates [159] and analytically obtained by Zhang *et al.* for a diagonally loaded plate with a square penetration pattern [160]. With ν close to 0.5, the micro-perforated steel sheet certainly exhibits more Poisson's effect (strains coupling) than the as-rolled steel sheet whose Poisson's ratio is closer to the value of 0.3 usually attributed to steel.

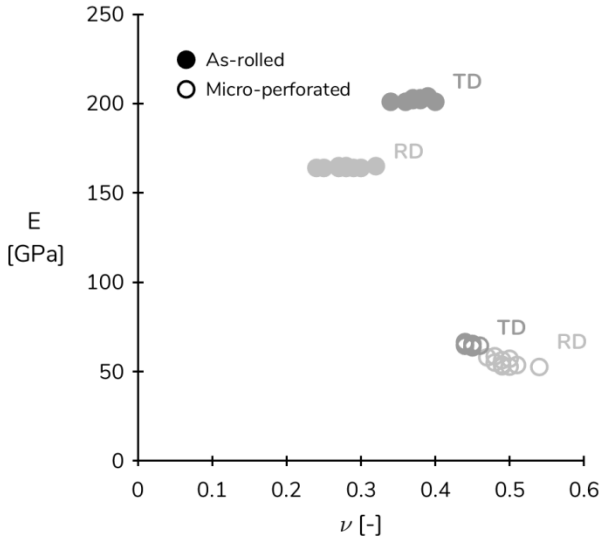

Figure 4-14. Influence of micro-perforations and reference direction on the Young's modulus and the Poisson's ratio of 316L SS strips measured with quasi-static uniaxial tensile tests.

4.4.2.2 Room temperature elastic constants identified with the Resonalyser procedure

Out of interest for its promising efficiency and its non-destructive nature, a second non-contact measurement technique was used for the measurement

of the steel strips mechanical properties. It is called the *Resonalyser procedure* and it was used for the identification of the in-plane elastic constants (Young's moduli E_1 and E_2, Poisson's ratio ν_{12}, and shear modulus G_{12}) of the as-rolled and micro-perforated steel sheets based on the measurement of the resonant frequencies of two sets of 10 beam-like samples (either aligned with RD or with TD) and 8 plate-like samples.

Although the particularly small thickness of the present steel sheets was considered challenging, the measurements were quick and straightforward and the technique proved efficient for the identification of the Young's modulus and the shear modulus. Figure 4-15 testifies to the quality of the results obtained for the Young's modulus in both reference directions of the plate-like samples, as all values are very close to their counterpart obtained by quasi-static tensile tests on macroscopic dog bone-shaped specimens.

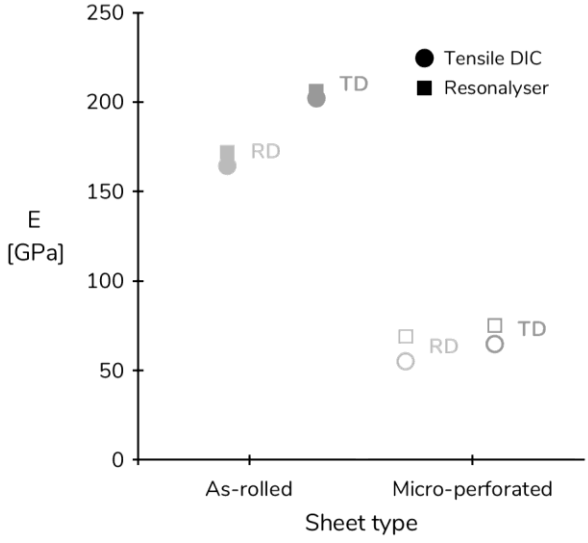

Figure 4-15. Comparison of the mean values of Young's modulus obtained by quasi-static uniaxial tensile testing and with the Resonalyser procedure, for both reference directions of both versions of the AISI 316 L SS sheet. The error bars marking the boundaries of the 95 % confidence intervals are in each case so small that they are hidden behind the data points.

The quality of the equipment and procedure as well as the careful preparation of the samples definitely helped reaching this level of accuracy. Table 4-9 and Table 4-10 contain the values resulting from the application of the Resonalyser procedure to beam and plate samples of as-rolled and micro-perforated steel sheets. The quasi-static tensile tests results are also included in the tables, for comparison purposes.

The Resonalyser procedure initially failed at identifying the in-plane Poisson's ratio of the steel sheets whose value was indeed invariably close to zero while its tensile test counterpart took more realistic values. This result was later improved by halving the dimensions of the Poisson plates, whereupon a mean value of 0.21 was identified for the Poisson's ratio of the as-rolled steel sheet and a mean value of 0.33 for the Poisson's ratio of the micro-perforated steel sheet.

*Table 4-9. Elastic constants of the **as-rolled** AISI 316 L SS sheet, as identified with the Resonalyser procedure on beam-shaped and Poisson plate-shaped samples. Values determined by quasi-static uniaxial tensile testing are included in the last column for comparison purposes.*

Sample type	Beam	Plate	Dog bone
# samples	10	6	9
Young's moduli [GPa]			
$E_1 = E_{RD}$	172 ± 1	172 ± 0	164 ± 0
$E_2 = E_{TD}$	206 ± 2	206 ± 1	202 ± 1
Poisson's ratios [-]			
ν_{12}	-	-	0.28 ± 0.02
ν_{21}	-	0.02 ± 0.03	0.37 ± 0.01
Shear modulus [GPa]			
G_{12}	-	88.9 ± 6.4	-

*Table 4-10. Elastic constants of the **micro-perforated** AISI 316 L SS sheet, as identified with the Resonalyser procedure on beam-shaped and Poisson plate-shaped samples. Values determined by quasi-static uniaxial tensile testing are included in the last column for comparison purposes.*

Sample type	Beam	Plate	Dog bone
# samples	10	7	≥ 8
Young's moduli [GPa]			
$E_1 = E_{RD}$	69.3 ± 1.8	69.1 ± 0.2	55.1 ± 1.6
$E_2 = E_{TD}$	75.5 ± 0.7	75.1 ± 0.2	64.8 ± 0.8
Poisson's ratios [-]			
ν_{12}	-	-	0.50 ± 0.01
ν_{21}	-	0.01 ± 0.01	0.45 ± 0.01
Shear modulus [GPa]			
G_{12}	-	33.6 ± 2.3	-

In summary, the Resonalyser procedure gave a quite direct access to the value of two important elastic constants -the Young's modulus (in both reference directions of the sheets) and the shear modulus- and was certainly less time and material consuming than quasi-static tensile testing. However, some reservations remain regarding the ability of the technique to identify the Poisson ratio of the present thin sheet material, given the significant deviation from the values obtained by coupling conventional macroscopic tensile testing with non-contact DIC strain measurement. Thus, as far as the identification of elastic properties are concerned, the Resonalyser procedure may be a clever choice if its reliability has first be ascertained in light of data obtained with another, more classical, mechanical testing method.

4.4.2.3 Coefficients of linear thermal expansion

The CTE along RD and TD was derived from TMA measurements on the as-rolled steel sheet over a large temperature range. For each reference direction, the length of one sample was monitored while it was exposed to a heat-

cool-heat temperature program defined on a temperature range going from -75 °C to 210 °C, with 5 minutes long isotherms at these temperatures and a heating/cooling rate of 2 °C/min.

On the one hand, Figure 4-16 shows the original data, i.e. the evolution of the sample length with temperature throughout the cycle for the sample aligned with the rolling direction (RD-sample) and the sample aligned with the transverse direction (TD-sample). On the other hand, Figure 4-17 presents the corresponding evolution of the CTE determined at each data point of the original curves. A shortage in liquid nitrogen unfortunately prevented cooling the RD-sample down to -75 °C after first heating. As a consequence, in this direction, only the first heating data can be used for the determination of the mean CTE at -40 °C.

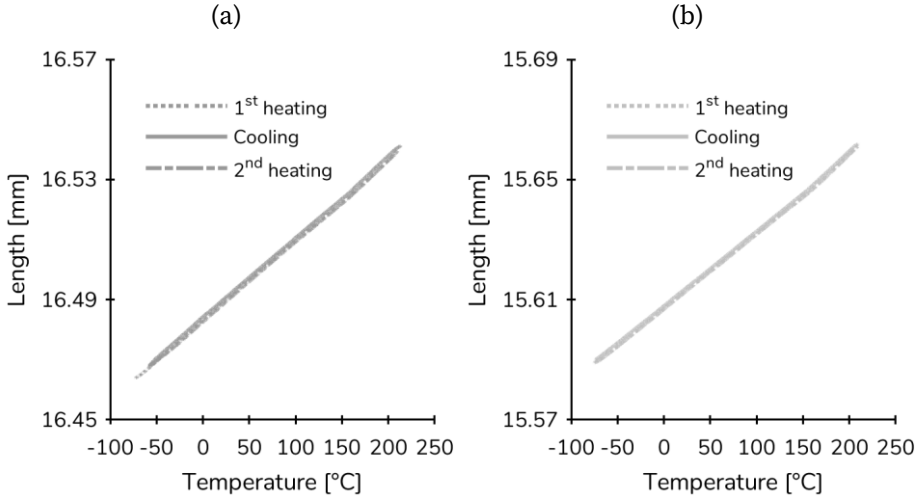

Figure 4-16. Evolution of the sample length with temperature throughout a full heat-cool-heat cycle of thermomechanical analysis on a sample of AISI 316 L aligned with (a) the rolling direction and (b) the transverse direction.

(a) (b)

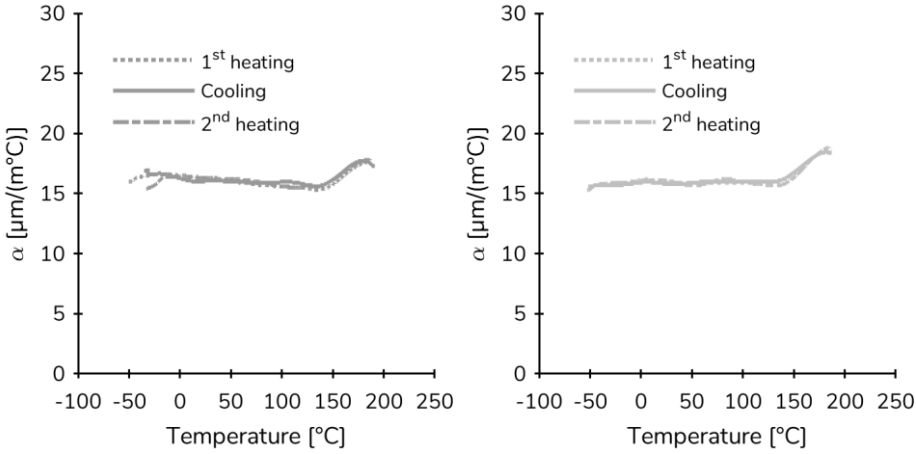

Figure 4-17. Evolution of the coefficient of linear thermal expansion with temperature of a sample of AISI 316L aligned with (a) the rolling direction and (b) the transverse direction, as determined from the change in sample length measured throughout a full heat-cool-heat cycle of thermomechanical analysis.

Contrarily to the earlier observations on RTM6 and Redux 322, all cooling and heating curves did here almost perfectly overlap and were thus considered equivalent. The sample length evolved linearly with temperature in all steps of the cycle (Figure 4-16) for both reference directions. This logically translated into a quasi-constant CTE over the full range of temperatures (Figure 4-17), whose value of about 16 µm/(m°C) is in very good agreement with those reported in the numerous product data sheets dedicated to AISI 316L (e.g. [167][168][169]). A slight increase of the CTE to about 18 µm/(m°C) was still detected between 138 °C and the maximum temperature, for both directions. This is also commonly reported in the product data sheets. The excellent agreement of the measured CTEs with the published ones confirms the reliability of the equipment and measurement procedure used in the present work.

Since the cold rolling texture of the steel sheet made the Young's modulus quite anisotropic, the CTE was likewise expected to be larger in the rolling

direction than in the transverse direction[21]. However, no anisotropy of the CTE was noticed in the single measurement performed in each direction.

The evolution of the CTE with temperature on first heating[22] was first fitted for the rolling and transverse directions separately, with bi-linear functions calculated on [-40 °C; 138 °C] and [138 °C; 180 °C]. Then, given the isotropy of the CTE, the mean of the first heating curves related to RD and TD was fitted as well. Discrete values of the mean CTE on first heating were also extracted at several temperatures of interest distributed across the whole interval. These continuous and discrete representations of the CTE may equivalently be used as input in the FE simulations. The fit and discrete points shown in Figure 4-18 correspond to the case of the first heating curves combined independently of the reference direction, while all first-order polynomials and discrete numerical values are provided in Appendix J.

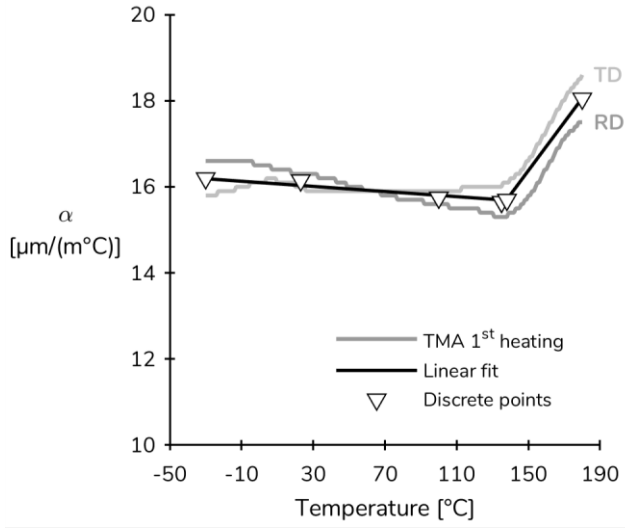

[21] The Young's modulus and stiffness of a material are inversely related to the strenght of its atomic bonds.

[22] One would have preferred to work with the cooling curve, by consistency with the processing of the thermosets data. Yet, the lack of data points at low temperature on cooling of the RD-sample imposed processing the heating data. This should anyway have practically no influence in this case, considering the closeness of the heating and cooling data curves.

Figure 4-18. Close view of the evolution of the CTE of as-rolled AISI 316L SS with temperature on first heating from -40 °C to 180 °C, as measured by TMA on one sample aligned with RD and one sample aligned with TD. The bi-linear fit common to both directions is also drawn, along with discrete mean CTE values calculated at -40 °C, 23 °C, 100 °C, 135 °C and 180 °C.

4.5 Conclusion

The work of characterisation presented in this chapter resulted in the acquisition of numerous data concerning the thermal and mechanical properties of the multilayer's constituent materials. These represent valuable inputs for the analytical and FE models of the multilayer to come in the next chapters. Table 4-11 lists the values of the material properties at 23 °C. The reader is kindly invited to refer to the appropriate sections of this manuscript (Section 4.3.4 and Appendix J) in case he is interested in the temperature dependence of the mechanical and thermal behaviour of the epoxies.

First, the effective thermoelastic properties of the composite laminate were predicted with the classical lamination theory, using the effective properties of the (impregnated) laminae themselves predicted and provided by the industrial partner. The predicted values were in good agreement with the reference experimental data provided by SAB. Besides, in view of these results, the homogenised material was considered orthotropic in the rest of this research work.

Second, regarding RTM6 and Redux 322, it was verified with thermal analyses that these materials are thermally stable in the [-40 °C; 135 °C] temperature range considered in the present application, their onset degradation temperature and their glass transition temperature being both far above 135 °C. Besides, the stress-strain responses in tension characterised at 23 °C and 125 °C-135 °C with uniaxial tensile tests on macroscopic dog bone specimens suggest a quite brittle mechanical behaviour for these polymers, especially at room temperature. Nevertheless, it is important to keep in mind that

this result is length scale dependent, since, owing to the statistical decrease of the quantity and size of defects in smaller gauge volumes, a macroscopically brittle material can actually be ductile at the micro-scale. Due to the relatively small contribution of viscosity to the mechanical response of RTM6 and Redux 322, the storage moduli measured by DMA in tensile mode appeared to coincide well with the Young's moduli conventionally derived from the tensile stress-strain curves. Hence, these properties may be considered equivalent for these polymers, and DMA becomes an efficient technique for the continuous measurement of the modulus of elasticity over large temperature ranges. Finally, the coefficient of thermal expansion was classically extracted from the evolution of sample length with temperature measured by TMA in the [-40 °C; 180 °C] temperature range. Amongst the three evolution curves recorded for each sample during the heat-cool-heat cycle, the cooling curve was selected for the post-processing since it appeared to be the least influenced by residual cure and free volume relaxation.

Table 4-11. Summary table of the thermal and mechanical properties at room temperature of the materials studied in this chapter.

			Laminae			
			Bal.	Warp Heavy	Weft Heavy	Glass
Thickness	t	[mm]	0.378	0.342	0.342	0.080
Onset degradation and glass transition temperatures	T_0	[°C]	-	-	-	-
	T_g (TMA)	[°C]	-	-	-	-
	T_g (DMA)	[°C]	-	-	-	-
Thermal expansion coefficient	α	[µm/(m°C)]	-	-	-	-
	α_1 /α_x /α_{RD}	[µm/(m°C)]	2.12	1.44	7.36	15.8
	$\alpha_2/\alpha_y/\alpha_{TD}$	[µm/(m°C)]	2.12	7.36	1.44	15.8
	α_3/α_z	[µm/(m°C)]	55.6	46.6	46.6	56.9
Storage modulus or Young's modulus						
	E'	[GPa]	-	-	-	-
	E	[GPa]	-	-	-	-
	$E_1/E_x/E_{RD}$	[GPa]	73.3	116.0	34.1	23.2
	$E_2/E_y/E_{TD}$	[GPa]	73.3	34.1	116	23.2
	E_3/E_z	[GPa]	8.70	11.1	11.1	8.76
Poisson's ratio	ν	[-]	-	-	-	-
	ν_{12}/ν_{xy}	[-]	0.06	0.10	0.03	0.10
	ν_{13}/ν_{xz}	[-]	0.40	0.36	0.36	0.37
	ν_{23}/ν_{yz}	[-]	0.40	0.37	0.37	0.37
	ν_{21}	[-]	-	-	-	-
Shear modulus	G_{12}/G_{xy}	[GPa]	5.10	5.40	4.40	3.08
	G_{13}/G_{xz}	[GPa]	2.50	2.70	2.70	2.90
	G_{23}/G_{yz}	[GPa]	2.50	3.70	3.70	2.90
0.2 % offset yield stress	$\sigma_{0.2}/\sigma_{0.2,RD}$	[MPa]	-	-	-	-
	$\sigma_{0.2,TD}$	[MPa]	-	-	-	-
Tensile strength	$\sigma_M/\sigma_{M,RD}$	[MPa]	-	-	-	-
	$\sigma_{M,TD}$	[MPa]	-	-	-	-
Tensile stress at break	$\sigma_B/\sigma_{B,RD}$	[MPa]	-	-	-	-
	$\sigma_{B,TD}$	[MPa]	-	-	-	-
Tensile strain at break	$\varepsilon_B/\varepsilon_{B,RD}$	[%]	-	-	-	-
	$\varepsilon_{B,TD}$	[%]	-	-	-	-

Laminate	RTM6	Redux	316L SS			
			A-R		M-P	
4.408	-	-	0.2		0.2	
-	365 ± 19	331 ± 6	-	-	-	-
-	194 ± 13	168 ± 0	-	-	-	-
-	216 ± 10	224 ± 1	-	-	-	-
-	56.4	43.8	-	-	-	-
2.75	-	-	16.3		-	-
2.76	-	-	16.0		-	-
51.0	-	-	-	-	-	-
			Tens.	Reso.	Tens.	Reso.
-	2.95	4.44	-	-	-	-
-	3.27 ± 0.07	4.64 ± 0.20	-	-	-	-
59.2	-	-	164 ± 0	172 ± 0	55.1 ± 1.6	69.1 ± 0.2
59.2	-	-	202 ± 1	206 ± 1	64.8 ± 0.8	75.1 ± 0.2
10.2	-	-	-	-	-	-
-	0.38 ± 0.04	0.39 ± 0.02	-	-	-	-
0.23	-	-	0.28 ± 0.02	-	0.50 ± 0.01	-
0.31	-	-	-	-	-	-
0.32	-	-	-	-	-	-
-	-	-	0.37 ± 0.01	-	0.45 ± 0.01	-
15.3	-	-	-	88.9 ± 6.4	-	33.6 ± 2.3
2.63	-	-	-	-	-	-
3.15	-	-	-	-	-	-
-	48.3 ± 0.6	40.4 ± 2.1	1203 ± 5	-	389 ± 8	-
-	-	-	1238 ± 6	-	289 ± 6	-
-	80.7 ± 6.7	53.3 ± 8.5	1310 ± 5	-	467 ± 9	-
-	-	-	1454 ± 4	-	457 ± 16	-
-	80.6 ± 6.8	53.2 ± 8.6	1250 ± 9	-	451 ± 9	-
-	-	-	1323 ± 12	-	400 ± 8	-
-	3.9 ± 0.6	1.7 ± 0.6	2.8 ± 0.1	-	3.5 ± 0.3	-
-	-	-	5.0 ± 0.3	-	14 ± 2	-

Third and lastly, a large set of mechanical and thermal properties were measured for the as-rolled and micro-perforated versions of the AISI 316L stainless steel sheet. Stress-strain curves up to fracture measured by uniaxial tensile tests on macroscopic dog bone specimens machined in both reference directions of the sheets revealed the anisotropy of this cold rolled material, and demonstrated the influence of the micro-perforations on its mechanical properties. The Resonalyser procedure used as an alternative method for the characterisation of the elastic properties of the steel strips.proved satisfactory as regards the identification of the Young's moduli and the shear moduli, as well as for the identification of the Poisson's ratios after revision of the specimens dimensions. However, this trial showed that it is advisable to check the resonant-based results in light of those of a trusted test method such as e.g. macroscopic uniaxial tensile testing. Finally, the coefficient of thermal expansion measured by TMA on the as-rolled material proved practically constant in the the [-40 °C; 180 °C] temperature range and uninfluenced by the anisotropy of the sheet.

5. Evaluation of the thermally induced residual stresses in the multilayer

5.1 Introduction

The thermally induced residual stress state of the multilayer needs to be evaluated, given the crucial role it plays in the initiation and propagation of microcracks. Different classes of methods can serve this purpose.

Analytical methods allow for the most straightforward evaluation of residual stresses, yet they usually incorporate several simplifying assumptions which can significantly influence the predicted stress level.

Experimental methods can prove complex and time consuming, but they offer the advantage of evaluating the residual stress level based on the measurement of physical attributes of the system of interest. Although they also incorporate some assumptions, the confidence in the obtained results can be increased if a set of independent experimental methods is applied. Two of them were selected in this work, namely X-ray Stress Analysis (XSA) and curvature-based stress evaluation. They were chosen for their applicability to the multi-layered system and to the macroscopic type of stress being studied, as well as for the availability of the necessary equipment. The results obtained with these methods will be presented first in this chapter.

Finite element simulations form a third class of methods for the evaluation of residual stresses. On the one hand, as for the analytical methods, FE methods generally incorporate simplifying assumptions which can influence the predicted stress value. On the other hand, as for the experimental methods, their use can reveal complex and time-consuming. However, FE methods allow representing the system of interest with more freedom and accuracy, for instance by taking into account specific geometrical features, the temperature-dependence of material properties, and material nonlinearity. Detailed residual stress fields can thereby be predicted within the material layers, potentially highlighting some regions of stress concentration. The results obtained with the FE method will be presented last in this chapter, so that the validity of the FE modelling can be assessed by comparison with the experimental and analytical results.

5.2 Experimental evaluation of the residual stress state

The techniques selected for the experimental evaluation of the thermally induced residual stresses actually provided a measure of the stress acting in the co-cured steel strip *only*. This partial information is nevertheless valuable as it can still allow assessing the through-thickness residual stress profiles predicted for the whole multilayer by analytical and FE methods.

5.2.1 X-ray stress analysis of free-standing and co-cured 316L SS strips

5.2.1.1 Introduction

X-ray stress analysis was chosen as a mean of experimentally evaluating the residual stresses in the multilayer. More exactly, it allowed quantifying the residual stress present *in the surface layer* of the *as-rolled steel strip*. Indeed,

this technique is based on X-Ray Diffraction (XRD) which only applies to crystalline materials and essentially provides surface information given the limited depth of penetration of X-rays. It is thoroughly described in Appendix K, to which the reader is kindly invited to refer complementarily to the present chapter.

Residual stress was first evaluated in three samples of *free-standing* as-rolled 316L SS strip, as this material was suspected of not being stress-free given the severe cold-rolling process it endures to become a thin sheet. Residual stress was then evaluated in three samples of as-rolled 316L SS strip *co-cured* with the composite laminate substrate. These samples were cut from peel test specimens whose composite laminate layup slightly differed from the standard layup used in this work as one balanced lamina was missing at the mid-plane. This particularity was taken into account in the analytical calculations and the FE simulations of the residual stress state.

5.2.1.2 Measurement and processing of the (331) diffraction peaks of free-standing and co-cured 316L SS strips

The "$\sin^2\psi$" method was used for the stress analysis. It is presented in detail in Appendix K and is based on Eq. (K-11). The diffraction peak of (331) atomic planes of free-standing and co-cured 316L SS strip samples was therefore recorded with Cu Kα radiation at eleven positive and eleven negative tilt angles (ψ) between 0° and ±60°. Three azimuths (ϕ), namely 0°, 90° and 45°, oriented the sample is such a way that either its RD, TD or their bisector direction was aligned with the X-ray beam. The peaks were evaluated by the DIFFRAC^{plus} LEPTOS 7 software (Bruker, Germany) with the Pearson VII peak fitting method, and the inter-planar spacing $d_{\phi\psi}$ corresponding to each of the measured (331) peaks was derived from its 2θ position. An example of a set of diffraction peaks obtained for a single ϕ angle is shown in Figure 5-1.

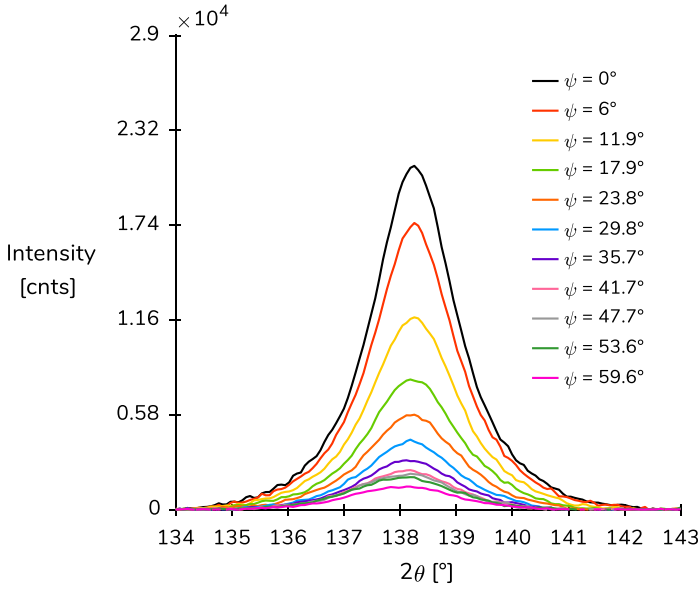

Figure 5-1. Set of (331) diffraction peaks measured at all tilt angles on the co-cured 316L SS sample with Cu Kα radiation, here at $\phi = 90°$ (TD).

The broad shape and the varying intensity of these diffraction peaks are a clear signature of the plastically deformed state and the textured nature of the steel sheet. On the one hand, the dislocations generated during plastic deformation are known to cause *peak broadening* [170]. Indeed, they distort the grains and divide them into sub-grains with some disorientation of the atomic planes from one sub-grain to another. So, the inter-planar spacing in neighbouring sub-grains is impacted differently by the measured strain, causing some dispersion of the corresponding 2θ angle. On the other hand, the preferred orientation of the grains is responsible for the varying peak intensity. Indeed, it makes the distribution of the atomic planes orientation anisotropic, so that at some tilt angles the sample is in a position where many (331) planes are properly oriented for diffraction and an intense diffraction peak is recorded, while at other tilt angles the sample is in a position where

few (331) planes are properly oriented for diffraction and a weaker diffraction peak is obtained.

All data obtained in this measurement process are graphically summarized in Figure 5-2 and Figure 5-3 for the free-standing steel strip and the co-cured steel strip, respectively. They contain the $d_{\phi\psi}$ vs. $\sin^2\psi$ distribution obtained for each ϕ angle, the evolution of the full width at half maximum of the diffraction peak (FWHM) with $\sin^2\psi$, and that of the relative intensity of the diffraction peak defined as the ratio of the intensity at the peak 2θ position to the maximum of the intensities recorded at all (ϕ, ψ). The stress tensors were evaluated with the DIFFRAC^{plus} LEPTOS 7 software, using the X-ray elastic constants s_1 and $\frac{1}{2}s_2$ automatically determined from the average macroscopic elastic constants of the as-rolled AISI 316L SS sheet (E, ν) and the anisotropy factor of the austenitic lattice (A_{rx}) given in Table 5-1 [171].

Table 5-1. X-ray elastic constants s_1 and $\frac{1}{2}s_2$, and parameters used for their calculation.

E	ν	A_{rx}	$s_1 = \left(\frac{\nu}{E}\right)_{(hkl)}$	$\frac{1}{2}s_2 = \left(\frac{1+\nu}{E}\right)_{(hkl)}$
189 GPa	0.33	1.72	1.454 10^{-6} MPa^{-1}	6.161 10^{-6} MPa^{-1}

The results are separately described and discussed for the free-standing and the co-cured steel strips in the next sub-sections.

5.2.1.3 Residual stress in the free-standing 316L SS strip

The stress analysis of the free-standing steel strip was performed based on the experimental data presented in Figure 5-2.

Firstly, note that the $d_{\phi\psi}$ vs. $\sin^2\psi$ distributions obtained at all three ϕ do intersect the vertical axis ($\psi = 0°$) at nearly the same value of inter-planar spacing. It corresponds to the spacing of the selected (hkl) atomic planes lying parallel to the sample surface, and does often replace the unknown

stress-free spacing d_0 in the mathematical developments. This superposition of the $d_{\phi,0}$ values is an evidence of the good performance of the experimental method [172].

The points obtained at positive and negative tilt angles (black and empty dots, respectively) appeared to be vertically offset, indicating the presence of non-zero components of out-of-plane shear stress (i.e. σ_{13} and/or σ_{23}). The *ψ-splitting* character of these distributions was taken into account by the choice of an elliptical regression rather than the simple linear regression. Moreover, none of the distributions was oscillatory so that the stress analysis could be performed without taking the crystallographic texture into account. The distribution corresponding to $\phi = 90°$ was however quite curved, indicating that the stress component acting along TD varies significantly in the depth of the sample surface layer. This could have required a more sophisticated treatment of the results obtained in this direction [173], yet the same elliptical regression was performed with the awareness that it may decrease the confidence level attributed to the stress thereby evaluated.

For each ϕ, the regression was performed based on the data points obtained with the first ten tilt angles. The data points obtained with the last tilt angles ($\psi = \pm 59.6°$) were indeed found outside the distribution, especially for $\phi = 0°$. The low intensity and superior broadness of the diffraction peak recorded at this tilt angle supported the choice of discarding these points which are therefore drawn in grey in the graphs.

The *negative* slope of the elliptical regressions indicated the presence of a *negative* (i.e. *compressive*) stress state in the sample surface layer. This stress state was quantified using the aforementioned X-ray elastic constants, and the following symmetric stress tensor was obtained (Eq. (5-1)). The values it contains are the average of the values obtained on the three samples and are presented with their 95 % confidence interval.

$$\sigma_{\text{free}} = \begin{pmatrix} -135 \pm 7 & 23.9 \pm 4.9 & -5.97 \pm 6.25 \\ . & -14.4 \pm 14.3 & 6.60 \pm 1.74 \\ . & . & 0 \end{pmatrix} \quad (5\text{-}1)$$

The stress component σ_{11} acting in the rolling direction ($\phi = 0°$) was evaluated to -135 MPa with a reasonable confidence interval, while, on the contrary, the stress component σ_{22} acting in the transverse direction ($\phi = 90°$) was closer to zero (-14.4 MPa). Recall, however, that it was evaluated with an elliptical regression that did not fit well the curved shape of the $d_{\phi\psi}$ vs. $\sin^2\psi$ distribution obtained in this direction. Finally, the out-of-plane shear stress components σ_{13} and σ_{23} were found to be quite small (-5.97 and 6.60 MPa). In any case, it is clear that the 316L SS strip is not initially stress-free: it presents a compressive surface stress state which certainly results from its forming process by severe cold-rolling.

5.2.1.4 Residual stress in the co-cured 316L SS strip

The stress analysis of the co-cured steel strip was performed based on the experimental data presented in Figure 5-3.

The $d_{\phi\psi}$ vs. $\sin^2\psi$ distributions obtained at all three azimuths do again intersect the vertical axis ($\psi = 0°$) at nearly the same value of inter-planar spacing, which is again an evidence of the good performance of the experimental method.

The points obtained at positive and negative tilt angles (black and empty dots, respectively) were not particularly offset, but the distributions were still fitted with elliptical regressions as they are more comprehensive than the simple linear regressions. Again, none of the distributions was significantly oscillatory so that the stress analysis was performed without taking the crystallographic texture into account. Furthermore, none of the distributions was curved, which indicates a rather homogeneous stress state in the thickness of the surface layer.

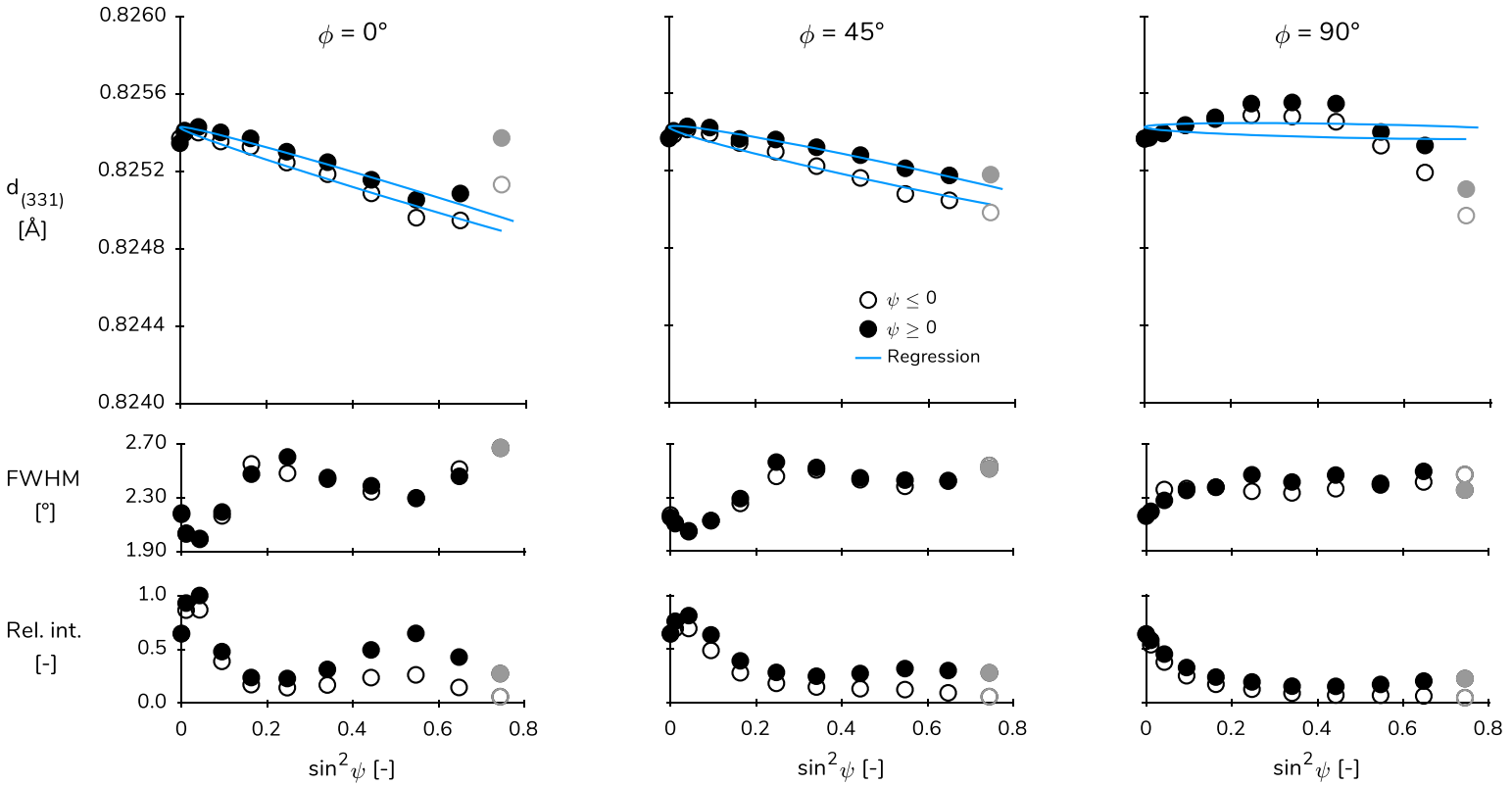

Figure 5-2. Inter-planar spacing, FWHM and relative intensity as a function of $\boldsymbol{sin^2\psi}$*, as measured on (331) diffraction peaks of a free-standing as-rolled 316L SS strip sample with Cu K*$\boldsymbol{\alpha}$ *radiation. Grey dots indicate discarded data points.*

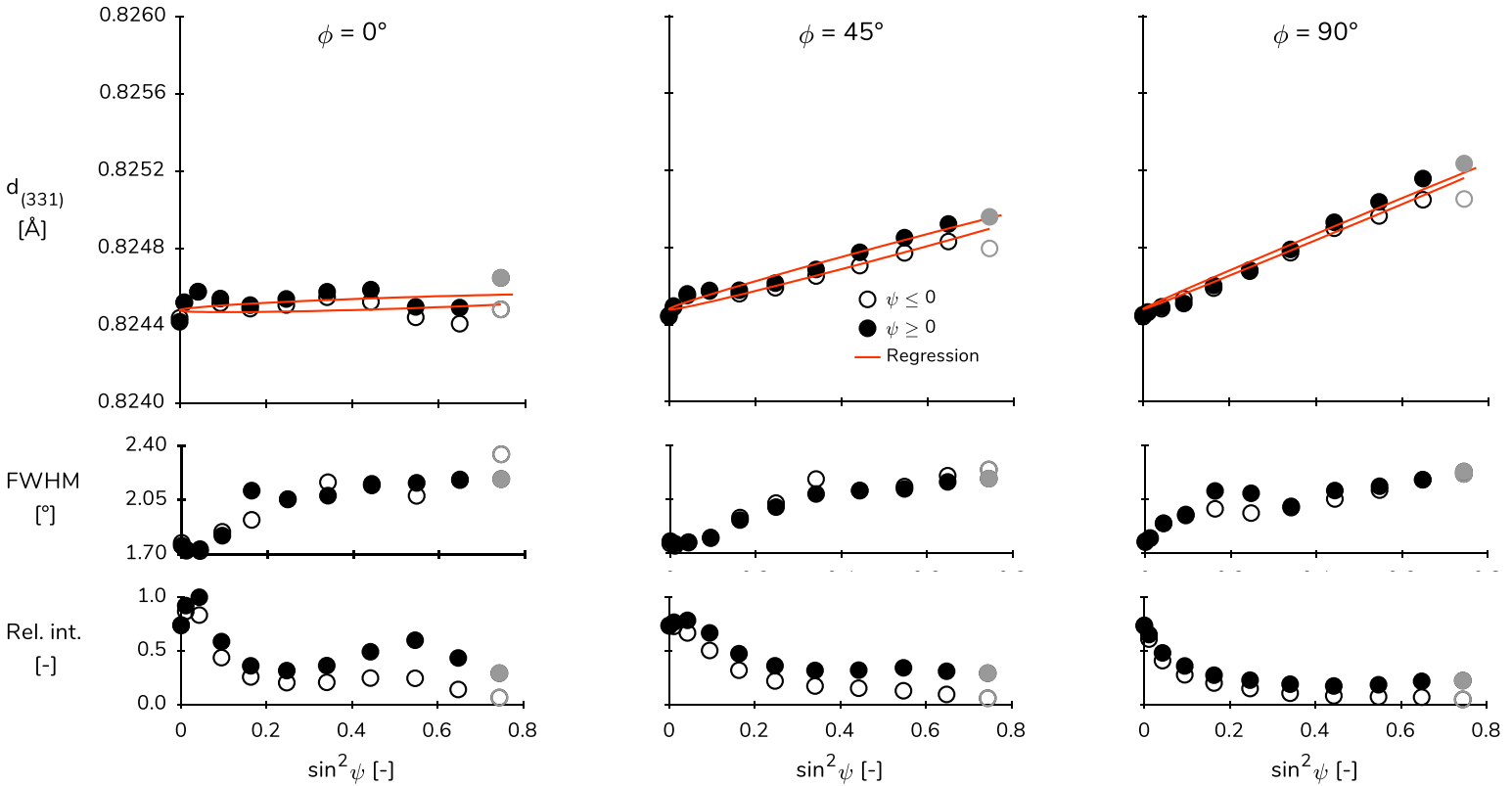

Figure 5-3. Inter-planar spacing, FWHM and relative intensity as a function of $\boldsymbol{sin^2\psi}$*, as measured on (331) diffraction peaks of a co-cured as-rolled 316L SS strip sample with Cu K*$\boldsymbol{\alpha}$ *radiation. Grey dots indicate discarded data points.*

Although they were not particularly offset, the data points obtained with the last tilt angles ($\psi = \pm 59.6°$) were discarded by consistency with the procedure followed for the free-standing steel strip. The regression was thus performed for each ϕ based on the data points obtained with the first ten tilt angles.

The *positive* slope of the elliptical regressions indicated the presence of a *positive* (i.e. *tensile*) stress state in the sample surface layer. This stress state was quantified using the aforementioned X-ray elastic constants, and the following symmetric stress tensor was obtained (Eq. (5-2)). The values it contains are again the average of the values obtained on the three samples and are presented with their 95 % confidence interval.

$$\sigma_{\text{co-cured}} = \begin{pmatrix} 15.3 \pm 13.6 & -15.6 \pm 15.5 & -3.13 \pm 2.77 \\ . & 181 \pm 10.4 & 5.07 \pm 3.17 \\ . & . & 0 \end{pmatrix} \quad \text{(5-2)}$$

The in-plane stress component σ_{11} acting in the rolling direction ($\phi = 0°$) seemed to be quite small (15.3 MPa), while a much larger value of 181 MPa was obtained for the stress component σ_{22} acting in the transverse direction ($\phi = 90°$). Besides, the out-of-plane shear stress components σ_{13} and σ_{23} barely existed (-3.13 and 5.07 MPa). Clearly however, the 316L SS strip presents a tensile surface stress state once co-cured with the composite substrate, as opposed to the compressive surface stress state it contains in its free-standing form.

5.2.1.5 Discussion on the thermally induced residual stress level

The thermally induced residual stress that builds up in the multilayer during the cooling step subsequent to the co-curing process is thus sufficient to reverse the original negative sign of the steel strip stress state. Furthermore, the stress tensor evaluated for the co-cured steel strip results from the superimposed contributions of its original compressive stress state and the tensile

thermally induced stress state. It must hence be compensated for the initial compression if one wishes to isolate the thermally induced residual stress contribution. Focusing on the normal stress components acting in the rolling and the transverse directions, this compensation would yield the values given in Eq. (5-3) where the subscript "th" recalls that they exclusively refer to the thermally induced stress.

$$\begin{cases} \sigma_{\text{th}}^{\text{RD}} \cong 150 \text{ MPa} \\ \sigma_{\text{th}}^{\text{TD}} \cong 195 \text{ MPa} \end{cases} \tag{5-3}$$

Although the anisotropy of the steel strip was not taken into account in this analysis, the stress level still appeared to depend on the measurement direction. The larger tensile stress measured along TD might then be caused by the fact that this direction of the steel strip was aligned with the 90° direction of the composite substrate in the samples. The layup of the composite laminate is indeed designed with a pair of weft laminae at each extremity, which are much stiffer in the 90° direction ($E_2 = 116$ GPa) than in the 0° direction ($E_1 = 34.1$ GPa). The thermal shrinkage of the steel strip may thus have been more constrained in this direction, resulting in a larger residual tensile stress. This realistic explanation would demonstrate the interest of using a ply-based representation of the composite laminate in the FE model of the multilayer.

5.2.2 Curvature-based experimental evaluation of the residual stress with an extension of the Stoney formula

5.2.2.1 Introduction

The basic Stoney formula (Eq. (5-4)) [61] provides an evaluation of the biaxial residual stress σ_f acting in a thin film on a thick substrate when the effective biaxial elastic modulus $E_s/(1-\nu_s)$ of the substrate, the thicknesses h_f and h_s of the film and substrate, and the curvature κ of the system are known.

$$\sigma_f = \frac{1}{6}\frac{E_s}{(1-\nu_s)}\frac{h_s^2}{h_f}\kappa \tag{5-4}$$

Originally, this formula was established for a specific system obeying several hypotheses:

- The film and substrate are homogeneous, isotropic and linear elastic.
- The film is much thinner than the substrate.
- The film and substrate thicknesses are small compared to the lateral dimensions of the system.
- The deflections are small compared to the overall dimensions of the system.
- The stress and curvature are uniform in the system's plane.
- The system presents a spherical deformation, characterised by an equal curvature in all directions of its plane.

Obviously, the steel/joint/composite three-layered system under consideration does not satisfy all of these assumptions. For instance, neither of the composite laminate (substrate) and the steel strip (film) is isotropic. Moreover, the ratio of h_s/h_f is equal to 4.5 %, which does not allow assuming that the film is much thinner than the substrate. However, the Stoney formula is often applied in its original basic form in situations where its validity is compromised [174]. Besides, it has been generalised through time so as to extend

its validity to various more realistic or specific cases, such as that of film and substrate of similar thicknesses. Hence, Eq. (5-5) developed by Freund *et al.* [174] was considered instead, which is the generalisation of the Stoney formula for arbitrary thickness ratios ($h = h_f/h_s$) and arbitrary modulus ratios ($m = M_f/M_s$ where M is the effective biaxial elastic modulus).

$$\sigma_f = \frac{1}{6}\frac{E_s}{(1-\nu_s)}\frac{h_s^2}{h_f}\kappa\left[\frac{1+h}{1+hm(4+6h+4h^2)+h^4m^2}\right] \tag{5-5}$$

5.2.2.2 Curvature of the three-layered systems

The curvature was measured with a Dektak 150 surface profiler (Veeco Inc., USA) in the longitudinal and transverse directions of four peel test specimens with co-cured *as-rolled* steel strip and four peel test specimens with co-cured *micro-perforated* steel strip. These directions respectively correspond to the 90° direction (or weft) and the 0° direction (or warp) of the composite laminate substrate (defined in Figure 1-13). The surface profiles and their parabolic fit are shown in Figure 5-4-a and Figure 5-4-b for the as-rolled and micro-perforated strips, respectively. They were measured on the composite face with the specimens turned upside down with respect to the usual representation of the multilayer showing the composite substrate underneath the steel strip. This results in the curvature appearing downwards on the graphs. Clearly, both trilayer configurations presented a double curvature, which was defined as *ellipsoidal* rather than *spherical* since it was accentuated in the 0° direction.

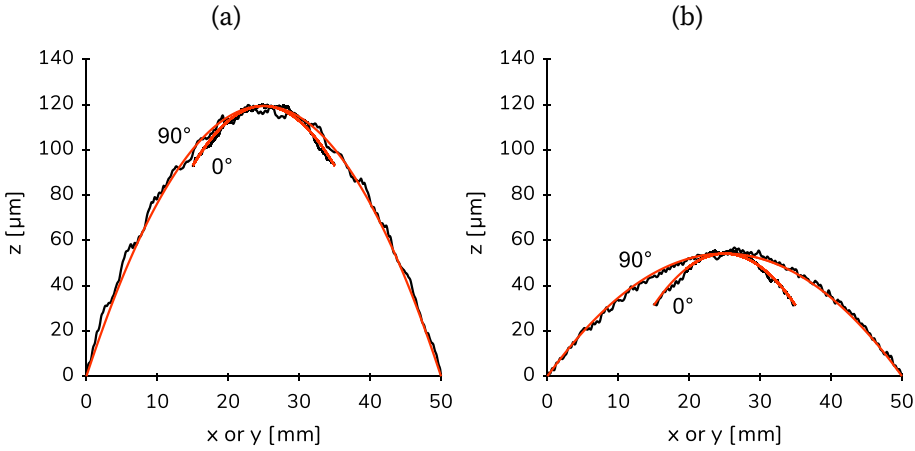

Figure 5-4. Typical sets of surface profiles measured on the composite face of peel test specimens along the 0° and 90°directions of the composite substrate, for the trilayer configuration with (a) co-cured as-rolled steel strip and (b) co-cured micro-perforated steel strip. The parabolic fits from which the curvatures were derived are drawn in red.

The trilayer configuration with as-rolled steel had an average curvature of 0.55 m^{-1} in the 0° direction and 0.39 m^{-1} in the 90° direction, while that with micro-perforated steel had an average curvature of 0.44 m^{-1} in the 0° direction and 0.18 m^{-1} in the 90° direction. Again, this coincides with the two top carbon laminae of the composite substrate having their fibres -and thus their stiffness- concentrated in the 90° direction. The steel strip is thus more capable of shrinking in the 0° direction and constrains the whole trilayered system to some additional bending in this direction. Besides, the larger stiffness of the as-rolled steel strip makes it more capable of competing with the substrate thermal shrinkage and of partly imposing its own (larger) thermal shrinkage. This results in the superior bending of the multi-layered system in the configuration with as-rolled steel strip than in the configuration with micro-perforated steel strip.

5.2.2.3 Thermally induced residual stress in the as-rolled and micro-perforated co-cured steel strips

One has just revealed the deviation of the present systems from the hypothesis of spherical curvature. An extension of the Stoney formula taking ellipsoidal curvature into account was developed by Fahnline *et al.* [175], but it exclusively applies to the case of a square plate sample for which non-spherical bending would be caused by large deflections rather than by the anisotropic nature of the film and/or substrate. The residual stress acting in the steel strip was thus still calculated with Eq. (5-5) for both trilayer configurations, with the isotropic material properties and the measured curvatures given in Table 5-2. The properties given to the steel strips are the arithmetic averages of those measured[23] in the reference directions RD and TD. Similarly, the properties given to the composite substrate are the arithmetic averages of those predicted analytically in the 0° and 90° directions of its plane. The results are enclosed in Table 5-3.

Table 5-2. Properties and measured curvatures used in the calculation of the residual stress acting in the as-rolled and micro-perforated co-cured steel strips with Eq. (5-5).

Material	E [GPa]	ν [-]	h [mm]	$\kappa^{0°}$ [m^{-1}]	$\kappa^{90°}$ [m^{-1}]
A-R strip	189	0.33	0.2	0.55 ± 0.12	0.39 ± 0.01
M-P strip	72.1	0.48	0.2	0.44 ± 0.05	0.18 ± 0.03
Composite	61.8	0.19	4.0	-	-

[23] By resonance (for E), quasi-static tensile test (for ν), and TMA (for α)

Table 5-3. Residual stress acting in the as-rolled and micro-perforated co-cured steel strips as calculated with Eq. (5-5).

Configuration	$\sigma_f^{0°}$ [MPa]	$\sigma_f^{90°}$ [MPa]	$\sigma_f^{\text{average}}$ [MPa]
A-R strip	327 ± 71	232 ± 6	280
M-P strip	338 ± 38	138 ± 23	238

The thermally induced residual stresses evaluated based on the curvatures of the trilayer with as-rolled steel strip have the same sign and order of magnitude as those obtained by XSA. However, they are somewhat larger, and -most importantly- the trend is reversed as regards the magnitude of the stress acting in the 0° and 90° directions. The first observation is probably linked to some stress relaxation that occurred in the samples for various reasons, but was not taken into account in this approach where the materials were considered to behave as linear elastic solids. The second observation was attributed to the fact that the Stoney formula assumes an isotropic substrate, whereas it is precisely the actual anisotropy of the substrate that causes the non-spherical curvature of the present systems. Indeed, as explained in the previous section (Section 5.2.2.2), the larger curvature in the 0° direction (as compared to the 90° direction) is enabled by the larger compliance of the two top carbon laminae in this direction. Since this anisotropy is not taken into account in the formula, the larger curvature in the 0° direction is *wrongly* translated into a larger component of stress in that direction. This shortcoming of the used formula obviously compromises the trustworthiness of the $\sigma_f^{0°}$ and $\sigma_f^{90°}$ residual stress values given in Table 5-3. As no adequate extension of the Stoney formula could be found in the literature, one calculated average residual stress values based on the average -thus spherical- curvature of the trilayer ($\kappa^{\text{average}} = \frac{\kappa^{0°} + \kappa^{90°}}{2}$) in both configurations. These are given in the third column of Table 5-3.

5.2.3 Conclusion

Clearly, both experimental methods had their share of simplifying assumptions which possibly lead to errors on the evaluated residual stresses. Yet, the combination of the experimental results pertaining to the trilayer with as-rolled steel strip formed a stress range of [150; 280] MPa, which is a valuable indication for the assessment of the analytical and FE approaches.

5.3 Analytical prediction of the through-thickness profile of thermally induced residual stress

5.3.1 Introduction

Analytical prediction is the simplest approach that can be followed to quantify the thermally induced residual stress generated in the multilayer in the course of its thermal history. The *through-thickness profile* of residual stress in the plane of the layers was approached with the analytical development detailed in Chapter 2 (Section 2.2.2), in particular with Eq. (2-4) and (2-5). It was evaluated for the thermal load case described by $\Delta T = -160$ °C, which corresponds to the temperature drop between the isothermal resin cure at 180 °C and the return to ambient temperature (taken as 20 °C).

5.3.2 Through-thickness residual stress profiles thermally induced in the three-layered systems

The same steel/joint/composite trilayers as before were considered: one with as-rolled steel strip and the other with micro-perforated steel strip. The isotropic material properties used in the calculations are given in Table 5-4.

Table 5-4. Properties used in the analytical calculations for the prediction of the residual stress acting in the multilayer in both configurations.

Material	E [GPa]	ν [-]	α [μm/(m°C)]	h [mm]
A-R strip	189	0.33	16.2	0.2
M-P strip	72.1	0.48	16.2	0.2
Bond	2.95	0.38	56.4	0.1
Composite	61.8	0.19	2.82	4.0

Again, the properties given to the steel strips are the arithmetic averages of those measured[24] in the reference directions RD and TD, and the properties given to the composite substrate are the arithmetic averages of those predicted analytically in both reference directions of its plane. For the sake of comparison with the experimental results, the latter were computed for the specific layup used in the manufacturing of peel test specimens[25]. Finally, the properties given to the bond layer are those of the RTM6 resin[26].

The calculated through-thickness profile of residual stress is drawn in Figure 5-5 for both trilayers. Besides, several quantities were extracted from this analysis and are presented in Table 5-5. Indeed, the predicted uniform spherical curvature of the trilayer[27] as well as the residual stress predicted *at the top surface* of the as-rolled steel strip can be compared with their experimental counterparts, while the mean residual stress in the plane of the co-cured joint -accessed for the first time- is important information regarding fracture initiation.

[24] By resonance (for E), quasi-static tensile test (for ν), and TMA (for α)
[25] Recall that this layup slightly differs from the laminate layup of the composite booster casing: it contains 13 laminae instead of 14, with one balanced lamina missing at the mid-plane of the laminate.
[26] Measured by DMA (for E), quasi-static tensile tests (for ν) and TMA (for α)
[27] The results are presented with a sign convention (i.e. positive curvature for the multilayer bending upwards) opposite of that used in the reference paper.

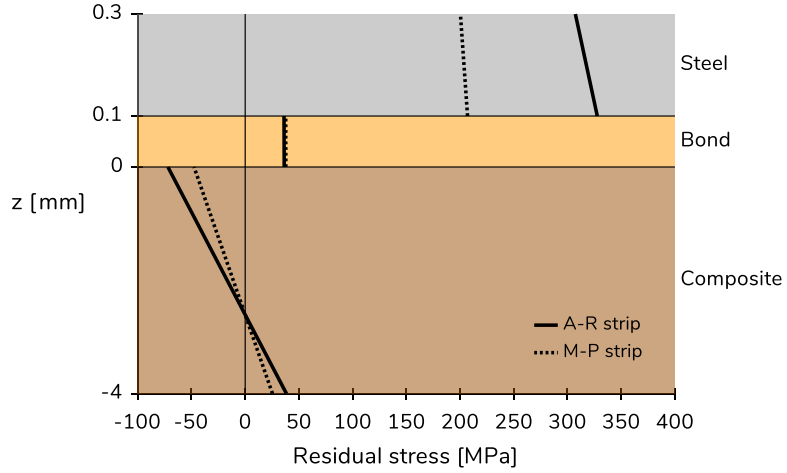

Figure 5-5. Through-thickness profiles of in-plane residual stress predicted with Eq. (2-4) and (2-5) for both configurations of trilayer exposed to a thermal loading of -160 °C.

Table 5-5. Selected results issuing from the prediction of the residual stress profiles: uniform curvature, stress at the top surface of the steel strip, mean stress in the bond layer.

Configuration	κ [m^{-1}]	σ_{steel} [MPa]	σ_{bond} [MPa]
A-R strip	0.36	307	36.2
M-P strip	0.24	200	37.8

The spherical curvatures predicted for both configurations of trilayer are about 23 % smaller than the reference *average* -thus spherical- experimental curvatures. Nonetheless, the predicted residual stress at the surface of the as-rolled steel strip (307 MPa) is close to the stress interval defined by the results of both experimental methods ([150; 280] MPa). This increased the confidence in this analytical approach for the evaluation of the through-thickness profile of the residual stress acting in the plane of the multilayer.

In both configurations, compressive residual stresses were predicted in approximately the upper half of the composite substrate, which correlates well

with the fact that it is not damaged by microcracking at the end of the RTM process. The predicted residual stress appeared to be tensile and practically constant in the thickness of the bond layer, with a mean value smaller than the 0.2 % offset yield stress of RTM6 (48.3 MPa). These stress levels could therefore *a priori* neither cause plastic deformation nor fracture of the bond material, whereas microcracks were observed in this layer after the RTM process. It is certainly where the role of stress concentration must be taken into account, underlying the need for refining the prediction of the thermally induced residual stresses. This was achieved with 3D finite element analyses of the multilayer, where specific geometric features such as the micro-perforations and the edges and corners of the steel strips segments were included in the modelling.

5.4 FE prediction of the thermally induced residual stresses

A three-dimensional finite element model of the steel/joint/composite three-layered system was built with the commercial FE package SAMCEF v16.1 (Siemens, Germany). Quite basic in the origin, the model still offered the best ground for comparison of the simulated results with the measured and analytically predicted ones. It was then upgraded by introducing the actual geometrical features of the studied area in the modelling, such as the micro-perforations and the inter-segments gap. These upgrades enhanced the prediction of the residual stress field, as will be shown subsequently.

5.4.1 Basic prediction of the residual stresses with model A

5.4.1.1 Description of model A

The basic 3D model of the trilayer was called model A. As illustrated in Figure 5-6, it takes the simple form of a square cuboid whose lateral dimensions

are those of the square unit cell enclosing two micro-perforations (Figure 1-16), that is 0.557 mm x 0.557 mm.

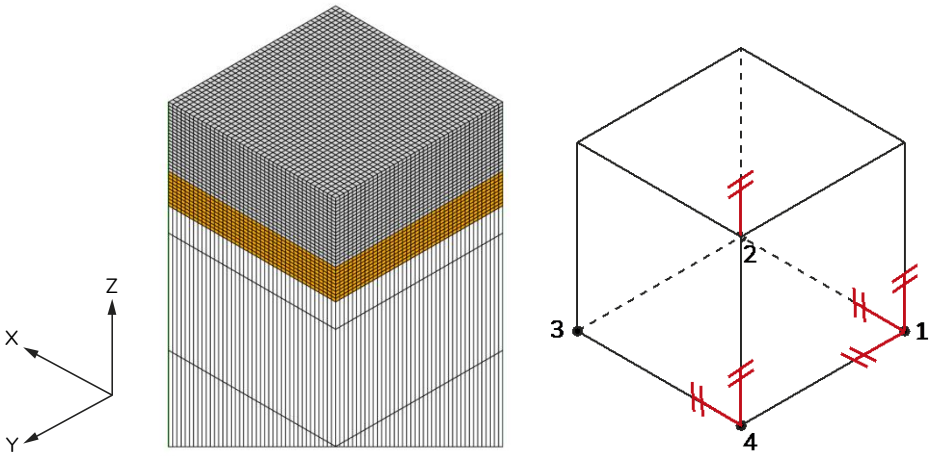

Figure 5-6. Top of the 3D FE model of the trilayer, showing the position of the layers and the transfinite mesh. The fixations used for constraining the rigid body modes are shown at right.

Two versions of model A were actually developed: one (version A1) with the composite laminate modelled as a homogeneous solid with effective equivalent properties (Table 4-2), and the other (version A2) with the composite laminate modelled with the ply-by-ply approach using the composites capabilities available in SAMCEF and the orthotropic properties of the individual laminae (Table 4-1). In this version, the 0° direction was aligned with the global X-axis of the structure. In version A1, the steel layer was successively given the average *isotropic* properties of the *as-rolled* steel strip (version A11), and the *effective equivalent isotropic* properties of the *micro-perforated* steel strip (version A12). In version A2, the steel layer was exclusively *as-rolled* but it was either defined with average *isotropic* properties (version A21) or with *transversely isotropic* properties (version A22). In this last version, its rolling direction was aligned with the 0° direction of the composite laminate. The properties given to the bond layer were, on the other hand, always those of

RTM6. All numerical values relative to the definition of the steel and bond materials in these versions of the model are given in Table 5-6.

A transfinite mesh was generated on the squared basis lying in the XY-plane, starting from 40 14 µm long quadratic elements on the sides of the unit cell. Indeed, by consistency with the other FE models presented in this chapter which are equipped with cohesive elements, the level of mesh refinement of model A was set high enough to satisfy the criterion for mesh convergence in the cohesive zone studied in Chapter 7 (Section 7.3.2). The 2D mesh was then extruded in the Z-direction, yielding 3D quadratic brick elements. The spatial discretisation of the layers in the Z-direction was defined as a function of the layer thickness: 20 elements were piled-up in the 0.2 mm thick steel strip layer and 10 elements in the 0.1 mm thick bond layer. In contrast, the 4.0 mm thickness of the composite substrate was discretised into 14 elements only, which actually comes down to one element per ply.

Table 5-6. Numerical values used for the definition of the properties of the bond and steel layers in each version of model A.

Model version	E_1	E_2	E_3	ν_{12}	ν_{13}	ν_{23}	G_{12}	G_{13}	G_{23}	α_1	α_2	α_3
	[GPa]			[-]			[GPa]			[µm/(m°C)]		
Bond layer												
All	2.95			0.38			-			56.4		
Steel layer												
A11 & A21	189			0.33			-			16.2		
A12	72.1			0.48			-			16.2		
A22	172	206		0.28	0.30		88.9	79.2		16.3	16.0	

As regards the boundary conditions, the rigid body modes were constrained through the fixation of translational degrees of freedom at three corner nodes of the basis (Figure 5-6), while the periodicity and symmetry of the

modelled volume was expressed in the form of planarity conditions applied to each vertical face of the cuboid.

Finally, a thermal load of -160 °C was applied in a linear elastic analysis, resulting in a homogeneous temperature drop from 180 °C to 20 °C for the whole trilayer. It was indeed assumed in this thesis that, given the small thickness of the multi-layered system, the effect of thermal gradients could be neglected in the first instance. Full thermal analyses were thus not performed in this work.

Version A1 of model A counted 218,284 nodes (or 669,104 DOF) and the linear analyses were completed in about 20 minutes (0.33 hours) in CPU time[28]. Version A2 counted 268,714 nodes (or 825,314 DOF) and the linear analyses were completed in about 42 minutes (0.7 hours) in CPU time in the same conditions.

5.4.1.2 Thermally induced residual stresses predicted with model A

Some essential information were extracted from the results of the linear elastic FE analyses performed with the different versions of model A, namely the curvature developed in the 0° and 90° directions of the composite substrate, the residual stress acting in these directions at the free surface of the steel layer, and the average residual stress acting in these directions in the bond layer. These results are gathered in Table 5-7.

[28] With a 2.50 GHz Intel® Core™ i7 – 4710MQ processor equipped with 16.0 GB RAM.

Table 5-7. Curvatures, residual stress at the top surface of the steel layer, and mean residual stress in the bond layer predicted in both reference directions of the composite laminate substrate with the different versions of model A for a thermal load of -160 °C.

Version	$\kappa^{0°}$ [m^{-1}]	$\kappa^{90°}$ [m^{-1}]	$\sigma_{steel}^{0°}$ [MPa]	$\sigma_{steel}^{90°}$ [MPa]	$\sigma_{bond}^{0°}$ [MPa]	$\sigma_{bond}^{90°}$ [MPa]
Homogeneous composite laminate						
A11	0.36	0.36	306	306	36.2	36.2
A12	0.24	0.24	198	198	37.8	37.8
Ply-by-ply composite laminate						
A21	0.52	0.28	252	321	35.5	36.4
A22	0.49	0.29	242	329	35.7	36.4

On the one hand, when the composite substrate was modelled as a homogeneous solid with effective equivalent properties (models A11 and A12), the simulation yielded the same spherical curvatures and the same tensile stress values as the analytical approach (Table 5-5). This allowed validating the fixations and boundary conditions defined in the FE model.

On the other hand, when the composite substrate was modelled with the more realistic ply-by-ply approach (models A21 and A22), the results of the simulations diverged from the analytical results but got closer to the experimental ones. Indeed, the ply-by-ply modelling of the composite laminate let the thermal shrinkage develop differently in the 0° direction and in the 90° direction. As a consequence, the ellipsoidal curvature measured in the context of the curvature-based approach was retrieved, and the predicted residual stress level differed in these reference directions, consistently with the results obtained by XSA. The average tensile residual stress in the bond layer was, on the contrary, not affected by this evolution in the modelling: it remained direction-independent and still equal to the analytical value a priori unable to cause the fracture of the bond material.

The results obtained with versions A21 and A22 of the model were pretty close, indicating that the major cause of stress directionality in the plane of the steel layer is not its own anisotropic nature but that of the neighbouring carbon laminae. The transversely isotropic definition of the steel strip's thermal and mechanical properties was still retained, given the latter had already been measured along RD and TD.

The curvature predicted with version A22 in the 0° direction was only 11 % smaller than the corresponding experimental value (0.55 m^{-1}), while that in the 90° direction was about 25 % smaller than the experimental value (0.39 m^{-1}). The components of residual stress predicted with version A22 at the free surface of the steel layer were between 60 and 70 % larger than those evaluated by XSA ($\sigma_{steel}^{0°} = 150$ MPa and $\sigma_{steel}^{90°} = 195$ MPa), while they differed by less than 20 % from the average value evaluated with the curvature-based approach ($\sigma_{steel}^{average} = 280$ MPa). The systematic underestimation of the residual stresses evaluated by XSA as compared to those evaluated with the other methods may be due to a certain amount of stress relaxation that probably occurred while cutting the samples to the relatively small dimensions required for the XRD measurement.

5.4.2 Refined prediction of the residual stress fields with model B

5.4.2.1 Introduction

The analysis of the results yielded by the previous FE model established its correct definition as well as it confirmed the importance of using the ply-by-ply approach for the modelling of the composite laminate. Yet, the predicted tensile residual stress remained too low to damage the bond material. The latest version of this model (A22) was thus upgraded into model B with the successive introduction of the main geometrical discontinuities which are

thought to be responsible for the occurrence of microcracks in the bond material and for the disbonds at the steel/bond interfaces. Micro-perforations of the steel strip were first included in the modelling (version B1), then the inter-segments gap since it was pointed out in Chapter 3 as the most severely damaged region of the abradable track. Two realistic configurations of ISG were modelled: one with the steel strip segments being carefully cut in between the micro-perforations (thereby showing straight edges; version B2), and the other with the edges of the steel strip segments passing through the micro-perforations (thereby being irregular; version B3).

5.4.2.2 Description of models B1, B2 and B3

The three upgraded versions of the 3D FE model of the trilayer are illustrated in Figure 5-7. Version B1 obviously represents a volume of trilayer found far from the boundaries of the steel strip segment, while versions B2 and B3 represent a volume of trilayer found at an inter-segments gap.

Model B is a square cuboid based on the repetition of the square unit cell enclosing two micro-perforations whose characteristic dimensions are given in Table 1-3. This unit cell chosen for the reproduction of the periodic penetration pattern of the micro-perforated steel strip is not symmetrical with respect to the structural axes XYZ, so that the constrains linked to the use of planarity conditions applied to each vertical face of a cuboid based on one single unit cell were suspected to be too strong. However, instead of modifying the formulation of these boundary conditions, one simply surrounded the unit cell of interest with other identical unit cells serving as buffers that attenuate the effect of these imperfect boundary conditions.

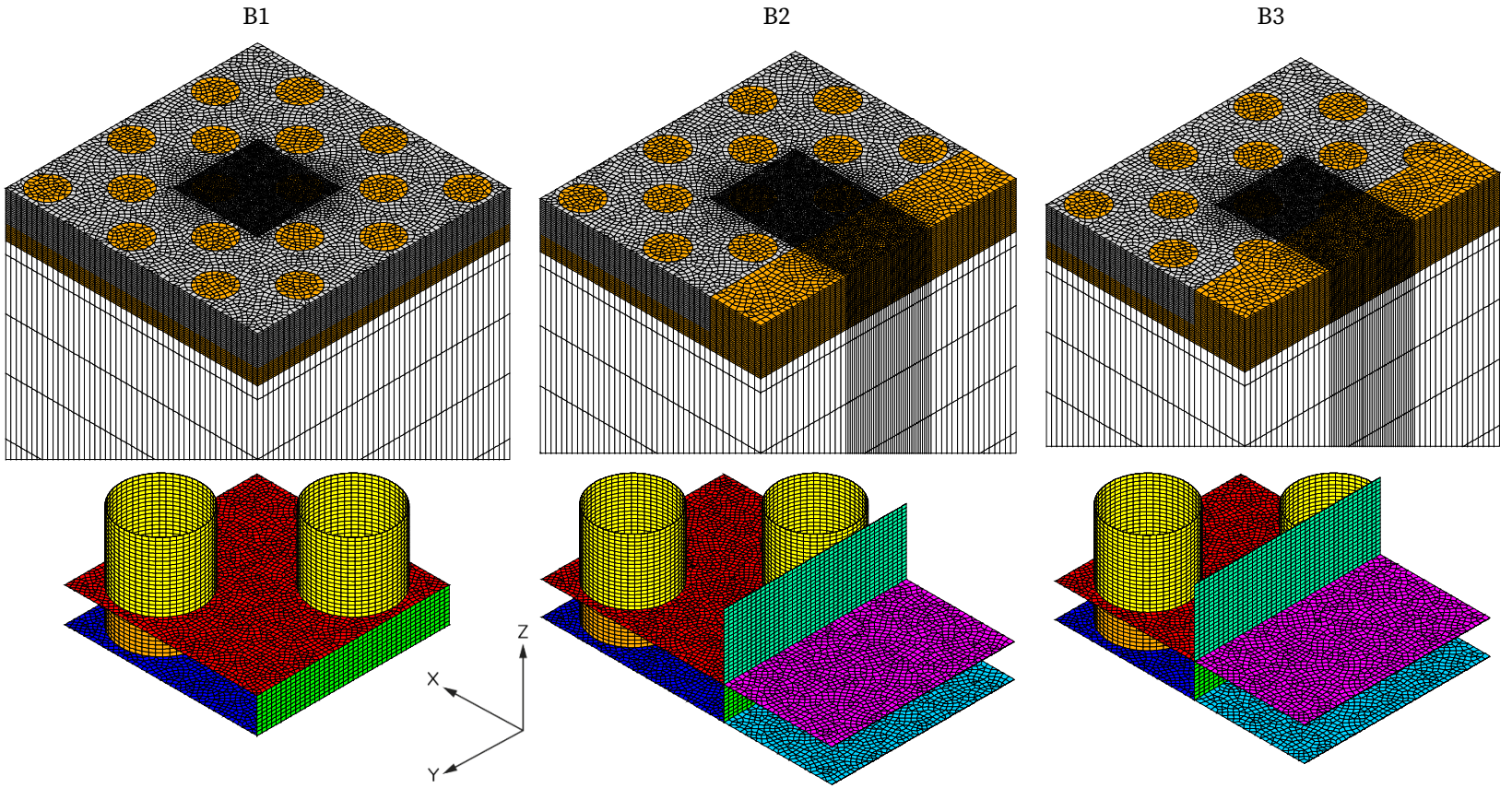

Figure 5-7. Top of the 3D FE model of the trilayer in its three upgraded versions, showing the geometry, the position of the different materials and the discretisation mesh.The interfaces created with cohesive zone elements in the central cell are shown on the second row.

While the geometry of versions B2 and B3 features half an ISG, the boundary conditions applied to its vertical face in the YZ-plane were adapted to express the symmetry of the volume with respect to the Y-axis[29].A complete ISG was thus modelled this way, the half width of which was set to 0.33 mm in accordance with the results of the statistical analysis of the multilayer presented in Chapter 3.

In each version of model B, the surface of the central unit cell lying in the XY-plane was finely meshed with three-sided and four-sided polygonal elements, starting with 40 quadratic elements on the sides of the unit cell and 50 quadratic elements on the circumference of the micro-perforations in models B1 and B2. The number of elements on the contours of the central cell in model B3 was defined so as to keep the same element dimensions as in the two other models. This level of mesh refinement was set high enough to satisfy the criterion for mesh convergence in the cohesive zone studied in Chapter 7 (Section 7.3.2), for a large set of cohesive zone parameter values. On the other hand, the surrounding "buffer" unit cells were more coarsely meshed with the same type of elements, starting from 16 quadratic elements on the sides of the unit cell and 20 quadratic elements on the circumference of the micro-perforations in models B1 and B2. In model B3, the number of elements on the contours of the buffer cells was again defined so as to keep the same element dimensions as in the two other models.

The 2D mesh was then extruded in the Z-direction, yielding 3D quadratic prism and brick elements. The spatial discretisation in the Z-direction of the bond and steel layers was defined as a function of the layer thickness, exactly as detailed for model A. The composite substrate was this time exclusively modelled with the ply-by-ply approach using the composites capabilities available in SAMCEF, and its 4.0 mm thickness was discretised into 14 ele-

[29] A condition of zero displacement along the X-direction was imposed to all nodes of this face.

ments (one element per lamina). Last but not least, quadratic *cohesive elements* were created at selected interfaces between structural volume elements in the refined domain, as shown in Figure 5-7. This type of finite elements was introduced in Chapter 2 (Section 2.5). In the particular case of a linear analysis, they allow accessing the interlaminar stress vector that characterises the stress transfer at an interface. Their penalty stiffness K^0 was set to 10^7 Nmm^{-3}. The ability of this value to simulate perfect bonding was indeed validated after careful examination of (i) the stress fields predicted in the volumes of model B2 with and without cohesive zone elements, and (ii) the interlaminar stress tensor predicted at the interfaces of model B2 with the penalty stiffness either set to 10^7 Nmm^{-3} or to the exaggerated value of 10^{10} Nmm^{-3}.

The definition of the thermal and mechanical behaviour of the materials in all versions of model B were retained from model A22, and the corresponding numerical values can thus be found in Table 5-6. Finally, the fixations and the prescribed thermal loading in all versions of model B were also retained from model A.

Despite the changes in geometry of the modelled zone from version B1 to version B3, the characteristic size and computational cost of these models were noticeably equivalent. Model B2 was just about the largest, with 1,248,381 nodes (or 3,751,854 DOF) and about 12.7 CPU hours required for the completion of its linear analysis[30].

5.4.2.3 Thermally induced residual stress fields predicted with models B1, B2 and B3

The stress and displacement fields resulting from the linear elastic FE analyses performed on the three versions of model B were closely examined, and

[30] With a 2.50 GHz Intel® Core™ i7 – 4710MQ processor equipped with 16.0 GB RAM.

the outcome of this study is presented in this sub-section with a focus on the stress predicted in the bond and steel layers. Since “a picture is worth a thousand words”, the reader will find in the following many figures with a selection of images showing different stress components displayed as *scalar values by element* on several parts of the structure. These images are interpreted in the adjoining text.

5.4.2.3.1 Residual stress fields in the steel strip

The effect of the presence of micro-perforations and the influence of the ISG were first observed globally on the whole micro-perforated steel layer, as shown in Figure 5-8 with the normal stress acting in the Y-direction in that layer.

On the one hand, the presence of micro-perforations clearly generated some stress concentration. As expected, σ_Y rose on the contour of the micro-perforations, more specifically where the normal to the circumference is aligned with the X-axis. Conversely, σ_X rose where that normal is aligned with the Y-axis. This appears in Figure 5-9 which shows the normal stress components along the X and Y-directions and the Von Mises equivalent stress (σ_{VM}) in the steel layer of the central cell (note that the angle of view varies from one model to the other and the location of the ISG is thus indicated by an arrow). The σ_X component acting in the steel layer is clearly lower than the σ_Y component ($\sigma_{X,max} \cong 360$ MPa vs. $\sigma_{Y,max} \cong 540$ MPa for model B1), which is again a demonstration of the influence of the orthotropic nature of the neighbouring weft carbon laminae. The highest stress concentration level ($\sigma_Y \cong 960$ MPa) and the highest level of Von Mises stress (about 920 MPa) were reached in model B2 where the contour of the micro-perforation was closest to the ISG. They were however respectively lower than the tensile stress at break measured in the transverse direction of the as-rolled AISI 316L steel strip (1323 MPa) and the threshold for plastic deformation defined by

the experimentally measured 0.2% offset yield stress of about 1200 MPa (Table 4-8).

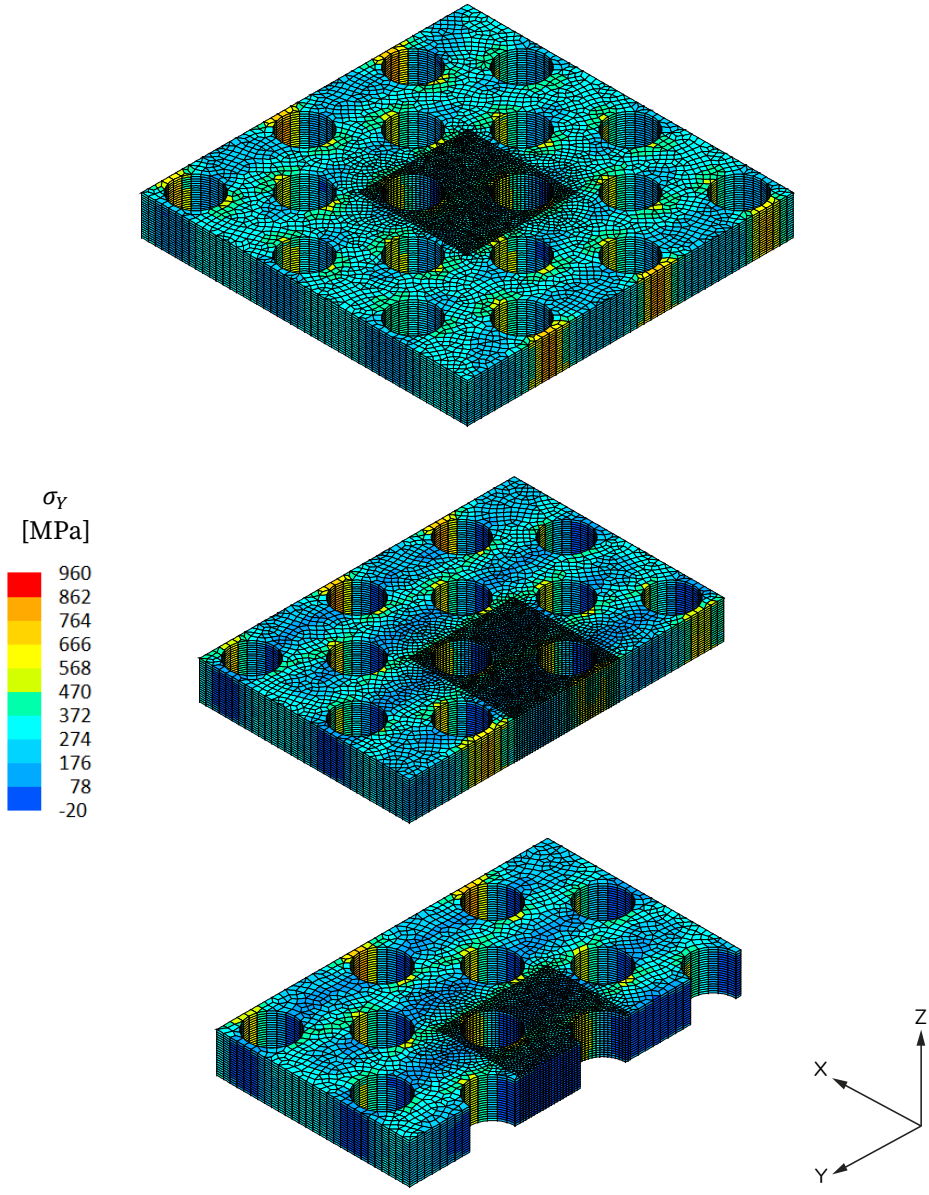

Figure 5-8. Component of normal stress along the Y-direction in the steel layer, as predicted by models B1, B2 and B3.

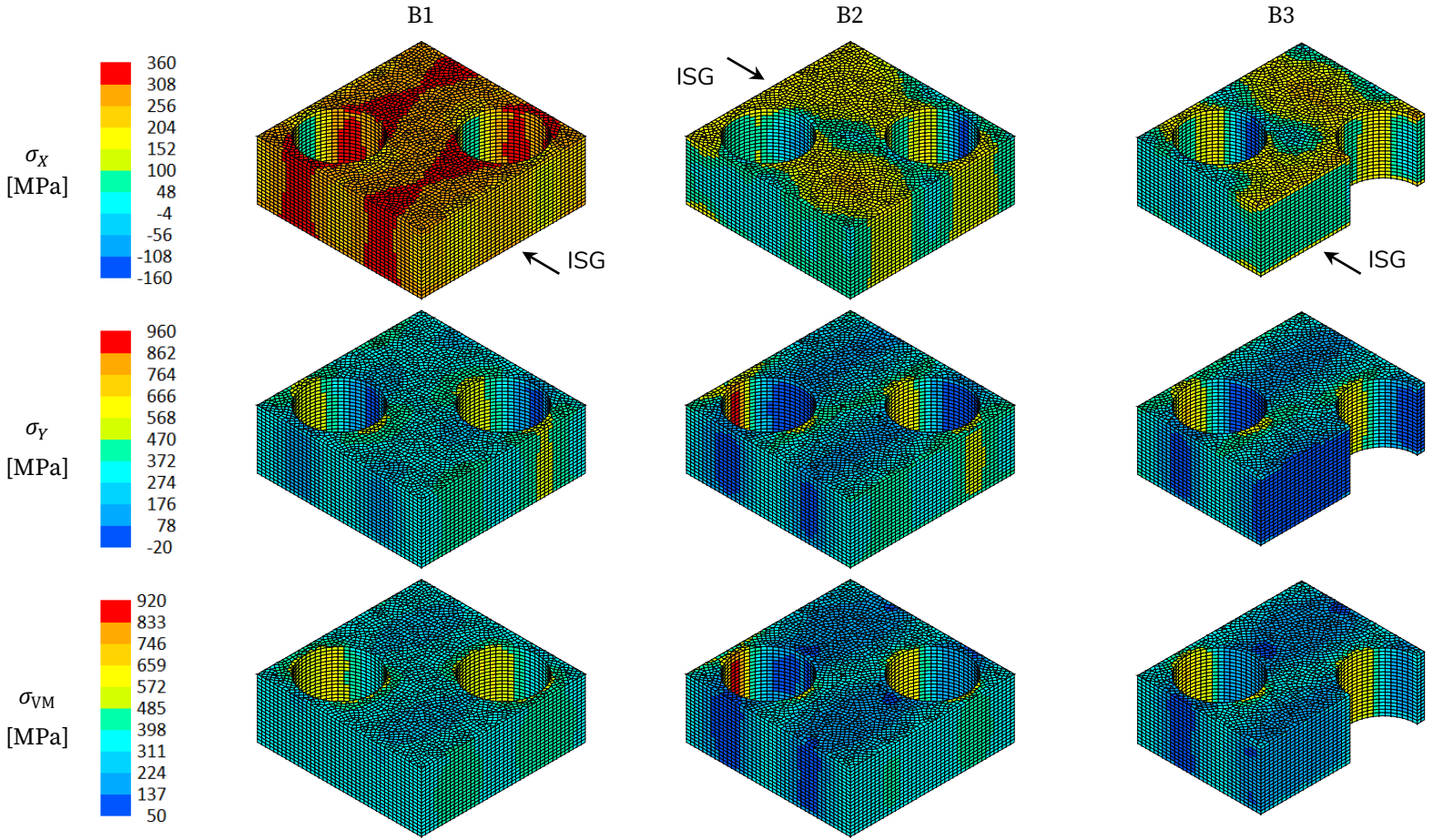

Figure 5-9. Components of normal stress along the X and Y-directions, and Von Mises equivalent stress in the steel layer of the central cell, for models B1, B2 and B3.

On the other hand, the presence of the ISG in models B2 and B3 did strongly alter the stress field in the steel strip. It released the maximum value of σ_X from 360 MPa in model B1 to 214 MPa and 278 MPa in models B2 and B3. This was attributed to the compliant bond material in the ISG allowing the steel strip to more freely accomplish its thermal shrinkage in this direction. Furthermore, the ISG modified the location of the regions of σ_X concentration. On the contrary, under the influence of the ISG, σ_Y rose from the maximum value of 538 MPa in model B1 to the maximum values of 960 MPa and 760 MPa in models B2 and B3.

5.4.2.3.2 Residual stress fields in the bond layer

The first component of principal stress (σ_I) and the Von Mises stress were selected for this discussion since they can respectively cause fracture and plastic deformation of the polymer material in the co-cured joint.

The distribution of σ_I in the bond layer of the central cell is shown in Figure 5-10 and Figure 5-11, respectively including and excluding the bond material which fills the micro-perforations and the ISG. These figures contain a volume view of the considered part of the structure for each version of model B, as well as several cross-sections which expose the distribution of σ_I inside the bond material. The distribution of σ_{VM} is shown in Figure 5-12 and Figure 5-13 which are constructed as the two previous ones.

As visible in Figure 5-10, the maximum level of σ_I (200 MPa) was predicted with model B3, as compared to about 145 MPa and 180 MPa with models B1 and B2. This largely exceeds the values of tensile stress at break which were measured experimentally for RTM6 and Redux 322 (about 81 MPa and 53 MPa, respectively). Large tensile stresses were indeed found at locations presenting geometrical and material discontinuities, such as the top edge of the inter-segments gap and the top contour of the micro-perforations.

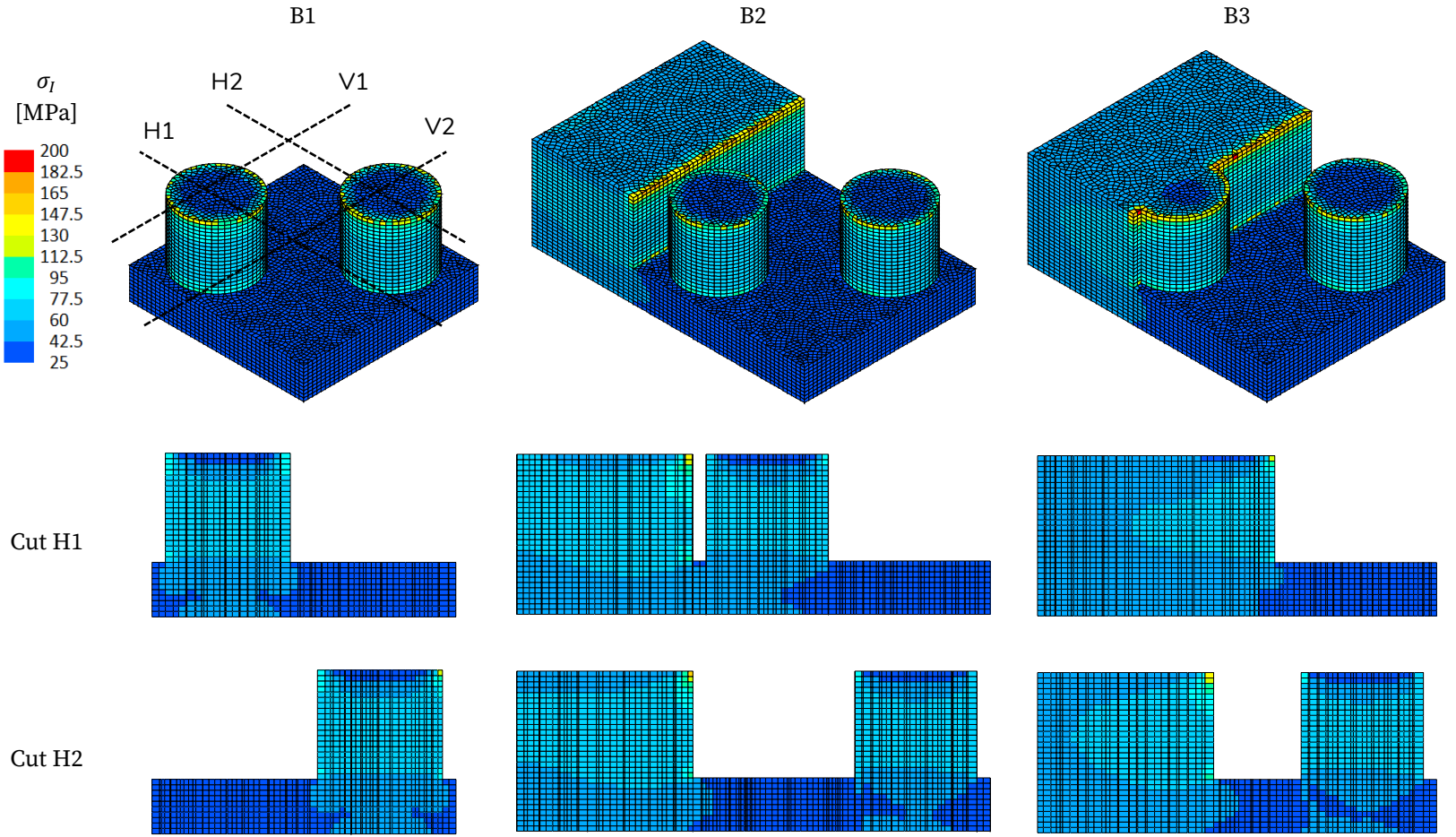
B1
B2
B3
σ_I
[MPa]
200
182.5
165
147.5
130
112.5
95
77.5
60
42.5
25
H1
H2
V1
V2
Cut H1
Cut H2

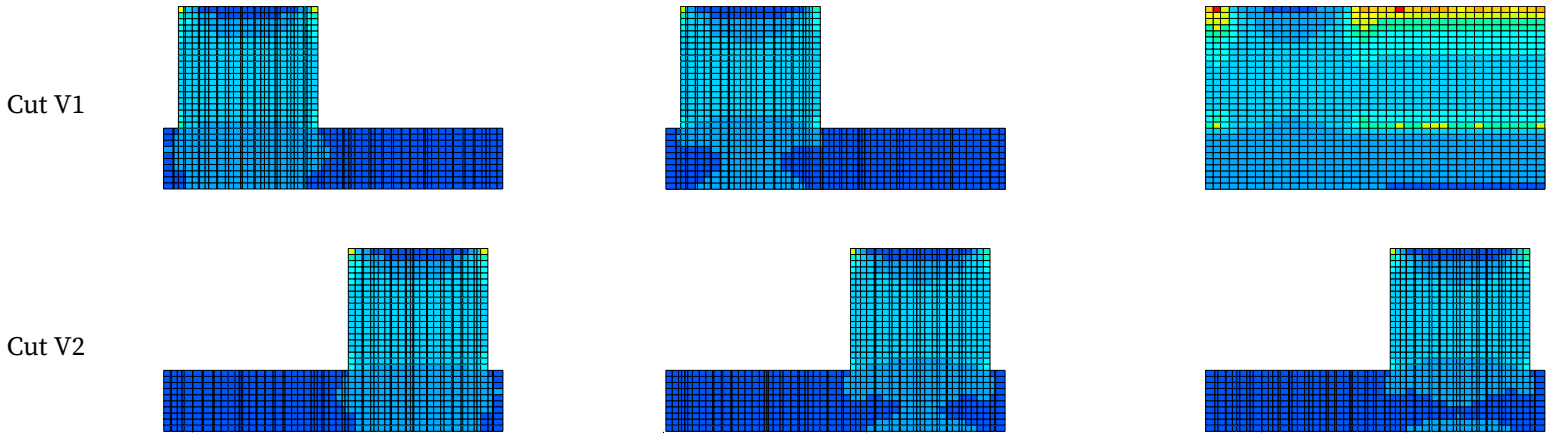

Figure 5-10. First component of principal stress in the bond layer (including the micro-perforations) of the central cell, for models B1, B2 and B3.

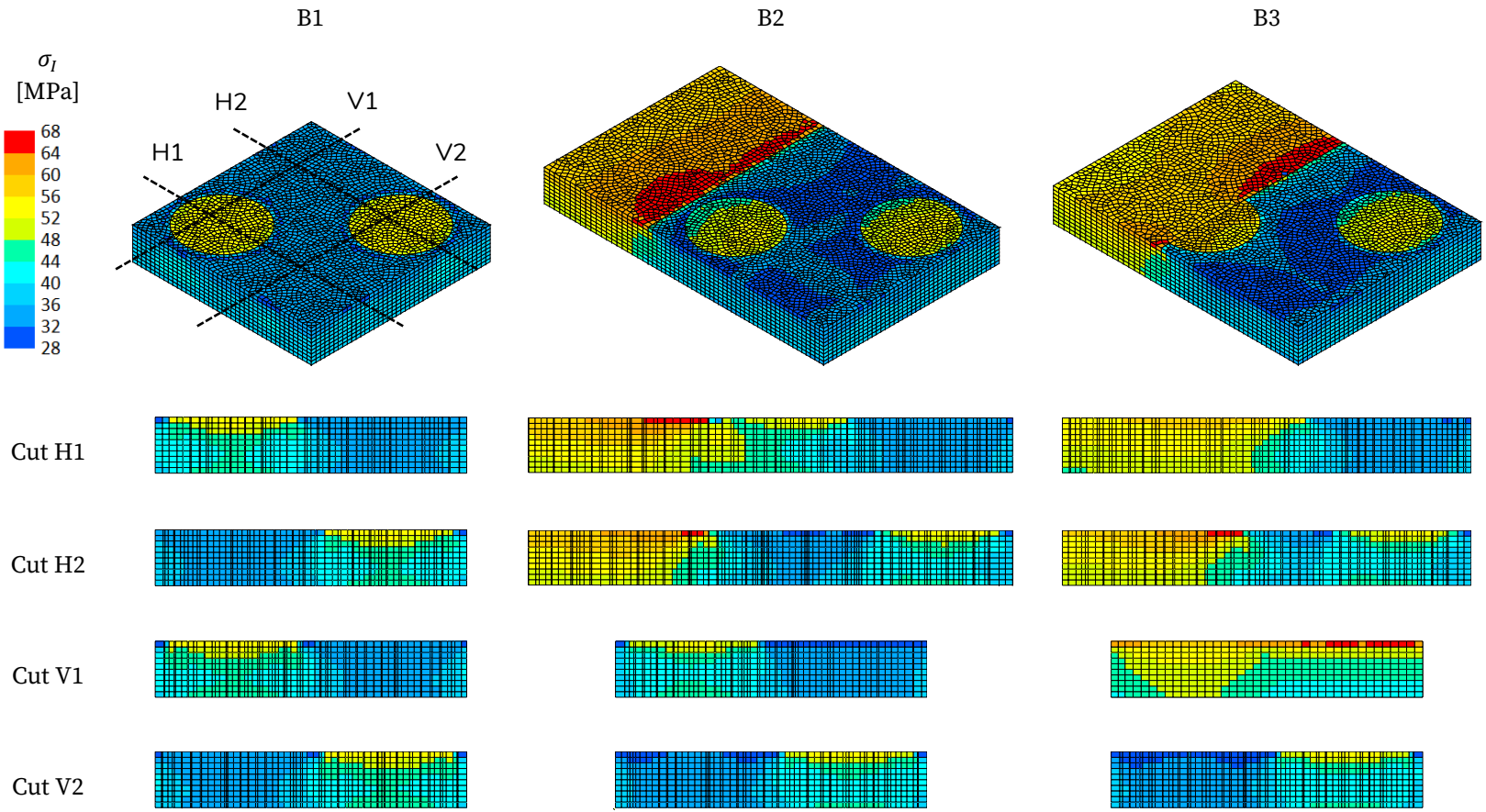

Figure 5-11. First component of principal stress in the bond layer (excluding the micro-perforations) of the central cell, for models B1, B2 and B3.

The cross-sections however revealed that these stress concentrations are extremely localised and do not extend into the material. The rest of the volume was almost invariably coloured in blue with a certain lack of nuances. A change in graduation scale is thus proposed in Figure 5-11 which focuses on the flat bond layer, excluding the bond material inside the micro-perforations and the ISG. Subtle variations in σ_I appear and bring important information: there is some stress concentration at the bottom edge of the ISG, a location that was shown to be a preferred site of crack initiation in the statistical analysis presented in Chapter 3. The stress indeed locally rose to about 68 MPa in models B2 and B3 at this location, and starting from there, an area of lower stress concentration extended at 45° on both sides of the ISG. While this highest value of σ_I predicted in the flat bond layer of the central cell is 16 % lower than the tensile stress at break of RTM6, it is nonetheless 28 % higher than the measured tensile stress at break of Redux 322. The potential for damage of this tensile stress should therefore not be neglected.

Interestingly, the similarity of the cross-sections issuing from cut V2 for the three versions of model B indicated that the effect of the inter-segments gap on σ_I has a quite limited span.

Similarly to σ_I, the Von Mises equivalent stress reached its highest values at the top edge of the ISG and the top contour of the micro-perforations, as can be seen in Figure 5-12. The maximum value of σ_{VM} (150 MPa) was predicted with model B3, as compared to about 100 MPa and 128 MPa with models B1 and B2. It largely exceeds the values of 0.2 % yield stress which were experimentally measured for RTM6 and Redux 322 (about 48 MPa and 40 MPa, respectively). The cross-sections this time do not only reveal the quite localised character of these maxima; they also highlight the presence of another region of Von Mises stress concentration which is again located at the bottom edge of the ISG.

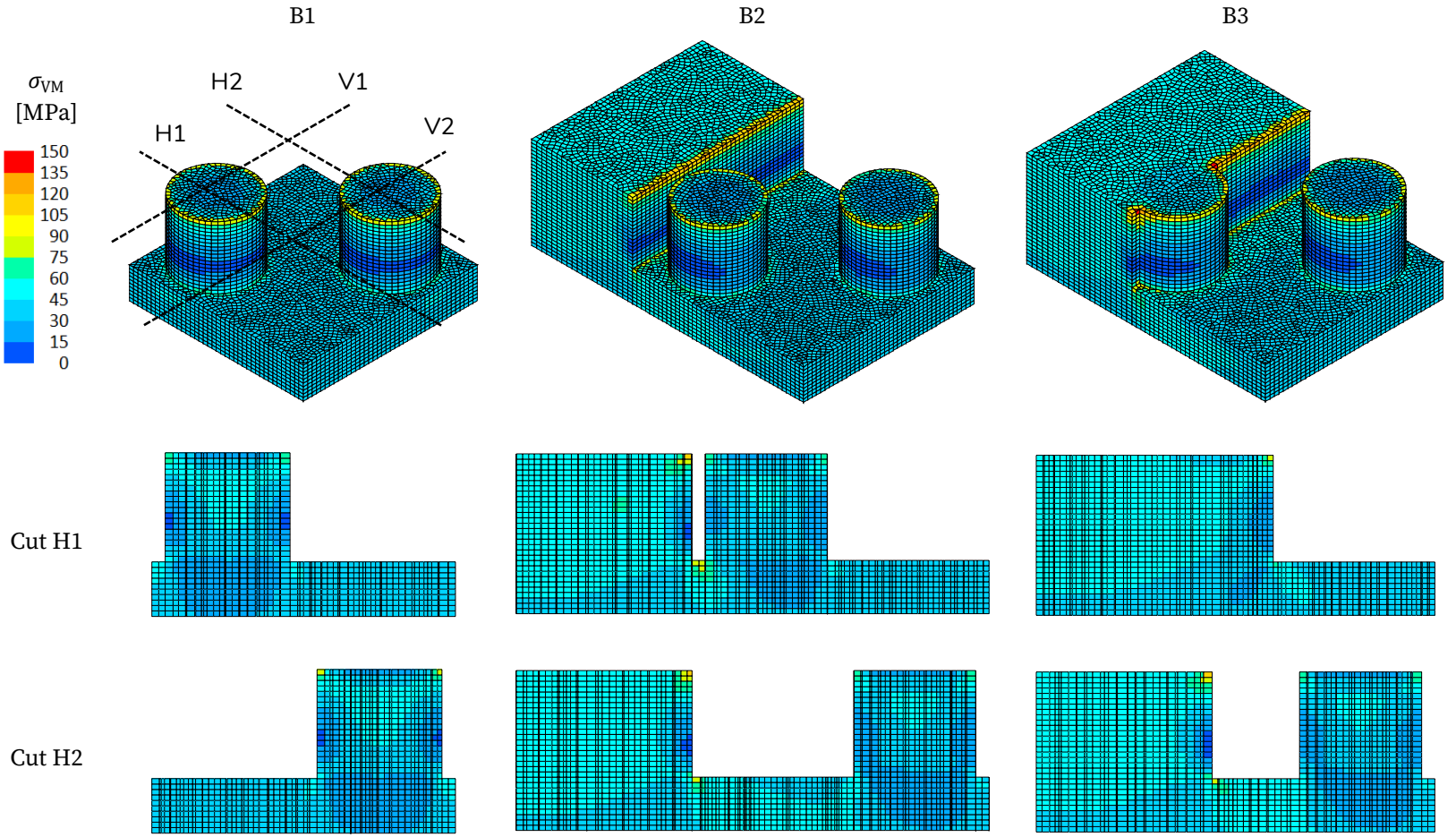
B1
B2
B3
σ_{VM}
[MPa]
150
135
120
105
90
75
60
45
30
15
0
H1
H2
V1
V2
Cut H1
Cut H2

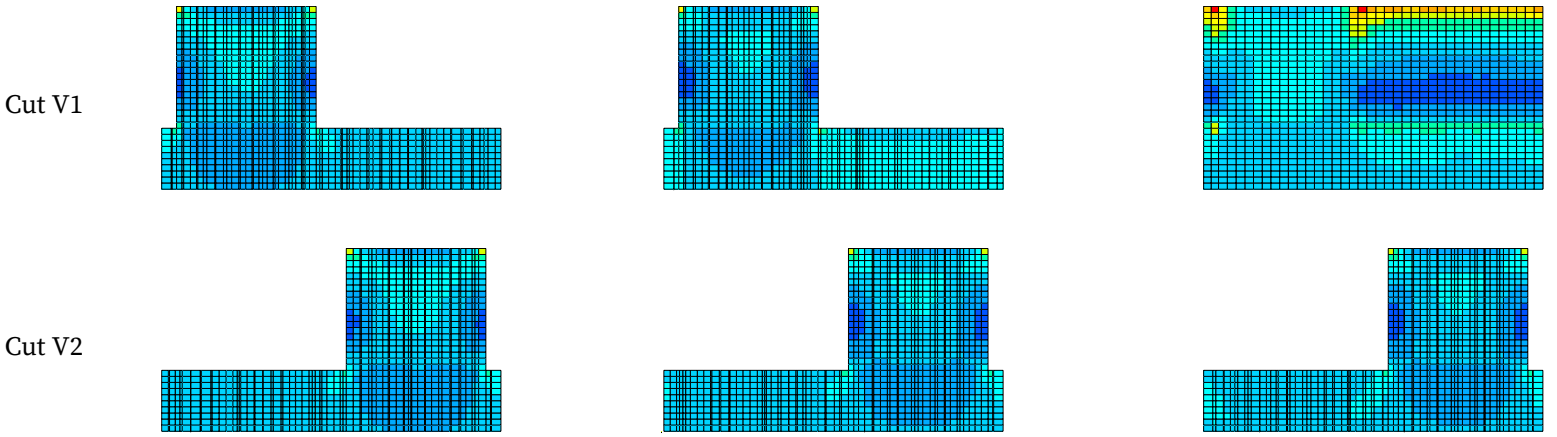

Figure 5-12. Von Mises equivalent stress in the bond layer (including the micro-perforations) of the central cell, for models B1, B2 and B3.

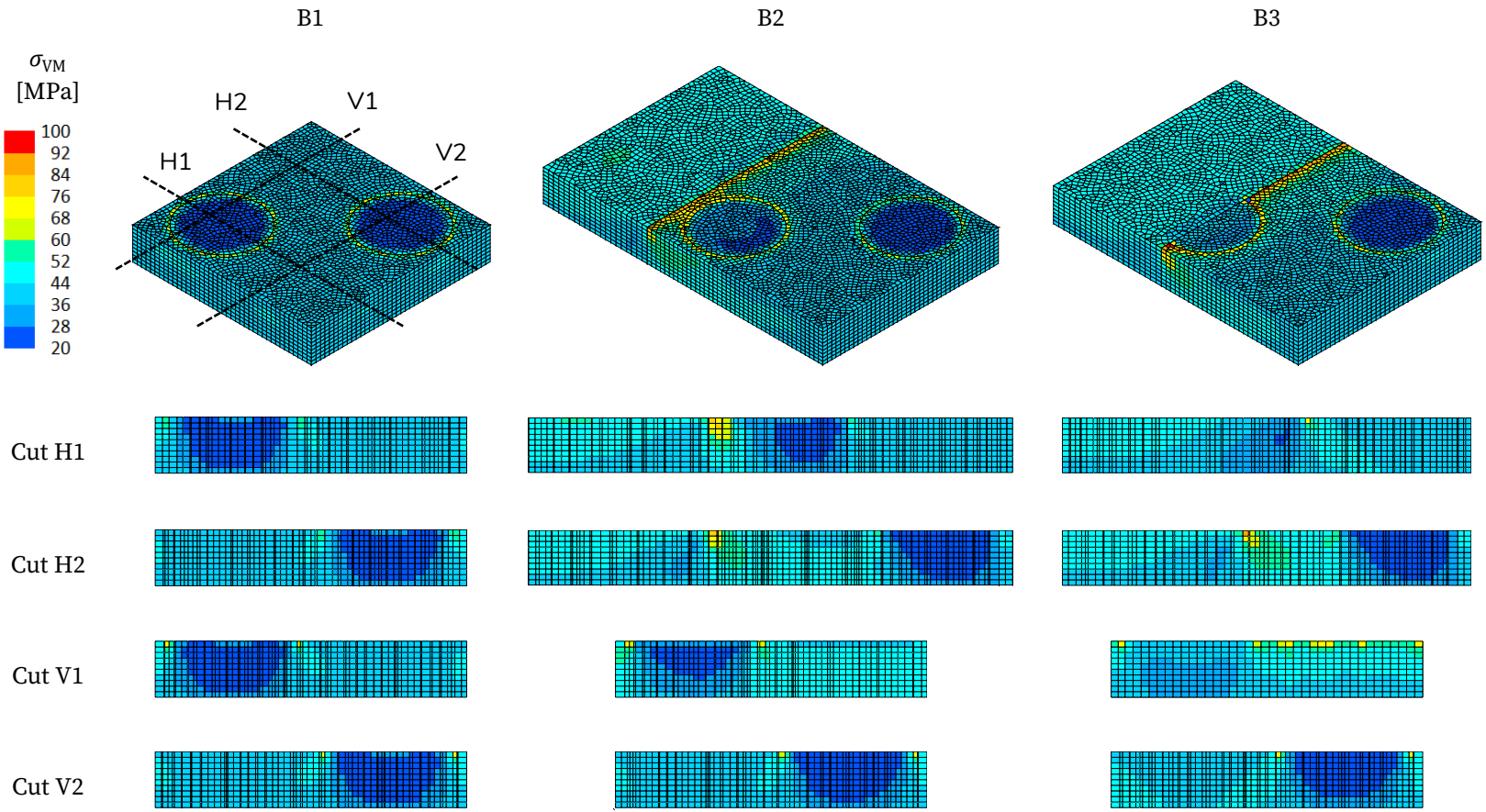

Figure 5-13. Von Mises equivalent stress in the bond layer (excluding the micro-perforations) of the central cell, for models B1, B2 and B3.

Figure 5-13 illustrates with more nuances the distribution of the Von Mises stress in the flat bond layer. The cross-sections show that σ_{VM} locally reaches about 90 MPa in models B2 and B3 at the bottom edge of the ISG, and extends into areas of lower stress at 45° on both sides of the ISG. This predicted value is 88% larger than the 0.2 % yield stress of RTM6 and 125% larger than the 0.2 % yield stress of Redux 322, meaning that plastic deformation of the bond material does most probably occur at this location.

5.4.2.3.3 Residual stress fields at the interfaces

The three components of the interlaminar stress vector were examined at all interfaces equiped with cohesive elements. In particular, the extended vertical interface at the ISG, the extended cylindrical interfaces in the micro-perforations, and the horizontal interface below the steel layer were selected for this discussion. These results are presented in Figure 5-14, Figure 5-15, and Figure 5-16, respectively. The components of the interlaminar stress tensor are expressed in the xyz local axis system of the cohesive elements, the z-direction being normal to the element. These x, y, z local axes are aligned with the structural Y, Z, X axes for the vertical interfaces in Figure 5-14, while they are aligned with the structural X, Y, Z axes for the horizontal interfaces in Figure 5-16.

As can be seen in Figure 5-14, particularly high normal (“peel-off”) interlaminar stresses were predicted at the top of the vertical steel-bond interface with models B2 and B3, as compared to the rest of the interface where the stress remained below 100 MPa. Regions found at the intersection of a bi-material interface and a free surface do indeed carry the largest amount of interlaminar stress in composite assemblies, whether the latter are mechanically loaded or contain residual stresses. The maximum normal interlaminar stress (190 MPa) was predicted at the top corners of the cut micro-perforation in model B3. This value should be compared to the normal peel strength of

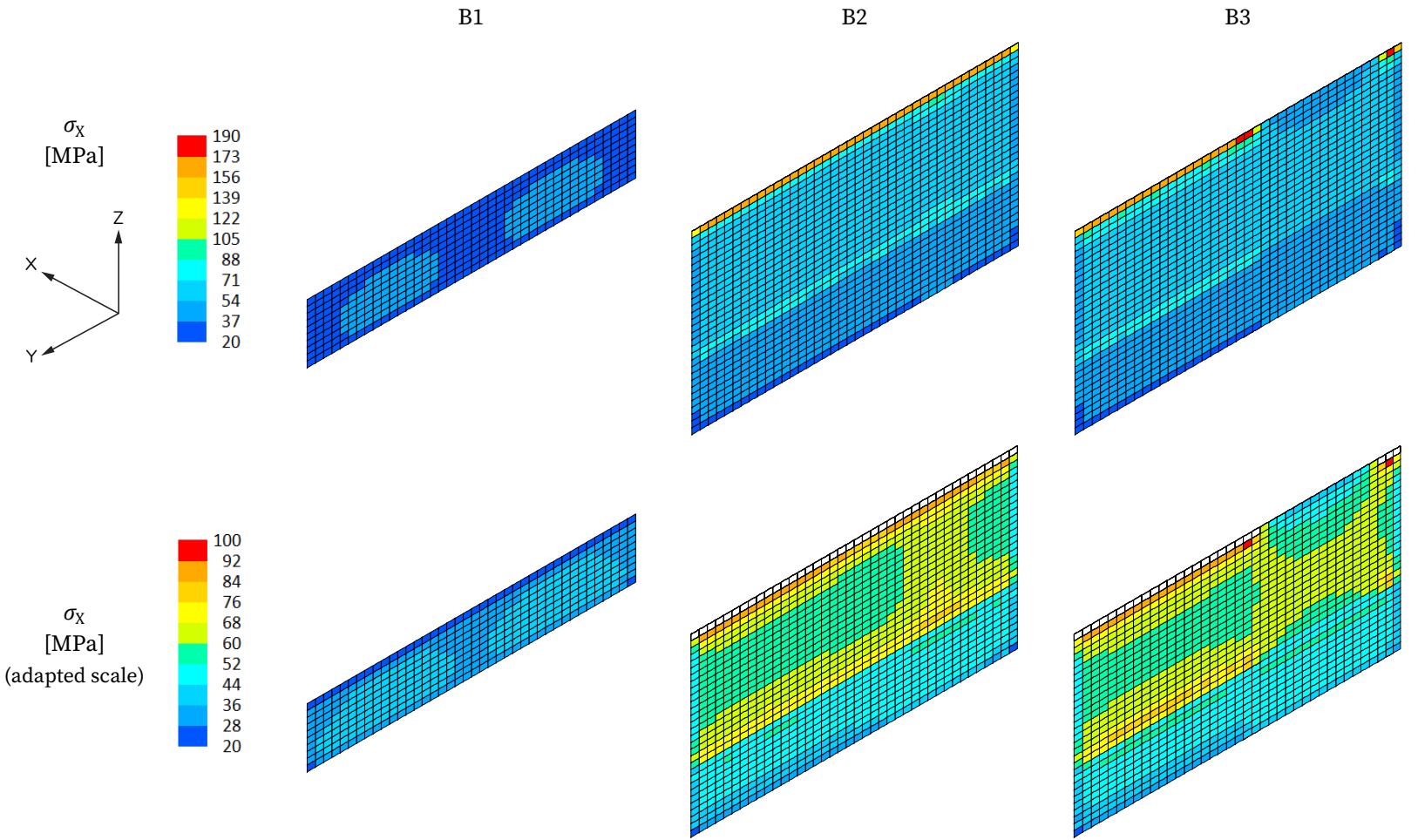
B1
B2
B3
σ_X
[MPa]
190
173
156
139
122
105
88
71
54
37
20
Z
X
Y
σ_X
[MPa]
(adapted scale)
100
92
84
76
68
60
52
44
36
28
20

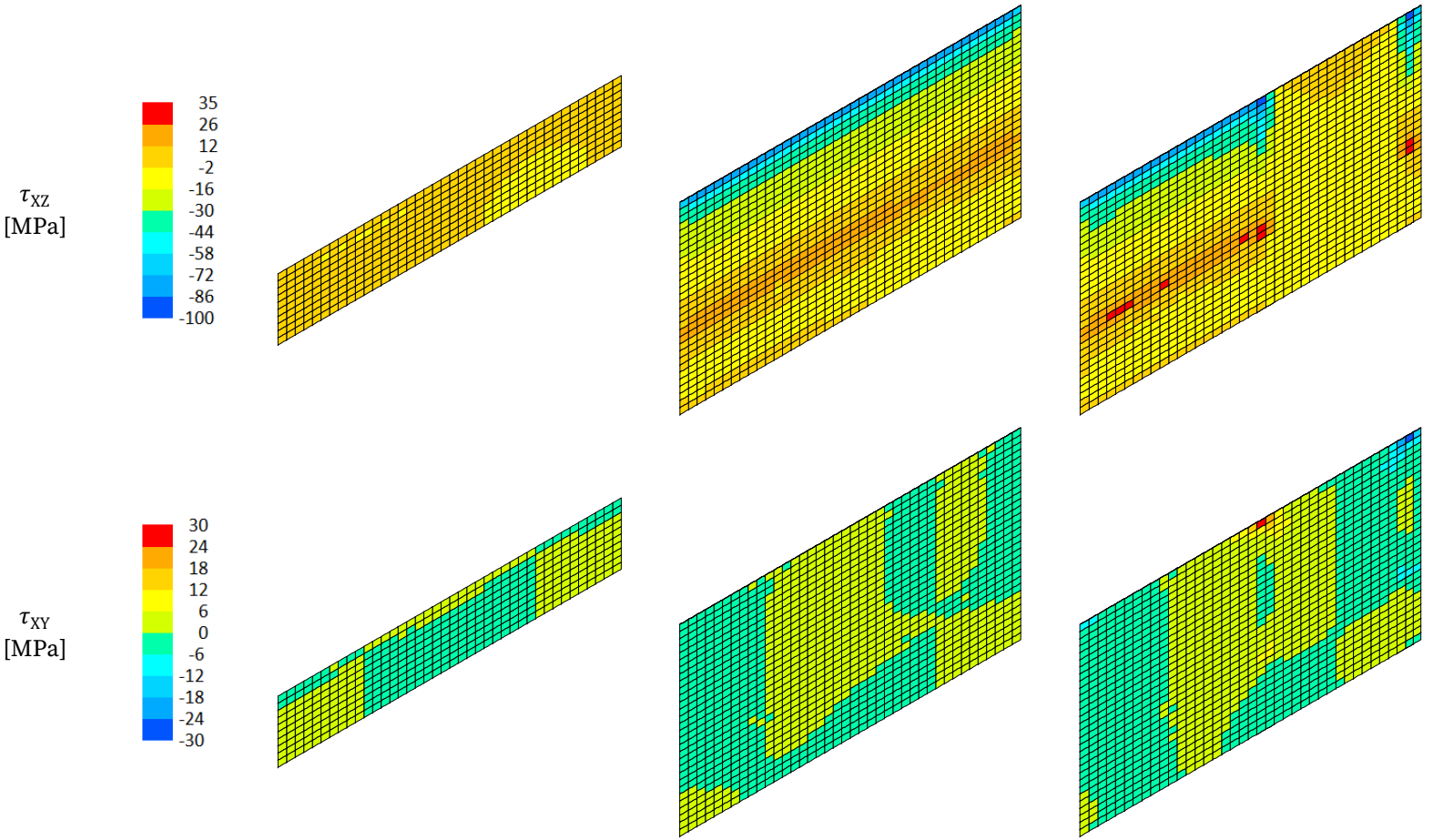

Figure 5-14. Components of the interlaminar stress vector (in structural axes) at the vertical steel-bond interface at the ISG, for models B1, B2 and B3.

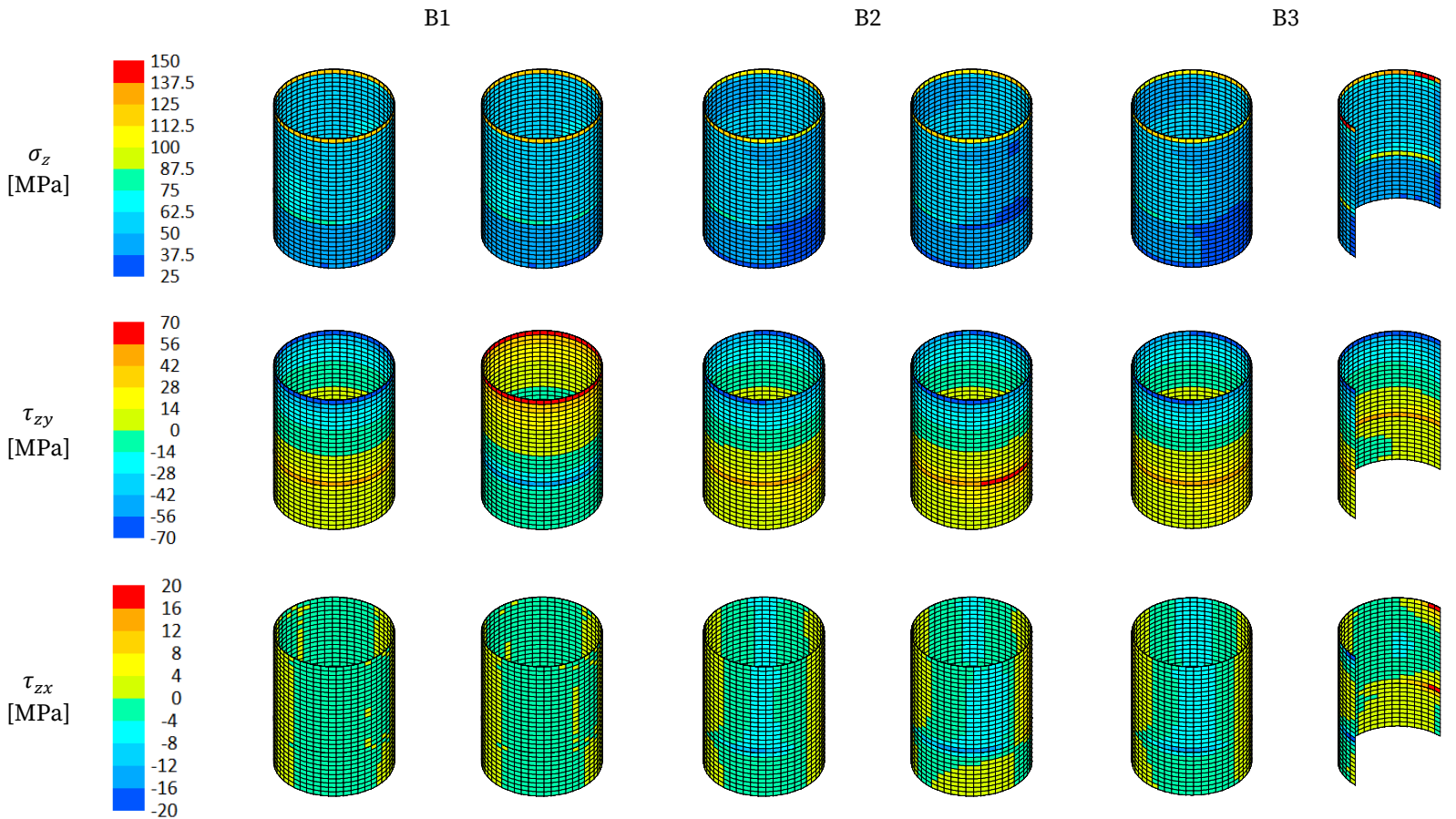

Figure 5-15. Components of the interlaminar stress vector (in local axes) at the cylindrical steel-bond interfaces in the micro-perforations, for models B1, B2 and B3.

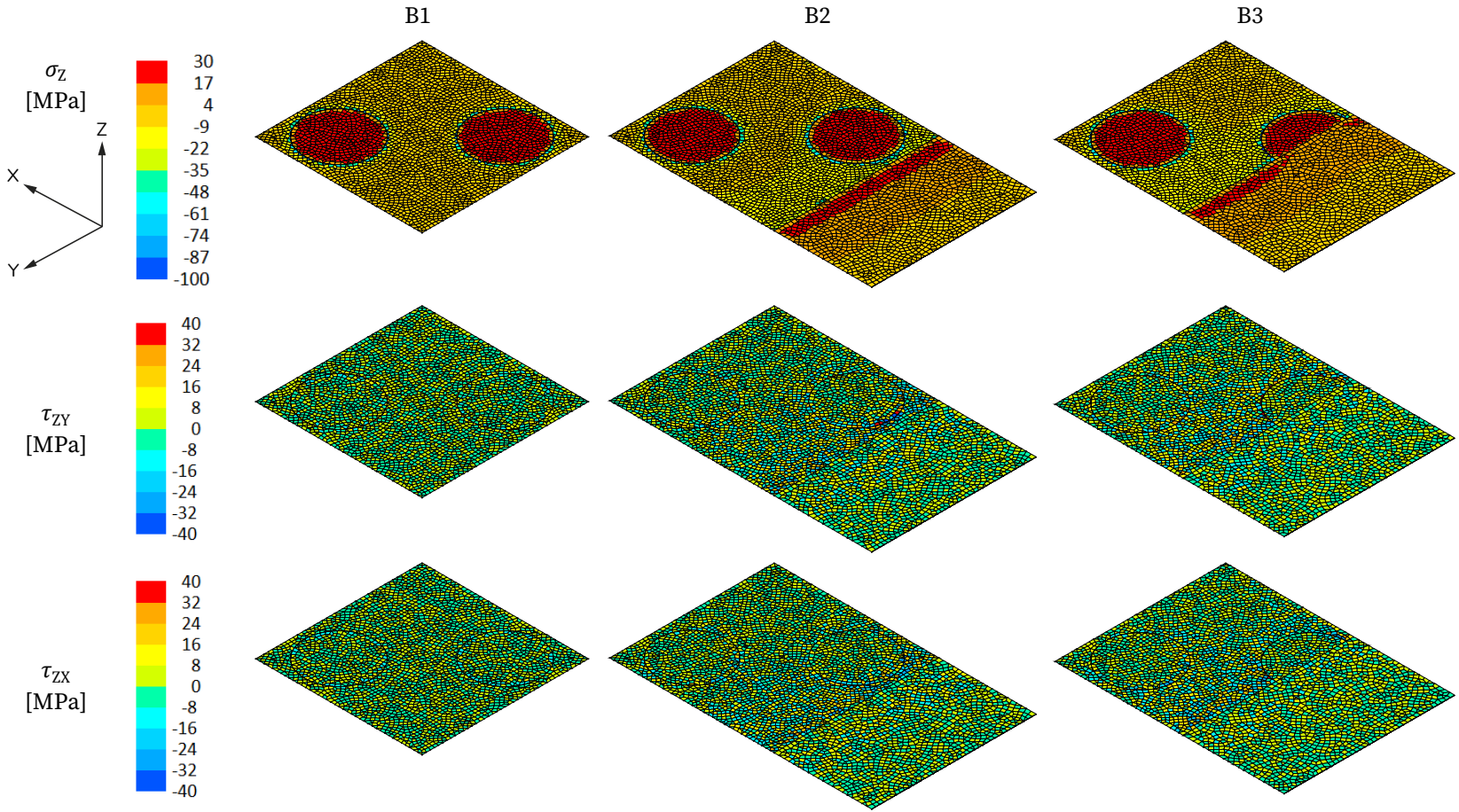

Figure 5-16. Components of the interlaminar stress vector (in structural axes) at the steel-bond horizontal interface, for models B1, B2 and B3.

the steel-bond interface which is unknown to this point. However, it does most probably take part to the initiation and propagation of the microcracks usually seen in the inter-segments gap. Their mechanism of formation, as elucidated in Chapter 3, does indeed start with a disbond at the steel-bond vertical interface that propagates straight ahead as a cohesive crack that separates the bond material filling the ISG and the bond material filling the cut micro-perforation (Figure 3-17).

The components of interlaminar stress acting in the plane of the interface were certainly less pronounced than the peel component. The interlaminar shear stress along the vertical direction of the interface (τ_{XZ}) attained its maxima (in absolute value) at the top edge of the interface, at locations where the steel strip and the bond material in the ISG contact each other. Its negative sign indicates that the bond material filling the ISG does shear downwards the vertical edge of the steel strip segment when performing its thermal shrinkage. The maximum (absolute) value of 100 MPa was more specifically found at the top corners of the cut micro-perforations in model B3. Conversely, the interlaminar shear stress along the horizontal direction of the interface (τ_{XY}) was practically null everywhere, except for model B3 where it concentrated at the top edges of the cut micro-perforations. This set of results makes it clear that the initial disbond occurs under the action of a mixed mode I/II driving force rather than under the action of a peel stress alone.

At the cylindrical steel-bond interface in the micro-perforations (and their extension in the flat bond layer), the normal component of interlaminar stress (σ_z) was again dominant and still concentrated at the top edge of the interface (Figure 5-15). Its maximum value (150 MPa) was predicted with model B3 where σ_z increased near the top corners of the cut micro-perforations. Another region of (weaker) peel stress concentration was found at the bottom surface of the steel strip, where σ_z was about 70 MPa in models

B1 and B2 and exceeded 100 MPa in the cut micro-perforation of model B3. The interlaminar shear stress along the vertical direction of the facets (τ_{zy}) was lower but concentrated at the same locations as σ_z.The interlaminar shear stress along the horizontal direction of the facets (τ_{zx}) was again practically null everywhere on the cylindrical interface, except at the top and bottom corners of the cut micro-perforations where it reached the (absolute) value of 20 MPa. This set of interlaminar stress components could lead to the failure of the steel-bond interface in the cut micro-perforations, and to microcracks in the flat bond layer starting from the bottom edge of the cut micro-perforations; two types of damage which appear in optical micrographs of cross-sections of the ISG, as illustrated in Figure 3-5 and Figure 3-7.

Lastly, the components of interlaminar stress were quite lower at the horizontal steel-bond interface, as can be seen in Figure 5-16. The maximum interlaminar peel stress σ_Z (100 MPa in absolute value) was found along the circumference of the micro-perforations, where the flat bond layer beneath the steel strip obviously exerts a localised tensile force downwards when performing its thermal shrinkage. The peel stress was much lower everywhere else. One still noticed that its sign was reversed in the micro-perforations and close to the edge of the steel strip segment in the ISG, highlighting that the bond material situated above the plane of that interface pulls the flat bond layer upwards when performing its thermal shrinkage. As for the components of interlaminar shear stress (τ_{ZY} and τ_{ZX}), they were again less pronounced than the peel component and were randomly distributed over the interface as compared to the normal component. Although the maximum values of σ_Z should still be compared to the normal peel strength of the steel-bond interface, this last set of results does already give a hint of why horizontal disbond of the steel strip has seldom been observed in practice[31].

[31] Recall that it represents maximum 7 % of the total occurrence of damage at the ISG.

5.5 Conclusion

Experimental, analytical and finite element methods were used to evaluate the thermally induced residual stress state of the multilayer.

The X-ray stress analysis demonstrated the existence of an initial compressive residual stress state in the free standing as-rolled steel strip. It was taken into account in the evaluation of the residual stress state of the co-cured steel strip which was found to be tensile, as expected. Furthermore, this technique revealed the directionality of the residual stress in the co-cured steel strip, the stress being larger in the 90° direction of the composite substrate than in its 0° direction. The responsibility of the two top orthotropic carbon laminae of the composite substrate was confirmed by the FE results, in particular when the laminate was modelled using the ply-by-ply approach.

For the same reason, the Stoney formula could not be used successfully to derive the residual stress from the curvatures which had been measured in these directions. The ellipsoidal character of the curvature does indeed also result from the influence of these weft carbon laminae neighbouring the bond and steel layers. This important consequence of the laminated nature of the composite substrate could not be taken into account in the analysis, which therefore erroneously attributed the larger (resp. smaller) curvature to a larger (resp. smaller) residual stress in the corresponding direction. The curvatures measured in the framework of this experimental method did nevertheless serve as basis for the assessment of the FE modelling of the trilayer in its primary stage (model A).

The analytical method proved more adapted, although it was also unable to predict the dependency of the stress and curvature on the direction in the trilayer plane.

Finally, the FE analyses performed on the three versions of the advanced model of the trilayer (model B) provided a detailed knowledge of the residual stress distribution in the steel and bond layers. These results did particularly well correlate with the outputs of the statistical analysis of the multilayer's damage state presented in Chapter 3. In particular, since model B3 presented the largest amount of critical stress concentration loci, it could be beneficial to avoid cutting through micro-perforations when preparing the steel strip segments.

Going one step further with the FE method would consist in performing non-linear analyses on model B so as to let fracture take place at the created interfaces, thereby using the full potential of the cohesive elements. However, this requires the critical energy release rates to be known since they represent the energy barriers that must be overcome for fracture to occur. The experimental measurement of these important physical properties is therefore the topic of the next chapter.

6. Measurement of the critical SERRs of the co-cured joint

6.1 Introduction

In the last part of the previous chapter, the outputs of the statistical analysis of the multilayer's damage state (Chapter 3) were found to be naturally related to the loci of stress concentration predicted with the finite element method.

The logical continuation of this numerical work is to let damage initiation and propagation happen at the locations where cohesive elements were placed in the FE models. This can only be accomplished if the critical energy release rates of the material are known for the different modes in which fracture is expected to occur. Indeed, the residual stress fields resulting from the previous linear elastic FE analyses may or may not initiate damage and drive its propagation: in this sense, a stress level is actually harmful only if the energy it provides is larger than the energy necessary for damage propagation.

The latter is nothing else than the critical strain energy release rate, or fracture toughness, and the present chapter is dedicated to the experimental work that was carried out in view of measuring this quantity for the co-cured joint.

A set of three LEFM tests was selected for the determination of the critical SERRs of the co-cured joint in three different fracture modes, potentially giving access to its fracture envelope. Double Cantilever Beam tests were performed to measure the pure mode I fracture toughness (G_{Ic}), End-Loaded Split tests were performed to measure the pure mode II fracture toughness (G_{IIc}), and Fixed Ratio Mixed Mode tests were performed to measure the fracture toughness of the bond loaded with a fixed combination of the previous fracture modes ($G_{I/IIc}$).

In addition, a specific type of peel test (the Fixed Arm Peel test) was selected and applied for its ability to provide a quantity comparable to the mode I fracture toughness, while being -from an industrial point of view- more easily applicable than the double cantilever beam test.

The specimens used for this work of characterisation are described in the next sub-section. The tests and the results obtained are then presented, starting with the fixed arm peel test.

6.2 Materials

Multi-layered specimens were specifically manufactured for the tests using the RTM process so as to produce a co-cured joint, the mixed RTM6/Redux 322 composition of which would as much as possible resemble that of the co-cured joint found in the composite booster casing. The peel test specimens and the beam-type LEFM test specimens are described separately in the following sub-sections.

6.2.1 Peel test specimens

The peel test specimens came from a 500 mm x 500 mm multi-layered plate with composite laminate substrate manufactured at SAB. It contained four

rectangular areas differing by the type of steel strip and its surface preparation: the steel strip was indeed either as-rolled (Figure 6-1-a) or micro-perforated (Figure 6-1-b), and *one or both* of its surfaces had been sandblasted before being degreased with isopropyl alcohol. The plate was cured with a final isotherm at 180 °C.

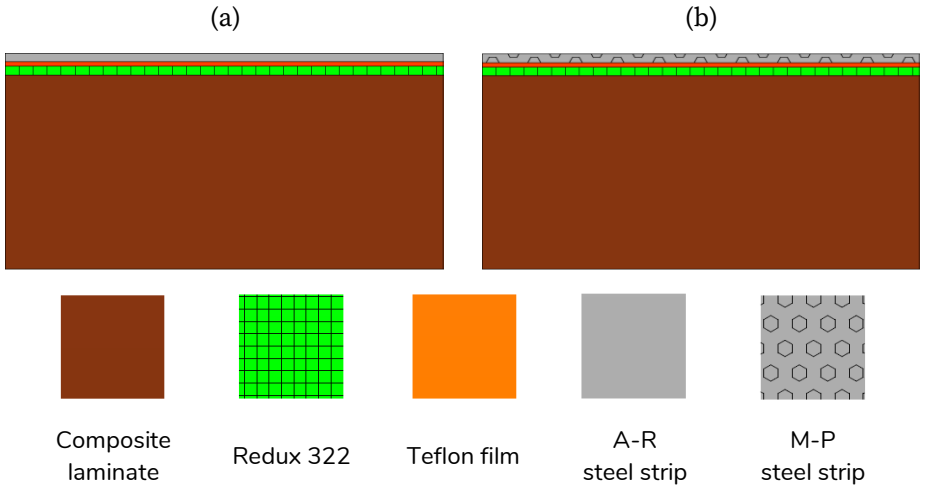

Figure 6-1. Global layup of the peel test specimens (here in the unadhered zone), (a) with as-rolled steel strip and (b) with micro-perforated steel strip.

Underneath the steel strips, the material used for the joint was everywhere one layer of Redux 322 supported adhesive film. A piece of Teflon film was placed between the adhesive film and the steel strip before co-curing to create a zone of unadhered material, but the 30 mm length originally foreseen turned out to be about 23 mm in practice. As it was found to be too short to start loading the peel arm, the initial unadhered zone of each specimen was manually extended over about 1 cm before the test.

The particular layup of the composite laminate substrate is detailed in Table 6-1. Each area of the plate was finally divided by water jet into test specimens of 160 mm x 22 mm nominal dimensions. Their width and thickness were

precisely measured with a digital Vernier calliper and a digital micrometre before the test. Note that the long side of the specimens was always aligned with the 90° reference direction of the laminate substrate, and with the TD reference direction of the as-rolled steel strip or with the RD direction of the micro-perforated steel strip[32]. A schematic peel test specimen is shown in Figure 6-2, with a reminder of these reference directions.

Table 6-1. Layup of the composite laminate substrate of the peel test specimens.

	Type of lamina	Orientation angle
1	Glass	45°
2	Weft heavy	0°
3	Weft heavy	0°
4	Balanced	45°
5	Warp heavy	0°
6	Warp heavy	0°
7	Balanced	45°
8	Warp heavy	0°
9	Warp heavy	0°
10	Balanced	45°
11	Weft heavy	0°
12	Weft heavy	0°
13	Glass	45°

Part of the peel test specimens were tested within a short period of time from their reception, after several days conditioning in the test room atmosphere (~23 °C and ~55 %RH). Another part was tested three years later, after normal ageing and several days conditioning in the test room atmosphere. The

[32] This difference in positioning of the steel strips was not intended: the primary intention was to have the RD reference direction aligned with the long side of the specimens for both types of steel strip. This should however not matter as long as the actual alignment of the steel strip is taken into account in the definition of its mechanical properties used in the processing of the peel test results.

last part was finally tested after three years of normal ageing and 168 hours conditioning by immersion in distilled water at 23 °C. These sets of specimens will thus respectively be called “fresh”, “3 years aged”, and “3 years aged + immersed”. At least two specimens were tested for each type of layup and conditioning, the exact numbers being reported in Table 6-2.

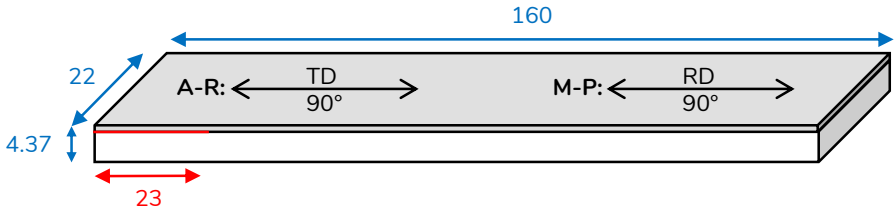

Figure 6-2. Geometry, nominal dimensions (in mm) and reference directions of the peel test specimen (the 90° direction of the composite substrate has been defined in Figure 1-13).

6.2.2 Beam-type LEFM tests specimens

The LEFM tests specimens came from a 500 mm x 500 mm x 10.12 mm multi-layered sandwich plate with composite laminate substrates manufactured at ÉireComposites (Ireland). It was also cured with a final isotherm at 180 °C. Two different layups were used within this plate, which are shown in Figure 6-3-a and Figure 6-3-b. They actually differ by the design of the inner co-cured joint which deserves some explanation. In the regions to be tested, it was formed by four layers of Redux 322 adhesive film in its *unsupported* version, i.e. *without* nylon mesh (Redux 322U in Figure 6-3-a). These were carefully assembled so as to avoid the presence of air pockets trapped between the films. The uniformity of the bond line thickness was taken care of elsewhere by replacing these layers with four layers of *supported* Redux 322 adhesive film at locations of the plate which would not be tested (Figure 6-3-b). The nylon mesh of Redux 322 was thus used as an intrinsic spacer. Besides, strips of FEP release film were placed at the plate’s mid-plane in order to create a 70 mm long unadhered zone at one end of each specimen (Figure

6-3-b). This created the initial cantilever arms, and helped pre-defining the plane of propagation of the crack.

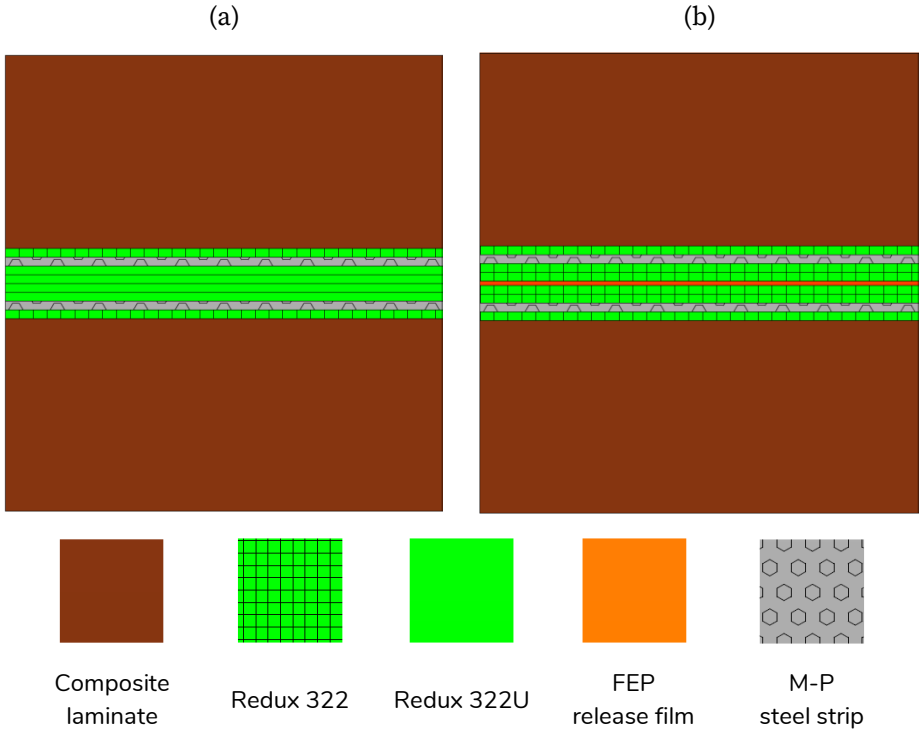

Figure 6-3. Layup used for the manufacturing of the sandwich plate in which the DCB specimens were cut: (a) with Redux 322U in the regions to be tested, (b) with Redux 322 outside the regions dedicated to the tests, in particular here in the originally unadhered zone.

The layups were otherwise symmetrical with respect to the plate's mid-plane. The composite laminate layup was the same as that used in the booster casing (Table 1-1), and micro-perforated steel sheets –whose faces had been sandblasted and degreased with isopropyl alcohol- were placed on either side of the inner co-cured bond with their rolling direction parallel to the 0° direction of the laminates. The plate was finally divided using an air-cooled circular diamond saw into test specimens of 175 mm x 20 mm nomi-

nal dimensions, the long side of which was aligned with the 0° direction of the laminates. A schematic LEFM test specimen is shown in Figure 6-4.

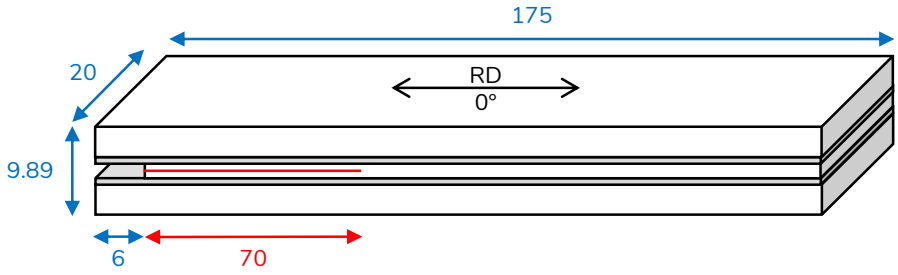

Figure 6-4. Geometry, nominal dimensions (in mm) and reference directions of the DCB test specimen (the 0° direction is the warp direction of the composite substrates, as defined in Figure 1-13).

The specimens' width and thickness were precisely measured with a digital Vernier calliper and a digital micrometre. Then, both of their long edges were painted with water based white correction fluid (Tipp-Ex ecolutions, BiC) before being marked with graduations drawn every 1 mm with a fine permanent marker, starting from the end of the non-adhesive insert. Finally, load blocks were glued on one or both sides of the pre-cracked end of each fracture specimen, as explained in the subsequent sections describing the experimental procedure of the three LEFM tests. A fracture specimen prepared for the DCB test can be seen in Figure 6-5.

Figure 6-5. Beam-type LEFM test specimen prepared for the DCB test.

Some specimens were tested shortly after they were produced, after several days conditioning in the test room atmosphere (~23 °C and ~55 %RH). The same tests were repeated one year later, after normal ageing and several days conditioning in the test room atmosphere. The first set of specimens will thus be called “fresh” while the second set will be called “1 year aged”.

6.3 Adhesive fracture energy of the co-cured bond measured with the Fixed Arm Peel test

Peel tests have been introduced in Chapter 2 (Section 2.4.3), where it has been emphasized that the measured peel strength must be converted into the adhesive fracture energy (G_a, the expression of which is recalled in Eq. (6-1)) in such a way that it becomes independent of the energy spent in the usually heavy plastic deformation of the peel arm(s). Peel testing is quite popular in the industrial sector; peel tests are available in a series of configurations (Figure 2-17), among which the Fixed Arm Peel test chosen in this work. The associated experimental procedure is described below.

6.3.1.1 Experimental procedure

The fixed arm peel test consists in pulling at a constant speed and with a constant angle on a flexible peel arm, while the bottom arm (in other words, the substrate) is fixed to a mobile platform so that the specimen is free to slide in the horizontal direction during the test. The peel force P continuously recorded during the test and the specimen width B are then used for the calculation of the peel strength, which is next transformed into the total input energy via the use of the peel angle θ (Eq. (2-58)), assuming that the tensile corrections accounted for in Eq. (2-59) are negligible [104].

$$G_a = \left[\frac{P}{B}(1-\cos\theta)\right] - G_{db} \tag{6-1}$$

The evaluation of G_{db}, the energy dissipated in plastic bending of the peel arm, does, on the other hand, involve the use of the elastic-plastic large-displacement beam theory, and requires the knowledge of the tensile stress-strain characteristics of the peel arm material, as addressed in Chapter 2. The *ICPeel (2006)* Microsoft Excel spreadsheet provided along with the test protocol[33] allows performing these operations and the conversion from peel strength to adhesive fracture toughness. The values of DRF and ε_{max} (that are the basis of the acceptance criteria described in Chapter 2) are calculated in the same spreadsheet.

In practice, the specimen was clamped at both ends onto a horizontal platform sliding on a rail fixed to the frame of a universal testing machine (Instron, USA), as illustrated in Figure 6-6.

Figure 6-6. Peel test specimen being peeled off at 90° with the fixed arm peel test apparatus mounted on the test bench of a universal testing machine.

[33] Both can be downloaded free of charge from the Imperial College website. (*https://www.imperial.ac.uk/mechanical-engineering/research/mechanics-of-materials/composites-adhesives-and-soft-solids/adhesion/test-protocols*)

In accordance with the protocol, the test was conducted at 90° with a peel test speed of 10 mm/min applied to the peel arm by the crosshead via a pin hole previously drilled in the steel strip. A 1 kN load cell was used to measure the peel force during the tests on "fresh" and "3 years aged" specimens. Given the small loads recorded in these tests, a 100 N load cell was used instead for the tests on "3 years aged + immersed" specimens and it was shown on this occasion that equivalent results were obtained with both load cells.

The peel force was recorded up to at least 65 mm crosshead displacement, and its plateau value was calculated between 15 mm and 65 mm crosshead displacement for each specimen. The *ICPeel* spreadsheet was then used to perform the conversion from peel force to adhesive fracture toughness. In accordance with the test protocol, the tensile stress-strain curves of the as-rolled steel strip and the micro-perforated steel strip were fitted with a bi-linear work hardening model following Eq. (6-2), as shown in Figure 6-7. In the equation, α is the work hardening coefficient given by the ratio of the plastic modulus E_p (i.e. the slope of the tensile curve in the plastic region starting at an initial guess of the yield point) and the modulus of elasticity E_e. The pair (ε_y,σ_y) defines the yield coordinates which are found at the intersection of the lines fitting the elastic and the plastic regions of the tensile curve.

$$\begin{cases} \sigma = E_e\varepsilon & \varepsilon \leq \varepsilon_y \\ \sigma = \sigma_y + \alpha E_e(\varepsilon - \varepsilon_y) & \varepsilon > \varepsilon_y \end{cases} \tag{6-2}$$

The bi-linear fit parameters are given in Appendix L for both reference directions of both types of steel strip, although only the sets corresponding to the transverse direction of the as-rolled steel strip and the rolling direction of the micro-perforated steel strip have actually been used in the present case. Note that the normally negative values of the fit parameters E_p and α obtained for the as-rolled steel strip were set to zero, as prescribed by the test protocol. In

this case, the yield coordinates are those of the approximate yield point given as initial guess in the bi-linear fit procedure.

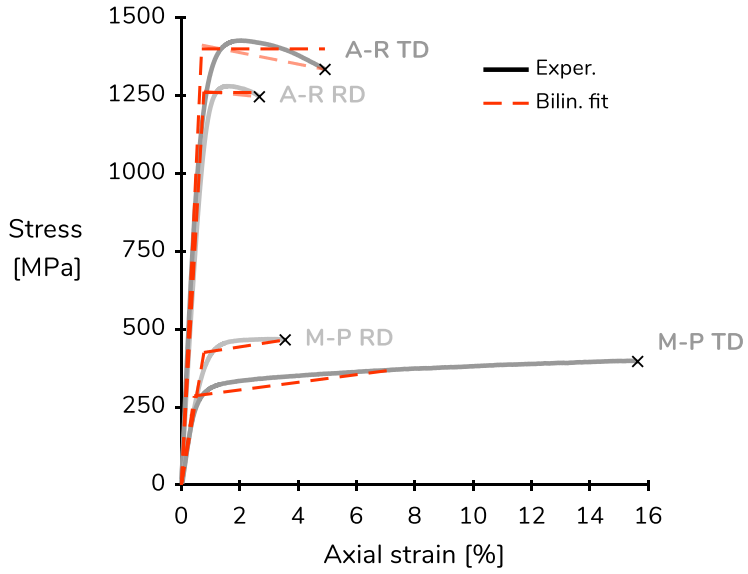

Figure 6-7. Bi-linear fit of the nominal stress-strain curves of the as-rolled and micro-perforated steel strips measured in both reference directions.

To complete the acquisition of experimental data, the fracture surfaces were observed under polarised light with the 5x objective lens of a DSX510 digital microscope (Olympus, Japan). Optical micrographs were thereby produced, covering a large area of about 22 mm (specimen width) x 12 mm (in the peel direction).

6.3.1.2 Peel strengths and adhesive fracture energies obtained with the Fixed Arm Peel test

Peel strength versus crosshead displacement traces were derived from the experimental data obtained with the fixed arm peel test. Typical ones are shown in Figure 6-8 where the display was limited to two curves per specimen type and conditioning, for the sake of readability. Besides, typical frac-

ture surfaces are shown in Figure 6-9 for the specimens with as-rolled steel strip and in Figure 6-10 for the specimens with micro-perforated steel strip. These optical micrographs bring essential information regarding the 90° peel bond failure mechanism and its evolution with conditioning. Finally, important numerical results are gathered in Table 6-2, among which the adhesive fracture energy. The following analysis and discussion of the fixed arm peel test results is based on these three types of data.

Let us underline at once that both acceptance criteria (Eq. (2-61)) were satisfied for all specimen types and conditioning since G_p/G is always lower than 85 % and $\varepsilon_{\max}$ is always lower than 4 % in Table 6-2. This validated the use of the fixed arm peel test and the *ICPeel* spreadsheet to determine the adhesive fracture energy of our flexible laminates. *ICPeel* predicted zero energy dissipation in plastic bending of the peel arm for the "3 years aged" and the "3 years aged + immersed" specimens with as-rolled steel strip. This was confirmed by visual observation of the peel arm residual curvature after the test: the steel strips with both faces sandblasted were indeed totally flat while the strips with one single face sandblasted presented their original slight curvature caused by the asymmetric sandblasting treatment.

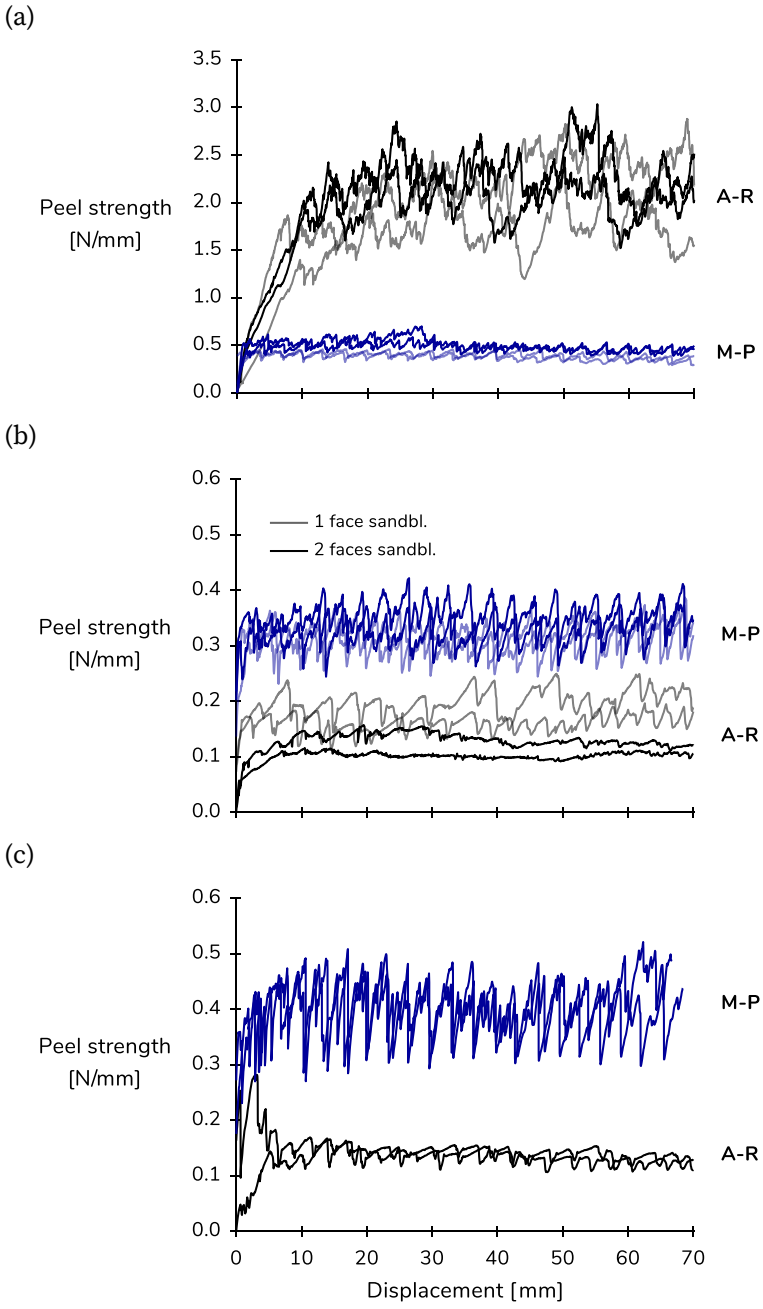

Figure 6-8. Peel strength versus crosshead displacement measured with the fixed arm peel test on (a) fresh, (b) "3 years aged" and (c) "3 years aged + immersed" specimens.

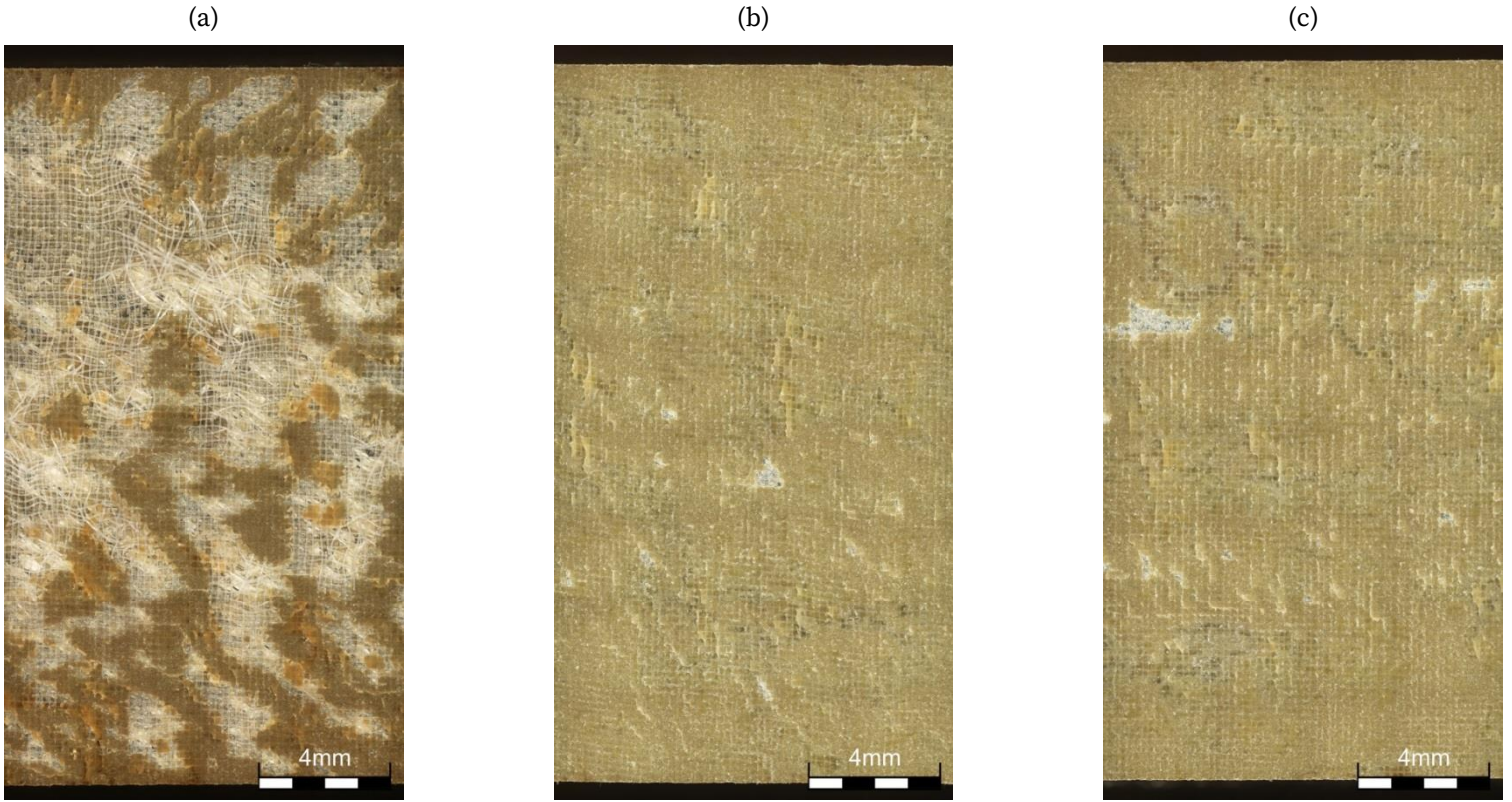

*Figure 6-9. Optical micrographs of typical fracture surfaces observed after peeling at 90° of (a) fresh, (b) "3 years aged", and (c) "3 years aged + immersed" specimens with **as-rolled** steel strip sandblasted on both faces. The peel direction is left to right.*

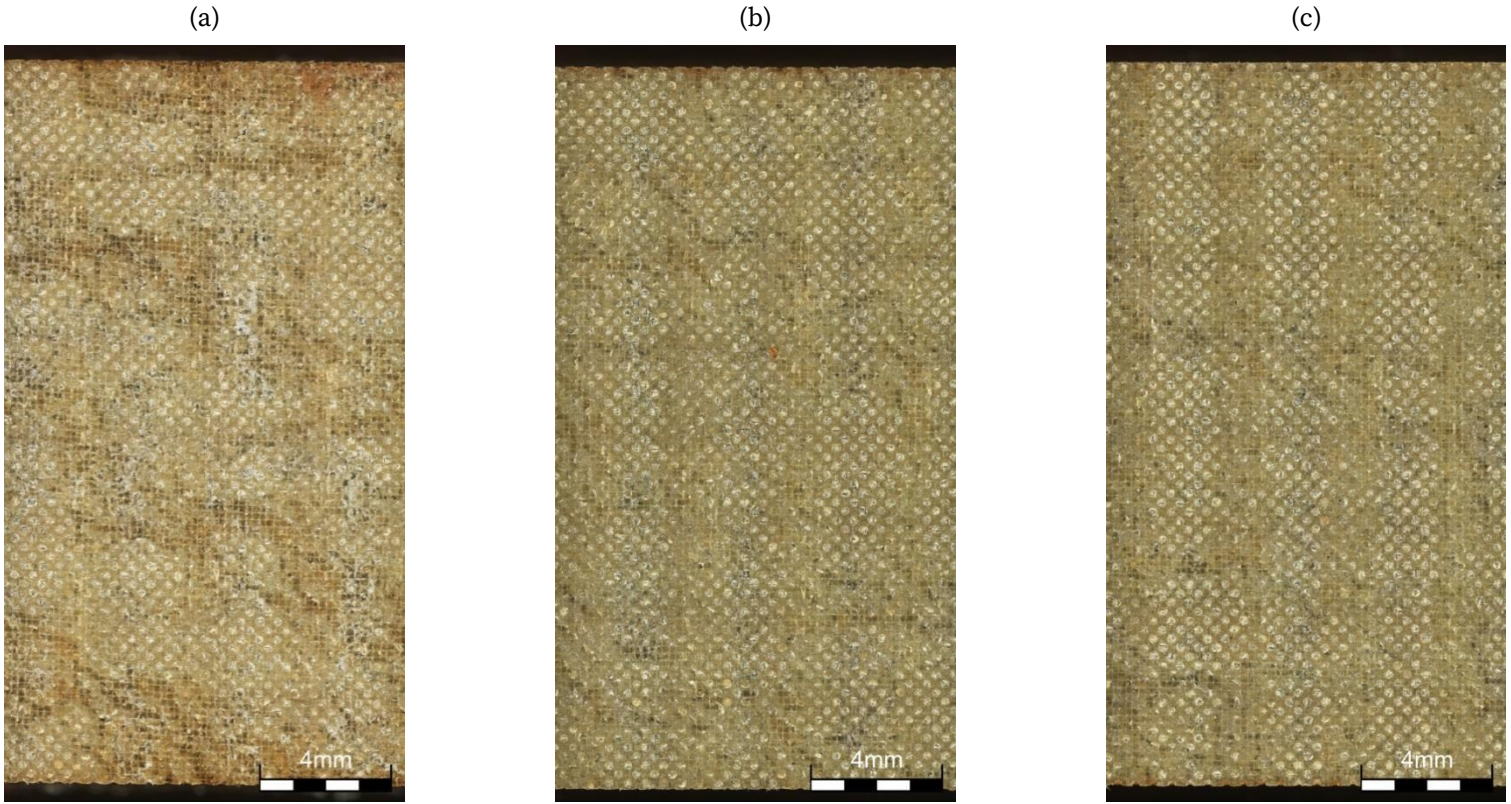

*Figure 6-10. Optical micrographs of typical fracture surfaces observed after peeling at 90° of (a) fresh, (b) "3 years aged", and (c) "3 years aged + immersed" specimens with **micro-perforated** steel strip sandblasted on both faces. The peel direction is left to right.*

Table 6-2. Mean values (and standard deviation) of the peel force and peel strength measured with the fixed arm peel test at an angle of 90°, and of the adhesive fracture energy, the plastic correction (DRF) and the maximum bending strain calculated with the ICPeel spreadsheet.

Specimen type	# specimen	Peel force [N]	Peel strength [Nmm^{-1}]	G_A [Jm^{-2}]	G_p/G [%]	$\varepsilon_{\max}$ [%]
Fresh						
A-R S1F	2	44.8 (7.4)	2.03 (0.33)	827 (54)	59	1.69
A-R S2F	2	49.2 (1.2)	2.22 (0.05)	857 (8)	61	1.77
M-P S1F	2	8.53 (0.48)	0.38 (0.19)	228 (5)	41	1.42
M-P S2F	2	10.9 (0.3)	0.49 (0.02)	250 (3)	49	1.60
3 years aged						
A-R S1F	3	3.67 (0.66)	0.17 (0.03)	167 (30)	0	0.49
A-R S2F	4	2.82 (0.62)	0.13 (0.03)	127 (28)	0	0.43
M-P S1F	4	7.48 (0.78)	0.34 (0.04)	216 (9)	36	1.33
M-P S2F	5	8.04 (0.97)	0.36 (0.04)	222 (10)	38	1.38
3 years aged + immersed						
A-R S2F	2	3.03 (0.04)	0.14 (0.00)	137 (2)	0	0.45
M-P S2F	2	8.85 (0.24)	0.40 (0.01)	231 (2)	42	1.45

6.3.1.2.1 Effect of the type of peel arm in « fresh » specimens

It transpires from Figure 6-8-a that fresh specimens with as-rolled steel strip reached higher steady-state peel strengths than fresh specimens with micro-perforated steel strip. This translated into G_A reaching 857 Jm^{-2} in the first case, versus 250 Jm^{-2} in the second case. Such dramatic difference in adhesive fracture energy correlates well with the observed fracture surfaces. On the one hand, the optical micrograph in Figure 6-9-a reveals a mix of adhesive and (predominantly) cohesive fracture for the specimen with as-rolled steel strip. Most importantly, in the areas where cohesive fracture occurred, the nylon mesh supporting the Redux 322 adhesive film appears severely

damaged. *Tearing* of the nylon mesh was indeed observed during the peel test on these specimens. It gave rise to sharp increases in the peel force at the extension and breakage of the nylon fibres bridging between the substrate and the peel arm (see the jagged aspect of the related curves in Figure 6-8-a). On the other hand, the micrograph in Figure 6-10-a reveals a totally different type of fracture surface for the specimen with the micro-perforated steel strip, with the micro-perforation pattern clearly appearing at many places. It was shown with 3D micrographs of the peel arm obtained at larger magnification (with a 50x objective lens, see Figure 6-11) that (i) the fracture plane was at the joint/peel arm interface and (ii) the bond material in the micro-perforations failed cohesively under 90° peeling. Fracture was thus again predominantly cohesive thanks to the presence of the micro-perforations, but this time exempt from tearing of the supporting nylon mesh.

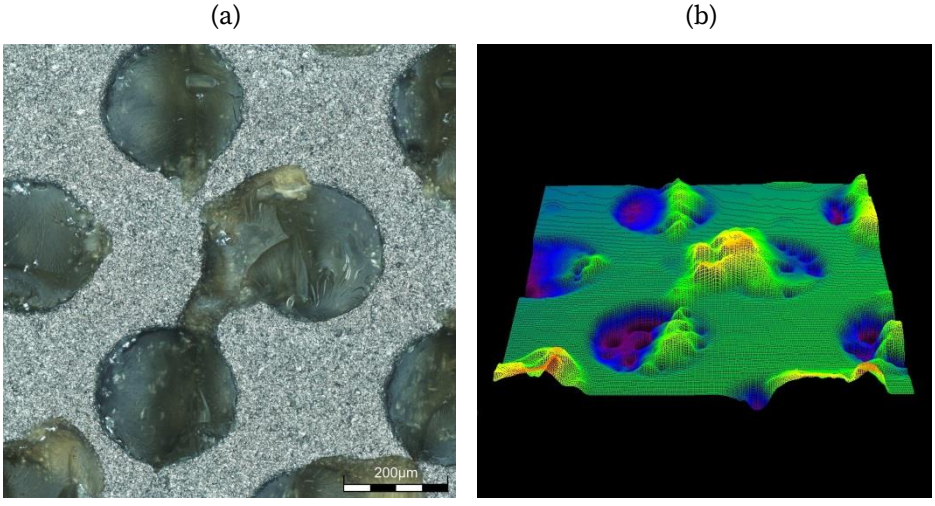

Figure 6-11. (a) Optical micrograph of the fracture surface of the micro-perforated peel arm of a fresh specimen, revealing cohesive failure of the bond material in the micro-perforations. (b) 3D color map of the optical micrograph shown in (a), with height scale going from 0 mm (purple) to 0.144 mm (orange). The peel direction is left to right.

In conclusion, the energy dissipated in the tearing of the nylon mesh beneficially contributed to an increase of the adhesive fracture energy by more than 240 % for specimens with as-rolled steel strip. Nevertheless, the adhesive fracture energy of 228-250 Jm^{-2} associated with the 90° peeling of the micro-perforated steel strip on fresh specimens is more likely to be representative of the fracture toughness of the fresh bond material. It furthermore compares well with values of mode I fracture toughness reported in the literature for cohesive fracture of pure RTM6 (e.g. 216 Jm^{-2} in [176]) and pure Redux 322 (e.g. [250; 434] Jm^{-2} depending on the type of fracture test in [177]).

The absence of nylon mesh breakage in specimens with micro-perforated steel strip could be explained by either or both of these hypotheses: (i) the composition of the bond material is richer in resin than in adhesive which is "flushed away" through the micro-perforations during the injection process; (ii) at the peel front, stress concentration at the micro-perforations favours fracture in their close vicinity, with a fracture plane being thereby closer to the steel strip surface than to the nylon mesh.

Finally, the influence of the type of sandblasting treatment was as expected: steel strips sandblasted on both faces are flat and require more energy for being peeled off than steel strips sandblasted on one single face, the curvature of which naturally tends to help the peeling process.

6.3.1.2.2 Effect of three years normal ageing

Figure 6-8 b presents a very interesting fact: the peel strength of specimens with as-rolled steel strip severely decreased by an order of magnitude after three years ageing in normal conditions, while that of specimens with micro-perforated steel strip was only very slightly impacted by ageing. The trend in terms of adhesive fracture energy was thus found to be reversed after normal ageing: aged specimens with micro-perforated steel strip had a maximum G_A of 222 Jm^{-2}, versus 167 Jm^{-2} for aged specimens with as-rolled steel strip. This

represents a respective decrease of about 10 % and 80 % with respect to the values determined for their fresh equivalents.

This difference was readily explained by examination of the fracture surfaces shown in Figure 6-9-b and Figure 6-10-b. On the one hand, the fracture surface of the "3 years aged" specimen with as-rolled steel strip is spectacularly different from that of its fresh counterpart. The surface is smooth and still covered with adhesive practically everywhere, indicating adhesive failure of the bond under 90° peeling of the as-rolled steel strip. Above all, there is no tearing of the nylon mesh which appears to be intact everywhere even at the small locations of cohesive failure. It can thus be understood that the adhesion of the as-rolled steel strip considerably decreased with normal ageing, which caused adhesive failure of the bond to occur almost exclusively during the test and prevented the beneficial occurrence of the nylon mesh breakage. On the other hand, the fracture surface of the "3 years aged" specimen with micro-perforated steel strip does, on the contrary, strongly resemble that of its fresh counterpart. The fracture plane is still at the joint/peel arm interface, producing cohesive failure of the bond material inside the micro-perforations. The latter did thus really fulfil their role of mechanical anchors. The relatively small decrease in G_A after three years of ageing would moreover indicate that the toughness for cohesive fracture of the bond material is quite stable over time.

6.3.1.2.3 Effect of 168 hours immersion in distilled water

Lastly, the comparison of the curves drawn in Figure 6-8-b and Figure 6-8-c shows that "3 years aged" and "3 years aged + immersed" specimens developed practically the same steady-state peel strength. Hence, immersion in distilled water for 168 hours before testing did not have a particular influence on the peel strength of the flexible laminates. The fracture surfaces of the immersed specimen with micro-perforated steel (Figure 6-10-c) and its "dry"

counterpart (Figure 6-10-b) also appear strictly identical. For the specimen with as-rolled steel strip, the fracture surfaces of the immersed specimen (Figure 6-9-c) look very similar to that of the dry specimen (Figure 6-9-b). A small difference is observed at longer range, though: the small locations of cohesive failure were found concentrated close to the mid-width of the immersed specimen while they were randomly spread over the width of the dry specimen. Still, the adhesive fracture energy of the immersed specimens was slightly higher than their "dry" counterparts, namely 137 Jm^{-2} vs. 127 Jm^{-2} for the specimens with as-rolled steel strip and 231 Jm^{-2} vs. 222 Jm^{-2} for the specimens with micro-perforated steel strip. This minor increase may however be related to the higher sensitivity of the load cell used to record the peel force in this last set of measurements.

6.4 Mode I critical SERR of the co-cured joint measured with the Double Cantilever Beam test

The Double Cantilever Beam test has been introduced in Chapter 2 (Section 2.4.2) as one of the most popular laboratory test methods used for determining mode I critical strain energy release rates. The DCB test specimen is a beam of thickness $2h$ which separates at one end into two beams of thickness h, called the *cantilever arms* (Figure 2-14). The specimen's arms are gradually and symmetrically separated during the test so as to trigger crack initiation and promote crack propagation under tensile opening loading conditions, i.e. mode I. G_{Ic} is then basically derived from the rate of change of the specimen compliance measured during crack growth. The data reduction schemes being based on *linear elastic* fracture mechanics (as described in Chapter 2), it is fundamental that the arms undergo *no plastic deformation* during the test.

6.4.1 Experimental procedure

Several standards do exist and set the frame for the consistent realisation of the DCB test with various types of specimen (see Section 2.4.2.2). In particular, the ISO standard (ISO 25217:2009(E), [82]) was predominantly followed for designing the present DCB specimens, conducting the fracture tests and performing part of the mode I strain energy release rate analysis.

Firstly, stainless steel piano hinges were glued with ethyl cyanoacrylate adhesive (Loctite SUPER GLUE-3, Henkel) on both sides of the pre-cracked end of each DCB specimen, where the composite surface had preliminary been manually abraded with SiC paper and cleaned with ethanol. Then, the tabs of the top and bottom hinges were inserted in the grips of a universal testing machine (Instron, USA), which were tightened manually until the specimen was found to be held horizontally, as in Figure 6-12-a. Once the test started, the top arm was pulled up at the constant crosshead speed of 1 mm/min, gradually forcing the separation of the cantilever arms as shown in Figure 6-12-b. The load was meanwhile continuously recorded with a 1 kN load cell, allowing to draw the load-displacement response.

One graduated face of the specimen was illuminated and observed with a magnifying glass all along the test. At a given opening, a crack was seen to start extending from the graduation zero. This was stated out loud in the test room so as to be recorded by a digital voice recorder started *simultaneously* with the test. As recommended in the standards, the initial unadhered area was first extended over about 6 mm before unloading the specimen, thereby forming a natural mode I pre-crack. The test and voice recorder were then resumed; the crack growth was carefully followed and its progression was reported out loud as often as possible, i.e. about every millimeter when the propagation was stable. The test was pursued at least until the crack reached the graduation marking 75 mm of propagation.

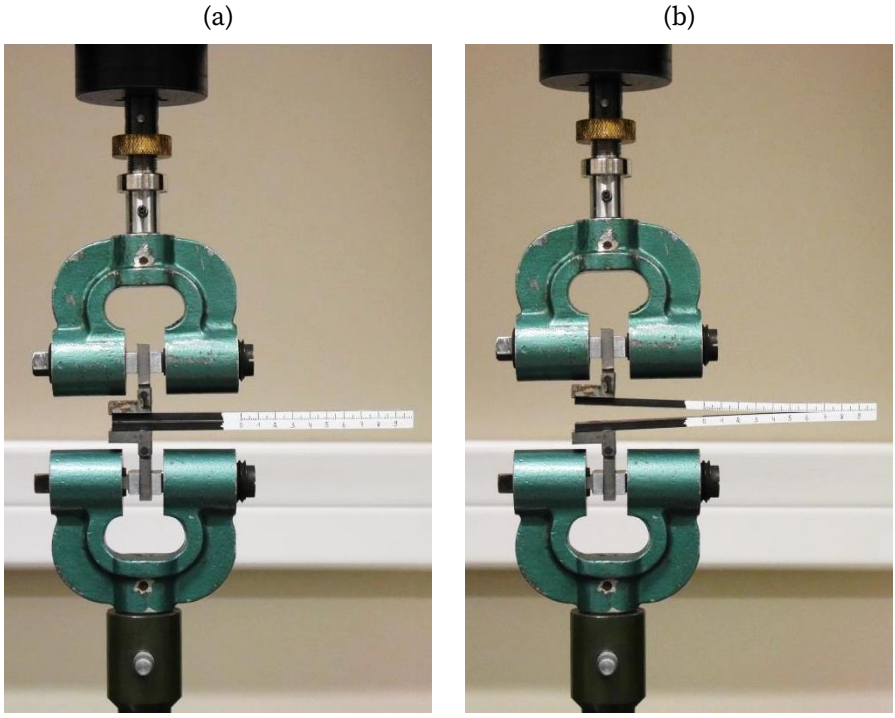

Figure 6-12. DCB specimen with piano hinges (a) held horizontally in the grips of a universal testing machine before the test, (b) being tested.

After the test campaign, the recordings were listened to so as to extract the information concerning the crack length and the corresponding time. Then, machine times coinciding with the digital recorder sample of times were automatically detected in the raw data file with a specially written Matlab script which finally formed the precious (opening; load; crack length) triplets of experimental data.

Note that, in accordance with the ISO standard, all displacements were corrected for the $4.85\ 10^{-4}$ mmN^{-1} system compliance. The latter was determined from four load-displacement responses obtained by testing a stiff steel beam of cross-section 25 mm x 12 mm in the DCB test configuration. These tests were performed up to a load of 300 N, which goes beyond the maximum load

reached in the tests on the actual composite specimens. This correction could yet have been omitted given the relatively small load level developed during the DCB tests.

Finally, the fracture surfaces were again observed under polarised light with a 5x objective lens in a DSX510 digital microscope (Olympus, Japan). Optical micrographs were thereby produced, covering a large area of about 20 mm (specimen width) x 12 mm (in the crack growth direction).

The whole procedure described for the cantilever beam test was performed a number of times as part of the learning curve in the domain of LEFM testing. The results obtained with three fresh and three “1 year aged” specimens were retained for the mode I critical energy release rate analysis.

6.4.2 Load-displacement curves and fracture surfaces

The load-displacement curves obtained with the double cantilever beam test are drawn in Figure 6-13-a. Note that the displacement is the crosshead displacement which in fact corresponds to the distance separating the top and bottom loading points found on the external surfaces of the arms. The load-displacement responses can generally be read as follows: the specimen arms are first separated by elastic deformation in an initial stage of loading (2 in Figure 6-13-a), then *crack initiation* occurs from a given amount of separation. This gives rise to *crack propagation* upon continuation of loading (3 in Figure 6-13-a), where the curve presents a descending slope as the specimen compliance increases along with the length of the crack.

In Figure 6-13-b the *crack monitoring points* have been superimposed to one of the experimental curves. They represent points at which the crack advance was recorded. *Crack initiation points* are marked as well, following two definitions given in the standard. These are the *non-linear* initiation point where the curve starts deviating from its initial compliance C_0, and the *Max/5 %*

offset initiation point where the curve's compliance is 5 % above its initial value[34]. In the course of an international round-robin, the first one was seen to give the most conservative load value while the second one was seen to give the best repeatability [178].

Besides, typical fracture surfaces of the top and bottom arms are shown in Figure 6-14 for the fresh specimens and in Figure 6-15 for the "1 year aged" specimens. These optical micrographs do again bring essential information regarding the bond failure mechanism and its evolution with conditioning. Finally, mean propagation values of G_{Ic} derived with various data reduction schemes are gathered in Table 6-3. The following analysis and discussion of the mode I double cantilever beam test results is based on these three types of information.

First of all, the crack oscillated between stable and unstable growth during the test, with usually rapid crack propagation at the start followed by some *moderate* unstable "stick-slip" crack propagation events[35], responsible for the bumped aspect of the load-displacement curves shown in Figure 6-13-(a).

[34] It is replaced by the point at maximum load if this one occurs first.
[35] Where the crack grows in a « series of rapid bursts, interspaced by periods of crack arrest » [78].

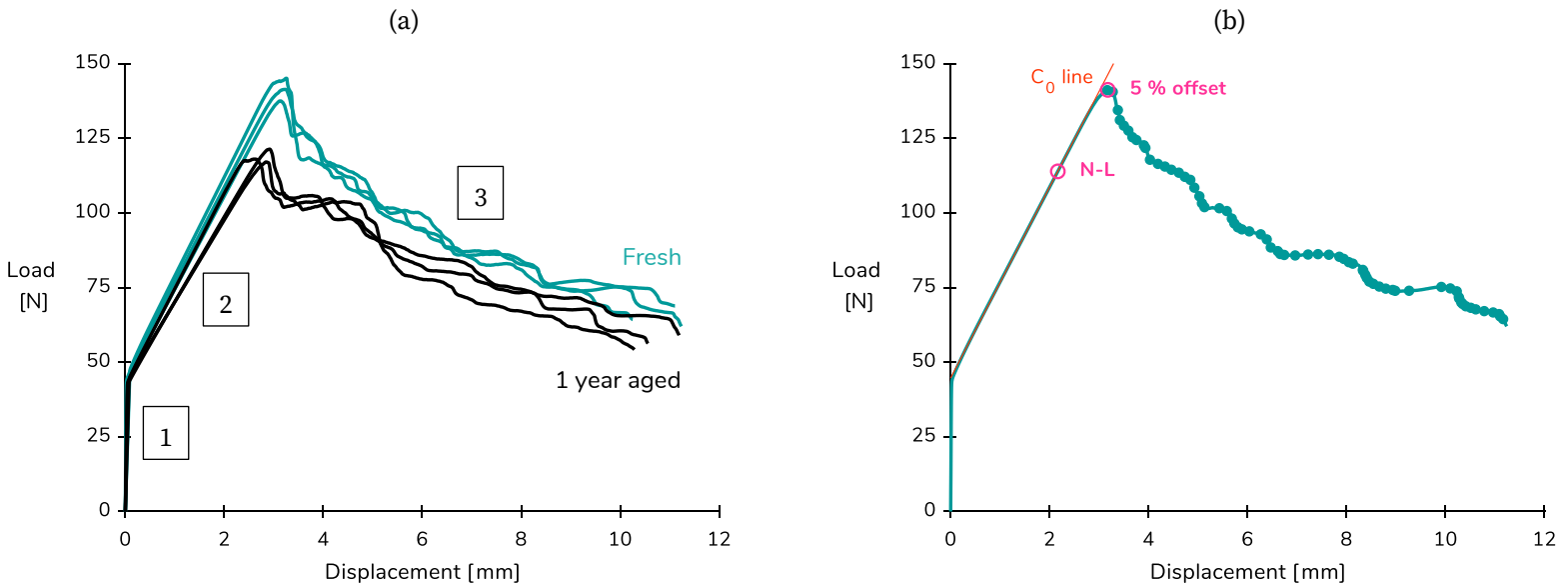

Figure 6-13. (a) Load-displacement curves obtained with the double cantilever beam test performed on fresh and "1 year aged" specimens, (b) Load-displacement curve and crack monitoring points obtained with the double cantilever beam test performed on one fresh specimen. The points corresponding to crack initiation are marked with empty circles and the points corresponding to crack propagation are marked with filled circles.

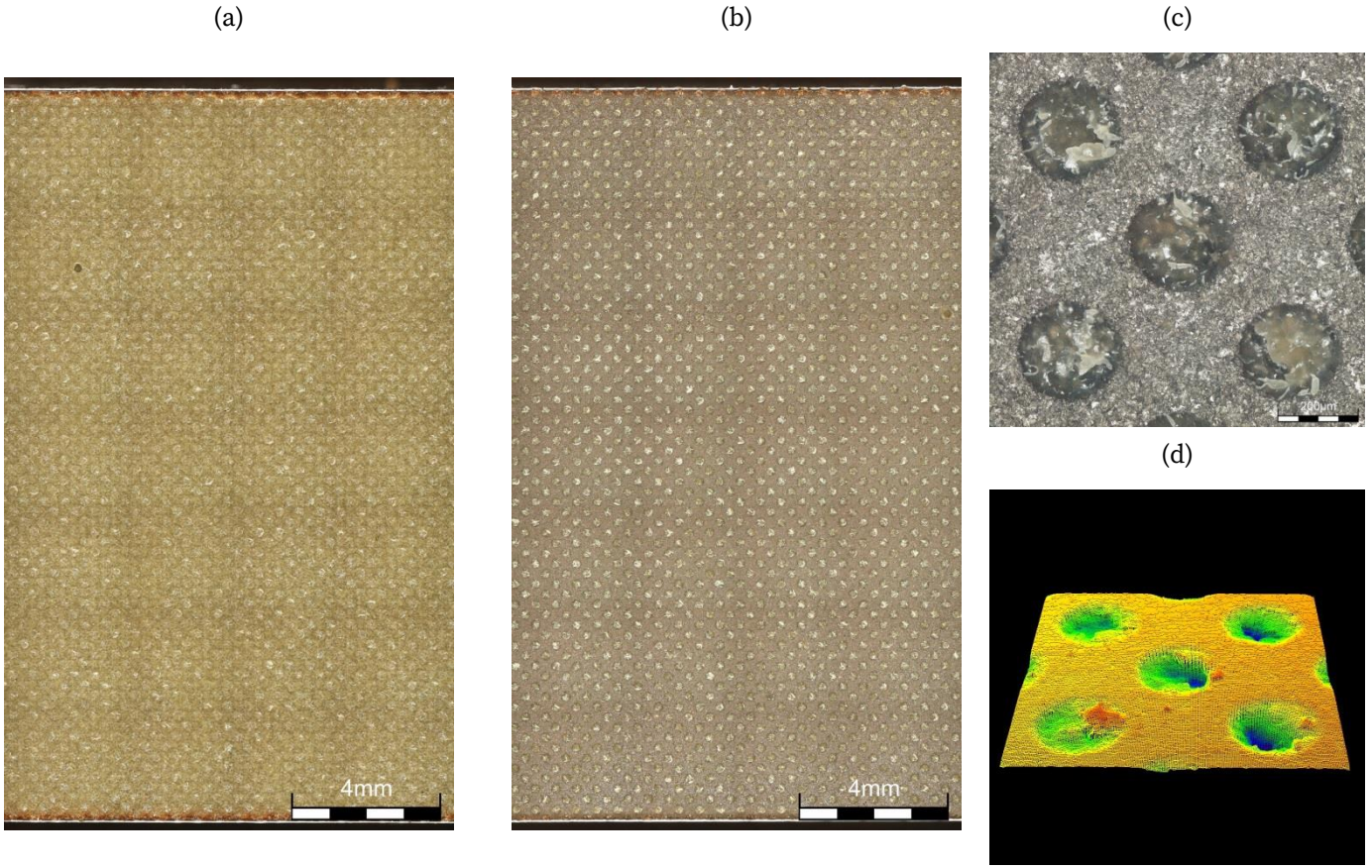

*Figure 6-14. Optical micrographs of typical fracture surfaces observed on (a) the bottom arm and (b) the top arm after mode I fracture of **fresh** DCB specimens. (c) and (d): closer view of the top arm fracture surface, with height scale going from 0 mm (purple) to 0.107 mm (orange). The crack growth direction is left to right.*

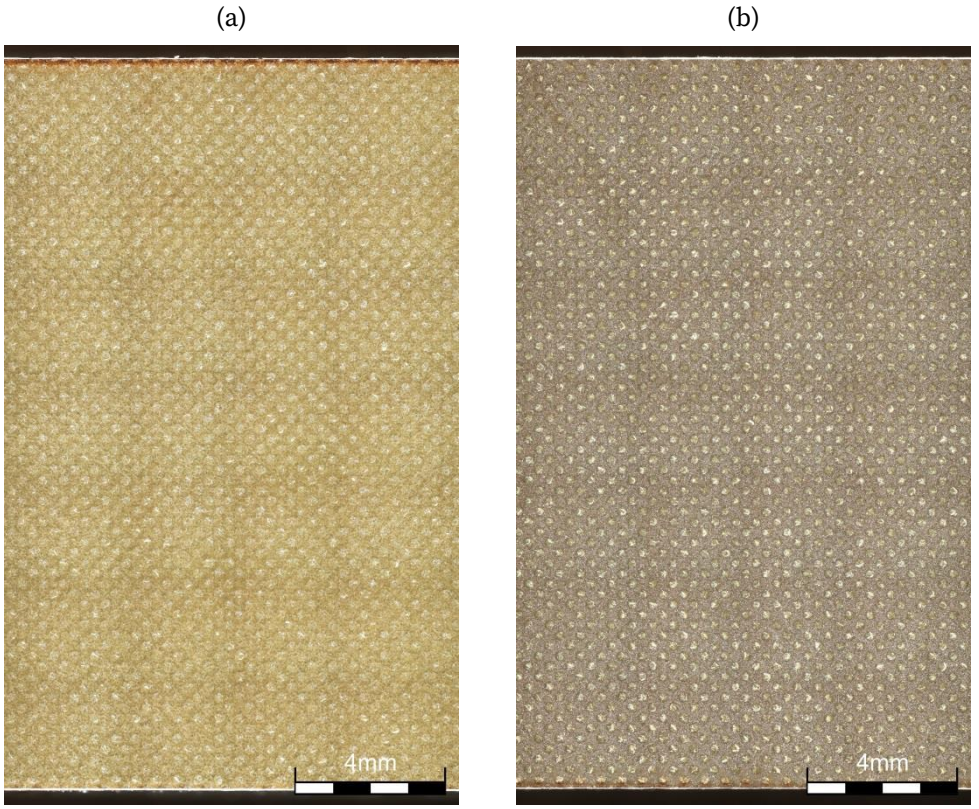

*Figure 6-15. Optical micrographs of typical fracture surfaces observed on (a) the bottom arm and (b) the top arm after mode I fracture of "**1 year aged**" DCB specimens. The crack growth direction is left to right.*

A global look at the load-displacement responses in Figure 6-13-a reveals the effect of normal ageing: crack propagation occurred at lower load and separation values after one year ageing as compared to the reference fresh specimens (note that the larger initial compliance of two of the three aged specimens is not due to ageing but simply to a larger initial crack length after precrack). One can thus anticipate that the mode I fracture toughness decreases with normal ageing, too.

The type of fracture observed on the fracture surfaces of fresh specimens (Figure 6-14) and "1 year aged" specimens (Figure 6-15) was identical, as already seen when peeling the micro-perforated steel strip. The crack obviously ran very close to the top arm interface in both cases, despite the effort made for promoting cohesive crack growth in the middle of the adhesive layer during manufacturing of the test specimens. This deviation could indicate that the specimen was not perfectly loaded in mode I and experienced some (most probably minor) combination of mode I and mode II instead [78]. 3D micrographs of the top cantilever arm obtained at larger magnification (with a 50x objective lens) revealed cohesive fracture of the bond material in the micro-perforations and adhesive fracture elsewhere (Figure 6-14-c and d), i.e. the same fracture mechanism as that encountered when peeling the micro-perforated steel strip.

A closer look at the load-displacement responses revealed a singular feature: at zero displacement, the load was not null as it usually is and logically should be. Instead, the recorded load initially increased very fast at almost negligible applied displacements during the test (1 in Figure 6-13-a), up to a mean value of 44.3 N where the slope of the curve changed to the real initial stiffness of the specimen.

A literature survey confirmed the oddness of our load-displacement responses: everywhere else the curves started at (0, 0) with a slope corresponding to

the initial compliance of the specimen. The survey also resulted in the discovery of a work by J.A. Nairn making the link between the non-zero force at zero displacement and some *initial curvature* of the cantilever arms due to *residual stresses* originally present in the DCB specimen, as illustrated in Figure 6-16 [179]. Residual stresses can indeed arise in adhesive DCB specimens and in composite laminate DCB specimens, from the *differential thermal shrinkage* of the components of the specimen and/or from the *chemical shrinkage* of the polymeric materials (adhesive and/or resin matrix) [179].

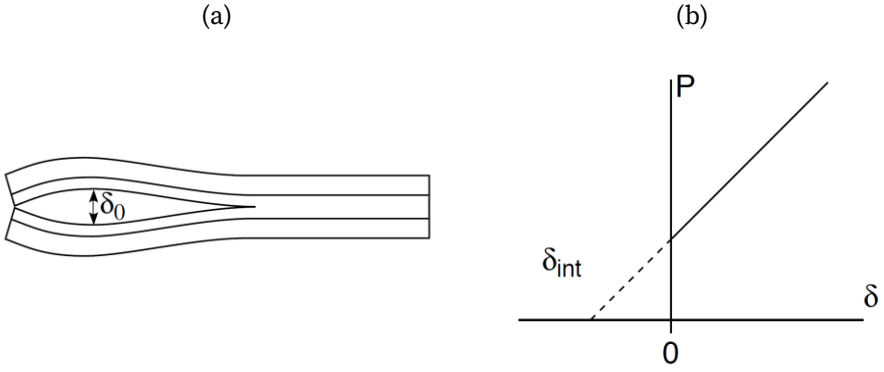

Figure 6-16. (a) DCB specimen with arms bending with a negative curvature due to residual stress. (b) Schematic load-displacement trace for negative arms curvature. From [179].

The non-zero load would then represent the force necessary to overcome the contact force found at the pre-cracked end of the specimen where the curved arms meet. This explanation appeared perfectly conceivable in the present case considering that, although our DCB specimens were balanced structures, their cantilever arms actually were asymmetric steel/bond/composite laminates which would indeed tend to bend towards each other under the effect of thermally induced residual stresses.

6.4.3 Curvature of the DCB specimen

For confirmation, the composite surface of cantilever arms was scanned with a Dektak 150 surface profiler (Veeco Inc., USA) over 50 mm and 18 mm in the longitudinal (x) and transverse (y) directions of the top and bottom arms of two DCB specimens with pre-crack. Curvature profiles indeed clearly appeared, as shown in Figure 6-17. Obviously, the arms curvature was not uniform over the whole scan length in the longitudinal direction: it progressively attenuated towards the crack tip location ($x \cong 50$ mm) where the cantilever arms are embedded into the uncracked portion of the specimen.

The curvatures were estimated by parabolic fitting of the surface profiles, on a reduced interval going from 0 to 20 mm in the longitudinal direction and over the whole 18 mm interval in the transverse direction. This yielded the following mean values and standard deviations: -0.12 m^{-1} ± 0.02 m^{-1} in the longitudinal direction and -0.25 m^{-1} ± 0.02 m^{-1} in the transverse direction.

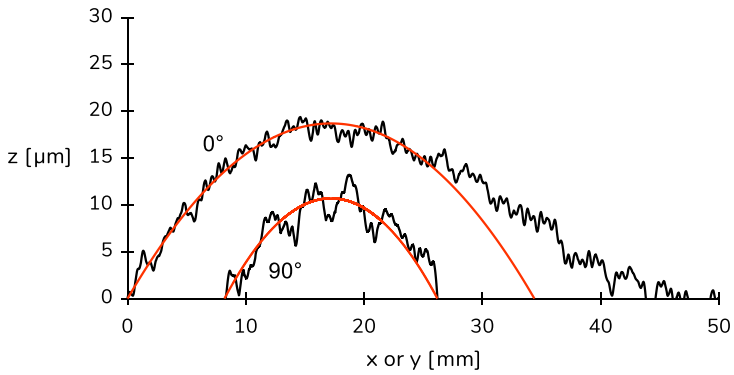

Figure 6-17. Typical set of surface profiles measured in the longitudinal direction (0° or x) and the transverse direction (90° or y) of the arm of a pre-cracked DCB specimen. The parabolic fits from which the curvatures were derived are drawn in red.

6.4.4 Data reduction schemes

6.4.4.1 Data reduction scheme accounting for residual stresses

An analytical method was proposed in the reference paper for the data reduction of DCB test results affected by residual stresses [179]. The latter do indeed affect the total amount of energy released during crack growth, so that if they are ignored in the analysis an *apparent* value of fracture toughness is calculated instead of the desired *true* value. In most cases, the cantilever arms bend towards each other under the effect of residual stresses, thereby requiring extra work from the loading system to separate the cantilever arms. The apparent toughness is then larger than the true toughness, and using this non-conservative, optimistic value in the design of adhesively bonded joints may lead to their premature failure [179].

For the sake of conciseness only the key equations that were actually used for the data reduction are given below, considering that the interested reader can find the full analytical development in the reference paper. The development holds for an adhesive DCB specimen of width B and initial crack length a (from load point to crack tip), the cantilever arms of which are bilayers made of the adherend (modulus E_1, thickness h_1, CTE α_1) and the adhesive (modulus E_2, thickness h_2, CTE α_2).

First, the energy release rate can be partitioned in two terms, as in Eq. (6-3): a term involving mechanical loads and a term involving residual stress.

$$G_I = (C_m P a_{corr} + C_{res})^2 \tag{6-3}$$

In the term related to mechanical loads, a_{corr} is the *effective* crack length, i.e. the crack length corrected for the actual rotation of the specimen arms at the crack tip. It writes as in Eq. (6-4), where Δ_W is the William's correction term given by Eq. (6-5) with $R = \frac{E_1}{E_2}$ and $\lambda = \frac{h_1}{h_2}$.

$$a_{corr} = a + 1.15\Delta_W \tag{6-4}$$

$$\Delta_W = h_1 \left(\frac{1 + \frac{R}{\lambda}}{6} \right)^{\frac{1}{4}} \tag{6-5}$$

Furthermore, P is the applied load, and C_m defines as in Eq. (6-6) where C_k^* is the effective bending compliance of the beam which writes as in Eq. (6-7).

$$C_m = \sqrt{\frac{C_k^*}{B}} \tag{6-6}$$

$$C_k^* = \frac{12}{E_1 B h_1^3} \frac{\lambda^2 (1 + R\lambda)}{\left(3(1+\lambda)^2 + (1 + R\lambda)\left(\lambda^2 + \frac{1}{R\lambda} \right) \right)} \tag{6-7}$$

The term of Eq. (6-3) linked to the residual stress in turn develops as in Eq. (6-8) where k_{res} is the residual stress induced curvature of the cantilever arms.

$$C_{res} = \frac{k_{res}}{\sqrt{C_k^* B}} \tag{6-8}$$

If the curvature is assumed to be primarily due to differential thermal shrinkage of the specimen layers, it can be expressed as in Eq. (6-9) where α_κ^* is the effective thermal-curvature coefficient of the beam that writes as in Eq. (6-11). The *true* mode I energy release rate can then be calculated with Eq. (6-3).

$$\kappa_{res} = \alpha_\kappa^* \Delta T \tag{6-9}$$

$$\alpha_\kappa^* = -\frac{6(\alpha_1 - \alpha_2)(1 + \lambda)}{h_2 \left(3(1+\lambda)^2 + (1 + R\lambda)\left(\lambda^2 + \frac{1}{R\lambda} \right) \right)} \tag{6-10}$$

In the event that other sources of residual stress should be taken into account, the curvature is evaluated experimentally rather than analytically. Among several methods proposed in the paper, k_{res} is preferentially determined from the intercept δ_{int} found by extrapolating the slope of the experimental load-displacement response to zero load, as shown in Figure 6-16-b. The arms curvature is then given by Eq. (6-11), and the *true* mode I energy release rate can finally be calculated with Eq. (6-3).

$$\kappa_{res} = \frac{\delta_{int}}{a^2} \tag{6-11}$$

One obtains a value of -0.13 m^{-1} for the initial curvature of the cantilever arms by application of Eq. (6-9), while a mean value of -0.35 m^{-1} was found with the graphical procedure (Eq. (6-11)) applied to the four specimens presenting the same initial compliance. The first compares very well with the value of -0.12 m^{-1} derived from the surface profiles in the longitudinal direction of the cantilever arms (Figure 6-17), while the second clearly exceeds these values by almost a factor of three. The experimentally measured value of k_{res} was therefore also introduced in Eq. (6-8), forming an alternative data reduction scheme that is referred to as "measured k_{res}".

6.4.4.2 Standard data reduction schemes

In addition to these particular data reduction schemes, three well known standard data reduction methods were applied to the experimental data for the purpose of comparison. These are the Simple Beam Theory method (SBT), the Corrected Beam Theory method (CBT) and the Experimental Compliance Method (ECM). As described in Chapter 2, they are all based on the Irwin-Kies equation (Eq. (2-41)); still, the first method is known to underestimate the mode I critical SERR as it omits the important effect of beam root rotation at the crack tip. The two others take this effect into account and yield similar results. Beyond the simple forms given in Chapter 2, the equations

for retrieving G_{Ic} with these methods are given in the standards (e.g. [82]) as well as in numerous papers (see e.g. [178]) and are thus not repeated here.

6.4.5 R-curves and mode I critical SERRs

A typical set of resistance curves is drawn in Figure 6-18. They were obtained by applying different data reduction schemes to the crack propagation points displayed on the experimental load-displacement response in Figure 6-13-b. The average propagation value of G_{Ic} was calculated from the propagation points for each specimen and all data reduction methods. The mean and standard deviation of these values are provided in Table 6-3 for the fresh and "1 year aged" families of specimens.

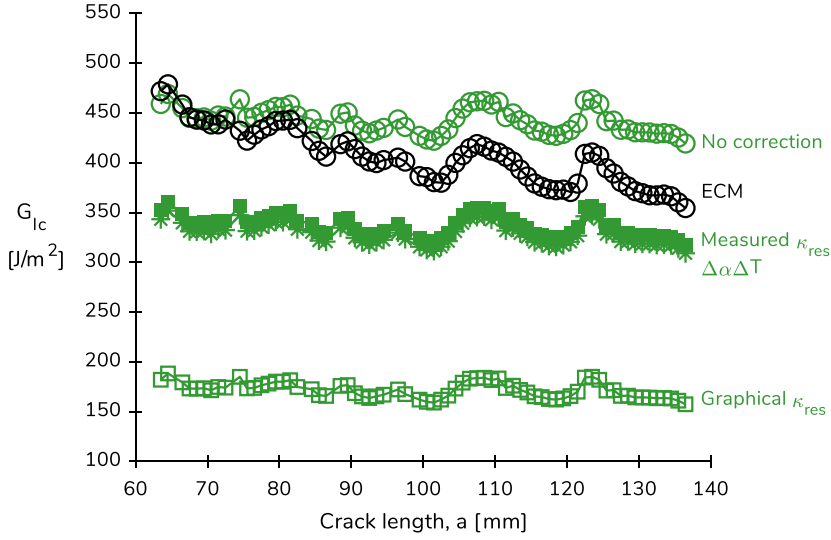

Figure 6-18. Set of R-curves resulting from the different data reduction schemes applied to the crack propagation points shown on the load-displacement trace of a fresh specimen in Figure 6-13-b. In green the data reduction schemes taking residual stress into account [179]*; in black the Experimental Compliance Method, one of the standard data reduction schemes.*

Table 6-3. Average propagation values of G_{Ic} obtained with the various data reduction schemes (mean and standard deviation on three specimens per type of conditioning).

		Correction for σ_{res}				Standard		
		None	$\Delta\alpha\Delta T$	Graph. κ_{res}	Meas. κ_{res}	SBT	CBT	ECM
Fresh								
G_{Ic}	[Jm^{-2}]	436 (8)	323 (7)	168 (3)	332 (7)	316 (5)	408 (15)	408 (16)
1 year aged								
G_{Ic}	[Jm^{-2}]	361 (13)	259 (11)	127 (15)	267 (11)	263 (8)	340 (20)	341 (19)

It seems that the "graphical k_{res}" method and the "no correction for k_{res}" method provided the lower and upper bounds of the interval in which the true value of G_{Ic} is likely to be found. On the one hand, the value obtained with the "graphical k_{res}" method appeared to be the most conservative but it was also largely offset as compared to (i) the level of G_{Ic} obtained with all other methods and (ii) the interval of [216; 434] Jm^{-2} constructed from literature data relative to pure RTM6 and pure Redux 322. On the other hand, the value obtained with the "no correction for k_{res}" method is close to that yielded by the CBT and ECM standard data reduction schemes involving a crack length corrected for root rotation at the crack tip. The "$\Delta\alpha\Delta T$" method and the "measured k_{res}" method provided quasi-identical results, as expected given the closeness of the involved curvature values. The values of 332 Jm^{-2} and 267 Jm^{-2} obtained with the "measured k_{res}" method are thought to be the most representative of the mode I critical SERR for cohesive fracture of the fresh and "1 year aged" co-cured joint. Note that G_{Ic} dropped by 17 % after one year ageing in normal conditions. Finally, amongst the standard reduction schemes, the SBT method was the most conservative while the CBT and ECM methods proved equivalent.

6.4.6 G_{Ic} compared to G_A

The assumed mode I critical SERRs of the fresh and "1 year aged" co-cured joints are larger than the adhesive fracture energies obtained with the 90° fixed arm peel test. For fresh joints, G_{Ic} (332 Jm^{-2}) is about 30 % larger than G_A measured with the fresh micro-perforated peel specimens (250 Jm^{-2}). After one year ageing in normal conditions, G_{Ic} (267 Jm^{-2}) is still 20 % larger than G_A measured with the 90° fixed arm peel test on "3 years aged" micro-perforated specimens (222 Jm^{-2}).

The same offset trend between peel and mode I LEFM tests results was reported by Kawashita *et al.* [180] and Martiny *et al.* [103] in studies of the adhesive fracture toughness of epoxy-aluminium alloy laminates. In the first paper, the authors noted a value of G_{Ic}(measured with the well-established LEFM TDCB test) about 23 % larger than the value of G_A (measured with the fixed arm peel test) when the peel arm was 0.5 mm thick, whereas the agreement was very good when the peel arm thickness was equal or above 1 mm. In the second paper, the authors quantified G_A by inverse analysis of various peel tests with the FE method and noted a difference of about 20 % with respect to the mode I critical SERR obtained with the TDCB test.

6.5 Mode II and mixed mode I/II critical SERR of the co-cured joint measured with the End-Loaded Split test and the Fixed Ratio Mixed Mode test

The End-Loaded Split test and the Fixed Ratio Mixed Mode test have been introduced in Chapter 2 (Section 2.4.2) as suitable laboratory test methods for measuring critical SERRs under loading conditions corresponding respectively to pure mode II and to a fixed ratio of $G_I/G_{II} = 4/3$. The fact that these tests share many similarities motivated their grouping in a common section. Besides, the fracture specimens and the procedures used for these tests are

very muh alike those already presented for the DCB test and will thus only be briefly described here. Basically, a beam of thickness $2h$ which separates at one end into two beams of thickness h is gradually loaded via one single beam so as to trigger crack initiation and promote crack propagation under sliding shear (mode II) or mixed mode I/II (see Figure 2-15 and Figure 6-19-a for ELS, or Figure 2-16 and Figure 6-19-b for FRMM). Unlike in the DCB test, the bonded end of the specimen is clamped on a linear bearing trolley which freely slides horizontally. After the test, G_{IIc} or $G_{I/IIc}$ is derived from the rate of change of the specimen compliance with crack growth.

6.5.1 Experimental procedures

The ISO standard (ISO 15114:2014(E), [95]) was followed for conducting the ELS tests and performing the mode II energy release rate analysis, while for the FRMM test which has not been standardised yet, the test protocol [98] was followed.

A mode I pre-crack of about 6 mm was first generated in each fracture specimen under the DCB test configuration. Then, only one stainless steel piano hinge was left on the specimen, on the lower beam for the ELS test and on the upper beam for the FRMM test. The bonded end of the specimen was clamped on a linear bearing trolley, leaving a free length of about 110 mm between the load line and the edge of the clamp. The tab was inserted into the grips of a universal testing machine (Instron, USA) and the loading arm was pulled up, as shown in Figure 6-19, at the constant crosshead speed of 0.5 mm/min for the ELS test and 1 mm/min for the FRMM test.

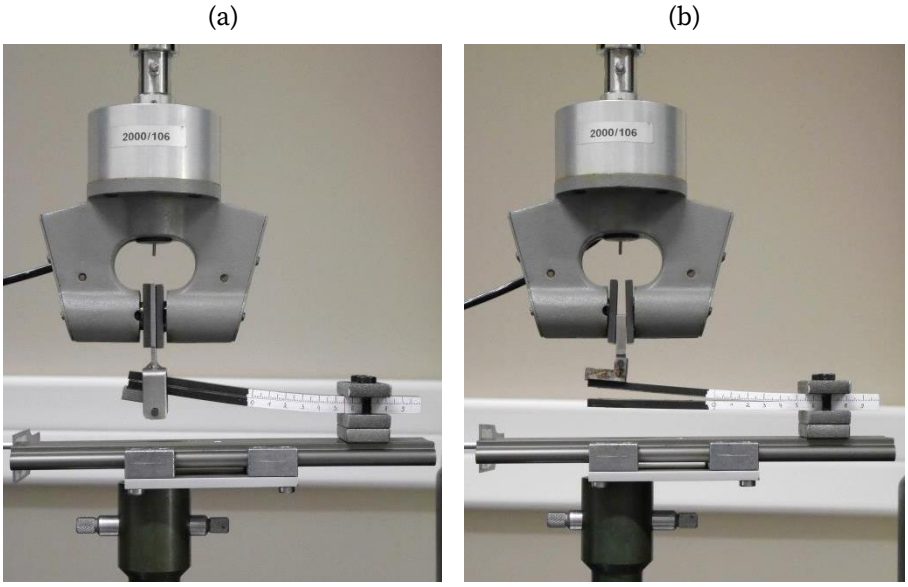

Figure 6-19. (a) ELS test specimen and (b) FRMM test specimen being tested with a universal testing machine.

The load was continuously recorded with a 1 kN load cell during the test, allowing to draw the load-displacement response.The method developed for reading, recording and post-processing the crack advance during the DCB test was also applied for the ELS and FRMM tests. The crack growth was carefully followed and its progression was recorded as often as possible, i.e. about every millimeter when the propagation was stable. The test was continued until the crack arrived within 10 mm of the clamped end, which represents about 40 mm of propagation. The results obtained with four ELS and four FRMM fracture specimens were retained for the mode II and mixed mode I/II critical energy release rate analyses.

These test campaigns were performed approximately one year after having manufactured the fracture specimens, so that the results obtained with the ELS and FRMM test configurations are related to those obtained with the "1 year aged" DCB test specimens.

6.5.2 Load-displacement curves

The load-displacement curves recorded during the end-loaded split tests and the fixed ratio mixed mode tests are drawn in Figure 6-20 and Figure 6-21, respectively.

A slope discontinuity appears in the linear region of the FRMM curves, which recalls that previously observed and discussed in the context of the DCB test results although it now occurs within a comparatively larger displacement interval. The ELS curves, on the contrary, present a constant slope until the onset of nonlinearity at crack initiation. These observations may again be related to the curvature caused by residual stresses in the specimens' arms due to their asymmetric layup (see Figure 6-16-a). During the first stage of the test, the curvature of the loaded arm of the FRMM test specimen is cancelled then reversed as it is progressively lifted up, and the contact force between the specimen's arms disappears. Conversely, in the ELS test specimen the contact force remains throughout the test as there is no separation of the specimen's arms which indeed follow the same movement upwards; hence, the slope is constant in the linear region of these load-displacement curves.

6.5.3 R-curves

Despite the presence of residual stresses in the fracture specimens, the tests results were analysed with conventional data reduction methods, i.e. the standard SBT and ECM methods, and no further analysis has yet been performed. The equations of G_{IIc} and $G_{I/IIc}$ corresponding to the SBT and ECM method have been derived in Chapter 2 and can also be found in the referenced standard and test protocol. Examples of typical R-curves resulting from the SBT and ECM analyses are plotted in Figure 6-22 and Figure 6-23 for the both tests.

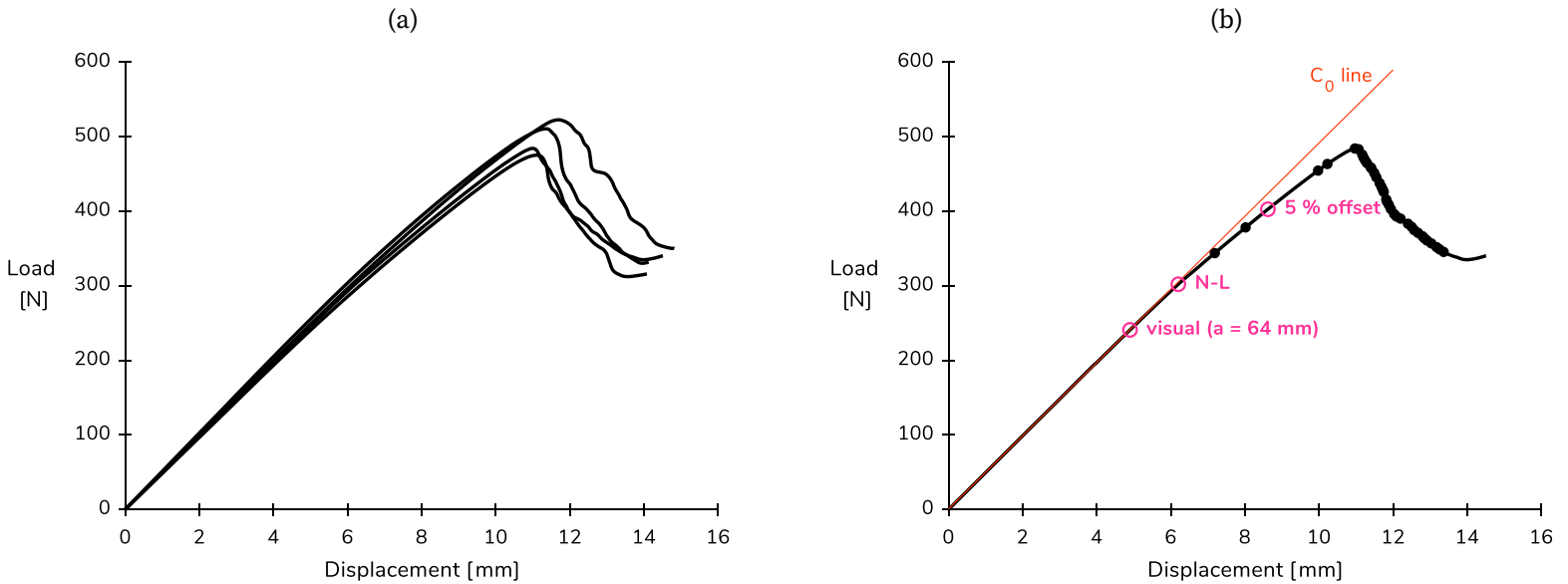

Figure 6-20 (a) Load-displacement curves obtained with the end-loaded split test performed on four "1 year aged" specimens, (b) Load-displacement curve and crack monitoring points obtained with the end-loaded split test performed on one of these "1 year aged" specimen. The points corresponding to crack initiation are marked with empty circles and the points corresponding to crack propagation are marked with filled circles.

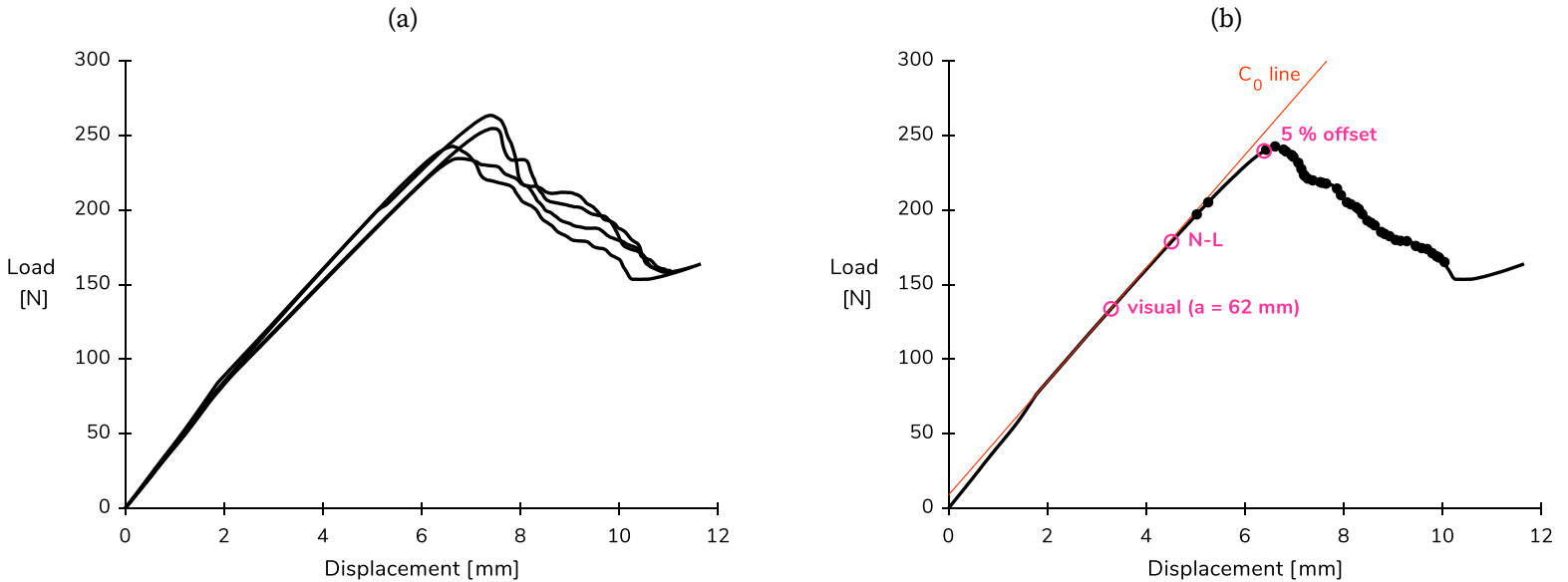

Figure 6-21. (a) Load-displacement curves obtained with the fixed ratio mixed mode test performed on four "1 year aged" specimens, (b) Load-displacement curve and crack monitoring points obtained with the fixed ratio mixed mode test performed on one of these "1 year aged" specimen. The points corresponding to crack initiation are marked with empty circles and the points corresponding to crack propagation are marked with filled circles.

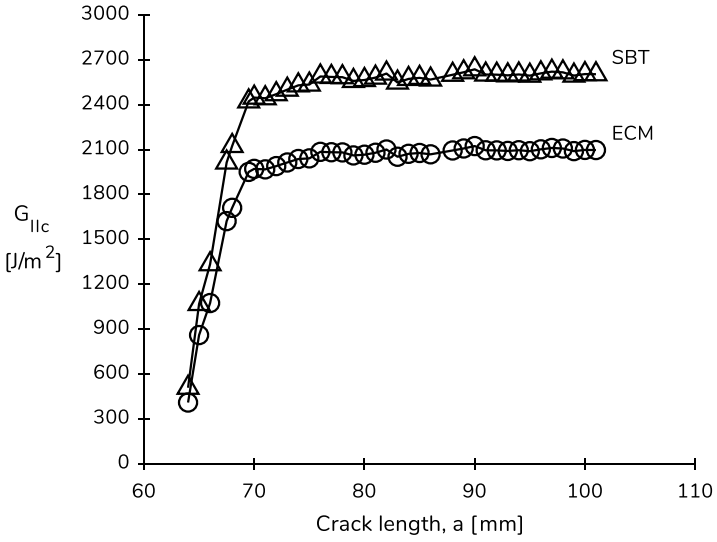

Figure 6-22. Mode II R-curves resulting from the SBT and ECM data reduction schemes applied to the crack propagation points shown on the load-displacement curve of a "1 year aged" ELS test specimen in Figure 6-20-b.

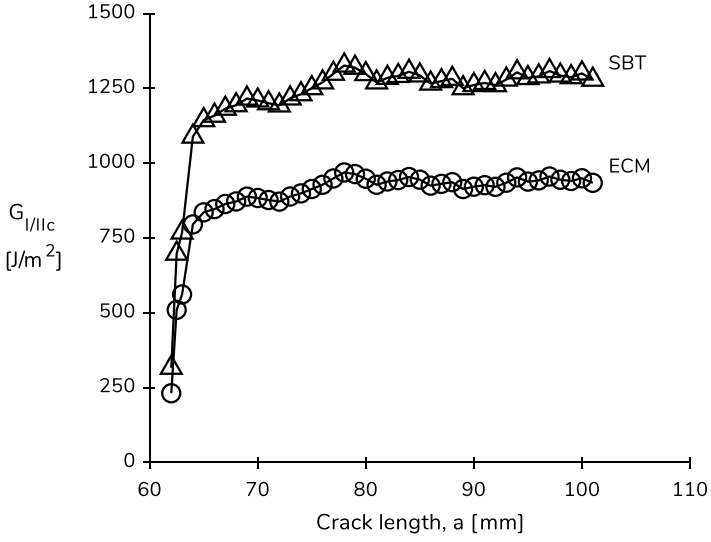

Figure 6-23. Mixed mode R-curves resulting from the SBT and ECM data reduction schemes applied to the crack propagation points shown on the load-displacement curve of a "1 year aged" FRMM test specimen in Figure 6-21-b.

6.5.4 Mode II and mixed mode I/II critical SERRs

Average values of the critical SERRs were calculated from the second half of propagation points obtained with all four specimens of each type. The mean and standard deviation of the average propagation values obtained with the four fracture specimens are reported in Table 6-4 for both tests.

Table 6-4. Average propagation values of G_{IIc} and $G_{I/IIc}$ obtained with the SBT and ECM data reduction schemes (mean and standard deviation on four "1 year aged" specimens).

1 year aged			
		SBT	ECM
G_{IIc}	[Jm^{-2}]	2764 (315)	2163 (202)
$G_{I/IIc}$	[Jm^{-2}]	1405 (96)	1012 (53)

G_{IIc} and $G_{I/IIc}$ were found to be in average equal to 2.16 kJm^{-2} and 1.41 kJm^{-2}, respectively, following the ECM analysis. Thus, as expected, the crack growth resistance was much larger in these modes than in pure mode I, and markedly increased with the proportion of the mode II component. The ratio of G_{IIc} to G_{Ic} measured for the present blend of epoxies is indeed about 6.3, and $G_{I/IIc}$ (for the fixed mode ratio $G_I/G_{II} = 4/3$) was still three times larger than G_{Ic}. The dissipation of energy during crack growth is actually accentuated in mode II due to the larger size of the fracture process zone. A pure mode II crack in a brittle adhesive indeed grows by coalescence of numerous sigmoidal tensile microcracks that form over several millimiters ahead of the main crack tip, in the FPZ. This fracture process -illustrated in Figure 6-24- has been reported and studied before, as for instance in [181]. It is known to cause the dramatic increase of the critical SERR in mode II with respect to mode I, such that G_{IIc} can be as much as 3 to 10 times larger than G_{Ic} for brittle or moderately brittle materials [181].

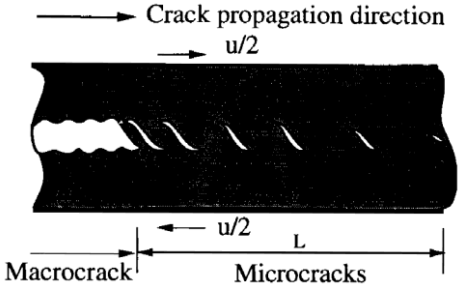

Figure 6-24. Schematic of the mode II fracture process in a brittle adhesive layer: growth and coalescence of sigmoidal tensile microcracks.

This fracture process did somewhat complicate the visual monitoring of the crack advance during the ELS tests, which in turn may have induced a slight overestimation of the measured crack lengths.

6.6 Conclusion

Testing flexible laminates with the fixed arm peel test configuration allowed quite straightforwardly highlighting remarkable differences in adhesive fracture energy and fracture surfaces among the various types of specimens studied. When tested shortly after their manufacturing, specimens with as-rolled steel strip profited from a boost in adhesive fracture energy thanks to the tearing of the supporting nylon mesh. This beneficial effect did unfortunately not persist in time and G_A dropped dramatically as the fracture mechanism changed from predominantly cohesive to almost totally adhesive after three years of normal ageing. The adhesive fracture energy measured on flexible laminates with micro-perforated steel was, on the contrary, found to be very stable even after three years of normal ageing and several days of water immersion. The use of micro-perforations for mechanical anchoring thus really proved effective as it ensured the prevalence of the cohesive fracture mechanism over time.

The same observations arose from the LEFM DCB test results: the fracture path ran very close to the top arm interface, still breaking the bond material filling the micro-perforations in fresh specimens as well as in "1 year aged" specimens. The curvature of the cantilever arms due to the presence of residual stress furthermore transpired from the load-displacement responses and motivated the use of specific, non-standard data reduction schemes. Among them, two methods provided quasi-equivalent G_{Ic} values and caught our attention: one attributing the arms curvature to thermally induced residual stress ("$\Delta\alpha\Delta T$" method) and the other relying on the experimentally measured curvature of the arms ("measured k_{res}" method). These methods yielded lower G_{Ic} values than the standard ECM and CBT data reduction schemes which are not equipped for accounting for residual stress and may therefore yield an apparent value of fracture toughness.

The values of G_A measured on peel specimens with micro-perforated steel strip sandblasted on both faces (M-P S2F) were initially thought to be the most representative of the energy required for the cohesive fracture of the fresh, "3 years aged" and "3 years aged + immersed" bond material. The first (250 Jm^{-2}) furthermore compared well with G_{Ic} values reported in the literature for the cohesive fracture of pure RTM6 and pure Redux 322. Yet, it proved lower than the mode I critical SERR measured on fresh DCB specimens (332 Jm^{-2}).

Finally, the mode II and mixed mode I/II critical SERRs of the "1 year aged" co-cured joint were derived from the ELS and FRMM tests results. G_{IIc} and $G_{I/IIc}$ were respectively about six and three times larger than the corresponding G_{Ic} value of 341 Jm^{-2}, and these ratios seem to be consistent with literature data. The summary graph in Figure 6-25 gives an overview of the experimental data points acquired with this whole set of measurement techniques.

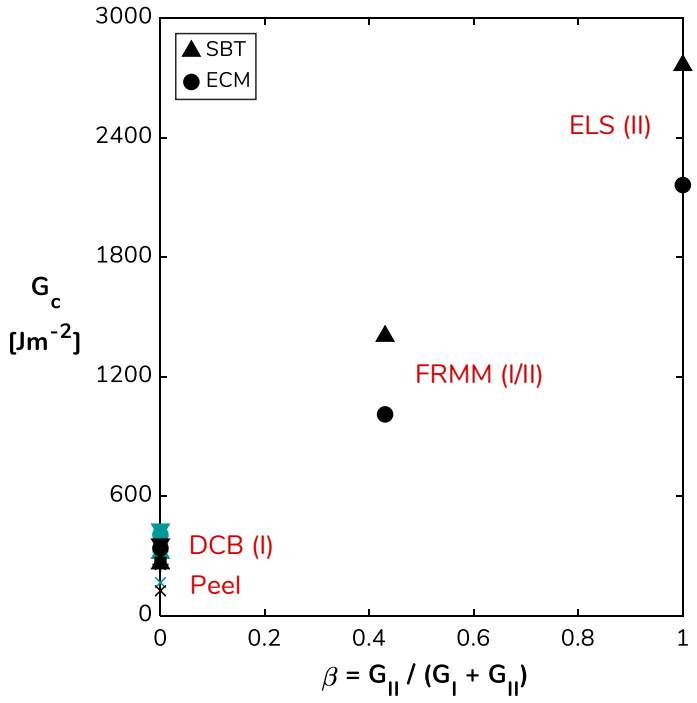

Figure 6-25. Graphical summary of the experimentally determined G_c values.

Nonetheless, some additional work is required to complete the determination of the fracture envelope of the co-cured joint. The data reduction of the mode II and mixed mode I/II tests results could be refined so as to account for the possible effect of residual stresses in the fracture specimens. Besides, given the multiplicity of values derived for G_{Ic} with the different data reduction schemes, it would be worth ascertaining the validity of the confidence placed in the values resulting from the "measured k_{res}" method. In response to these needs, and motivated by the numerical character of the predictive simulation tool to which this doctoral thesis ultimately contributes, inverse FE analysis was chosen as another data reduction technique. The next and last chapter hence presents the work done for the finite element simulation of the double cantilever beam test using a cohesive zone formulation.

7. Identification of the mode I cohesive law parameters by inverse FE analysis of the DCB test

7.1 Introduction

The experimental DCB tests results presented in detail in the previous chapter showed the presence of residual stresses that make the cantilever arms to bend towards each other and impact the shape of the load-displacement curve. Several standard and specific data reduction schemes were therefore applied to the tests results, yielding quite different values for the mode I critical SERR G_{Ic} of the co-cured bond but no certainty as for which one to trust.

The present chapter describes the numerical treatment of the experimental tests results that was carried out in order to discriminate the values of G_{Ic} derived analytically. It involved the FE modelling of the DCB test and the determination of the fracture properties by inverse FE analysis. The latter consists in tuning the value of one or several model parameters until the simulated result satisfactorily reproduces the experimental reference result. This method thus more generally allowed adjusting the value of several model parameters, in particular those defining the constitutive law of the cohesive elements used for simulating mode I fracture of the co-cured bond.

The values of mode I critical SERR and fracture strength obtained experimentally were chosen as initial candidates for G_{Ic} and the mode I cohesive strength σ^0 in the inverse analysis. These are recalled in Table 7-1.

Table 7-1. Initial candidate values chosen for G_{Ic} and σ^0 in the inverse analysis.

σ^0 [MPa]	Justification	G_{Ic} [Jm^{-2}]	Justification
50	σ_B Redux 322	170	DCB κ_{res} graphical
80	σ_B RTM6	250	Peel test
300	Ref. [152]	330	DCB κ_{res} measured
		440	DCB no correction

Many publications report the successful application of inverse methods for calibrating the cohesive zone constitutive laws in the single fracture modes (see e.g. [66][118][182]). The current application however differentiates from the generally existing ones by the fact that it takes the presence of thermally induced residual stresses into account. The present FE analyses were indeed conducted in two consecutive steps:

1. A thermal loading step reproducing the specimen's thermal history and giving rise to the double curvature of its cantilever arms.
2. A mechanical loading step forcing the opening of the curved arms of the specimen to simulate the DCB test.

The FE models of the DCB test developed for this study are presented in the next section. They were refined through a parametric study before being used for the inverse analysis.

7.2 Presentation of the FE models

Finite element analyses of fracture tests found in the literature are predominantly based on two-dimensional models (see e.g. [121][183][184][185][110], among many others). This choice of modelling dimension allows benefiting from reasonable computation times while generally providing satisfactory simulation of crack propagation [186].

Yet, it was not an obvious choice in the present case: the presence of residual stresses and curvatures in the multi-layered DCB test specimen and the anisotropic nature of its constituent materials logically directed the choice towards 3D modelling in the first place.

However, the mesh refinement requirement accompanying the use of cohesive elements (Chapter 2, Section 2.5.3) leads to a significant increase of the computation time that makes 3D modelling inappropriate for parametric studies. Indeed, it will be shown that the maximum cohesive element length is about 60 µm for realistic values given to the set of parameters describing the constitutive law of the cohesive zone. In 2D, this leads to more than 250 cohesive elements on a 15 mm-long cohesive zone. In 3D, this amount explodes as it is multiplied by the number of elements found along the width direction, which in addition must be high enough to keep an acceptable aspect ratio for the cohesive elements. This for instance leads to more than 5000 cohesive elements (500 µm x 60 µm) on a 15 mm x 10 mm cohesive zone.

2D modelling therefore became an essential tool for the parametric study and the inverse analysis. A 3D model was however still used to ascertain the validity of the identified set of parameters values in a framework containing less simplifying assumptions.

Both models were developed with the commercial FE package SAMCEF. Their main features are presented below.

7.2.1 2D and 3D geometries

The geometry of the DCB test FE model faithfully reproduces the average characteristics of the three tested specimens given in Figure 7-2-(a). The only freedom taken in the definition of the model geometry is an augmentation of the initial crack length by 0.5 mm as a means of increasing the initial compliance of the 3D specimen model. This minor modification can however represent a realistic error on the reading of the crack length during physical tests.

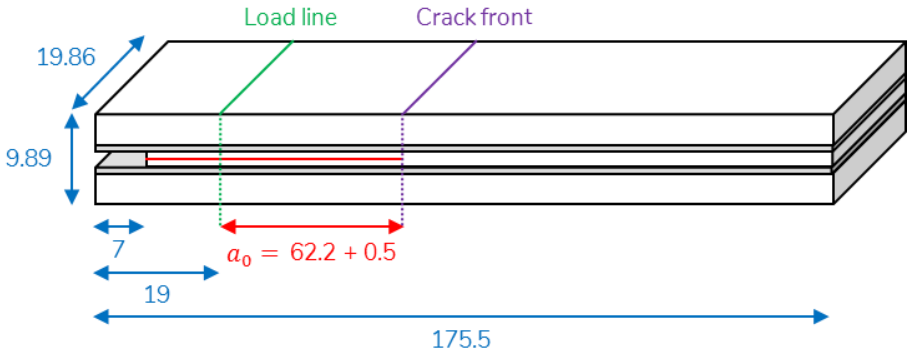

Figure 7-1. Geometry and average dimensions (in mm) of the DCB specimens tested.

7.2.2 Mesh

The models were meshed with quadratic plane strain surface elements in 2D and quadratic volume elements in 3D, as shown in Figure 7-2. Their smallest length is found along the cohesive zone and was calculated so as to ensure mesh convergence, as explained in a subsequent section (Section 7.3.2). Outside this region and the surrounding transition regions, the elements length was set to 1 mm on the pre-cracked side and to 2 mm on the other side. In 3D, all elements have the same width of 500 µm which was seen to provide a good

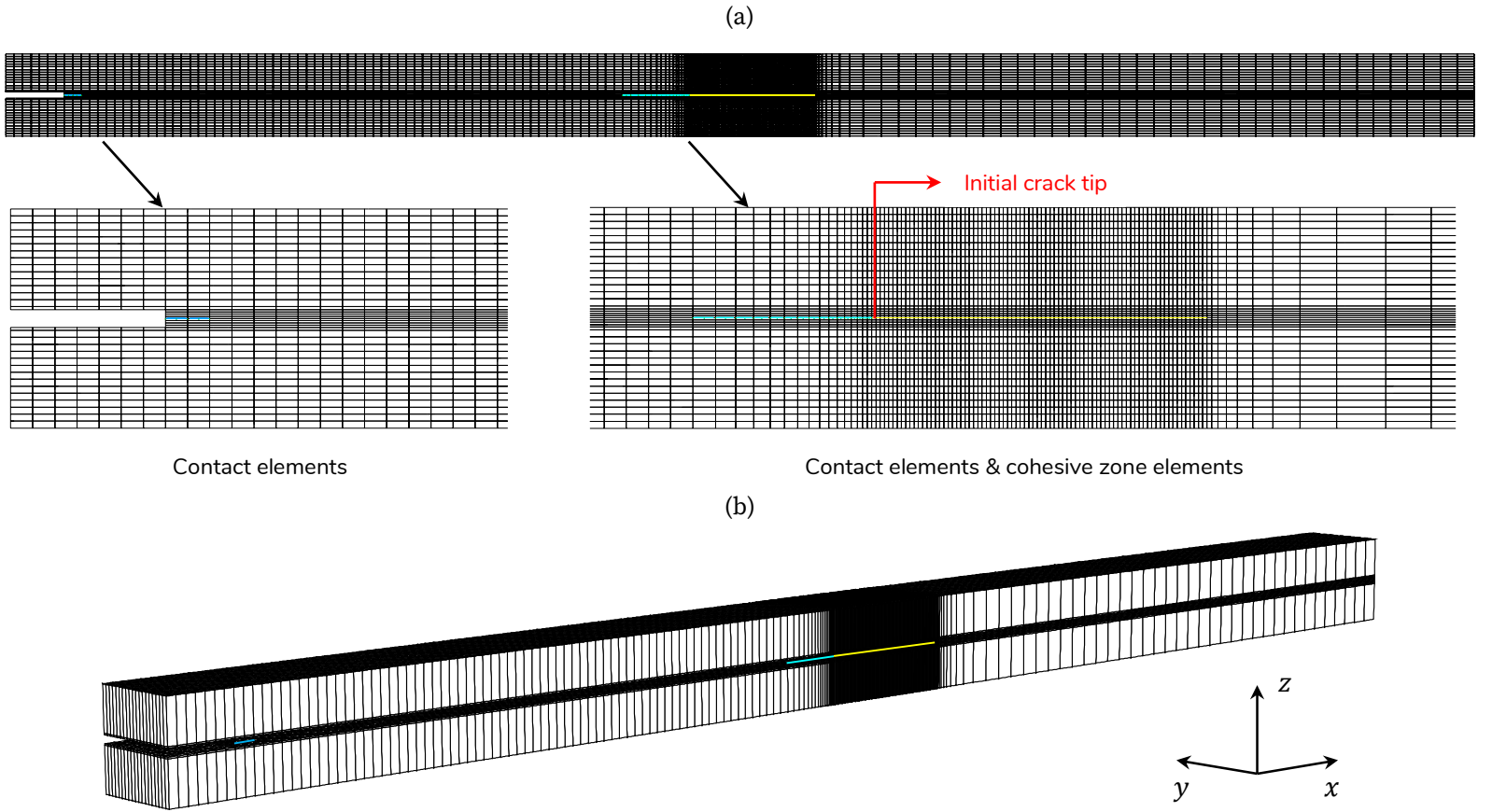

Figure 7-2. Mesh of the (a) 2D and (b) 3D DCB test specimen model and location of specialised finite elements (blue: contact elements, yellow: cohesive zone elements). The thickness of the laminate composite is discretised with 14 elements in 2D and one single element in 3D.

resolution of the transverse arm curvature. The elements thickness varies according to the material layer. The central bond line thickness was meshed with four elements of 100 µm, while the thickness of the external joints was meshed with one element of 135 µm. The steel strip thickness was meshed with two elements of 100 µm. The composite substrate was meshed with 14 elements of equal thickness (315 µm) in 2D. In 3D, the composite substrate thickness could either be meshed with one single element or with 14 elements of thickness defined by that of the corresponding lamina. The first option had to be taken in order to keep the model computationally tractable.

Furthermore, contact elements were placed over particular areas of the specimen mid-plane to allow the double curvature to develop without interpenetration of the cantilever arms. These elements cover 2 mm at the pre-cracked end of the specimen, and 8 mm right behind the crack tip.

Finally, cohesive zone elements with zero thickness were placed at the specimen mid-plane, over the first 15 mm ahead of the crack tip. These specialised finite elements allowed simulating crack initiation and propagation through the progressive separation of their initially coincident paired nodes. Their optimal length for this role was determined in a parametric study.

7.2.3 Materials

All materials were attributed a linear elastic physical behaviour. This reflects the assumption of minimal plastic deformation of the cantilever arms, in line with the prescriptions of the LEFM theory. For the material in the central co-cured joint where the crack is forced to propagate, this choice may seem reductive knowing the existence of the crack tip plastic zone (Chapter 2, Section 2.3.2). However, the use of this simplifying assumption was supported by the limited amount of plastic strain observed on the experimental tensile stress-strain curves of both RTM6 and Redux 322 in Chapter 4.

In 3D, the orthotropic composite laminate was modelled by means of a ply-by-ply approach, using the individual temperature-independent plies properties (Table 4-1). This advanced modelling tool could not be used in 2D where the composite laminate was thus given its temperature-independent effective properties (Table 4-2). The initial specimen compliance was however underestimated with this approach and the effective longitudinal modulus E_x of about 60 GPa was therefore reduced to 35 GPa as a way to fit the experimental compliance.

The transversely isotropic steel strip was defined with the set of temperature-independent properties given in Table 7-2 while the isotropic bond line material was defined with a set of properties taking into account the thermal dependency of its Young's modulus and CTE (Table 7-3).

Table 7-2. Properties defining the mechanical and thermal behaviour of the transversely isotropic steel strip.

Young's moduli [GPa]		Shear moduli [GPa]		Poisson's ratios [-]		CTEs [µm/(m°C)]	
E_x	$E_y = E_z$	$G_{xy} = G_{xz}$	G_{yz}	$\nu_{xy} = \nu_{xz}$	ν_{yz}	α_x	$\alpha_y = \alpha_z$
69.1	75.1	33.6	28.9	0.50	0.30	16.3	16.0

Table 7-3. Properties defining the mechanical and thermal behaviour of the co-cured bond material.

Temperature ranges [°C]	[-40; 70]	[70; 180]
Young's modulus E [GPa]	$2.52e^{-5}T^2 - 1.11e^{-2}T + 3.17$	$2.73e^{-6}T^2 - 6.74e^{-3}T + 2.98$
Poisson's ratio ν [-]	0.38	0.38
CTE α [µm/(m°C)]	$-2.21e^{-5}T^3 + 8.99e^{-4}T^2 + 1.64e^{-1}T + 52.1$	$5.339e^{-5}T^3 - 1.500e^{-2}T^2 + 1.419T + 16.29$

Finally, the cohesive elements behaviour was defined with the DAMINT bi-linear constitutive law and the "delayed damage" formulation was used to help convergence of the analyses. The parameters were initially set to the values given in Table 7-4, which were progressively refined through the study presented in the following sections.

Table 7-4. Values initially given to the parameters of the mode I cohesive law.

Penalty stiffness	K^0	10^7	Nmm^{-3}
Peak stress	σ^0	80	MPa
Mode I critical SERR	G_{Ic}	330	Jm^{-2}
Characteristic time	τ_c	10^{-4}	s
Mode coupling coefficient	α	1	-

7.2.4 Loads and boundary conditions

Rigid body translation was locked in the longitudinal direction through fixation of the x-component of displacement at 19 mm from the pre-cracked end of each arm, where mechanical loading was performed. In the normal direction, rigid body translation was locked through fixation of the z-component of displacement at the specimen uncracked end. These fixations were applied to a single node in 2D and to a row of successive nodes along the width of the specimen in 3D.

In 3D, the specimen symmetry in the longitudinal direction was used as a means of beneficially reducing the volume to be meshed. The model thus only contains half the specimen width, and the y-component of displacement was fixed at all nodes lying in the vertical plane at y = 0. This also allowed locking the rigid body translation in the transverse direction.

Both versions of the model were used in nonlinear static analyses solved with the Newton-Raphson iteration scheme and automatic time stepping. Linear

analysis was not an option given the use of cohesive elements and the intrinsic material nonlinearity they imply.

The loading starts with thermal loading of the whole specimen following the piecewise linear function of time schematised in Figure 7-3-(a) (note that time here represents a sequencing parameter, not a true physical time). The specimen's thermal history and residual stress state were thereby reproduced, giving rise to the initial double curvature of its cantilever arms. In 3D, the initial temperature T_i was set to 155 °C, which represents a correction of -25 °C with respect to the final cure temperature of 180 °C. The latter value indeed led to the overestimation of the initial force at zero displacement F_0, and T_i was thus diminished knowing that the stress-free temperature may be as much as 25 °C lower than the cure temperature [187]. In 2D, a larger correction of -70 °C was applied to bring the initial force back to the experimental value (~45 N). It has no physical justification but serves the purpose of compensating the 2D kinematic constraints which prevent the development of the transverse curvature and lift F_0 to higher values.

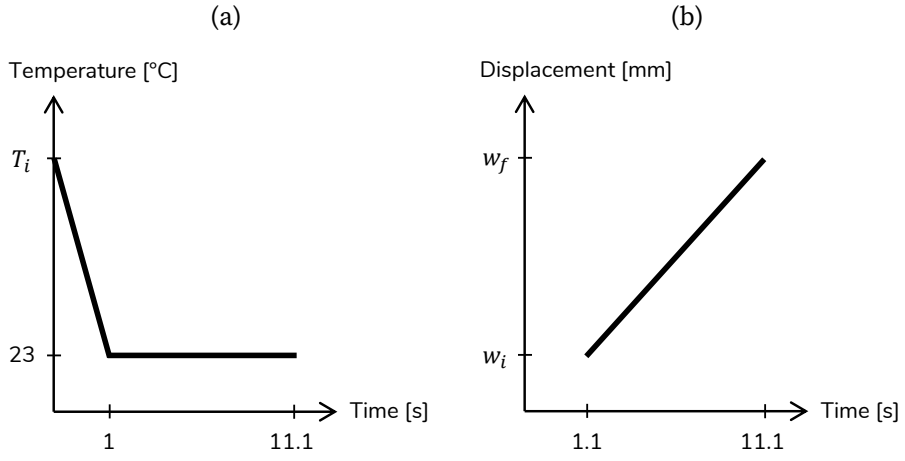

Figure 7-3. Functions for (a) thermal and (b) mechanical loading of the DCB test specimen model.

The total vertical displacement w_i achieved by the load line node(s) during cooling was extracted and used as initial displacement in the function prescribing the subsequent mechanical loading. It results from the combination of two opposing effects, namely the arm curvature(s) and the thermal shrinkage of the constituent materials. In 3D, the existence of the transverse curvature required the definition and attribution of as many displacement functions as loading nodes. The ramp of vertical displacement schematised in Figure 7-3-(b) was prescribed to a single node in the 2D version of the model and to a row of successive nodes in the 3D version. The top arm's displacement is positive while the bottom arm's displacement is negative with respect to the positive z-direction.

Deformed views of the DCB test specimen after thermal loading and after the subsequent mechanical loading are shown in Figure 7-4 for illustrative purposes.

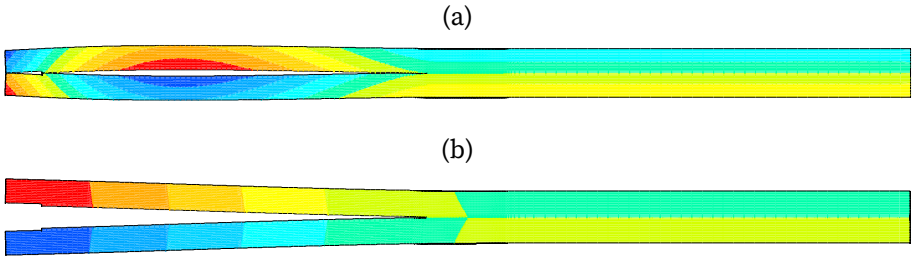

Figure 7-4. Deformed view of the DCB test specimen (2D model) after (a) thermal loading and (b) mechanical loading. The amplitude of the deformation in (a) is ten times magnified.

Finally, the characteristic size and the associated computational cost of these models depend on the cohesive law parameters, the values of which dictate the size of the cohesive elements and influence the convergence of the nonlinear solution procedure. Information on the number of nodes, the number of DOF and the CPU time is given for both models in Section 7.4 at the end of

this chapter, for the final set of parameter values identified throughout the parametric study and the inverse analysis described in the next section.

7.3 Parametric study and inverse analysis of the DCB test

Upstream of the identification of values for the mode I critical SERR and the peak stress, a parametric study was performed on the 2D model of the DCB test. The objective was to understand the influence of the other cohesive zone law parameters and make an informed choice of their appropriate value. The main outcomes of this study are reported in the next sections, followed by the identification of G_{Ic} and σ^0 by inverse analysis.

7.3.1 Influence and selection of the penalty stiffness value

The notion of penalty stiffness has been introduced in Chapter 2, where it was emphasized that this cohesive zone law parameter should be given a value large enough so that the presence of cohesive elements does not modify the system compliance before they undergo irreversible damage.

Eq. (7-1) and (7-2) from the literature (respectively [125][188] and [117]) were used to calculate initial guesses of the adequate mode I penalty stiffness value.

$$K_I^0 \cong \frac{E_3}{e} \tag{7-1}$$

$$K_I^0 \geq \frac{\alpha E_3}{t} \tag{7-2}$$

E_3 is the through-the-thickness Young's modulus of the material, e is a fraction of the thickness of the adjacent material layer, t is the thickness of the adjacent layer, α is a factor much larger than 1. With E_3 set to 2.95 GPa for

the room temperature modulus of the RTM6 resin, e set to one fifth of 200 µm, t set to 200 µm and α set to 50, these equations respectively provided the value of 7.5 10^4 Nmm^{-3} and 7.5 10^5 Nmm^{-3} for the mode I penalty stiffness.

Nonlinear analyses of the DCB test were performed with these values. For their assessment, simulations were also performed with two larger values, namely 10^7 Nmm^{-3} and 10^8 Nmm^{-3}. Finally, as an illustration of the consequence of defining a too low penalty stiffness, an additional simulation was run with a value of 1.1 10^4 Nmm^{-3}, close to the lowest admissible value calculated for this parameter knowing that the threshold separation δ^0 must remain inferior to the separation at failure δ^c.

The load-displacement curves issuing from these simulations are drawn in Figure 7-5-(a).

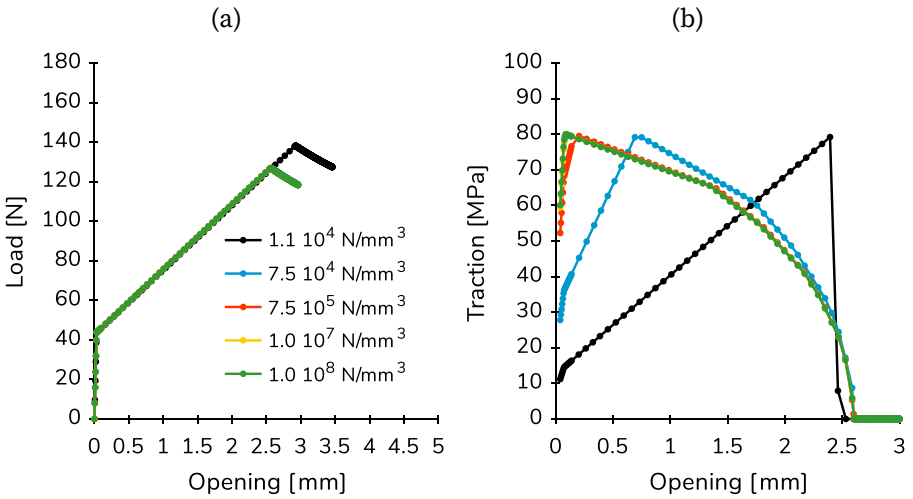

Figure 7-5. (a) Load-displacement curves predicted with different values of mode I penalty stiffness. (b) Corresponding evolution of the cohesive traction on the cohesive node at the initial crack tip.

It is clear that there is almost no difference between the curves obtained with values of penalty stiffness greater or equal to 7.5 10^4 Nmm^{-3}. Convergence is

apparently reached for these values which thus all seem to be eligible for this parameter. The same can on the other hand not be said for the value of 1.1 10^4 Nmm^{-3} which fails producing crack growth in the same load range. The influence of the penalty stiffness also appears locally in the cohesive zone, for instance when following the evolution of the cohesive traction on a cohesive node during loading. This is illustrated in Figure 7-5-(b) for the cohesive node at the initial crack tip[36]. The traction obviously reaches its maximum value with some delay when the penalty stiffness has a low value. Indeed, the interface is then more compliant, and a larger separation of the cohesive nodes is required for the cohesive traction to reach the peak stress value. This results in crack growth starting at larger opening when the penalty stiffness is too low.

Although there was no significant difference in the load-displacement curves obtained with penalty stiffness values down to 7.5 10^4 Nmm^{-3}, the evolution of the cohesive traction shows that this value does already introduce some extra compliance with respect to the 10^8 Nmm^{-3} reference case. Eq. (7-2) thus proves to perform better than Eq. (7-1) at calculating an adequate value for the penalty stiffness, and the check for the validity of this calculated value should preferably be based on local cohesive zone variables (e.g. the cohesive traction) rather than on global variables obtained at the scale of the specimen (e.g. the reaction force).

By this study, values greater or equal to 7.5 10^5 Nmm^{-3} were shown to be adequate for the mode I penalty stiffness. For the sake of consistency with the choice previously made in Chapter 5, the value of 10^7 Nmm^{-3} was retained and assigned to this parameter.

[36] Note that the curves in Figure 7-5-(b) do not represent the shape of the actual triangular cohesive law, since the cohesive traction at the considered pair of cohesive nodes is plotted against the global opening of the DCB specimen instead of the local separation between these paired cohesive nodes.

7.3.2 Influence of the spatial discretisation of the cohesive zone and selection of a criterion for mesh convergence

As seen in Chapter 2 (Section 2.5.3), the cohesive zone parameters G_{Ic} and σ^0 do not only define the constitutive cohesive material law, but also set the value of a characteristic distance called *cohesive zone length*. As a reminder, the latter represents the region of the crack plane where damage is actually ongoing and can be approached by Eq. (7-3), the parameters of which have been defined in Chapter 2.

$$l_{cz} = ME\frac{G_{Ic}}{(\sigma^0)^2} \tag{7-3}$$

In this equation, M was set to 1 and E to 2.95 GPa for the room temperature modulus of the RTM6 resin. With a peak stress σ^0 of 80 MPa and a mode I SERR G_{Ic} of 330 Jm^{-2}, l_{cz} was thus estimated to 152 µm.

Alternatively, this characteristic distance can be determined graphically by plotting the traction at each cohesive node of a crack face with respect to its position ahead of the initial crack tip, for a chosen crack advance or opening; l_{cz} is then given by the smallest distance between nodes with $\sigma = 0$ and $\sigma = \sigma^0$ [117]. A nonlinear analysis was run with 10 µm long cohesive elements providing good spatial resolution. Figure 7-6-(a) illustrates the graphical determination of the numerical l_{cz} for a crack advance of 0.8 mm.

This procedure was repeated for every saved time step of the simulation to get the evolution of l_{cz} with crack growth. As can be seen in Figure 7-6-(b), it actually remained close to a plateau value of 190 µm all along crack propagation.

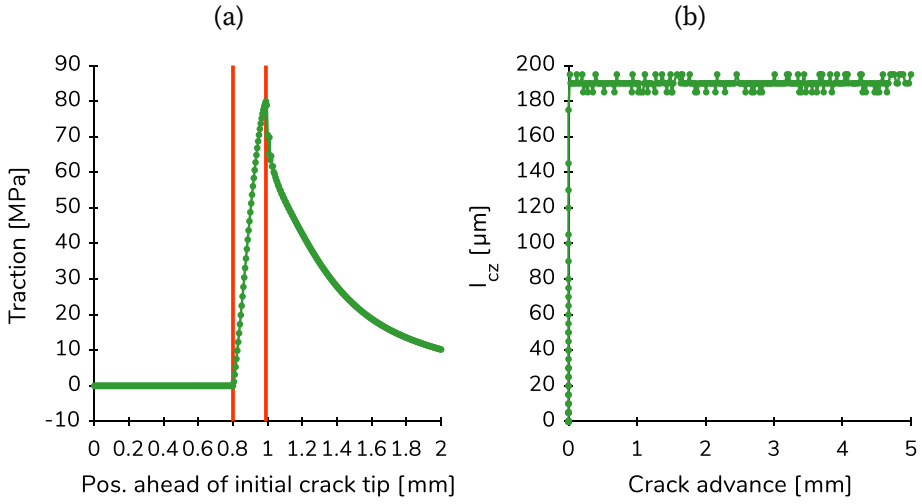

Figure 7-6. (a) Graphically, the cohesive zone length is given by the distance found between the two red lines. (b) Evolution of the length of the cohesive zone during crack growth.

Nonlinear analyses were then performed with cohesive elements lengths between 380 µm and 63 µm, so that N_e (the number of elements on the cohesive zone length) ranged from 0.5 to 3 elements. The influence of the cohesive zone mesh refinement on the predicted load-displacement curve is illustrated in Figure 7-7-(a). Clearly, the use of large cohesive elements delays the occurrence of crack growth while finer meshes conversely bring the occurrence of crack growth back to smaller openings. At some point however, mesh convergence is attained and further reduction of the cohesive elements length does not modify anymore the value of opening at which crack propagation takes place. In the present study, this seemed to be the case as soon as at least two quadratic elements were found on the cohesive zone length.

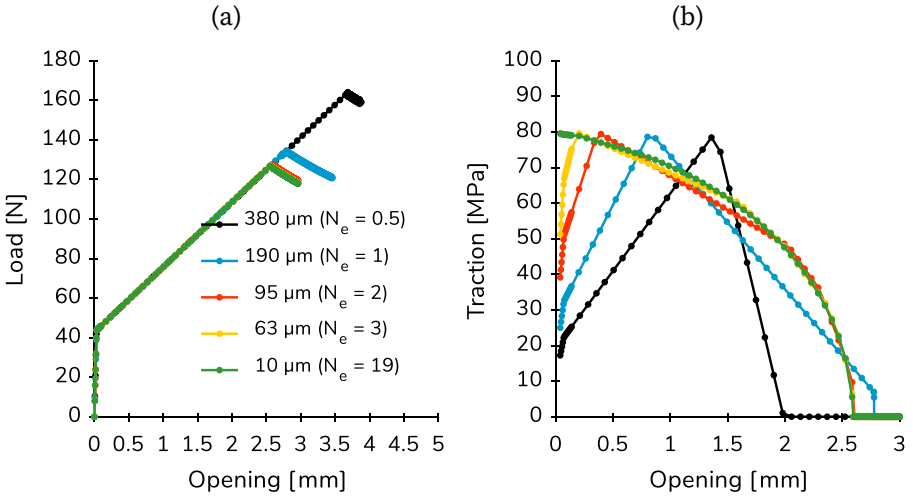

Figure 7-7. (a) Load-displacement curves predicted with different degrees of mesh refinement in the cohesive zone. (b) Corresponding evolution of the cohesive traction on the cohesive node at the initial crack tip.

Again, results obtained locally in the cohesive zone were used to challenge the conclusion based on global results, i.e. load-displacement curves. Figure 7-7-(b) indeed reveals that the evolution of the cohesive traction at the initial crack tip node for N_e equals 2 already departs from that of the reference, finely meshed, simulation. The traction obviously reaches its maximum value with a certain delay when the length of the cohesive zone spans two or less cohesive elements. So, although there was no significant difference in the load-displacement curves obtained with N_e between 2 and 19, the evolution of the cohesive traction shows that it would be preferable to have at least three quadratic elements on the cohesive zone length.

It is worth noting that the values of l_{cz} obtained analytically (152 µm) and numerically (190 µm) are close but not identical. It was decided, for the rest of the study, to guarantee mesh convergence by use of Eq. (7-3) and $N_e = 3$, which provides the most conservative mesh refinement requirement.

A consistent frame has been set for simulation of crack growth in the DCB test specimen. The last part of the study thus naturally consists in identifying proper values for G_{Ic} and σ^0. For this purpose, the results of the simulations will be compared with the experimental ones.

7.3.3 Identification of a value for the mode I critical SERR

The critical strain energy release rate has been introduced in Chapter 2 (Section 2.3.6). Shortly, it represents the energy needed to create a unit of new crack faces. In the context of FE analysis with cohesive elements, this quantity determines the separation that must be reached within the pairs of cohesive nodes for *failure* to take place. On the load-displacement curve, an increase in critical energy release rate thus translates into a shift of crack *propagation* to larger values of opening.

Nonlinear analyses of the DCB test were performed with five values of G_{Ic} between 170 Jm^{-2} and 440 Jm^{-2}. In view of ensuring mesh convergence, the length of the cohesive elements was always determined so that three elements were found on the cohesive zone length.

Figure 7-8 shows the load-displacement curves obtained with the different values of critical SERR. The critical SERR obviously has a strong influence on the *onset of crack propagation* as it clearly appears to control the value of the maximum load. However, it did not seem to have such an influence on crack propagation itself as the slope of the curve in the softening region was found to be almost independent of the value given to the critical SERR.

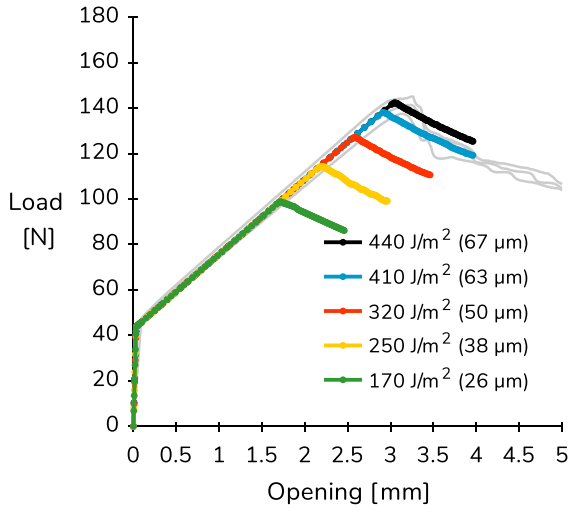

Figure 7-8. Experimental load-displacement traces (in grey) and load displacement curves predicted with different values of $\boldsymbol{G_{Ic}}$. The cohesive elements lengths used for the FE analyses are given in parentheses.

Clearly, the values of 170 Jm^{-2} (graphical κ_{res}) and 250 Jm^{-2} (peel) did not allow reproducing the experimental results as they conferred a much too brittle character to the co-cured joint. The value of 330 Jm^{-2} (measured κ_{res}) allowed more closely approaching the experimental results but still underestimated the fracture toughness of the joint. Finally and quite surprisingly, the critical SERR of 440 Jm^{-2} (no correction for κ_{res}) proved to perform much better at matching the experimental results. More precisely, a more conservative match was obtained when G_{Ic} was given the value of 410 Jm^{-2}, which is practically the same as that obtained experimentally with the CBT and ECM standard data reduction schemes (408 Jm^{-2}). This value was thus retained for the last part of the inverse analysis, which consists in the identification of an appropriate value for the peak stress.

7.3.4 Identification of a value for the mode I peak stress

The peak stress determines the critical separation that must be reached within the pairs of cohesive nodes for *irreversible* damage to initiate[37]. On the load-displacement curve, an increase in peak stress thus translates into a shift of crack *initiation* to larger values of opening.

Nonlinear analyses of the DCB test were performed with four values of σ^0 between 50 MPa and 300 MPa. Again, the length of the cohesive elements was determined so that three elements were found on the cohesive zone length for each analysis.

Figure 7-9 shows the load-displacement curves obtained with the smallest and largest values of peak stress.

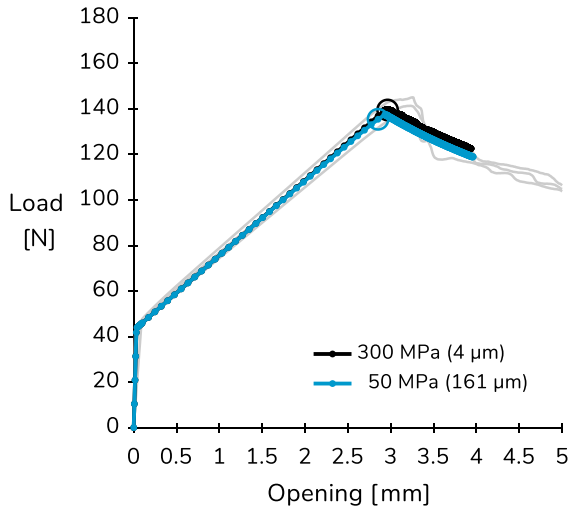

Figure 7-9. Experimental load-displacement curves (in grey) and load displacement curves predicted with different values of σ^0. The empty circles mark the crack initiation points. The cohesive elements lengths used for the FE analyses are given in parentheses.

[37] For a given value of penalty stiffness.

Crack initiation was detected using a method already employed in Chapter 6 for the determination of the non-linear initiation point on the experimental load-displacement curves. It is thus defined as the first point at which the curve deviates by more than 1 % from the initial compliance. This point is marked with a circle on the predicted curves. The force-displacement couple corresponding to total damage of the crack tip cohesive nodes was extracted from the results of all three simulations. It was each time found to coincide almost exactly with the non-linear initiation point.

Damage began slightly sooner with the low peak stress value than with the large one. The appearance of the curve was otherwise very little affected by a change in peak stress: the maximum force did only very slightly increase with the peak stress while the softening slope remained virtually unchanged. The dominant parameter regarding these two features is thus the critical SERR, as presupposed in the previous section.

Similar conclusions have been drawn by various authors concerning the quite small influence of the cohesive strength on the output of DCB test simulations [110][189][121]. Hence, it was decided to abandon the value of 300 MPa that causes a significant increase in computational expense as (i) it requires the use of particularly small cohesive elements (4 µm) and (ii) it increases the instability of the nonlinear analysis. The time required for the computation hence for instance jumped from 2.73 to 387.25 CPU hours[38] when the value of σ^0 was increased from 50 MPa to 300 MPa. The limited influence of this parameter in this elastic case is not worth such an increase in computational cost, but please note that this conclusion might not be true in case plastic flow was allowed to occur in the co-cured joint.

[38] With a 3.00 GHz Intel® Core™ i7 – 3940XM processor equipped with 32.0 GB RAM.

The value of 80 MPa was retained amongst the three initial candidates: it represents the experimentally measured fracture strength of the RTM6 resin that received more credit than the fracture strength measured for the Redux 322 adhesive.

7.4 Validation of the 2D approach with the 3D model

As noted previously, the 2D FE model of the DCB test comprises more simplifying assumptions than a 3D FE model. Yet, it has been used so far as an efficient tool for the parametric study and the inverse FE analysis procedure. In view of assessing the parameters values identified with this model, a nonlinear analysis was performed with the 3D FE model of the DCB test, using the same set of parameters. Information concerning the characteristic size and the computational cost of this model is given in Table 7-5, together with the characteristics of the equivalent 2D model. The resulting load-displacement curve is displayed in Figure 7-10, along with its 2D counterpart plotted for comparison.

Table 7-5. Characteristic size and CPU time of the 2D and 3D models with the 63µm-long cohesive elements complying with the pair $(G_{Ic}, \sigma^0) = (410\ \mathrm{Jm^{-2}}, 80\ \mathrm{MPa})$.

Model	# nodes	# DOF	CPU time [hours]	Processor
2D	45,007	90,271	3.45	4 cores Intel Core i7-3940 XM @ 3.00 GHz with 16.0 GB RAM
3D	402,719	1,207,155	882.65	18 cores Intel Xeon Gold 6140 @ 2.30 GHz with 128 GB RAM

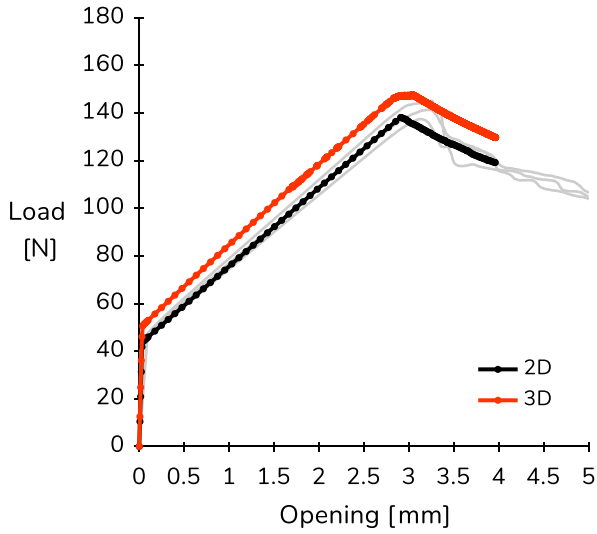

Figure 7-10. Experimental load-displacement traces (in grey) and load displacement curves predicted with the 2D and 3D FE models, with the pair $(G_{Ic}, \sigma^0) = (410\ \mathrm{Jm^{-2}}, 80\ \mathrm{MPa})$.

Clearly, despite a slight overestimation of the predicted force at "zero" displacement, the 3D FE simulation captured quite accurately the experimental behaviour of the co-cured DCB test specimen in terms of initial compliance, opening at maximum load, and softening upon crack growth. This confirms the ability of the pair $(G_{Ic}, \sigma^0) = (410\ \mathrm{Jm^{-2}}, 80\ \mathrm{MPa})$ to fairly well reproduce the fracture behaviour of the co-cured joint under mode I loading, thereby demonstrating the thrustworthiness of the 2D approach for the identification of these parameters. This is definitely good news given that the 2D analysis was completed in just a few hours on a personal computer while the 3D analysis had to be performed on a powerful compute server and still took more than a month to complete (as indicated in Table 7-5). Finally, this result also highlights the quality of the geometrical, mechanical and thermal input data, the last two categories of which were carefully derived from physical tests campaigns.

7.5 Preliminary identification of the fracture envelope and the mode coupling coefficient

Although there was unfortunately no time for the inverse FE analysis of the FRMM and ELS tests on the duration of this thesis, it would be a pity to close this work without exploiting the experimental and numerical knowledge of the critical SERRs gained throughout Chapter 6 and Chapter 7. T in a preliminary attempt to determine the fracture envelope of the co-cured joint. This, of course, is not a pure mode I subject anymore, but it would have been excessive to isolate this small section in a dedicated new chapter following this one.

The inverse finite element analysis of the DCB test indicated that, despite the residual stresses present in the specimen, the mode I toughness of the fresh co-cured joint was correctly evaluated with the analytical ECM and CBT standard reduction schemes. Based on that, and because only aged specimens were tested in the two other fracture modes, one selected for the fracture envelope the values of G_c obtained with the ECM scheme and characterising the toughness of the « 1 year aged » co-cured joint (i.e. 341 Jm^{-2} in mode I, 1012 Jm^{-2} in mixed mode, 2163 Jm^{-2} in mode II). These experimental data points are drawn in red in Figure 7-11, together with several fit attempts produced by varying the curve fitting parameters α and η of the power law and the Benzeggagh-Kenane 2D mixed mode criteria, the equations of which (expressed as a function of the mixed mode ratio β) are given in the figure. As introduced in Chapter 2 (Section 2.3.7), these criteria are respectively used in SAMCEF (via Eq. (2-68)) and ABAQUS [190] to describe the dependence of the fracture energy on the mode mix.

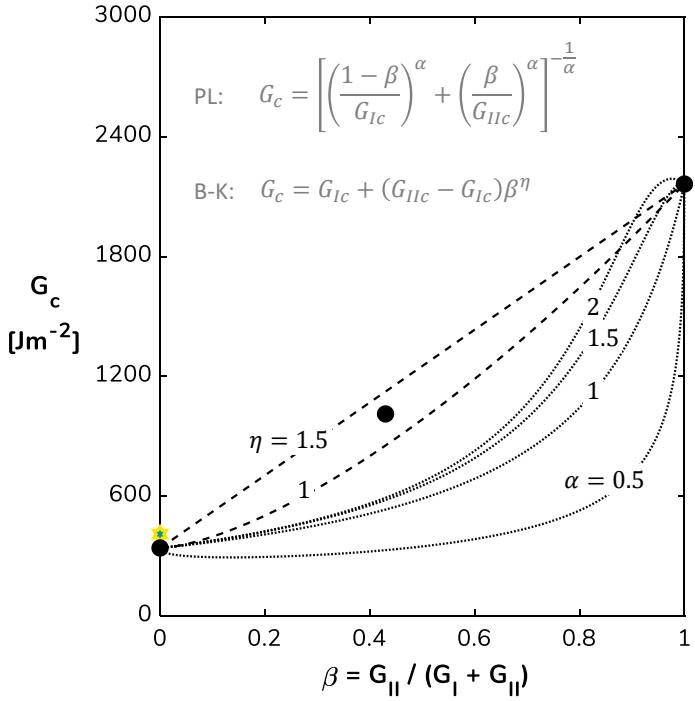

Figure 7-11. Experimental critical SERRs of the "1 year aged" co-cured joint obtained with the ECM schemes, and attempts of extrapolating the aged co-cured joint's fracture envelope with the power law (PL) and the Benzeggagh-Kenane (B-K) 2D mixed mode fracture criteria. The yellow star on the vertical axis represents the mode I fracture toughness of the fresh co-cured joint identified by inverse FE element analysis in this chapter.

It was obviously impossible to fit the experimental data with the power law criterion, indicating that this criterion is not able to reproduce the mixed mode fracture behaviour of the aged co-cured joint. Increasing the mode coupling coefficient α above 2 did not help straightening the curve and even produced a peak in the high mode II region that is hardly explainable for an actual material, as already noted in an anterior study [69]. The B-K criterion performed much better at fitting the experimental data points. A value of 1 would be retained for the curve fitting parameter η, as the extrapolated fracture envelope is then slightly conservative with regards to the measured mixed mode fracture toughness of the « 1 year aged » co-cured joint.

7.6 Conclusion

The mode I triangular cohesive law was calibrated for the simulation of damage in the co-cured joint by inverse FE analysis. The load-displacement curve predicted by a 2D FE model of the DCB test was fitted to the experimental curves using a value of 410 Jm^{-2} for the SERR, which is practically the same as that obtained experimentally with the standard data reduction schemes ignoring the effect of residual stresses. The peak stress value was shown to negligibly influence the simulation output in this case where the mechanical behaviour of the co-cured joint has been assumed linear elastic, and it was thus set to 80 MPa, that is, the experimentally determined fracture strength of the RTM6 resin. The complete set of cohesive law parameters identified with the 2D model also allowed quite successfully matching the experimental results when incorporated to a 3D FE model of the DCB test. This legitimates the use of the former model for the inverse FE analysis despite the simplifying assumptions it contains, which greatly reduces the expense of the simulations. Finally, the preliminary attempt to extrapolate the fracture envelope of the "1 year aged" co-cured joint showed that the PL criterion cannot capture the mixed mode fracture response of the joint properly, while the B-K criterion provides a much better fit of the experimental data.

The main outputs of this FE study are summarised in Table 7-6 which lists the values identified for the parameters of the cohesive law describing mode I fracture of the fresh co-cured joint.

Table 7-6. Final set of parameter values identified for the description of the mode I fracture of the fresh co-cured joint with a triangular cohesive law.

Penalty stiffness	K^0	10^7	Nmm^{-3}
Discretisation of the FPZ	N_e	3	elements
Peak stress	σ^0	80	MPa
Mode I critical SERR	G_{Ic}	410	Jm^{-2}
Characteristic time	τ_c	10^{-4}	s

8. Conclusion and perspectives

This final chapter comprises the review of the contributions made in this doctoral research, and the description of several development areas for the continuation of the work carried out in this thesis.

8.1 Conclusion

The objective of this doctoral thesis was to develop a FE model capable of predicting thermomechanical damage of the multilayer, which would be a valuable tool for the establishement of a solution to this current issue. A scientific research methodology has been developed to work towards this objective, and could definitely be followed, in whole or in part, to accompany future changes in the design of the present multi-layered system.

In Chapter 3, the damage state of the multi-layered system was examined based on hundreds of optical micrographs from cross-sections of composite booster casings at different production stages and with different degrees of thermal ageing. For the first time in the history of this project, the critical areas and the types of defects were listed and the damage state of these zones was objectively quantified with a statistical analysis, highlighting the effect of the above-cited casing's characteristics. Clearly, the inter-segments gaps require special attention from designers and numericians, as they stood out as the most damaged zone. The major type of damage in this zone were microcracks, which remained sparse and confined to the co-cured joint before

thermal spray but multiplied and extended to the first laminae of the composite substrate under the effect of the tensile residual stresses generated there during plasma spray and thermal shock. The criticality of these transverse microcracks has yet to be examined. In addition to the statistical study, the 3D path and morphology of a microcrack at an ISG was revealed with a specially designed incremental polishing technique, yielding essential information for the FE modelling. The damage mechanism hypothesis that we formed based on these observations suggests improving the steel/epoxy interfacial bond strength (e.g. with a primer) as a solution to the initiation of damage in the ISG.

In Chapter 4 we presented the values of several thermal and mechanical properties of the constituent materials measured with a number of advanced characterisation techniques. Dynamic mechanical analysis and the Resonalyser procedure provided the most direct access to the elastic behaviour of the materials, DMA furthermore allowing to follow its temperature-dependent evolution. Macroscopic tensile tests, however, although more labour and material-intensive, remain the most established technique for accessing the mechanical behaviour of a very wide range of materials and its evolution up to fracture. It is thus advised that mechanical test campaigns on new candidate materials at least comprise this last category of characterisation technique. This whole experimental work nevertheless yielded a valuable and reliable source of input data for the definition of the materials constitutive laws in the FE model of the multi-layered system.

In Chapter 5, the thermally induced residual stress level was evaluated by different means. The stress tensor in the co-cured steel strip was physically accessed for the first time using the advanced X-ray stress analysis technique. This experimental approach was valuable in at least two ways. First, although the in-plane stress components were systematically lower than

those estimated with the other methods (probably due to some stress relaxation in the samples cut from larger specimens), the fact that they had the same sign and order of magnitude than the other results made them reference values for the assessment of these other results. Second, these measurements highlighted the need for considering the anisotropy of the carbon laminae adjoining the co-cured joint, as it makes the in-plane stress anisotropic as well. For this reason, estimating the residual stress state in the steel strip based on the measured curvatures of a multi-layered sample (with the Stoney formula) is actually not recommended. The residual stress profile through the full thickness of the multilayer was approached with a closed-form analytical development. It showed that the co-cured joint undergoes tensile stresses at the end of the RTM process while the top surface of the composite is in compression, which correlates well with the observation of microcracks confined in the joint layer at that stage of the manufacturing process. Finally, the residual stress profile was predicted with a FE model of the multi-layered system specifically developed and progressively refined in light of the previous stress results. The residual stress fields at the ISG obtained with this model revealed several loci of stress concentration, consistent with the loci of damage initiation observed in a multitude of cross-sections of the casings and with the hypothesis formulated about the damage mechanism at the ISG. In view of these results, it is advisable to avoid the presence of cut micro-perforations on the contour of the steel strip segments, for instance by revising the mask used for chemical etching. Last but not least, allowing for plastic flow of the polymer material in the co-cured joint would make this model a proper tool for a “maximum stress at a distance criterion” approach to fracture (e.g. [191]).

In Chapter 6, we exposed the results of the experimental measurement of the mode I, mode II and mixed mode I/II critical SERR of the co-cured joint by means of state-of-the-art tests such as the fixed arm peel test and the DCB,

ELS and FRMM fracture tests. The careful interpretation of the unconventional shape of the load-displacement curves resulting from the DCB tests highlighted that the specimens produced for this purpose were actually subject to thermally induced residual stresses. This unforeseen characteristic modified the direction of the thesis as it complicated the evaluation of the critical SERRs. Retrospectively, although a true value of SERR can be derived by properly post-processing these tests data, it is strongly recommended to design the multilayered tests specimens with a symmetrical layup of the arms, so that their bending under the effect of the processing residual stresses can be avoided. Finally, the fixed arm peel test proved to be an efficient test method for the measurement of the adhesive fracture energy. Indeed, it is easy to perform (insofar the sliding test fixture is available) and post-process (insofar plastic strain of the peel arm remains in a reasonable range); and the offset of the present peel test results with the mode I LEFM test results is believed to be due to an unforeseeen difference in composition of the co-cured joint from one type of specimen to the other, rather to a difference in test method. Moreover, the peel tests results clearly demonstrated the advantage of using micro-perforated instead of as-rolled steel strips in the long term.

In Chapter 7, the experimental DCB tests results were post-treated by inverse FE analysis with special attention given to the reproduction of the thermally induced residual stress state of the physical test specimen. The FE model of the DCB test was developed with wise choices of model parameters such as mesh refinement, loading scheme, material properties and cohesive law parameters. This numerical work resulted in the identification of a realistic couple of values for the $(\hat{\sigma}, G_{Ic})$ pair, thereby calibrating the cohesive law for mode I fracture. The value of 410 J/m^2 identified for the mode I critical SERR being practically equal to that obtained with the analytical ECM and CBT standard data reduction schemes seems to indicate that the presence of re-

sidual stresses in the fracture specimens did finally not have such an influence on the measured toughness of the co-cured joint. This model and the associated parametric study anyway clearly pave the way for the inverse FE analysis of the ELS and FRMM tests, for which such conclusion on the influence of residual stresses has not been drawn yet.

8.2 Perspectives

Despite our continuous efforts, work remains to do to complete the vast project undertaken in this doctoral research. It is summarised in the following sequence of points:

- Inverse FE analysis of the ELS and FRMM fracture tests

The experimental data acquired with the ELS and FRMM tests were treated with standard data reduction schemes that might be too basic considering the presence of residual stresses in the fracture specimens. Given the clarifications gained with the inverse FE analysis of the DCB test, it is recommended to follow the same procedure for the ELS test so as to ascertain the value of peak stress and critical SERR to be used for the proper simulation of mode II fracture of the co-cured joint. Then, the identified mode I and mode II cohesive parameters should be grouped in a common cohesive law for the inverse FE analysis of the FRMM test. Fitting the numerical result to the mixed mode experimental load-displacement curves would finally allow determining a value for α, the coefficient controlling the shape of the fracture envelope in the power law type fracture criterion used in this work. This part might actually require, if feasible, implementing a more performant fracture criterion in SAMCEF, since the available PL one could not fit the mixed mode experimental data point in Chapter 7 (Figure 7-11).

- Introduction of the bond coat and abradable coating in the FE model of the multilayer

The bond coat and the abradable coating play, without a doubt, a major role in the build-up of residual stresses, both during their projection by plasma spray, and during the subsequent thermal cycles in service. The presence of these layers should therefore not be neglected in the FE model of the multilayer, where they could first be directly added with their final thickness. Note that the thermoelastic properties of these materials are already approximately known by SAB, which also possesses experimental curvature data recorded during plasma spray.

- Progressive damage analysis of the multi-layered system

Nonlinear FE analyses should be performed on the model of the multilayer with the calibrated mixed mode cohesive law. The extent of damage predicted under various realistic thermal loads would then be critically examined in light of the outcome of the statistical study of the multilayer's damage state. The effect of the presence of the bond coat and abradable coating could be studied as well, as another way of checking the predictive capabilities of the model.

- Evaluation of practical changes in materials and/or geometry

It has transpired from the present work that the combination of materials chosen for the development of the composite booster casing was not ideal, considering the level of thermally induced residual stresses and their damaging effect. Although there is relatively little leeway when it comes to selecting materials for aerospace applications it is probably necessary to make some changes. For instance, the epoxy resin and adhesive used in this project are relatively brittle materials; using a tougher adhesive may allow eliminating the issue of initiation and growth of microcracks. The predictive FE model of the multilayer would be an excellent ally in this task.

- Extension of the local FE model to the compressor scale

The very initial objective of this research project was to culminate in the development of a predictive FE model at the casing's scale, to which more comprehensive load cases could be applied, e.g. combining thermal and mechanical loads. This objective could finally not be met in the course of this doctoral research, which has rather contributed to prepare and put together several building blocks needed to achieve this goal. Given the size of such model, profound modifications of the modelling hypotheses will be required to keep it computationally tractable, as compared to those used in the local FE model of the multilayer.

A. Dundurs' parameters

As introduced in Section 2.3.7.3, the mismatch in elastic properties at a bimaterial interface is described by the Dundurs' parameters, α and β. They are respectively given in Eq. (A-1) and Eq. (A-2) [58], where $\bar{E}$ is the plane strain or plane stress modulus, μ is the shear modulus, and $\kappa = 3 - 4\nu$ in plane strain or $(3 - \nu)/(1 + \nu)$ in plane stress. These parameters vanish when there is no mismatch, and change sign if material 1 and material 2 are switched.

$$\alpha = \frac{\bar{E}_1 - \bar{E}_2}{\bar{E}_1 + \bar{E}_2} \tag{A-1}$$

$$\beta = \frac{\mu_1(\kappa_2 - 1) - \mu_2(\kappa_1 - 1)}{\mu_1(\kappa_2 + 1) + \mu_2(\kappa_1 + 1)} \tag{A-2}$$

B. Kinking, penetration, and deflection of an interface crack

As briefly introduced in Section 2.3.7.3, bimaterial interfaces induce some competition between several propagation modes: an interface crack may grow *straight-ahead in the interface* or it may *kink out of the interface*, an impinging crack may *penetrate through the interface* or it may be *deflected into the interface*.

B.1 Crack kinking

Interface cracks face some competition between the propagation modes illustrated in Figure 2-9: the crack may grow *straight-ahead in the interface* or it may *kink out of the interface*, with an angle Ω that usually minimises the mode II contribution to the SERR [58]. When the interface crack is loaded such that G increases monotonically and $\psi > 0$ is fixed, it will kink into material 2 if the criterion in Eq. (B-1) is satisfied [73]. In this equation, G^t_{max} represents the maximum value of G at the tip of the small putative kinked crack over all Ω for a given (G, ψ) pair, and G_c is the mode I fracture toughness of material 2. The left-hand-side ratio has been determined against ψ for various levels of elastic mismatch (with $\beta = 0$)[73].

$$\frac{G}{G^t_{max}} < \frac{G_c(\psi)}{G_c} \tag{B-1}$$

B.2 Crack penetration/deflection

When a crack impinges an interface, the competition rather lies between crack *penetration* through the interface and crack *deflection* into the interface, as illustrated in Figure 2-11. In fact, crack penetration occurs when the criterion defined in Eq. (B-2) is satisfied [74], where $G^{t,d}$ and $G^{t,p}$ do respectively denote the energy release rate of the deflected interface crack and that of the penetrating crack, the latter being also characterised by the mode mixity angle, ψ.

$$\frac{G^{t,d}}{G^{t,p}} < \frac{G_c(\psi)}{G_c} \tag{B-2}$$

Again, the left-hand-side ratio has been determined for a variety of elastic mismatches (still with $\beta = 0$). It came out that, when the elastic mismatch parameter is close to zero, crack penetration is more likely than crack deflection if the interface toughness exceeds about one fourth of the toughness of the material to be penetrated; otherwise, when $\alpha \cong 0.5$, the critical ratio increases to about one half [74].

C. Derivation of the analytical expression of G_{II} for the ELS test

The short development below refers to the beam model of the ELS test illustrated in Figure 2-15 of Section 2.4.2.3.

Upon application of Eq. (2-42) and Eq. (2-43), the deflection of the beams is given by Eq. (C-1), where $I_1 = 2(Bh^3/12)$ is twice the moment of inertia of a single beam, and $I_2 = (B(2h)^3/12)$ is the moment of inertia of the specimen ahead of the crack tip. Solving this equation yields Eq. (C-2), which can be used to derive an expression for the compliance knowing that $C = u/P$.

$$u = \int_0^a \frac{M}{EI_1}\frac{\partial M}{\partial P}dx + \int_a^{L_F} \frac{M}{EI_2}\frac{\partial M}{\partial P}dx \tag{C-1}$$

$$u = \frac{(3a^3 + L_F^3)P}{2EBh^3} \tag{C-2}$$

Finally, using the Irwin-Kies equation (Eq. (2-41)), one obtains the analytical expression for the mode II SERR:

$$G_{II} = \frac{9P^2a^2}{4EB^2h^3} \tag{C-3}$$

D. Derivation of the analytical expression of $G_{I/II}$ for the FRMM test

The short development below refers to the beam model of the FRMM test illustrated in Figure 2-16 of Section 2.4.2.4.

The deflection u is expressed by Eq. (C-1), as for the ELS test, except that I_1 is now the moment of inertia of a single beam, i.e. $I_1 = Bh^3/12$. Solving this equation yields Eq. (D-1), which can be used to derive an expression for the compliance.

$$u = \frac{(7a^3 + L_F^3)P}{2EBh^3} \tag{D-1}$$

Finally, the analytical expression for $G_{I/II}$ given in Eq. (D-2) is obtained by invoking the Irwin-Kies equation.

$$G_{I/II} = \frac{21P^2a^2}{4EB^2h^3} \tag{D-2}$$

E. Derivation of the analytical expression of G_{db}, the total energy dissipated in bending of the peel arm

The development below completes that given in Section 2.4.3.3 for the derivation of the adhesive fracture energy G_a. This quantity, as a reminder, can be expressed as the difference of the adhesive fracture energy for elastic bending (G_a^{eb}) and the total energy dissipated in the peel arm (G_{db}) [79]. This writes

$$G_a = G_a^{\mathrm{eb}} - G_{\mathrm{db}} \tag{E-1}$$

G_{db}, is evaluated with the large displacement beam theory [100]. It is given by the area OABCO in the moment-curvature diagram in Figure E-1, and can be expressed as

$$G_{\mathrm{db}} = \hat{G} f_1(k_0) \tag{E-2}$$

where $f_1(k_0)$ is a function dependent on the stress-strain characteristics of the peel arm material that has been solved analytically for the bi-linear and the power law work hardening material models [79][192], and $\hat{G}$ represents the maximum energy per unit width that can be stored in an elastic-perfectly plastic material, as given by Eq. (E-3) [80].

$$\hat{G} = \frac{hE\varepsilon_y^2}{2} \tag{E-3}$$

Besides, the total energy input into the system via bending is given by the area OFABCO in the moment-curvature diagram, and it can be shown that it writes [80]

$$G_{\mathrm{b}} = \frac{P}{B}[1 - \cos(\theta - \theta_0)] = \hat{G} f_2(k_0) \tag{E-4}$$

where $f_2(k_0)$ is a function similar to $f_1(k_0)$, which has been solved for the same material models. The root rotation θ_0 is determined by means of a beam on elastic foundation analysis [100]. Then, k_0 is evaluated with Eq. (E-4) and used to evaluate G_{db} via Eq. (E-2). Finally, having quantified G_a^{eb} and G_{db}, the adhesive fracture energy may be calculated with Eq. (E-1).

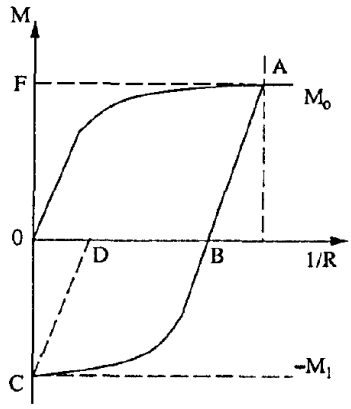

Figure E-1. Moment-curvature diagram of the peel arm [79]

F. Classical Lamination Theory for the prediction of the effective thermoelastic properties of laminated media

F.1 Introduction

This theory allows calculating the *macroscopic effective* properties of anisotropic layered media, based on their layup and the properties of the individual layers (laminae). The use of CLT is widespread; it comes in numerous models differing in their mathematical development and notations, or in their range of application. Among them, the three-dimensional semi-analytical model developed by Gudmundson and Zang [133] was used in this work. It was converted to a Matlab script automating the calculation of effective properties for different laminate configurations. The homogenisation procedure for the calculation of effective engineering constants is summarised in Figure F-1, and the associated mathematical development is thoroughly described further in this appendix.

In brief, the constitutive stress-strain relations of the laminae are first written in the principal material (lamina) coordinate system, based on the engineering constants and material symmetry of each type of lamina. Stiffness matrices are hence obtained for each type of lamina.

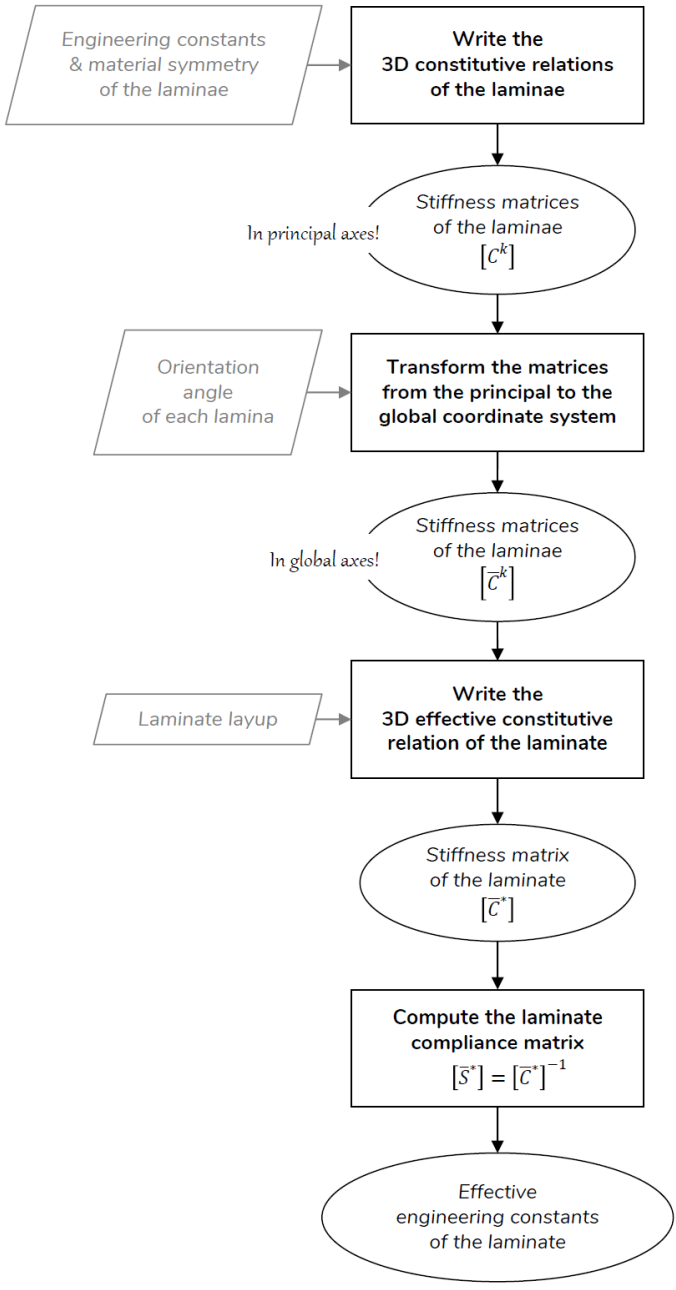

Figure F-1. Flowchart of the homogenisation procedure used to predict the effective elastic constants of the composite laminate.

Knowing the orientation angle of each lamina, one then performs a second order tensor transformation so as to express the stiffness matrices in the global (laminate) coordinate system. The effective constitutive stress-strain relation of the laminate is subsequently constructed from the stiffness matrices of the individual laminae and the knowledge of the laminate layup. This also involves setting restrictions on the stress and strain of each lamina - ensuring the uniformity of out-of-plane stress components and in-plane strain components within a lamina, and their continuity across the lamina interfaces. The coefficients of the effective stiffness matrix of the laminate are thereby determined. Finally, the effective engineering constants of the homogeneous equivalent material are extracted from the laminate compliance matrix which is itself obtained by inversion of the laminate stiffness matrix. The effective linear coefficients of thermal expansion were calculated as well in the homogenisation procedure.

F.2 Model by Gudmundson and Zang

The model developed by Gudmundson and Zang [133] provides the constitutive relationship defining the effective stress-strain response of an anisotropic composite laminate based on the properties of the individual layers. Effective thermoelastic properties may therefrom be derived, which can be used as input of analytical and FE calculations where the composite laminate would be modelled as a homogeneous equivalent solid.

The laminate is made of N layers, called laminae, which generally are anisotropic. They are defined by their properties and thickness, and by the angle formed by their own coordinate axes with respect to the global axes of the laminate (Figure F-2).

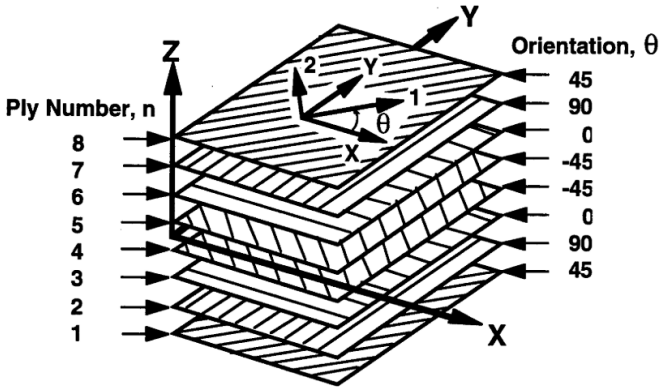

Figure F-2. Schematic example of laminate layup showing therelative orientations of the global (x, y, z) and principal (1, 2, 3) axes system [193].

F.2.1 Constitutive relation of the lamina

The constitutive stress-strain relation of each individual lamina is given by Eq. (F-1), which takes thermal strain and residual stress into account[39].

$$\{\varepsilon^k\} = [S^k](\{\sigma^k\} - \{\sigma^{k(\mathrm{r})}\}) + \{\alpha^k\}\Delta T \tag{F-1}$$

The superscript k denotes that the quantities pertain to the kth lamina in the stacking sequence of the laminate.

In the developed form, this relation writes as in Eq. (F-2), where the compliance matrix $[S^k]$ is defined in Eq. (F-3).

$$\begin{Bmatrix} \varepsilon_{11}^k \\ \varepsilon_{22}^k \\ \varepsilon_{33}^k \\ 2\varepsilon_{23}^k \\ 2\varepsilon_{13}^k \\ 2\varepsilon_{12}^k \end{Bmatrix} = [S^k] \left(\begin{Bmatrix} \sigma_{11}^k \\ \sigma_{22}^k \\ \sigma_{33}^k \\ \sigma_{23}^k \\ \sigma_{13}^k \\ \sigma_{12}^k \end{Bmatrix} - \begin{Bmatrix} \sigma_{11}^{k(\mathrm{r})} \\ \sigma_{22}^{k(\mathrm{r})} \\ \sigma_{33}^{k(\mathrm{r})} \\ \sigma_{23}^{k(\mathrm{r})} \\ \sigma_{13}^{k(\mathrm{r})} \\ \sigma_{12}^{k(\mathrm{r})} \end{Bmatrix} \right) + \begin{Bmatrix} \alpha_{11}^k \\ \alpha_{22}^k \\ \alpha_{33}^k \\ 2\alpha_{23}^k \\ 2\alpha_{13}^k \\ 2\alpha_{12}^k \end{Bmatrix} \Delta T \tag{F-2}$$

[39] For instance those due to chemical shrinkage of the polymer matrix.

$$[S^k] = \begin{bmatrix} S^k_{1111} & S^k_{1122} & S^k_{1133} & S^k_{1123} & S^k_{1113} & S^k_{1112} \\ S^k_{2211} & S^k_{2222} & S^k_{2233} & S^k_{2223} & S^k_{2213} & S^k_{2212} \\ S^k_{3311} & S^k_{3322} & S^k_{3333} & S^k_{3323} & S^k_{3313} & S^k_{3312} \\ S^k_{2311} & S^k_{2322} & S^k_{2333} & S^k_{2323} & S^k_{2313} & S^k_{2312} \\ S^k_{1311} & S^k_{1322} & S^k_{1333} & S^k_{1323} & S^k_{1313} & S^k_{1312} \\ S^k_{1211} & S^k_{1222} & S^k_{1233} & S^k_{1223} & S^k_{1213} & S^k_{1212} \end{bmatrix} \tag{F-3}$$

The compliance matrix of an orthotropic lamina is symmetric and its coefficients can further be defined as a function of the engineering constants of the lamina, as in Eq. (F-4) [194].

$$[S^k] = \begin{bmatrix} 1/E_1 & -\nu_{21}/E_2 & -\nu_{31}/E_3 & 0 & 0 & 0 \\ -\nu_{12}/E_1 & 1/E_2 & -\nu_{32}/E_3 & 0 & 0 & 0 \\ -\nu_{13}/E_1 & -\nu_{23}/E_2 & 1/E_3 & 0 & 0 & 0 \\ 0 & 0 & 0 & 1/G_{23} & 0 & 0 \\ 0 & 0 & 0 & 0 & 1/G_{13} & 0 \\ 0 & 0 & 0 & 0 & 0 & 1/G_{12} \end{bmatrix} \tag{F-4}$$

Note that this constitutive relation is for now expressed in the principal coordinate system of the lamina, which is not necessarily aligned with the global coordinate system of the laminate. Therefore, in order to derive the constitutive relation of the laminate, the components of stress, strain, the coefficients of the compliance matrix and the thermal expansion coefficients of each lamina should first be expressed in the coordinate system of the laminate.

F.2.2 Transformation from the lamina (principal) to the laminate (global) coordinate system

This change of coordinate system is achieved with a second order tensor transformation as in Eq. (F-5) and (F-6) [194], where the upper bar denotes that the quantity is expressed in the global axes of the laminate.

$$\{\bar{\sigma}^k\} = [T^\sigma]\{\sigma^k\} \tag{F-5}$$

$$\{\bar{\varepsilon}^k\} = [T^\varepsilon]\{\varepsilon^k\} \tag{F-6}$$

The stress and strain transformation matrices $[T^\sigma]$ and $[T^\varepsilon]$ write in terms of the orientation angle θ^k of the lamina as in Eq. (F-7) and (F-8), with $c = \cos\theta^k$ and $s = \sin\theta^k$ [194].

$$[T(\theta^k)^\sigma] = \begin{bmatrix} c^2 & s^2 & 0 & 0 & 0 & -2cs \\ s^2 & c^2 & 0 & 0 & 0 & 2cs \\ 0 & 0 & 1 & 0 & 0 & 0 \\ 0 & 0 & 0 & c & s & 0 \\ 0 & 0 & 0 & -s & c & 0 \\ cs & -cs & 0 & 0 & 0 & (c^2 - s^2) \end{bmatrix} \tag{F-7}$$

$$[T(\theta^k)^\varepsilon] = \begin{bmatrix} c^2 & s^2 & 0 & 0 & 0 & -cs \\ s^2 & c^2 & 0 & 0 & 0 & cs \\ 0 & 0 & 1 & 0 & 0 & 0 \\ 0 & 0 & 0 & c & s & 0 \\ 0 & 0 & 0 & -s & c & 0 \\ 2cs & -2cs & 0 & 0 & 0 & (c^2 - s^2) \end{bmatrix} \tag{F-8}$$

The constitutive relation of the lamina originally expressed in its principal coordinate system (Eq. (F-1)) now writes in the coordinate system of the laminate as in Eq. (F-9).

$$\{\bar{\varepsilon}^k\} = [T^\varepsilon]\{\varepsilon^k\} = [T^\varepsilon]\left([S^k]\left(\{\sigma^k\} - \left\{\sigma^{k(r)}\right\}\right) + \{\alpha^k\}\Delta T\right)$$

$$\{\bar{\varepsilon}^k\} = [T^\varepsilon][S^k][T^\sigma]^{-1}\left(\{\bar{\sigma}^k\} - \left\{\sigma^{k(r)}\right\}\right) + [T^\varepsilon]\{\alpha^k\}\Delta T$$

$$\{\bar{\varepsilon}^k\} = [\bar{S}^k]\left(\{\bar{\sigma}^k\} - \left\{\sigma^{k(r)}\right\}\right) + \{\bar{\alpha}^k\}\Delta T \tag{F-9}$$

Which means that the compliance matrix $[S^k]$ and the vector of thermal expansion coefficients $\{\alpha^k\}$ were transformed as shown in Eq. (F-10) and (F-11).

$$[\bar{S}^k] = [T^\varepsilon][S^k][T^\sigma]^{-1} \tag{F-10}$$

$$\{\bar{\alpha}^k\} = [T^\varepsilon]\{\alpha^k\} \tag{F-11}$$

F.2.3 Constitutive relation of the laminate

The stress-strain constitutive relation of the laminate may now be constructed. The global stresses $\{\bar{\sigma}^*\}$ and strains $\{\bar{\varepsilon}^*\}$ acting in the laminate are therefore expressed as the volume average of the stresses and strains acting in the N laminae, as in Eq. (F-12) and (F-13) where the star-like superscript denotes that these are averaged quantities.

$$\{\bar{\sigma}^*\} = \sum_{k=1}^{N} v^k\{\bar{\sigma}^k\} \tag{F-12}$$

$$\{\bar{\varepsilon}^*\} = \sum_{k=1}^{N} v^k\{\bar{\varepsilon}^k\} \tag{F-13}$$

Note that v^k is the volume fraction of the k$^{\text{th}}$ lamina, and $\sum_{k=1}^{N} v^k = 1$.

Additional hypotheses accompany these equations. First, mechanical equilibrium imposes that the volume average of residual stress vanishes (Eq. (F-14)).

$$\sum_{k=1}^{N} v^k\left\{\bar{\sigma}^{k(\mathrm{r})}\right\} = 0 \tag{F-14}$$

Second, strain compatibility conditions impose that the in-plane strain is uniform in each lamina and equal to the laminate's in-plane strain (iso-strain hypothesis), and stress continuity conditions impose that the out-of-plane stress is uniform in each lamina and equal to the laminate's out-of-plane stress (iso-stress hypothesis). This is expressed in Eq. (F-15) and (F-16), where the in-plane and out-of-plane components are respectively indicated with the subscript I and O.

$$\left\{\bar{\varepsilon}_I^k\right\} = \{\bar{\varepsilon}_I^*\} \tag{F-15}$$

$$\left\{\bar{\sigma}_O^k\right\} = \{\bar{\sigma}_O^*\} \tag{F-16}$$

Writing Eq. (F-9) with the matrices and vectors partitioned into the in-plane and the out-of-plane components yields Eq. (F-17), which can thus next be adapted to the above conditions, as in Eq. (F-18).

$$\begin{Bmatrix}\{\bar{\varepsilon}_I^k\}\\ \{\bar{\varepsilon}_O^k\}\end{Bmatrix} = \begin{bmatrix}[\bar{S}_{II}^k] & [\bar{S}_{IO}^k]\\ ([\bar{S}_{IO}^k])^T & [\bar{S}_{OO}^k]\end{bmatrix}\begin{Bmatrix}\{\bar{\sigma}_I^k\} - \left\{\bar{\sigma}_I^{k(\mathrm{r})}\right\}\\ \{\bar{\sigma}_O^k\}\end{Bmatrix} + \begin{Bmatrix}\{\bar{\alpha}_I^k\}\\ \{\bar{\alpha}_O^k\}\end{Bmatrix}\Delta T \tag{F-17}$$

$$\begin{Bmatrix}\{\bar{\varepsilon}_I^*\}\\ \{\bar{\varepsilon}_O^k\}\end{Bmatrix} = \begin{bmatrix}[\bar{S}_{II}^k] & [\bar{S}_{IO}^k]\\ ([\bar{S}_{IO}^k])^T & [\bar{S}_{OO}^k]\end{bmatrix}\begin{Bmatrix}\{\bar{\sigma}_I^k\} - \left\{\bar{\sigma}_I^{k(\mathrm{r})}\right\}\\ \{\bar{\sigma}_O^*\}\end{Bmatrix} + \begin{Bmatrix}\{\bar{\alpha}_I^k\}\\ \{\bar{\alpha}_O^k\}\end{Bmatrix}\Delta T \tag{F-18}$$

Where the in-plane and out-of-plane components are:

$$\left\{\bar{\sigma}_I^k\right\} = \begin{Bmatrix}\sigma_{xx}^k\\ \sigma_{yy}^k\\ \sigma_{xy}^k\end{Bmatrix}, \quad \left\{\bar{\varepsilon}_I^k\right\} = \begin{Bmatrix}\varepsilon_{xx}^k\\ \varepsilon_{yy}^k\\ 2\varepsilon_{xy}^k\end{Bmatrix}, \quad \left\{\bar{\alpha}_I^k\right\} = \begin{Bmatrix}\alpha_{xx}^k\\ \alpha_{yy}^k\\ 2\alpha_{xy}^k\end{Bmatrix}, \quad \left\{\bar{\sigma}_I^{k(\mathrm{r})}\right\} = \begin{Bmatrix}\sigma_{xx}^{k(\mathrm{r})}\\ \sigma_{yy}^{k(\mathrm{r})}\\ \sigma_{xy}^{k(\mathrm{r})}\end{Bmatrix}$$

$$\left\{\bar{\sigma}_O^k\right\} = \begin{Bmatrix}\sigma_{zz}^k\\ \sigma_{xz}^k\\ \sigma_{yz}^k\end{Bmatrix}, \quad \left\{\bar{\varepsilon}_O^k\right\} = \begin{Bmatrix}\varepsilon_{zz}^k\\ 2\varepsilon_{xz}^k\\ 2\varepsilon_{yz}^k\end{Bmatrix}, \quad \left\{\bar{\alpha}_O^k\right\} = \begin{Bmatrix}\alpha_{zz}^k\\ 2\alpha_{xz}^k\\ 2\alpha_{yz}^k\end{Bmatrix}, \quad \left\{\bar{\sigma}_O^{k(\mathrm{r})}\right\} = \begin{Bmatrix}0\\ 0\\ 0\end{Bmatrix}$$

$$\left[\bar{S}_{II}^{k}\right]=\begin{bmatrix} S_{xxxx}^{k} & S_{xxyy}^{k} & S_{xxxy}^{k} \\ S_{yyxx}^{k} & S_{yyyy}^{k} & S_{yyxy}^{k} \\ S_{xyxx}^{k} & S_{xyyy}^{k} & S_{xyxy}^{k} \end{bmatrix},\qquad \left[\bar{S}_{IO}^{k}\right]=\begin{bmatrix} S_{xxzz}^{k} & S_{xxxz}^{k} & S_{xxyz}^{k} \\ S_{yyzz}^{k} & S_{yyxz}^{k} & S_{yyyz}^{k} \\ S_{xyzz}^{k} & S_{xyxz}^{k} & S_{xyyz}^{k} \end{bmatrix},$$

$$\left[\bar{S}_{OO}^{k}\right]=\begin{bmatrix} S_{zzzz}^{k} & S_{zzxz}^{k} & S_{zzyz}^{k} \\ S_{xzzz}^{k} & S_{xzxz}^{k} & S_{xzyz}^{k} \\ S_{yzzz}^{k} & S_{yzxz}^{k} & S_{yzyz}^{k} \end{bmatrix}$$

An expression of the lamina in-plane stress can be extracted from Eq. (F-18), which writes as in Eq. (F-19).

$$\{\bar{\varepsilon}_I^*\}=\left[\bar{S}_{II}^{k}\right]\left(\{\bar{\sigma}_I^k\}-\left\{\bar{\sigma}_I^{k(\mathrm{r})}\right\}\right)+\left[\bar{S}_{IO}^{k}\right]\{\bar{\sigma}_O^*\}+\{\bar{\alpha}_I^k\}\Delta T$$

$$\Rightarrow \{\bar{\varepsilon}_I^*\}-\left[\bar{S}_{IO}^{k}\right]\{\bar{\sigma}_O^*\}-\{\bar{\alpha}_I^k\}\Delta T=\left[\bar{S}_{II}^{k}\right]\left(\{\bar{\sigma}_I^k\}-\left\{\bar{\sigma}_I^{k(\mathrm{r})}\right\}\right)$$

$$\Rightarrow \{\bar{\sigma}_I^k\}=\left[\bar{S}_{II}^{k}\right]^{-1}\left(\{\bar{\varepsilon}_I^*\}-\left[\bar{S}_{IO}^{k}\right]\{\bar{\sigma}_O^*\}-\{\bar{\alpha}_I^k\}\Delta T\right)+\left\{\bar{\sigma}_I^{k(\mathrm{r})}\right\} \tag{F-19}$$

According to the definition of the global stresses and strains (Eq. (F-12) and (F-13)), volume averages are applied on both sides of Eq. (F-19), and an expression for the global in-plane strain is obtained:

$$\{\bar{\varepsilon}_I^*\}=\left(\sum_{k=1}^{N} v^k\left[\bar{S}_{II}^{k}\right]^{-1}\right)^{-1}\left(\{\bar{\sigma}_I^*\}+\sum_{k=1}^{N} v^k\left[\bar{S}_{II}^{k}\right]^{-1}\left[\bar{S}_{IO}^{k}\right]\{\bar{\sigma}_O^*\}+\sum_{k=1}^{N} v^k\left[\bar{S}_{II}^{k}\right]^{-1}\{\bar{\alpha}_I^k\}\Delta T\right) \tag{F-20}$$

This last equation is the effective constitutive stress-strain relation of the laminate expressed in its global coordinate system. It can be written in a condensed form as in Eq. (F-21), where -by analogy- the effective compliance sub-matrices $[\bar{S}_{II}^*]$ and $[\bar{S}_{IO}^*]$ are defined by Eq. (F-22) and (F-23) and the vector of effective in-plane thermal expansion coefficients $\{\bar{\alpha}_I^*\}$ is defined by Eq. (F-24).

$$\{\bar{\varepsilon}_I^*\} = [\bar{S}_{II}^*]\{\bar{\sigma}_I^*\} + [\bar{S}_{IO}^*]\{\bar{\sigma}_O^*\} + \{\bar{\alpha}_I^*\}\Delta T \tag{F-21}$$

$$[\bar{S}_{II}^*] = \left(\sum_{k=1}^{N} v^k \left[\bar{S}_{II}^k\right]^{-1}\right)^{-1} \tag{F-22}$$

$$[\bar{S}_{IO}^*] = [\bar{S}_{II}^*] \sum_{k=1}^{N} v^k \left[\bar{S}_{II}^k\right]^{-1} \left[\bar{S}_{IO}^k\right] \tag{F-23}$$

$$\{\bar{\alpha}_I^*\} = [\bar{S}_{II}^*] \sum_{k=1}^{N} v^k \left[\bar{S}_{II}^k\right]^{-1} \{\bar{\alpha}_I^k\} \tag{F-24}$$

The sub-matrix $[\bar{S}_{OO}^*]$ and the sub-vector $\{\bar{\alpha}_O^*\}$ are in turn obtained in a similar manner by extracting an expression of the out-of-plane strain $\{\bar{\varepsilon}_O^k\}$ from Eq. (F-18). They are given in Eq. (F-25) and (F-26).

$$[\bar{S}_{OO}^*] = [\bar{S}_{IO}^*]^T [\bar{S}_{II}^*]^{-1} [\bar{S}_{IO}^*] + \sum_{k=1}^{N} v^k \left(\left[\bar{S}_{OO}^k\right] - \left[\bar{S}_{IO}^k\right]^T \left[\bar{S}_{II}^k\right]^{-1} \left[\bar{S}_{IO}^k\right] \right) \tag{F-25}$$

$$\{\bar{\alpha}_O^*\} = [\bar{S}_{IO}^*]^T [\bar{S}_{II}^*]^{-1} \{\bar{\alpha}_I^*\} + \sum_{k=1}^{N} v^k \left(\{\bar{\alpha}_O^k\} - \left[\bar{S}_{IO}^k\right]^T \left[\bar{S}_{II}^k\right]^{-1} \{\bar{\alpha}_I^k\} \right) \tag{F-26}$$

Finally, the effective thermoelastic properties of the laminate are derived from the coefficients of its compliance matrix and of its vector of coefficients of thermal expansion. The relations between these quantities are given in Table 8-1.

Table 8-1. Expression of the effective thermoelastic properties of the laminate as a function of the coefficients of its compliance matrix and of its vector of coefficients of thermal expansion.

Effective Young's moduli	Effective shear moduli	Effective Poisson's ratios	Effective CTEs
$E_x = 1/\bar{S}^*_{xxxx}$	$G_{yz} = 1/\bar{S}^*_{yzyz}$	$\nu_{yz} = -\bar{S}^*_{yyzz}/\bar{S}^*_{yyyy}$	$\alpha_x = \bar{\alpha}^*_{xx}$
$E_y = 1/\bar{S}^*_{yyyy}$	$G_{xz} = 1/\bar{S}^*_{xzxz}$	$\nu_{xz} = -\bar{S}^*_{xxzz}/\bar{S}^*_{xxxx}$	$\alpha_y = \bar{\alpha}^*_{yy}$
$E_z = 1/\bar{S}^*_{zzzz}$	$G_{xy} = 1/\bar{S}^*_{xyxy}$	$\nu_{xy} = -\bar{S}^*_{xxyy}/\bar{S}^*_{xxxx}$	$\alpha_z = \bar{\alpha}^*_{zz}$

G. Experimental methods

G.1 Thermogravimetric Analysis

Thermogravimetric Analysis (TGA) is a thermal analysis technique commonly used in the characterisation process of polymer materials. It allows identifying and quantifying the composition of the material, as well as studying its thermal stability [78].

The technique is based on the simple principle of precisely monitoring the sample mass during its exposure to a controlled temperature program where thermal degradation is expected to occur. It is hence sensitive to transformations inducing changes in the sample mass, such as weight loss which generally arises through the emission –and purge– of volatile decomposition products upon thermal degradation of the material [78][135]. The whole measurement is run under controlled atmosphere, whether oxidative (O_2, air) or inert (e.g. N_2, He).

Two temperatures characteristic of the thermal degradation process can be graphically determined from the measurement results, namely the extrapolated onset temperature (T_0) and the first derivative peak temperature (T_p) [195]. The first is determined from the intersection of the tangent to the weight loss curve before the sigmoidal change, with the tangent at the point of maximum slope in the sigmoidal change; it is known to be a reproducible identification of the temperature at which thermal degradation begins. The

latter is located at the peak of the first derivative of the weight loss; it indicates the point of greatest rate of change on the weight loss curve.

In practice, two samples of each material were precisely weighed to about 1.5 mg before being placed in the balance of the Q5000 equipment (TA Instruments, USA). The measurement was run over a temperature range going from 60 °C to 500 °C, crossed at a heating rate of 10 °C/min. An initial isotherm of 30 minutes at 60 °C was observed so as to allow for the stabilisation of the chamber nitrogen atmosphere.

G.2 Thermomechanical Analysis

Thermomechanical Analysis (TMA, or dilatometry) is a thermal analysis technique used to study the transitions and determine the coefficient of linear thermal expansion of materials. It is based on the measurement of dimensional changes of a material sample being heated, cooled, or studied at a constant temperature [78][196]. ASTM standards exist for these purposes and were followed for the realisation of the measurements and the treatment of the results (ASTM E1545-11)(ASTM E831-12).

The coefficient of linear thermal expansion of RTM6, Redux 322 and AISI 316L SS was determined by TMA with a DMA7 instrument (PerkinElmer, USA). The sample was therefore placed upright on a suspended quartz platform, and a suspended rigid quartz probe touched its top surface with a small contact force of 20 mN (Figure G-1).

A controlled temperature program was applied by the thermal chamber in which the quartz tube containing the sample is enclosed for the measurement.

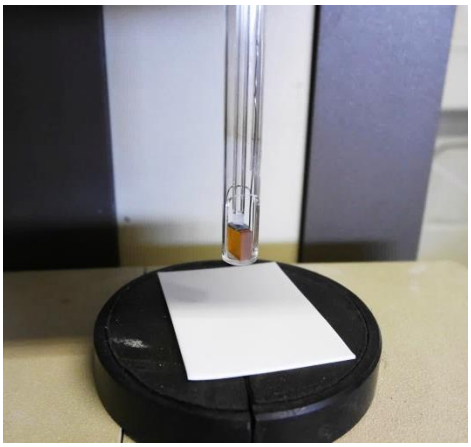

Figure G-1. RTM6 sample in the quartz tube of the DMA7 instrument.

Constant cooling rate and cooling to sub-ambient temperature were enabled by repeatedly filling the reservoir adjoining the thermal chamber with liquid nitrogen. Finally, the chamber atmosphere was renewed with a continuous flow of 10 ml/min nitrogen gas so as to limit the oxidation of the sample occurring at high temperature.

Data acquired during the measurements were treated as follows in order to compute coefficients of linear thermal expansion according to the standard procedure. The curve representing the evolution of the sample length with temperature was first fitted to a straight line within intervals of 50 °C centred on each data point found between $(T_{min} + 25\,°C)$ and $(T_{max} - 25\,°C)$. The mean coefficient of linear thermal expansion was then computed at each of these points by means of Eq. (G-1) where $\frac{\Delta L}{\Delta T}$ is given by the slope of the fitted straight line, and L is the sample length recorded at 23 °C in the corresponding heating or cooling step.

$$\alpha_m = \frac{\Delta L}{L \times \Delta T} \tag{G-1}$$

G.2.1 Thermomechanical analysis of RTM6 and Redux 322

The analysis was run on two samples of each material machined to the 10 mm x 10 mm x 4 mm nominal dimensions by digital milling. Since the end of the quartz probe available for the measurements presented irregularities caused by the former fracture of the originally flat end, a piece of silicon wafer was used as an intermediate layer between the sample and the quartz probe[40] in order to avoid penetration of any peak in the sample -especially in the glass transition region. This allowed distributing the force over the sample top surface and avoiding biased changes in the probe position due to indentation of the sample.

The controlled temperature program applied for the measurement is a heat-cool-heat cycle which slightly differs from one material to the other, as shown in Figure G-2.

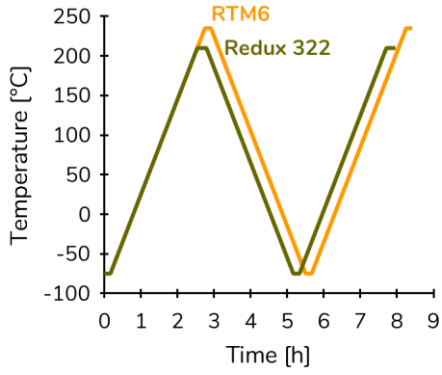

Figure G-2. Controlled temperature programs applied for the measurement of the CTE of RTM6 and Redux 322 by TMA (heating & cooling rates: 2 °C/min).

Indeed, while the minimum temperature of -75 °C was common to both materials, the maximum temperature was chosen according to the material

[40] The contribution of the silicon wafer to the measured thermal expansion of the sample was assessed along a complete temperature cycle performed individually on this small piece of material. Its presence was found to be negligible, as expected given its small thickness and low thermal expansion coefficient.

thermal stability and set to 210 °C for Redux 322 and 235 °C for RTM6. 10 minutes long isotherms were observed at these temperatures, and the heating and cooling rates were set to 2 °C/min, which is the lowest rate advised by the standard. Given the generally low thermal conductivity of polymers, this choice allows improving the homogeneity of the temperature within the sample and limiting the thermal lag between the sample temperature and the thermal chamber temperature.

G.2.2 Thermomechanical analysis of the as-rolled AISI 316L SS strip

For each reference direction of the as-rolled steel sheet, the analysis was performed on one sample of nominal dimensions 15 mm x 10 mm x 4 mm. The controlled temperature program applied for the measurement is a heat-cool-heat cycle between -75 °C and 210 °C, with 5 minutes long isotherms at these temperatures and heating and cooling rates set to 2 °C/min (Figure G-3-a).

The production of the samples required some preparation. Indeed, the steel sheet is so thin that it is unable to stand alone on its edge, which could have compromised the measurement of thermal expansion in any direction of the sheet plane. This difficulty was overcome by manufacturing bundles of twenty rectangular pieces of steel sheet all cut to the nominal dimensions 15 mm x 10 mm x 0.2 mm. These sheets were assembled and tied together by means of steel wire allowing the free expansion of the steel sheet, especially in the measurement direction (Figure G-3-b). Two bundles were prepared: one with the long side of the rectangular pieces aligned with the sheet's rolling direction, and the other with their long side aligned with the transverse direction.

(a) (b)

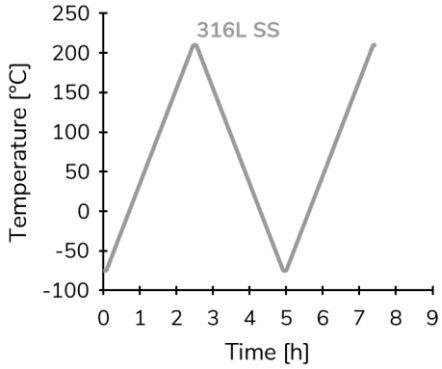

Figure G-3. (a) Controlled temperature program applied for the measurement of the steel sheet CTE by TMA (heating & cooling rates: 2 °C/min), (b) samples prepared in the form of bundles of rectangular pieces of steel sheet (one sample by reference direction).

G.3 Dynamic Mechanical Analysis

Dynamic Mechanical Analysis (DMA) is an advanced thermal analysis technique dedicated to the characterisation of mechanical properties of viscoelastic materials. It is mostly used under conditions where energy-elasticity prevails (solid-like behaviour)[41], but it is also very useful to reveal thermal transitions -such as the glass transition- through the associated changes in mechanical behaviour of the material [136][139] [135][157].

The DMA instrument generally exposes the sample to a steady-state oscillatory mechanical solicitation (Eq. (G-2)) and records its response as a function of time or temperature [136][78]. The solicitation is normally small enough (or slow enough) so that the sample mechanical behaviour stays in the *linear* viscoelastic regime[42] [139]. The response is oscillatory as well (Eq. (G-3)); it has the same amplitude as the excitation but is generally shifted by some phase angle δ the magnitude of which increases with the viscoelastic damp-

[41] Dynamic rheometry is the complementary technique for the analysis of materials under conditions where entropy-elasticity prevails (liquid-like behaviour) [157].
[42] Meaning that, at a given temperature and frequency, stress is a linear function of strain [139].

ing capacity of the material [157]. The knowledge of the applied solicitation (for instance a sinusoidal strain, ε) and the measured sample response (for instance a sinusoidal stress, σ) allows the determination of a complex dynamic modulus E^* for the viscoelastic material (Eq. (G-4) and (G-5)), which represents its overall resistance to deformation [135][140]. The real and imaginary parts of E^* are respectively called the storage modulus (or E-modulus, E') and the loss modulus (or S-modulus, E"); the first represents the amount of strain energy stored elastically in the material, while the latter represents the amount of strain energy lost as heat dissipated by friction between the macromolecules [139][198][135][140]. The phase angle (or loss angle) is also determined and is a characteristic measure of viscoelastic damping [157]. It is comprised between 0° and 90°, these bounds being set by ideal elastic and ideal viscous materials, respectively [140]. This is all shown in the following equations where σ_0 and ε_0 are the respective amplitudes of the sinusoidal stress and strain, ω is the angular frequency and t is time [140][136].

Input: $$\varepsilon = \varepsilon_0 \sin(\omega t) = \varepsilon_0 \exp(i\omega t) \quad \text{(G-2)}$$

Output: $$\sigma = \sigma_0 \sin(\omega t + \delta) = \sigma_0 \exp(i\omega t + i\delta) \quad \text{(G-3)}$$

$$E^* = \frac{\sigma_0}{\varepsilon_0} \exp(i\delta) = \frac{\sigma_0}{\varepsilon_0} (\cos\delta + i \sin\delta)$$

With $$\frac{\sigma_0}{\varepsilon_0} \cos\delta = E' \qquad \frac{\sigma_0}{\varepsilon_0} \sin\delta = E''$$

So $$\boxed{E^* = E' + iE''} \quad \text{(G-4)}$$

And $$\boxed{\tan\delta = \frac{E''}{E'}} \quad \text{(G-5)}$$

G.3.1 Dynamic Mechanical Analysis of RTM6 and Redux 322

In practice, DMA was performed on three samples of RTM6 resin and three samples of Redux 322 film adhesive. They were neatly cut to the desired dimensions (about 30 mm x 4 mm x 0.260 mm) by means of an Accutom precision cut-off machine (Struers, Denmark); then dried for 1 h 30 at 60 °C just before the tests. These samples were mounted with a 10 to 15 mm gauge length on an uniaxial tensile clamp placed in the chamber of a Q800 Dynamic Mechanical Analyser (TA Instruments, USA), as can be seen in Figure G-4.

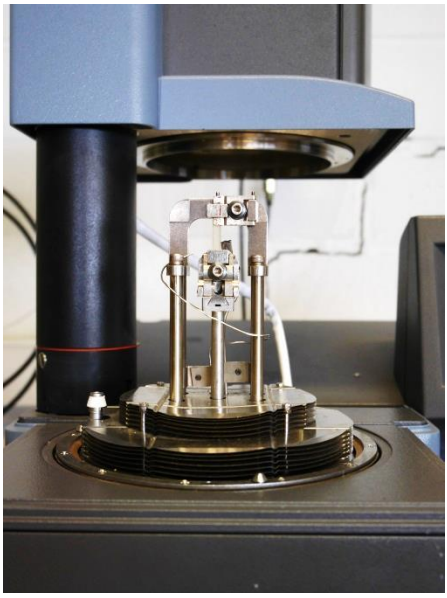

Figure G-4. RTM6 sample in the uniaxial tensile clamp of the Q800 DMA instrument.

A sinusoidal strain of 0.08 % was applied with a 1 Hz frequency, yielding a displacement amplitude of about 12 µm. The sample temperature was meanwhile increased from -50 °C to 250 °C at a constant rate of 2 °C/min. An initial isotherm of 10 minutes at -50 °C was observed in order to stabilise the sample temperature and response signal. The force resulting from the prescribed strain was monitored over the whole temperature range, and automatically translated into the corresponding stress according to the sample cross-section measured with a digital micrometre before the test.

Note that the test frequency was chosen so as to provide a displacement rate $\dot{d}$ equivalent to that of 2 mm/min used in the quasi-static macroscopic tensile tests. This was calculated as per Eq. (G-6) adapted from [199], where l_0 stands for the specimen gauge length and f stands for the test frequency.

$$\dot{d} = \frac{\varepsilon l_0}{t} = \frac{\varepsilon l_0}{\frac{1}{4f}}$$

$$\Rightarrow f = \frac{\dot{d}}{4\varepsilon l_0} \tag{G-6}$$

Finally, the evolution of the E-modulus, S-modulus and loss angle with temperature was obtained from these dynamic mechanical tests.

G.4 Quasi-static macroscopic tensile testing

Quasi-static macroscopic tensile testing is the most widespread test choice when it comes to measuring a material's mechanical response [37][196]. Extensometers in contact with the tensile specimen are generally used for the measurement of the axial strain and possibly the transverse strain [200]. This was the case for tensile testing of RTM6 and Redux 322. Yet, this technique resulted in the very poor quality of the recorded transverse strain signal of the AISI 316L SS tensile test specimens. This was attributed to the particularly small thickness of the steel sheet which could make it unsuited to the use of extensometers. Strain gauges were considered for a while as alternative equipment for the measurement of the axial and transverse strain, but the idea was abandoned due to the precision and time required for their mounting on the specimen [201], and their relatively high cost.

Digital Image Correlation (DIC) was finally used instead, allowing for the *non-contact* measurement of the axial and transverse strains deforming the specimen during the tensile test. DIC currently has a huge range of applica-

tions and is trusted for 2D and 3D strain mapping in quasi-static and dynamic tests, at ambient as well as elevated temperatures, in-door or even out-door [202]. Non-exhaustively, it has already been used for strain measurement in numerous types of mechanical tests, among which beam bending tests [203] and flat specimen or fibre tensile tests [204][205], for the detection of damage in composite laminates [206][207], for crack growth monitoring and measurement of crack opening for various types of materials and loadings [208][209], and as design assessment tool for the reduction of stress concentration [210].

G.4.1 Quasi-static macroscopic tensile testing of RTM6 and Redux 322

Quasi-static tensile tests were performed on dog bone-shaped specimens machined by digital milling to the specimen geometry and nominal dimensions prescribed by the relevant standard (EN ISO 527-2) and shown in Figure G-5.

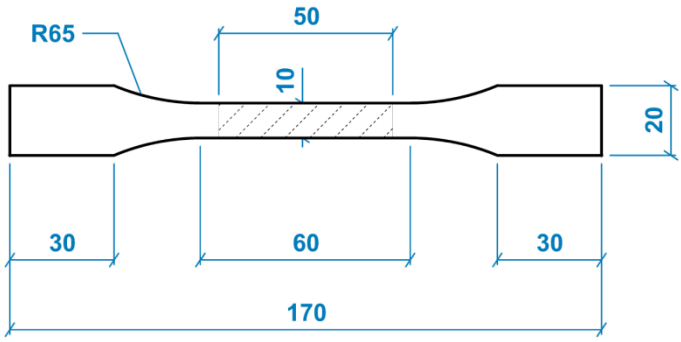

Figure G-5. Geometry and nominal dimensions (in mm) of the dog bone-shaped specimens prepared for quasi-static uniaxial tensile testing of RTM6 and Redux 322, following the standard (EN ISO 527-2).

The specimens were conditioned in the test room atmosphere (~23 °C, ~58 %RH) for at least one week, in accordance with the standards (ASTM D

618-00)(ASTM D 638-02a). Then, right before testing, the specimen width and thickness were measured at three equidistant positions along the calibrated length with a digital Vernier calliper and a digital micrometre, respectively.
The tensile tests were carried out at two temperatures, namely 23°C and 125°C[43]. On the one hand, room temperature tensile testing was performed on a universal testing machine (ZwickRoell, Germany) with a 250 kN load cell. The specimen strain was simultaneously measured in the axial and transverse direction thanks to a double extensometer (Figure G-6-a), allowing for the determination of the material Poisson's ratio. On the other hand, high temperature tensile testing was performed in a thermal chamber fitted to the test frame of another universal testing machine (ZwickRoell, Germany) with a 250 kN load cell. The strain was then measured only in the axial direction of the specimen by means of the single extensometer compatible with this experimental setup (Figure G-6-b). In both cases, tensile tests were performed on at least three specimens loaded up to fracture at a constant crosshead speed of 2 mm/min.

G.4.2 Quasi-static macroscopic tensile testing of as-rolled and micro-perforated AISI 316L SS

Quasi-static macroscopic tensile tests were performed in accordance with the standard procedure (ISO 6892-1), in both reference directions of the as-rolled and micro-perforated AISI 316L SS sheets. Dog bone-shaped specimens were therefore precisely machined by Electrical Discharge Machining (EDM) to the geometry and nominal dimensions shown in Figure G-7-a.

(a) (b)

[43] The original intention was to perform the test at 135 °C, but a defectiveness of the thermocouple placed on the test specimens resulted in confusion about the chamber temperature, and testing at 125 °C instead of the target temperature.

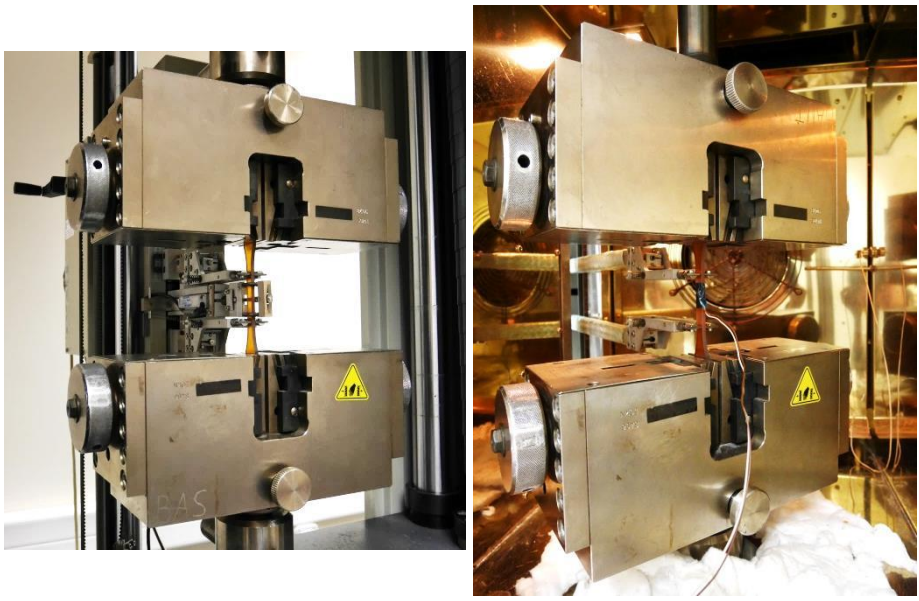

Figure G-6. RTM6 specimen mounted for quasi-static uniaxial tensile testing (a) at room temperature and (b) at elevated temperature in a thermal chamber.

Their width and thickness were measured at three equidistant positions along the calibrated length with a digital Vernier calliper and a digital micrometre, respectively. At least 8 specimens of as-rolled steel and 8 specimens of micro-perforated steel were tested at room temperature for each reference direction of the steel sheet. They were loaded up to fracture at a constant crosshead speed of 1 mm/min applied by a universal testing machine (Instron, USA) with a 10 kN load cell. Pneumatic grips were selected to avoid some twist of the specimen observed when tightening the grips manually.

(a)

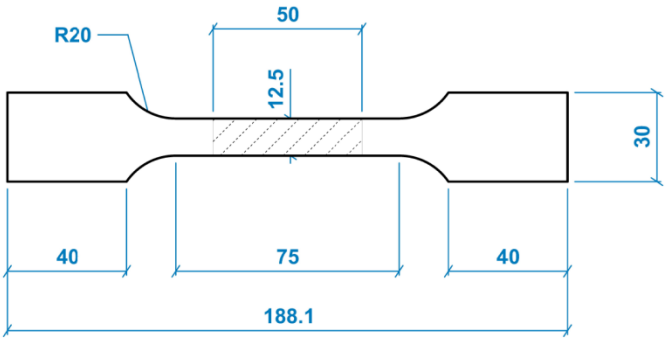

(b)

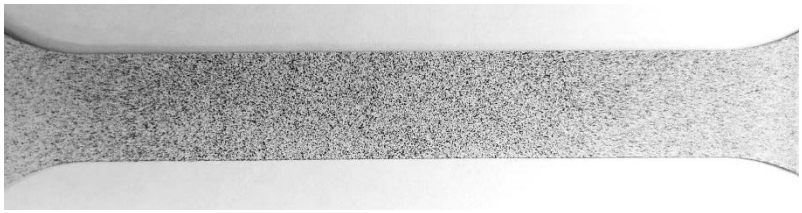

Figure G-7. Dog bone-shaped specimens for quasi-static uniaxial tensile test on the stainless steel sheet. (a) Geometry and nominal dimensions (in mm) as per the ISO standard (ISO 6892-1), (b) zoom on a test specimen prepared with speckle pattern for DIC strain monitoring.

Digital Image Correlation (DIC) was used for the *non-contact* measurement of the axial and transverse strains deforming the specimen during the tensile test. It is a powerful and promising *optical-numerical* full-field measurement technique based on the calculation of the specimen's surface displacement fields by matching digital images acquired *during* the test with one *reference image* acquired *before* the test [215]. Therefore, a specialised software virtually divides the specimen surface into small *subsets* of several pixels in width and length on the reference image. The software then performs the correlation procedure for each reference subset, i.e. it finds in the current image of the deforming specimen the pixel subset –possibly translated, rotated and deformed– which best corresponds to a given pixel subset in the reference image [209][215]. Detailed displacement fields are thereby obtained from the

displacement of the centre point of each subset, and their evolution with loading emerges from the processing of the consecutive images captured during the test [209]. In order to improve the correlation capability, the region of interest on the specimen surface is generally covered with a speckle pattern, consisting in a contrasting overlay of e.g. dark dots properly sized and *randomly dispersed* on a bright background [215][216][217]. The tensile test specimens were therefore painted with white and black spray paints as shown in Figure G-7-b.

A pair of 5 MP Stingray cameras with 23 mm lenses were arranged on a tripod facing the test bench. The mechanical and optical parts of the resulting test set-up are depicted in Figure G-8.

Figure G-8. Steel sheet specimen mounted on the test bench for quasi-static uniaxial tensile testing with strain monitoring by digital image correlation. The pair of cameras is visible at right of the picture, while the light source used for correct illumination of the specimen speckle pattern is even further to the right, out of the picture frame.

The specimen was not filmed continuously during the test; the acquisition of the images was instead triggered every two seconds by the Vic Snap software (Correlated Solutions, USA). After the test, the pairs of images were processed by means of the Vic-3D 7 software (Correlated Solutions, USA) which provided the evolution of the full-field strains maps calculated on the visible surface of the specimen. The axial and transverse strains were extracted at each acquisition time with virtual extensometers initially drawn in the gauge length area on the reference image of each specimen. The stress corresponding to each acquisition time was derived from the recorded load and the sample initial cross-section.

G.5 Resonant-based identification of elastic constants

The present mixed numerical-experimental technique (MNET) allows for the *non-destructive* and *non-contact* determination of the *in-plane engineering constants* of relatively thin materials, the material symmetry of which may range from isotropic to orthotropic, and whose properties and thickness are uniform over the test area [218].

The technique is based on the experimental measurement of the *natural frequencies* of the test specimen associated to its characteristic mode shapes of *free vibration*. An accurate finite element model of the test specimen is then generated and used to reproduce the experiment in order to identify one or several elastic constants of the material [218]. This is a good example of what is called an *inverse method* [219], in which some input material parameters of the numerical model are fine-tuned until they provide the best fit between the numerical solution –here the *computed* natural frequency– and the experimental data –the *measured* natural frequency [220]. The optimisation proce-

dure is here automatized by the iterative minimisation of the cost function linked to the output residual.

This MNET applied to the determination of elastic constants from the natural resonant frequencies is named the *Resonalyser procedure* and was first developed in [221]. Its general working principle is schematically summarized in Figure G-9.

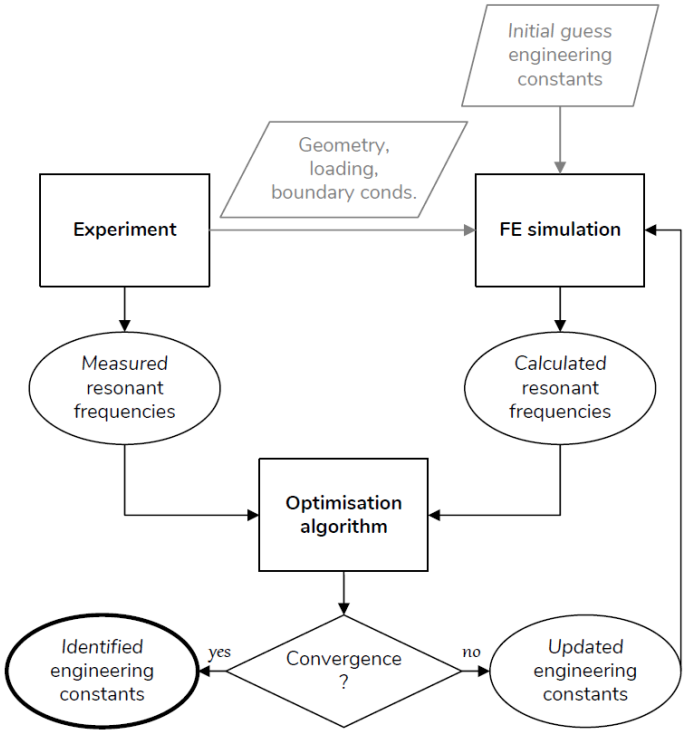

Figure G-9. Flowchart summarizing the general working principle of the Resonalyser procedure.

The Resonalyser procedure has already successfully been applied to the determination of the in-plane engineering constants of a great variety of materials such as rolled steel, aluminium and brass sheets, or epoxy [222][223], as well as layered systems among which CFRP composite laminate, sandwich

plates and thermal barrier coatings on metallic substrate [224][225]. Yet, the particularly small thickness of our steel sheet material presented a new opportunity of challenging the technique.

The test specimen either has a beam-like shape which vibrates in the fundamental bending mode and gives access to the Young's modulus E_1 or E_2 in the axial direction of the beam; or a rectangular plate-like shape which can vibrate in the torsion, saddle, and breathing modes and gives access to the Young's modulus E_1 and E_2 in both reference directions of the plate plane, the in-plane shear modulus G_{12}, and the major Poisson ratio ν_{12}. These modal shapes are illustrated in Figure G-10.

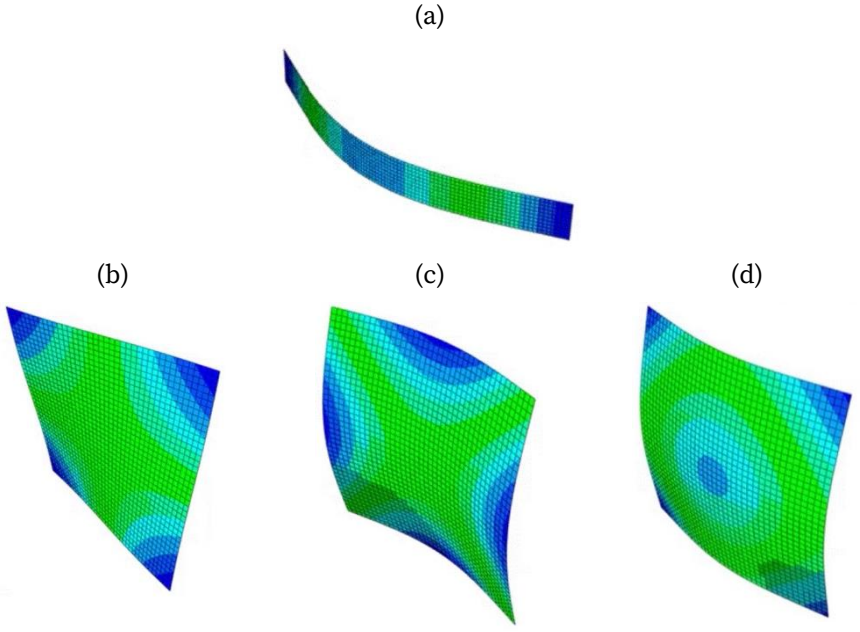

Figure G-10. (a) Bending modal shape of a beam; (b), (c) and (d) Torsion, saddle and breathing modal shapes of a Poisson plate.

Note that plate-like samples are designed with specific in-plane dimensions improving the sensitivity to the Poisson's ratio. The ideal ratio of the length l

to the width w of the so-called "Poisson plate" is determined by use of Eq. (G-7), with the length being found in the direction of greatest modulus [224][226]. E_2 is the Young's modulus in this direction, and E_1 is the Young's modulus in the plane direction perpendicular thereto; knowledge of these moduli is thus required preliminary to the calculation of the plate's aspect ratio.

$$\frac{l}{w} = \sqrt[4]{\frac{E_2}{E_1}} \tag{G-7}$$

G.5.1 Resonant-based identification of as-rolled and micro-perforated AISI 316L SS elastic constants

Two sets of 10 rectangular beam-like specimens of nominal dimensions 100 mm x 10 mm x 0.2 mm were machined by EDM with their long axis either parallel to the rolling or the transverse direction of the as-rolled and micro-perforated steel sheets. They were weighed with an analytical balance, then their width and length were measured with a Vernier calliper and their thickness with a micrometre. For the experimental part of the Resonalyser procedure, the specimens were neatly suspended to a test frame by means of a light sewing thread, enabling their free vibration under the effect of an impulse triggered with the same microphone used for recording the resulting resonant frequency. This is illustrated in Figure G-11-a.

The numerical part of the Resonalyser procedure then provided the Young's modulus computed in both reference directions of the rolled steel sheets. This in turn allowed determining the ideal dimensions of the Poisson plates with Eq. (G-7), namely 105 mm x 100 mm x 0.2 mm for as-rolled steel and 102 mm x 100 mm x 0.2 mm for micro-perforated steel.

(a) (b)

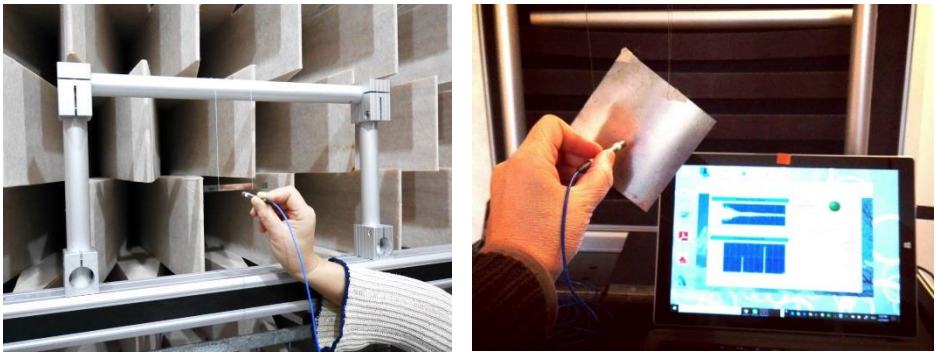

Figure G-11. Measurement of the resonant frequencies of (a) a beam-shaped (with background wall of acoustic deadening chamber) and (b) a Poisson plate-shaped steel sheet sample.

Eight Poisson plates were machined by EDM in as-rolled steel with their long side parallel to the transverse direction, and another eight Poisson plates were similarly machined in micro-perforated steel. They were precisely weighed and measured like the beam samples. Testing with the Resonalyser procedure yielded the two of the three main engineering constants characterizing the elastic behaviour of the sheets, i.e. the Young's modulus in both reference directions of the rolled steel sheets and the in-plane shear modulus. The identification of the major Poisson's ratio was, on the other hand, unsuccessful. The measurement of resonant frequencies of a Poisson plate sample is illustrated in Figure G-11-b.

H. Global analysis of the TMA curves

This appendix contains the global analysis of the TMA data presented in Section 4.3.3.1.

On the one hand, first heating curves of both materials in Figure 4-5 and Figure 4-11 display obvious signs of residual cure. The crosslinking reaction resumes upon devitrification when the sample temperature approaches the current glass transition temperature, resulting in some chemical shrinkage. The characteristic change in slope in the plot of sample length versus temperature is therefore not visible on these curves, since the increase in free volume at glass transition is at least counterbalanced by chemical shrinkage. For RTM6, residual cure did for the most part occur before the isothermal plateau closing the first heating step. It mainly shows up as the second "valley" visible on the first heating curve of Figure 4-5-a. Redux 322, however, did react both upon heating above T_g and during the isothermal plateau, as respectively evidenced by the marked reduction in sample length at the end of first heating, and the vertical offset of the cooling curve with respect to the first heating curve at the plateau temperature (Figure 4-5-b). For both materials, residual cure is responsible for the large uncertainty affecting the linear thermal expansion coefficient derived from the first heating data at high temperature (Figure 4-11).

On the other hand, vertical offset of the whole cooling curve with respect to the whole first heating curve was observed for each material in Figure 4-5. It reveals some relaxation of excess free volume, which simply indicates that the cooling rate seen by the material at the end of the plate manufacturing was larger than the 2 °C/min measurement scan rate. In the first heating curves of RTM6, free volume relaxation also manifests as a “valley” (or “undershoot”) followed by a “hill” (or “overshoot”) when the sample enters its glass transition region, as already observed elsewhere [227]. Logically, both effects appeared to be less pronounced upon second heating.

I. Comment on the DMA curves

Analysis of Figure 4-6 reveals a shoulder at glass transition in the RTM6 E-modulus and tan(δ) traces, as well as the flatness of the S-modulus peak. It indicates an inhomogeneous degree of cure of the material, whether originally present in the sample, or caused by the resumption of the cross-linking reaction during the DMA measurement. Reticulation has actually most probably resumed upon devitrification of RTM6 when the temperature was raised above the original T_g during the measurement. The original glass transition temperature of the RTM6 material samples could actually be derived from the approximate location of the shoulder in the tan(δ) peak. It would then be about 216 °C, i.e. nearly 25 °C lower than the value previously determined from the peak maximum (Table 4-5). The same correction can however not be applied to the glass transition temperatures determined for Redux 322, as neither of the three DMA signals did present obvious signs of residual cure.

J. Polynomial fits and discrete values of E-modulus and CTE

The tables gathered in this appendix contain the polynomial fits and the discrete numerical values extracted from the continuous evolution of the E-modulus and CTE of the RTM6, Redux 322 and as-rolled AISI 316 L with temperature, respectively measured by DMA and TMA.

*Table 8-2. Fits and discrete points calculated for the E-modulus of **RTM6**.*
Top: equations of the bi-linear and bi-polynomial fits of the mean E-modulus curves.
Bottom: discrete values of the mean E-modulus at several temperatures of interest.

Temperature ranges [°C]	[-40; 70]	[70; 180]
Bi-linear fit	$-1.03e^{-2}T + 3.24$	$-6.05e^{-3}T + 2.94$
Bi-polynomial fit	$2.52e^{-5}T^2 - 1.11e^{-2}T + 3.17$	$2.73e^{-6}T^2 - 6.74e^{-3}T + 2.98$

Temperatures of interest [°C]	-40	23	70	100	135	180
Mean E-modulus values [GPa]	3.66	2.95	2.52	2.31	2.13	1.85

*Table 8-3. Fits and discrete points calculated for the E-modulus of **Redux 322**.*
Top: equations of the bi-linear and bi-polynomial fits of the mean E-modulus curves.
Bottom: discrete values of the mean E-modulus at several temperatures of interest.

Temperature ranges [°C]	[-40; 70]	[70; 180]
Bi-linear fit	$-1.72e^{-2}T + 4.74$	$-1.05e^{-2}T + 4.27$
Bi-polynomial fit	$-2.81e^{-5}T^2 - 1.64e^{-2}T + 4.82$	$-1.05e^{-6}T^3 + 4.19e^{-4}T^2 - 6.29e^{-2}T + 6.24$

Temperatures of interest [°C]	-40	23	70	100	135	180
Mean E-modulus values [GPa]	5.43	4.44	3.54	3.09	2.81	2.38

*Table 8-4. Fits and discrete points calculated for the CTE of **RTM6**. Top: equations of the bi-polynomial fit of the CTE curve. Bottom: discrete values of the CTE at several temperatures of interest.*

Temperature ranges [°C]	[-40; 70]	[70; 180]
Bi-polynomial fit	$-2.21e^{-5}T^3 + 8.99e^{-4}T^2 + 1.64e^{-1}T + 52.1$	$5.339e^{-5}T^3 - 1.500e^{-2}T^2 + 1.419T + 16.29$

Temperatures of interest [°C]	-40	23	70	100	135	180
CTE values [µm/(m°C)]	48.4	56.4	60.4	61.5	65.6	97

*Table 8-5. Fits and discrete points calculated for the CTE of **Redux 322**.*
Top: equations of the bi-polynomial fit of the mean CTE curve.
Bottom: discrete values of the mean CTE at several temperatures of interest.

Temperature ranges [°C]	[-40; 70]	[70; 180]
Bi-polynomial fit	$1.20e^{-5}T^3 + 2.42e^{-4}T^2 + 5.16e^{-2}T + 42.3$	$5.380e^{-5}T^3 - 1.619e^{-2}T^2 + 1.732T - 9.163$

Temperatures of interest [°C]	-40	23	70	100	135	180
Mean CTE values [µm/(m°C)]	39.9	43.8	51.2	56	61.3	91.8

*Table 8-6. Fits and discrete points calculated for the CTE in both directions of the as-rolled **AISI 316 L SS** sheet. Top: equations of the bi-linear fit of the mean CTE curve. Bottom: discrete values of the CTE along RD and TD at several temperatures of interest, and mean of the values corresponding to these directions.*

Temperature ranges [°C]	[-40; 138]	[138; 180]
Bi-linear fit in RD	$-7.74e^{-3}T + 16.4$	$5.24e^{-2}T + 8.07$
Bi-linear fit in TD	$1.79e^{-3}T + 15.9$	$5.95e^{-2}T + 7.89$
Bi-linear fit common to RD & TD	$-2.98e^{-3}T + 16.1$	$5.60e^{-2}T + 7.98$

Temperatures of interest [°C]	-40	23	100	135	180
CTE values in RD [µm/(m°C)]	16.6	16.3	15.6	15.3	17.5
CTE values in TD [µm/(m°C)]	15.8	16.0	15.9	16.0	18.6
Mean CTE values (RD & TD) [µm/(m°C)]	16.2	16.1	15.8	15.7	18.1

K. X-ray stress analysis

K.1 Introduction

X-ray Stress Analysis (XSA) was chosen as a mean of experimentally evaluating the residual stress in the multilayer. More exactly, it allowed quantifying the residual stress present *in the surface layer* of the *as-rolled steel strip* co-cured with the composite laminate substrate.

The fundamental principles of X-ray diffraction will be recalled first, as they are necessary for the understanding of how residual stresses can be measured by XSA. Then, the basics of X-ray Stress Analysis will be exposed, including the main equations paving the mathematical development.

The theory gathered in this section essentially comes from the content of Chapter 3, Chapter 5 and Chapter 15 of the reference book by B.D. Cullity and S.R. Stock [170], and from the reference book by I.C. Noyan and J.B. Cohen [173]. Additional sources that have been used are referred to in the text.

K.2 Fundamental principles of X-ray diffraction

X-rays are electromagnetic waves whose wavelength is about 1Å, that is, a thousand times smaller than the wavelength of visible light. This length is in fact comparable to the size of atoms and inter-atomic spacing in crystalline materials. This allows the phenomenon of *diffraction* to take place as a result of the interaction of X-rays with matter.

Along their travel in matter, X-rays strike the atoms lying on their path. Elastic *scattering* occurs from these collisions, so that the atoms that were hit emit secondary X-ray waves in all directions. In crystalline materials the atoms are organised following an ordered periodic pattern forming well-defined crystallographic planes. *Constructive interference* of the secondary X-rays is likely to occur in this environment, provided that the scattering is *coherent*[44]. Constructive interference is the necessary condition for diffraction, since "*a diffracted beam may be defined as a beam composed of a large number of scattered rays mutually reinforcing one another*" [170]. Whether constructive interference will happen was rationalised by William Lawrence Bragg and his father in 1912, who formulated what is nowadays called "Bragg's law".

This law derives directly from the fact that only *in phase* waves can interfere constructively. The difference in path length travelled by waves scattered by atoms from successive parallel crystallographic planes therefore has to be an integer multiple of their wavelength. This is illustrated in Figure K-1, where a beam of *parallel, monochromatic* X-rays collide a set of atomic planes with an angle of incidence[45] θ. The scattered rays satisfying Bragg's law form a diffracted beam with an exit angle equal to the angle of incidence.

Mathematically, Bragg's law takes the form of the following equation (where n is the positive integer factor, usually taken equal to 1):

$$n\lambda = 2d_{(hkl)} \sin\theta \tag{K-1}$$

[44] Scattering is defined as coherent when the wavelength and frequency of the incident X-ray are retained.
[45] This angle is also called the *Bragg angle*, and is measured between the incident beam and the crystallographic planes under consideration.

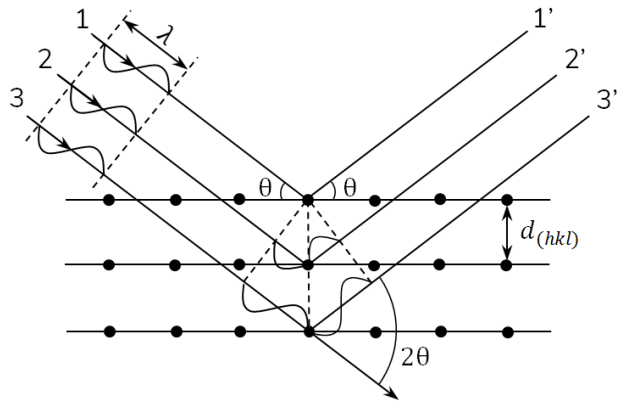

Figure K-1. Diffraction of X-rays by (hkl) atomic planes in a crystal, as an illustration of Bragg's law. Figure adapted from [173].

This condition for diffraction expresses that among all possible combinations of wavelength λ, inter-planar spacing $d_{(hkl)}$, and incidence angle θ, solely the $(\lambda, d_{(hkl)}, \theta)$ triplets satisfying Bragg's law will allow for diffraction. Hence, when λ and $d_{(hkl)}$ are fixed, the angle 2θ formed by the directions of the diffracted beam and the incident beam is fixed as well. Reciprocally, when λ and θ are fixed, the spacing $d_{(hkl)}$ characterising the (hkl) set of diffracting lattice planes is also fixed.

While the first relation is used in X-ray stress analysis as will soon be thoroughly detailed, the reciprocal forms the basis of phase analysis by X-ray diffraction. A source irradiates the sample with a beam of parallel monochromatic high energy X-rays with an angle of incidence θ increasing with time, enabling diffraction by different sets of crystallographic planes; meanwhile, a detector placed at a simultaneously increasing angle 2θ collects the diffracted X-rays. A diffraction pattern[46] is obtained, where each diffraction peak can be related to a characteristic (hkl) set of crystallographic planes

[46] Plot of the intensity of X-rays detected at each angular position 2θ.

thanks to the combined knowledge of its 2θ position and the wavelength of the X-rays.

In polycrystalline materials, whether they are powder or bulk, grains are usually quite randomly oriented and so are the families of crystallographic planes. Consequently, diffraction of the incident X-rays by a given set of atomic planes will only occur in grains oriented in a way allowing Bragg's law to be satisfied for these planes. This is the case when the normal to these planes is aligned with the diffraction vector, which is the bisector of the angle between the incident and diffracted X-rays. In other words, the atomic planes must be oriented in such a way that they form an angle θ with the incident X-rays. In polycrystalline samples it is however generally assumed that a sufficient number of grains are suitably oriented for the measurement of the desired crystallographic data.

K.3 XRD applied to stress analysis

By its ability to measure inter-planar spacing, XRD provides a means of *indirectly* measuring stress, using the spacing of selected crystallographic planes as a strain gauge working at the atomic scale. This is detailed below.

K.3.1 Why stress can be quantified

When a material is stressed elastically, the resulting macroscopic elastic strain arises from changes in inter-planar spacings relative to their stress-free value (top of Figure K-2). The sign and magnitude of these changes depend on the sign and magnitude of the stress, on the orientation of the grains relative to the stress direction, and on the {hkl} planes.

According to Bragg's law (Eq. (K-1)), a change in inter-planar spacing induces a change in the angle at which the X-rays are diffracted by the crystallograph-

ic planes. In practice, this appears as a shift $\Delta 2\theta$ in the position of the corresponding diffraction peak in Figure K-2, from which the actual spacing can be determined. The strain corresponding to this change in $d_{(hkl)}$ can therefrom be derived, and the associated stress is calculated using the theory of elasticity as will next be explained.

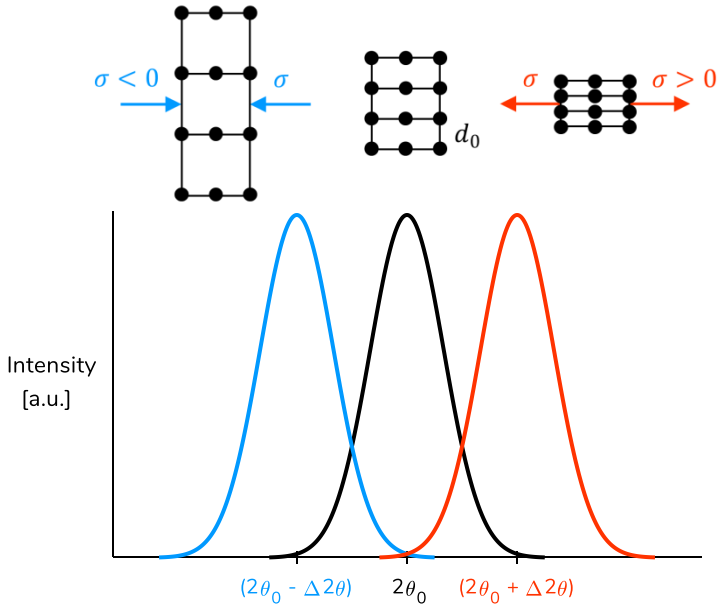

Figure K-2. Position of the diffraction peak modified by the presence of macro-stress. Compressive stress causes a shift of the peak to lower 2θ, while tensile stress causes a shift of the peak to larger 2θ (here represented in an exaggerated manner).

When the stress is macroscopically uniform (*macro-stress, type I*), the inter-planar spacing is equally modified for all (hkl) planes found in grains similarly oriented with respect to the stress direction. On the contrary, when the stress is non-uniform (*micro-stress, type II*), the spacing of (hkl) planes may vary inside grains and from one grain to another. The measured diffraction peak is then not only shifted, but also *broadened* as a result of these non-uniform *micro-strains*. This is for instance the case in plastically deformed materials.

It is recalled here that only *surface stress* can be quantified by X-ray diffraction [228][229]. Indeed, the *depth of penetration* of X-rays is generally at most a few tens of microns, as they are readily absorbed by metals and alloys. Consequently, a large part of the diffracted beam comes from a thin surface layer of the material, and the measured stress is thus mainly the *arithmetic average* of the stress found in the depth of this shallow volume [230].

The effective depth of penetration is given by Eq. (K-2), where G_x is the contribution of the material surface layer of thickness x to the total integrated intensity diffracted by a sample of infinite thickness. Setting G_x to 0.95 then yields the thickness x of the surface layer that contributes to 95 % of the total diffracted intensity.

$$x = \frac{\ln\left(\frac{1}{1-G_x}\right)}{\mu\left(\frac{1}{\sin(\theta+\psi)}+\frac{1}{\sin(\theta-\psi)}\right)} \tag{K-2}$$

This quantity is thus influenced by the Bragg angle (function of the radiation wavelength and the (hkl) family of planes), an angle ψ describing the inclination of the sample with respect to the horizontal position, and the linear ab-

sorption coefficient μ (depending on the material, its density and the radiation wavelength).

K.3.2 How stress is quantified

The main equations of the mathematical development used to calculate the stress corresponding to the measured strain will now be exposed. One will start by expressing the individual stress component acting in any direction of the sample surface. Then, the "$\sin^2\psi$" method will be exposed, which can give access to the full stress tensor.

K.3.2.1 Component of stress in any direction of the sample surface

Plane stress can often be assumed in the thin surface layer penetrated by X-rays, since the stress component normal to a free surface in equilibrium is always zero. Such *biaxial* stress state can be completely defined by the principal stresses σ_1 and σ_2, with $\sigma_3 = 0$. The indices 1, 2 and 3 refer to the in-plane (1,2) and normal (3) directions forming the principal coordinate system in which the shear stress components do vanish.

The strain component in the normal direction is however not zero, as a result of the Poisson effect caused by the in-plane stresses. It is then expressed as in Eq. (K-3), where ν and E are the Poisson's ratio and the Young's modulus of the considered material.

$$\varepsilon_3 = -\nu(\varepsilon_1 + \varepsilon_2) = -\frac{\nu}{E}(\sigma_1 + \sigma_2) \tag{K-3}$$

Besides, ε_3 is also given by the change in spacing of (hkl) crystallographic planes oriented parallel to the surface, which can be determined by means of Eq. (K-4) as soon as the stress-free spacing d_0 is known and the actual strained spacing d_n has been measured.

$$\varepsilon_3 = \frac{d_n - d_0}{d_0} \tag{K-4}$$

The expression of ε_3 given in Eq. (K-3) shows that its measurement alone does not allow dissociating the principal stresses. This limitation can nevertheless be overcome with an additional measurement of inter-planar spacing. One can indeed relate the strain $\varepsilon_{\phi\psi}$ in any direction defined by the angles ϕ and ψ to the normal strain ε_3 and the in-plane stress σ_ϕ acting in the direction forming an angle ϕ with direction 1. Figure K-3 shows these angles and directions.

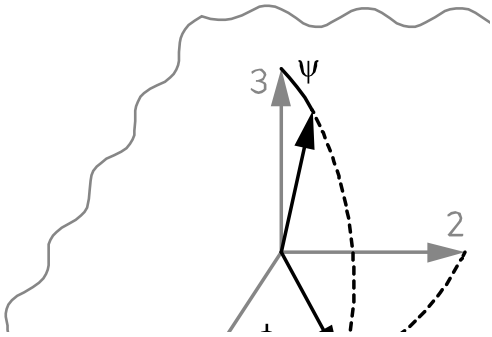

Figure K-3. Angles and directions generally used in the framework of XRD stress analysis.

By application of the theory of elasticity for isotropic solids, one obtains the fundamental equation of stress measurement by X-ray diffraction:

$$\varepsilon_{\phi\psi} - \varepsilon_3 = \frac{(1+\nu)}{E}\sigma_\phi \sin^2\psi \tag{K-5}$$

The $\varepsilon_{\phi\psi}$ strain component may in turn be expressed in terms of the stress-free (d_0) and strained ($d_{\phi\psi}$) inter-planar spacings, as follows.

$$\varepsilon_{\phi\psi} = \frac{d_{\phi\psi} - d_0}{d_0} \tag{K-6}$$

Replacing $\varepsilon_{\phi\psi}$ and ε_3 in Eq. (K-5) by their spacing-based definition (Eq. (K-4)[47] and (K-6)) and rearranging yields an expression for the stress component σ_ϕ in any direction of the sample surface:

$$\sigma_\phi = \frac{E}{(1+\nu)} \frac{d_{\phi\psi} - d_{\phi 0}}{d_0} \frac{1}{\sin^2 \psi} \tag{K-7}$$

The value of d_0 is seldom known since it must be measured on a stress-free version of the sample material (e.g. a powder). Therefore, it is often assumed that the normal strain caused by Poisson effect is very small, so that $d_{\phi 0}$ does not differ from d_0 by more than 1% [228]. Eq. (K-7) thus finally becomes Eq. (K-8), where it clearly appears that the component of in-plane stress acting in *any direction* ϕ of the sample surface can be calculated from the measured values of two inter-planar spacings of the {hkl} crystallographic planes.

$$\boxed{\sigma_\phi = \frac{E}{(1+\nu)} \frac{d_{\phi\psi} - d_{\phi 0}}{d_{\phi 0}} \frac{1}{\sin^2 \psi}} \tag{K-8}$$

In practice, these measurements are performed on the sample rotated by a chosen angle ϕ with respect to its direction 1, and tilted by an angle ψ which takes any value smaller than 65° for the measurement of $d_{\phi\psi}$, and the value of 0° for the measurement of $d_{\phi 0}$.

The use of a tilt angle can be understood considering that Eq. (K-8) requires *two different* spacings of the (hkl) crystallographic planes to be known, i.e. $d_{\phi\psi}$ and $d_{\phi 0}$. Since different inter-planar spacings can only be found in grains differently strained by the stress component of interest, they can only be accessed by diffraction from grains differently oriented with respect to the direction of this stress. Yet, differently oriented (hkl) planes cannot diffract under the same experimental configuration and it is therefore needed

[47] Note that the index n used to define the spacing of (hkl) planes parallel to the sample surface has been replaced by its equivalent set of (ϕ,ψ) indices in Eq. (K-7), i.e. (ϕ,0).

to tilt the sample so as to sequentially activate the diffraction from {hkl} planes parallel to the surface ($\psi = 0°$) or oriented with a chosen angle ψ with respect to the sample surface. This is illustrated in Figure K-4.

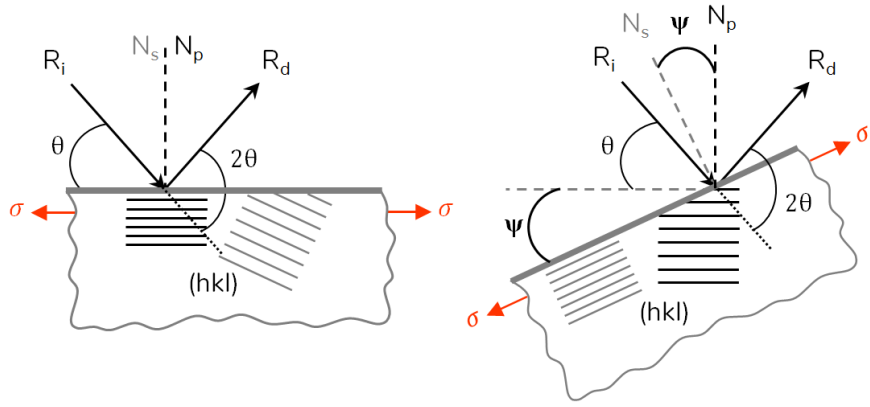

Figure K-4. Illustration of the use of a tilt angle to activate the diffraction by (hkl) atomic planes which are not parallel to the sample surface (tilting the sample brings the normal N_P of these planes in the required position of bisector of the angle formed by the incident ray R_i and the diffracted ray R_d).

The measurement is commonly performed for more than two ψ angles, which allows increasing its robustness. The stress is then calculated with the "$\sin^2 \psi$" method, as explained below.

K.3.2.2 The "$sin^2 \psi$" stress calculation method

The stress state of a polycrystalline material is often determined using the $\sin^2 \psi$ method originally developed by Macherauch and Müller [231].

Combining Eq. (K-3), (K-5) and (K-6) and rearranging yields Eq. (K-9) which gives the inter-planar spacing $d_{\phi\psi}$ of the set of diffracting planes whose normal makes an angle ψ with the normal to the sample surface. This equation describes the fundamental relationship between lattice spacing and the biaxial stress at the sample surface. The indices (hkl) indicate that E and ν are not the bulk elastic constants but the elastic constants specific to the direction

normal to the (hkl) crystallographic planes from which the strain is measured. The factors $\left(\frac{1+\nu}{E}\right)_{(hkl)}$ and $\left(\frac{\nu}{E}\right)_{(hkl)}$ are called the *X-ray elastic constants* (XECs). The crystal lattice being anisotropic, the XECs usually differ significantly from the bulk values which are an average of the XECs in all lattice directions.

$$d_{\phi\psi} = \left[\left(\frac{1+\nu}{E}\right)_{(hkl)} \sigma_\phi \sin^2\psi \, d_0 - \left(\frac{\nu}{E}\right)_{(hkl)} (\sigma_1 + \sigma_2) \, d_0\right] + d_0 \qquad \text{(K-9)}$$

Eq. (K-9) also shows that the inter-planar spacing can be expressed as a *linear function* of $\sin^2\psi$, which is the cornerstone of the present method. Inter-planar spacings $d_{\phi\psi}$ measured for several tilt angles and plotted versus $\sin^2\psi$ are therefore arranged on a straight line, the slope of which is given by

$$\frac{\partial d_{\phi\psi}}{\partial \sin^2\psi} = \left(\frac{1+\nu}{E}\right)_{(hkl)} \sigma_\phi \, d_0 \qquad \text{(K-10)}$$

The in-plane stress component acting in direction ϕ can then be isolated at left of Eq. (K-10) and calculated from the slope of the best fit line, as follows.

$$\sigma_\phi = \left(\frac{E}{1+\nu}\right)_{(hkl)} \frac{1}{d_{\phi 0}} \left(\frac{\partial d_{\phi\psi}}{\partial \sin^2\psi}\right) \qquad \text{(K-11)}$$

The sign and magnitude of the stress component are thus obviously determined by the sign and magnitude of this slope. Again, as the stress-free spacing is not necessarily known, d_0 is usually replaced by the measurable $d_{\phi 0}$ spacing.

Nonlinear $d_{\phi\psi}$ vs. $\sin^2\psi$ relations may otherwise be encountered. Some typical ones are illustrated in Figure K-5, showing (b) *elliptical*, (c) *curved* and (d) *oscillatory* distributions, in addition to the basic linear relation shown in (a).

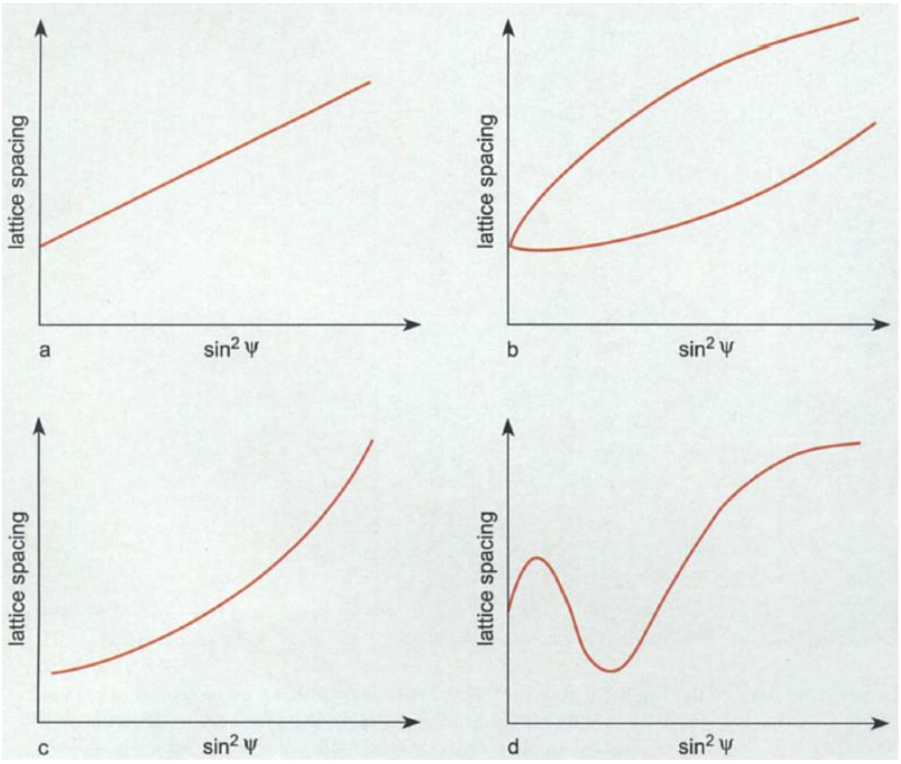

Figure K-5. Main types of existing $d_{\phi\psi}$ vs. $sin^2\,\psi$ relations [53].

The shape of the $d_{\phi\psi}$ vs. $\sin^2\psi$ distribution contains meaningful information on the sample surface stress state. While the linear relation indicates an homogeneous uniaxial or biaxial stress state in the surface layer of a macroscopically elastically isotropic polycrystalline material, the elliptical one indicates the presence of a triaxial stress state with non-zero components of out-of-plane shear stress (i.e. σ_{13} and/or σ_{23}). It is also called *ψ-splitting* since it results from the splitting of the data points according to the sign of the tilt angle. This case requires a triaxial stress analysis and is treated in Chapter 5 of reference [173]. A curved relation is in turn the sign of a significant stress gradient normal to the sample surface: different depths of penetration achieved with different tilt angles result in different stress levels being measured in the surface layer thickness. Finally, an oscillatory relation indi-

cates an inhomogeneous stress state in the surface layer of a macroscopically elastically anisotropic polycrystalline material, often caused by crystallographic texture. It may require a more complex treatment, for instance involving the measurement of the sample's orientation distribution function [173][232].

K.3.3 Measurement procedure

The measurements were performed on three samples of free-standing as-rolled 316L SS strip and three samples of as-rolled 316L SS strip co-cured with the composite laminate. They were cut to the 30 mm x 20 mm approximate dimensions from the coil of as-rolled steel sheet and from peel test specimens, respectively. Their long side was always aligned with the transverse direction (TD). A D8 equipment (Bruker, Germany) was used for the measurements, with the sample mounted in iso-inclination mode, as illustrated in Figure K-6. It was levelled on the sample holder with Plasticine, and its rolling direction was initially aligned with the beam direction so that $\varphi = 0°$ corresponds to RD.

The $\sin^2 \psi$ method generally involves performing the measurement for three azimuth angles and at least six to eight positive tilt angles ($\psi > 0°$), and repeating the procedure with the same azimuths but tilt angles of opposite sign ($\psi < 0°$). Yet, the use of high negative tilt angles is not recommended in iso-inclination mode. An alternative is to achieve "pseudo-negative" tilt angles by performing the second set of measurements for $\phi + 180°$ and the same positive tilt angles [230]. The present measurements were thus performed for the following six azimuths and eleven positive tilt angles.

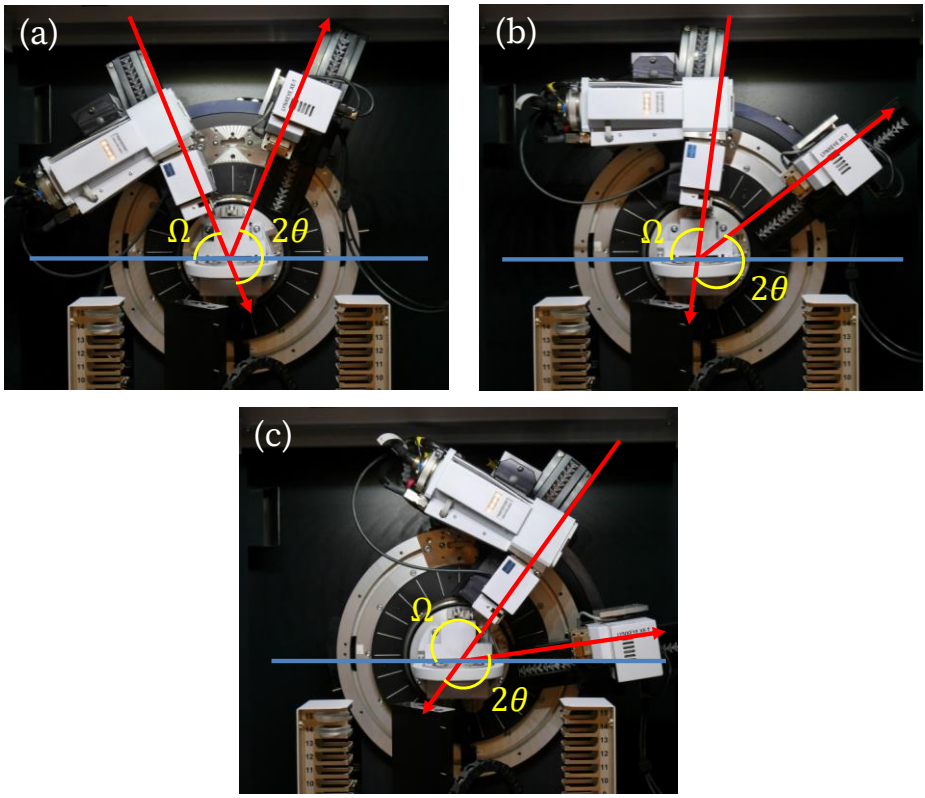

Figure K-6. Experimental setup on the D8 XRD equipment shown for three tilt angles ψ defined as $\psi = \Omega - \theta$ in the acquisition software. (a) $2\theta = 134°$, $\Omega = 67°$, $\psi = 0°$; (b) $2\theta = 134°$, $\Omega = 97°$, $\psi = 30°$; (c) $2\theta = 134°$, $\Omega = 127°$, $\psi = 60°$

$$\phi = 0°, 45°, 90°, 180°, 225°, 270°$$

$$\psi = 0°, 6°, 11.9°, 17.9°, 23.8°, 29.8°, 35.7°, 41.7°, 47.7°, 53.6°, 59.6°$$

However, the data points obtained for ϕ and $\phi + 180°$ will still be referred to as corresponding to the equivalent $\psi > 0°$ and $\psi < 0°$, as most often encountered in the scientific literature.

Given the availability of a copper anode ($\lambda_{\mathrm{Cu\ K}\alpha} = 0.15419$ nm)[48], it was decided to work with the (331) atomic planes of AISI 316L, the diffraction peak

[48] The tube voltage was 40.0 kV and the tube current was 25 mA.

of which was located at a high enough 2θ position of 138.1° in a diffraction pattern recorded prior to the present measurements. For each (ϕ,ψ) combination, the linear detector moved from an initial position $2\theta = 134°$ to a final position $2\theta = 143°$ by angular steps of 0.07° to record the diffraction peak[49].

The requirement for a high 2θ angle results from the need to *minimize* the error on the measurement of the inter-planar spacing. This error can indeed be expressed by differentiating Bragg's law, which yields Eq. (K-12) where it appears that it is proportional to the cotangent of the Bragg angle.

$$\Delta d = \frac{\lambda}{2}\left(\frac{\cos\theta}{\sin^2\theta}\right)\Delta\theta$$

$$\Rightarrow \frac{\Delta d}{d} = -\cot\theta\,\Delta\theta \qquad \text{(K-12)}$$

Knowing that the cotangent function reaches zero when the angle reaches 90°, it is clear that the angle θ should be as close as possible to 90° and the angle 2θ should hence be as close as possible to 180°. In practice, the set of (hkl) planes is chosen so that 2θ is larger than 125° [230].

Once all diffraction peaks were collected, they were corrected[50] and evaluated by the Pearson VII peak fitting method with the DIFFRAC^{plus} LEPTOS 7 software (Bruker, Germany) which provided their 2θ position and their full width at half maximum (FWHM). The software calculated the inter-planar spacing corresponding to the 2θ evaluated at each (ϕ,ψ), allowing to draw the $d_{\phi\psi}$ vs. $\sin^2\psi$ distributions for $\phi = 0°, 45°$ and 90°. As a final step, the stress analysis was performed with the same software, with elliptical regressions and X-ray elastic constants ($s_1, \frac{1}{2}s_2$) automatically calculated based on the average macroscopic elastic constants of the as-rolled AISI 316L SS sheet

[49] The counting time at each step was 5 s.
[50] All available corrections were applied, namely absorption, background, polarisation, Kα_2 and smoothing.

(E, ν) and the elastic anisotropy factor of the austenitic lattice (A_{rx}) given in Table K-1 [171].

Table K-1. X-ray elastic constants s_1 and $\frac{1}{2}s_2$, and parameters used for their calculation.

E	ν	A_{rx}	$s_1 = \left(\frac{\nu}{E}\right)_{(hkl)}$	$\frac{1}{2}s_2 = \left(\frac{1+\nu}{E}\right)_{(hkl)}$
189 GPa	0.33	1.72	1.454 10^{-6} MPa^{-1}	6.161 10^{-6} MPa^{-1}

L. Bi-linear fit parameters of the steel strips' nominal tensile curves

The bi-linear fit parameters are given in Table L-1 for both reference directions of both types of steel strip, although only the sets corresponding to the transverse direction of the as-rolled steel strip and the rolling direction of the micro-perforated steel strip had to be used in the present case. Let us recall that the normally negative values obtained for the fit parameters E_p and α for the as-rolled steel strip were set to zero, as prescribed by the test protocol. In this case, the yield coordinates are those of the approximate yield point which is otherwise given as initial guess in the bi-linear fit procedure.

Table L-1. Parameters values for the bi-linear fit of the nominal tensile curves of the as-rolled and micro-perforated steel strips in both reference directions.

Direction	E_e [GPa]	E_p [GPa]	$\alpha = \frac{E_p}{E_e}$ [-]	ε_y [%]	σ_y [MPa]
As-rolled					
RD	164	0	0	0.77	1260
TD	**202**	**0**	**0**	**0.70**	**1400**
Micro-perforated					
RD	**55.1**	**1.45**	**0.0263**	**0.77**	**425**
TD	64.8	1.23	0.0190	0.44	286

Bibliography

[1] International Air Transport Association, “Vision 2050,” 2011.

[2] International Civil Aviation Organization (ICAO), “The World of Air Transport in 2018,” *ICAO Annual Report 2018*. [Online]. Available: https://www.icao.int/annual-report-2018/Pages/the-world-of-air-transport-in-2018.aspx. [Accessed: 20-Feb-2020].

[3] International Civil Aviation Organization, “ICAO global environmental trends – Present and future aircraft noise and emissions (A40-WP/54),” 2019.

[4] B. Graver, K. Zhang, and D. Rutherford, “CO2 emissions from commercial aviation, 2018,” 2019.

[5] International Air Transport Association, “Fact sheet : CORSIA,” 2019.

[6] International Air Transport Association, “Fact Sheet - Climate Change & CORSIA,” 2018.

[7] R. Harrabin, “Aviation industry agrees deal to cut CO2 emissions,” *BBC News*, 2016.

[8] P. Hollinger, “Airlines bid to beat their weight problem,” *Financial Times*, 2016.

[9] C. N. Jardine, “Calculating The Carbon Dioxide Emissions Of Flights,” 2009.

[10] “Boeing 787 Dreamliner Completes First Flight.” [Online]. Available: https://boeing.mediaroom.com/2009-12-15-Boeing-787-Dreamliner-Completes-First-Flight. [Accessed: 19-Feb-2020].

[11] “First A350 XWB successfully completes first flight.” [Online]. Available: https://www.airbus.com/newsroom/press-releases/en/2013/06/first-a350-xwb-successfully-completes-first-flight.html. [Accessed: 19-Feb-2020].

[12] Boeing Commercial Airplanes, “Backgrounder - Boeing 787 Dreamliner,” 2014.

[13] Boeing, “2009 Environment Report,” 2009.

[14] Airbus Media Relations, “Facts & Figures - A350 XWB FAMILY: SHAPING THE FUTURE OF AIR TRAVEL,” 2019.

[15] “787 DREAMLINER BY DESIGN - Advanced Composite Use.” [Online]. Available: https://www.boeing.com/commercial/787/by-design/#/advanced-composite-use. [Accessed: 19-Feb-2020].

[16] Philippe Cognard, Ed., *Adhesives and Sealants - Basic Concepts and High Tech Bonding*, First. Oxford: Elsevier Ltd, 2005.

[17] M. D. . da S. Banea L.F.M., “Adhesively bonded joints in composite materials: an overview,” *J. Mater. Des. Appl.*, vol. 219, 2009.

[18] GE Aviation, “New GEnx Engine Advancing Unprecedented Use of Composites in Jet Engines,” 2004. [Online]. Available: https://www.geaviation.com/press-release/genx-engine-family/new-genx-engine-advancing-unprecedented-use-composites-jet-engines. [Accessed: 19-Feb-2020].

[19] Rolls-Royce, “Rolls-Royce tests composite fan systems for Advance and UltraFan™ at John C. Stennis Space Center,” 2014. [Online]. Available: https://www.rolls-royce.com/media/press-releases/2014/010914-rolls-royce-tests-composite-fan-systems.aspx. [Accessed: 19-Feb-2020].

[20] T. Kellner, “The Art of Engineering: The World’s Largest Jet Engine Shows Off Composite Curves,” *GE Reports*, 2016. [Online]. Available: https://www.ge.com/reports/the-art-of-engineering-the-worlds-largest-jet-engine-shows-off-composite-curves/. [Accessed: 19-Feb-2020].

[21] “GEnx picture.” [Online]. Available: https://i.insider.com/5788f29488e4a727008b8588?width=2400. [Accessed: 19-Feb-2020].

[22] R. E. Chupp, R. C. Hendricks, S. B. Lattime, and B. M. Steinetz, “Sealing in Turbomachinery,” *J. Propuls. Power*, vol. 22, no. 2, 2006.

[23] “Turbofan schematic.” [Online]. Available: https://upload.wikimedia.org/wikipedia/commons/8/84/Tfan-

schematic-kk-20050816.png. [Accessed: 20-Feb-2020].

[24] S. Milne, “Advanced Metal Alloys and their Applications in Jet Engines,” *AZO Materials*, 2014. [Online]. Available: https://www.azom.com/article.aspx?ArticleID=11454. [Accessed: 19-Feb-2020].

[25] Safran Aero Boosters, “A Safran center of excellence in low-pressure compressors for turbofan engines.” [Online]. Available: https://www.safran-aero-boosters.com/safran-center-excellence-low-pressure-compressors-turbofan-engines. [Accessed: 20-Feb-2020].

[26] Safran Aero Boosters, “Lightweight booster.” [Online]. Available: https://www.safran-aero-boosters.com/fr/innovation-0. [Accessed: 20-Feb-2020].

[27] CFM International, “LEAP.” [Online]. Available: https://www.cfmaeroengines.com/engines/leap/. [Accessed: 20-Feb-2020].

[28] K. Potter, *Resin Transfer Moulding*, First. London: Chapman & Hall, 1997.

[29] C. D. Rudd, A. C. Long, K. N. Kendall, and C. G. . Mangin, Eds., *Liquid moulding technologies*. Woodhead Publishing Ltd and The Society of Automotive Engineers, Inc, 1997.

[30] D. Gay, *Matériaux composites*, Third. Paris: Hermès, 1991.

[31] P. Latteier, “Carbon Fiber Weaves: What they are and why to use them,” *ELEVATED MATERIALS*, 2019. [Online]. Available: https://www.elevatedmaterials.com/carbon-fiber-weaves-what-they-are-and-why-to-use-them/. [Accessed: 20-Feb-2020].

[32] Hexcel, “HexFlow® RTM6 Product Data,” 2014.

[33] Hexcel, “Redux® 322 - Product Data,” 2015.

[34] R. Kahraman, M. Sunar, and B. Yilbas, “Influence of adhesive thickness and filler content on the mechanical performance of aluminum single-lap joints bonded with aluminum powder filled epoxy adhesive,” *J. Mater. Process. Technol.*, no. 205, pp. 183–189, 2008.

[35] M. A. Boyle, C. J. Martin, and J. D. Neuner, “Epoxy Resins,” in *ASM Handbook Volume 21*, ASM International, 2001, pp. 78–89.

[36] C. Barrere and F. Dal Maso, “Résines époxy réticulées par des polyamines : structure et propriétés,” *Rev. l’institut français du pétrole*, vol. 52, no. 3, pp. 317–335, 1997.

[37] D. Roylance, “Mechanical properties of materials,” 2008. [Online]. Available: http://web.mit.edu/course/3/3.225/book.pdf.

[38] A. Zotti, S. Zuppolini, M. Zarrelli, and A. Borriello, “Fracture Toughening Mechanisms in Epoxy Adhesives,” in *Adhesives - Applications and Properties*, Anna Rudawska, Ed. IntechOpen, 2016.

[39] A. J. Kinloch, “Toughening epoxy adhesives to meet today’s challenges,” *MRS Bull.*, no. June, pp. 445–448, 2003.

[40] S.-A. Xu and X.-X. Song, “Introduction to Rubber toughened Epoxy Polymers,” in *Handbook of Epoxy Blends*, Springer International Publishing, 2015.

[41] P. Van Velthem *et al.*, “Influence of thermoplastic diffusion on morphology gradient and on delamination toughness of RTM-manufactured composites,” *Compos. Part A Appl. Sci. Manuf.*, vol. 72, pp. 175–183, 2015.

[42] M. McGuire, *STAINLESS STEELS FOR DESIGN ENGINEERS*. ASM International, 2008.

[43] H. Bhadeshia and R. Honeycombe, *STEELS - Microstructure and Properties*, Fourth. Elsevier Ltd, 2017.

[44] S. Tanhaei, K. Gheisari, and S. R. Alavi Zaree, “Effect of cold rolling on the microstructural, magnetic, mechanical, and corrosion properties of AISI 316L austenitic stainless steel,” *Int. J. Miner. Metall. Mater.*, vol. 25, no. 6, pp. 630–640, 2018.

[45] M. Naghizadeh and H. Mirzadeh, “Microstructural Evolutions During Reversion Annealing of Cold-Rolled AISI 316 Austenitic Stainless Steel,” *Metall. Mater. Trans. A*, vol. 49, no. 6, pp. 2248–2256, 2018.

[46] A. Baldan, “Adhesion phenomena in bonded joints,” *Int. J. Adhes. Adhes.*, vol. 38, pp. 95–116, 2012.

[47] T. Pardoen, O. Dezellus, and M. Braccini, “Controlling Adherence,” in *Mechanics of Solid Interfaces*, M. Braccini and M. Dupeux, Eds. ISTE Ltd and John Wiley & Sons, Inc., 2012.

[48] W. Kim, I. Yun, J.-J. Lee, and H.-T. Jung, “Evaluation of mechanical interlock effect on adhesion strength of polymer-metal interfaces using micro-patterned surface topography,” *Int. J. Adhes. Adhes.*, vol. 30, no. 6, pp. 408–417, 2010.

[49] D. C. Webb, K. Kormi, and S. T. S. Al-Hassani, “Use of FEM in performance assessment of perforated plates subject to general loading conditions,” *Int. J. Press. Vessel. Pip.*, vol. 64, pp. 137–152, 1995.

[50] S. Wilson, “Thermally sprayed abradable coating technology for sealing in gas turbines,” in *The Future of Gas Turbine Technology, 6th International Conference*, 2012.

[51] J. R. Davis, Ed., *Handbook of Thermal Spray Technology*. ASM International, 2004.

[52] S. D. Pandita, G. Huysmans, M. Wevers, and I. Verpoest, “Tensile fatigue behaviour of glass plain-weave fabric composites in on- and off-axis directions,” *Compos. Part A*, vol. 32, pp. 1533–1539, 2001.

[53] I. C. Noyan and J. B. Cohen, “Residual Stresses in Materials,” *Am. Sci.*, vol. 79, no. 2, pp. 142–153, 1991.

[54] P. J. Withers and H. K. D. H. Bhadeshia, “Residual stress. Part 2 – Nature and origins,” *Mater. Sci. Technol.*, vol. 17, pp. 366–375, 2001.

[55] L. B. Freund and S. Suresh, *Thin Film Materials: Stress, Defect Formation and Surface Evolution*. Cambridge University Press, 2006.

[56] Granta Design, “Chart: Thermal expansion Modulus,” 2005. [Online]. Available: https://grantadesign.com/teachingresource/charts-and-posters/. [Accessed: 18-Feb-2020].

[57] M. Braccini and M. Dupeux, Eds., *Mechanics of Solid Interfaces*, 1st ed. ISTE Ltd and John Wiley & Sons, Inc., 2012.

[58] J. W. Hutchinson and Z. Suo, “Mixed Mode Cracking in Layered Materials,” in *Advances in Applied Mechanics Vol. 29*, J. W. Hutchinson and T. Wu, Eds. Academic Press, Inc., 1992, pp. 63–191.

[59] P. J. Withers and H. K. D. H. Bhadeshia, “Residual stress Part 1 – Measurement techniques,” *Mater. Sci. Technol.*, vol. 17, pp. 355–365, 2001.

[60] C.-H. Hsueh, “Modeling of elastic deformation of multilayers due to

residual stresses and external bending," *J. Appl. Phys.*, vol. 91, no. 12, pp. 9652–9656, 2002.

[61] G. G. Stoney, "The Tension of Metallic Films Deposited by Electrolysis," *Proc. R. Soc. A Math. Phys. Eng. Sci.*, vol. 82, no. 553, pp. 172–175, 1909.

[62] S. K. Maiti, *FRACTURE MECHANICS: Fundamentals and Applications*. Delhi: Cambridge University Press, 2015.

[63] D. Gross and T. Seelig, *Fracture Mechanics: With an Introduction to Micromechanics*, 2nd ed. Berlin: Springer-Verlag, 2011.

[64] T. L. Anderson, *FRACTURE MECHANICS: Fundamentals and Applications*, 4th ed. Boca Raton: CRC Press, 2017.

[65] E. E. Gdoutos, *Fracture Mechanics: An Introduction*, 2nd ed. Dordrecht: Springer, 2005.

[66] C. Balzani, W. Wagner, D. Wilckens, R. Degenhardt, S. Büsing, and H. G. Reimerdes, "Adhesive joints in composite laminates - A combined numerical/experimental estimate of critical energy release rates," *Int. J. Adhes. Adhes.*, vol. 32, no. 1, pp. 23–38, 2012.

[67] Z. Suo, "Reliability of Interconnect Structures," *Comprehensive Structural Integrity*, vol. 8. Elsevier, Amsterdam, pp. 265–324, 2003.

[68] H. Tada, P. C. Paris, and G. R. Irwin, *The Stress Analysis of Cracks Handbook*, 3rd. ed. New York: ASME Press, 2000.

[69] J. R. Reeder, "3D Mixed-Mode Delamination Fracture Criteria – An Experimentalist's Perspective," in *Damage in Composites*, B. V. Sankar, A. M. Waas, and M. W. Hyer, Eds. DEStech Publications, Inc., 2013.

[70] J. R. Reeder, "A Bilinear Failure Criterion for Mixed-Mode Delamination," in *Composite Materials: Testing and Design (Eleventh Volume), ASTM STP 1206*, E. T. Camponeschi, Ed. Philadelphia: American Society for Testing and Materials, 1993, pp. 303–322.

[71] D. A. Dillard, "Improving adhesive joint design using fracture mechanics," in *Advances in Structural Adhesive Bonding*, 1st ed., D. A. Dillard, Ed. Woodhead Publishing Limited, 2010, pp. 350–388.

[72] M. L. Benzeggagh and M. Kenane, "Measurement of mixed-mode delamination fracture toughness of unidirectional glass/epoxy

composites with mixed-mode bending apparatus," *Compos. Sci. Technol.*, vol. 56, no. 4, pp. 439–449, 1996.

[73] M.-Y. He, A. Bartlett, A. G. Evans, and J. W. Hutchinson, "Kinking of a crack out of an interface: role of in-plane stress," *J. Am. Ceram. Soc.*, vol. 74, no. 4, pp. 767–771, 1991.

[74] M.-Y. He and J. W. Hutchinson, "Crack deflection at an interface between dissimilar elastic materials," *Int. J. Solids Struct.*, vol. 25, no. 9, pp. 1053–1067, 1989.

[75] M.-Y. He, A. G. Evans, and J. W. Hutchinson, "Crack deflection at an interface between dissimilar elastic materials: role of residual stresses," *Int. J. Solids Struct.*, vol. 31, no. 24, pp. 3443–3455, 1994.

[76] F. J. P. Chaves, L. F. M. da Silva, M. F. S. F. de Moura, D. A. Dillard, and V. H. C. Esteves, "Fracture Mechanics Tests in Adhesively Bonded Joints : A Literature Review," *J. Adhes.*, vol. 90, no. 12, pp. 955–992, 2014.

[77] R. Lacombe, *Adhesion Measurement Methods: Theory and Practice*. CRC Press, 2005.

[78] L. F. M. da Silva, A. Öchsner, and R. D. Adams, Eds., *Handbook of Adhesion Technology*. Heidelberg: Springer-Verlag, 2011.

[79] A. J. Kinloch, C. C. Lau, and J. G. Williams, "The peeling of flexible laminates," *Int. J. Fract.*, vol. 66, no. 1, pp. 45–70, 1994.

[80] L. F. M. da Silva, D. A. Dillard, B. Blackman, and R. D. Adams, Eds., *Testing Adhesive Joints: Best Practices*. Wiley-VCH, 2012.

[81] ASTM Standard D3762-03, "Standard Test Method For Adhesive-Bonded Surface Durability Of Aluminum (Wedge Test)," ASTM International, West Conshohocken, PA, 2010.

[82] International Standard ISO 25217:2009(E), "Adhesives - Determination of the mode 1 adhesive fracture energy of structural adhesive joints using double cantilever beam and tapered double cantilever beam specimens," International Organization for Standardization, Geneva, 2009.

[83] ASTM Standard D 5528-01 (2007), "Standard Test Method for Mode I Interlaminar Fracture Toughness of Unidirectional Fiber-Reinforced Polymer Matrix Composites," ASTM International, West

Conshohocken, PA, 2007.

[84] ASTM Standard D 3433-99 (2020), “Standard Test Method for Fracture Strength in Cleavage of Adhesives in Bonded Metal Joints,” ASTM International, West Conshohocken, PA, 2020.

[85] I. S. Floros, K. I. Tserpes, and T. Löbel, “Mode-I, mode-II and mixed-mode I+II fracture behavior of composite bonded joints: Experimental characterization and numerical simulation,” *Compos. Part B Eng.*, vol. 78, pp. 459–468, 2015.

[86] M. D. Banea, L. F. M. da Silva, and R. D. S. G. Campilho, “Effect of Temperature on Tensile Strength and Mode I Fracture Toughness of a High Temperature Epoxy Adhesive,” *J. Adhes. Sci. Technol.*, vol. 26, no. 7, pp. 939–953, 2012.

[87] R. D. S. G. Campilho, D. C. Moura, D. J. S. Gonçalves, J. F. M. G. da Silva, M. D. Banea, and L. F. M. da Silva, “Fracture toughness determination of adhesive and co-cured joints in natural fibre composites,” *Compos. Part B Eng.*, vol. 50, pp. 120–126, 2013.

[88] A. B. Pereira and A. B. de Morais, “Mode I interlaminar fracture of carbon/epoxy multidirectional laminates,” *Compos. Sci. Technol.*, vol. 64, pp. 2261–2270, 2004.

[89] P. Davidson and A. M. Waas, “Non-smooth mode I fracture of fibre-reinforced composites : an experimental , numerical and analytical study,” *Philos. Trans. R. Soc. - A*, vol. 370, pp. 1942–1965, 2012.

[90] A. J. Kinloch, A. C. Taylor, M. Techapaitoon, W. S. Teo, and S. Sprenger, “Tough, natural-fibre composites based upon epoxy matrices,” *J. Mater. Sci.*, vol. 50, no. 21, pp. 6947–6960, 2015.

[91] M. F. S. F. de Moura, J. J. L. Morais, and N. Dourado, “A new data reduction scheme for mode I wood fracture characterization using the double cantilever beam test,” *Eng. Fract. Mech.*, vol. 75, pp. 3852–3865, 2008.

[92] N. M. M. Dourado, M. F. S. F. de Moura, J. J. L. Morais, and M. A. L. Silva, “Estimate of resistance-curve in wood through the double cantilever beam test,” *Holzforschung*, vol. 64, pp. 119–126, 2010.

[93] J. J. L. Morais *et al.*, “The double cantilever beam test applied to mode I fracture characterization of cortical bone tissue,” *J. Mech. Behav.*

Biomed. Mater., vol. 3, no. 6, pp. 446–453, 2010.

[94] B. Blackman and A. Kinloch, "Protocol for the Determination of the Mode I Adhesive Fracture Energy," *Eur. Struct. Integr. Soc.*, 2001.

[95] International Standard ISO 15114:2014(E), "Fiber-reinforced plastic composites - Determination of the mode II fracture resistance for unidirectionally reinforced materials using the calibrated end-loaded split (C-ELS) test and an effective crack length approach," International Organization for Standardization, Geneva, 2014.

[96] B. R. K. Blackman, "Developing Fracture Standards for Composites and Adhesive Joints," in *ESIS Newsletter #59*, 2017, pp. 20–25.

[97] B. R. K. Blackman, A. J. Kinloch, and M. Paraschi, "The determination of the mode II adhesive fracture resistance, GIIC, of structural adhesive joints: an effective crack length approach," *Eng. Fract. Mech.*, vol. 72, no. 6, pp. 877–897, 2005.

[98] B. R. K. Blackman, A. J. Brunner, and P. Davies, "Delamination Fracture of Continuous Fibre Composites: Mixed-Mode Fracture," in *Fracture Mechanics Testing Methods for Polymers, Adhesives and Composites*, D. R. Moore, A. Pavan, and J. G. Williams, Eds. Elsevier Science and ESIS, 2001, pp. 335–359.

[99] D. R. Moore, "An Introduction to the Special Issue on Peel Testing," *Int. J. Adhes. Adhes.*, vol. 28, no. 4–5, pp. 153–157, 2008.

[100] N. Murphy and L. F. Kawashita, "The Analysis of Peel Tests," in *Testing of Adhesive Joints: Best Practices*, L. F. M. da Silva, D. A. Dillard, B. Blackman, and R. D. Adams, Eds. Wiley-VCH, 2012, pp. 257–266.

[101] Y. Wei and J. W. Hutchinson, "Interface strength, work of adhesion and plasticity in the peel test," *Int. J. Fract.*, vol. 93, pp. 315–333, 1998.

[102] K.-S. Kim and N. Aravas, "Elastoplastic analysis of the peel test," *Int. J. Solids Struct.*, vol. 24, no. 4, pp. 417–435, 1988.

[103] P. Martiny, F. Lani, A. J. Kinloch, and T. Pardoen, "Numerical analysis of the energy contributions in peel tests: A steady-state multilevel finite element approach," *Int. J. Adhes. Adhes.*, vol. 28, no. 4–5, pp. 222–236, Jun. 2008.

[104] D. R. Moore and J. G. Williams, "A protocol for determination of the adhesive fracture toughness of flexible laminates by peel testing:

fixed arm and T-peel methods," *ESIS TC4 Protocol*. Mechanical Engineering Department, Imperial College London, 2010.

[105] L. F. Kawashita, D. R. Moore, and J. G. Williams, "Comparison of peel tests for metal-polymer laminates for aerospace applications," *J. Adhes.*, vol. 81, no. 6, pp. 561–586, 2007.

[106] A. J. Kinloch, H. Koay, S. H. Lee, and L. Ng, "Using the simple peel test to measure the adhesive fracture energy, GA," in *Proceedings of the 35 th Annual Meeting of the US Adhesion Society*, 2012.

[107] L. da Silva and R. Campilho, *Advances in numerical modelling of adhesive joints*. Berlin, Heidelberg: Springer Berlin Heidelberg, 2012.

[108] X. He, "A review of finite element analysis of adhesively bonded joints," *Int. J. Adhes. Adhes.*, vol. 31, no. 4, pp. 248–264, Jun. 2011.

[109] N. Valoroso and S. De Barros, "Adhesive joint computations using cohesive zones," pp. 1–9, 2013.

[110] P. a. Gustafson and A. M. Waas, "The influence of adhesive constitutive parameters in cohesive zone finite element models of adhesively bonded joints," *Int. J. Solids Struct.*, vol. 46, no. 10, pp. 2201–2215, May 2009.

[111] G. Alfano, "On the influence of the shape of the interface law on the application of cohesive-zone models," *Compos. Sci. Technol.*, vol. 66, pp. 723–730, 2006.

[112] R. D. S. G. Campilho, M. D. Banea, J. A. B. P. Neto, and L. F. M. da Silva, "Modelling adhesive joints with cohesive zone models: effect of the cohesive law shape of the adhesive layer," *Int. J. Adhes. Adhes.*, vol. 44, pp. 48–56, Jul. 2013.

[113] R. L. Fernandes and R. G. S. G. Campilho, "Testing different cohesive law shapes to predict damage growth in bonded joints loaded in pure tension," *J. Adhes.*, vol. 93, 2017.

[114] D. Xie and A. M. Waas, "Discrete cohesive zone model for mixed-mode fracture using finite element analysis," *Eng. Fract. Mech.*, vol. 73, pp. 1783–1796, 2006.

[115] P. W. Harper and S. R. Hallett, "Cohesive zone length in numerical simulations of composite delamination," *Eng. Fract. Mech.*, vol. 75, no. 16, pp. 4774–4792, 2008.

[116] V. Tvergaard and J. W. Hutchinson, "The relation between crack growth resistance and fracture process parameters in elastic-plastic solids," *J. Mech. Phys. Solids*, vol. 40, no. 6, pp. 1377–1397, 1992.

[117] A. Turon, C. G. Davila, P. P. Camanho, and J. Costa, "An engineering solution for mesh size effects in the simulation of delamination using cohesive zone models," *Eng. Fract. Mech.*, vol. 74, no. 10, pp. 1665–1682, 2007.

[118] T. Pardoen, T. Ferracin, C. M. Landis, and F. Delannay, "Constraint effects in adhesive joint fracture," *J. Mech. Phys. Solids*, vol. 53, no. 9, pp. 1951–1983, Sep. 2005.

[119] Q. D. Yang and M. D. Thouless, "Mixed-mode fracture analyses of plastically-deforming adhesive joints," *Int. J. Fract.*, vol. 110, pp. 175–187, 2001.

[120] P. Martiny, F. Lani, A. J. Kinloch, and T. Pardoen, "A multiscale parametric study of mode I fracture in metal-to-metal low-toughness adhesive joints," *Int. J. Fract.*, vol. 173, no. 2, pp. 105–133, 2012.

[121] C. D. M. Liljedahl, a. D. Crocombe, M. a. Wahab, and I. a. Ashcroft, "Damage modelling of adhesively bonded joints," *Int. J. Fract.*, vol. 141, no. 1–2, pp. 147–161, Sep. 2006.

[122] P. P. Camanho, C. G. Davila, and S. S. Pinho, "Fracture analysis of composite co-cured structural joints using decohesion elements," *Fatigue Fract. Eng. Mater. Struct.*, vol. 27, no. 9, pp. 745–757, Oct. 2004.

[123] G. Alfano and M. A. Crisfield, "Finite element interface models for the delamination analysis of laminated composites: mechanical and computational issues," *Int. J. Numer. Meth. Eng.*, vol. 50, no. March 2000, pp. 1701–1736, 2001.

[124] O. Allix and P. Ladevèze, "Damage Mechanics of interfacial media: basic aspects, identification and application to delamination," in *Damage and Interfacial Debonding in Composites*, 1st ed., G. Z. Voyiadijs and D. H. Allen, Eds. Elsevier Science, 1996, pp. 167–188.

[125] O. Allix and A. Corigliano, "Modeling and simulation of crack propagation in mixed-modes interlaminar fracture specimens," *Int. J. Fract.*, vol. 77, pp. 111–140, 1996.

[126] O. Allix and P. Ladevèze, "Interlaminar interface modelling for the

prediction of delamination," *J. Compos. Struct.*, vol. 22, pp. 235–242, 1992.

[127] J. L. Chaboche, F. Feyel, and Y. Monerie, "Interface debonding models: a viscous regularization with a limited rate dependency," *J. Solids Struct.*, vol. 38, no. 18, pp. 3127–3160, 2001.

[128] M. Bruyneel *et al.*, "Damage modeling of laminated composites: validation of the inter-laminar damage model of SAMCEF at the coupon level for UD plies," in *5th European Conference on Computational Mechanics (ECCM V)*, 2014.

[129] O. Allix and J.-F. Deü, "Delay-damage modelling for fracture prediction of laminated composites under dynamic loading," *Eng. Trans.*, vol. 45, pp. 29–46, 1997.

[130] O. Allix, P. Feissel, and P. Thévenet, "A delay damage mesomodel of laminates under dynamic loading: basic aspects and identification issues," *Comput. Struct.*, vol. 81, no. 12, pp. 1177–1191, 2003.

[131] H. Khoramishad, A. D. Crocombe, K. B. Katnam, and I. A. Ashcroft, "Predicting fatigue damage in adhesively bonded joints using a cohesive zone model," *Int. J. Fatigue*, vol. 32, no. 7, pp. 1146–1158, 2010.

[132] C. Bouvet, B. Castanié, M. Bizeul, and J.-J. Barrau, "Low velocity impact modelling in laminate composite panels with discrete interface elements," *Int. J. Solids Struct.*, vol. 46, no. 14–15, pp. 2809–2821, 2009.

[133] P. Gudmundson and W. Zang, "An analytic model for thermoelastic properties of composite laminates containing transverse matrix cracks," *Int. J. Solids Struct.*, vol. 30, no. 23, pp. 3211–3231, 1993.

[134] P. Taylor, M. Uemura, H. Iyama, and Y. Yamaguchi, "Thermal residual stresses in filament-wound carbon-fiber-reinforced composites," *J. Therm. Stress.*, no. February 2015, pp. 393–412, 2007.

[135] L. H. Sperling, *Introduction to Physical Polymer Science*, Fourth. 2006.

[136] R. J. (Robert J. Young and P. A. (Peter A. . Lovell, *Introduction to Polymers*, Third. CRC Press, 2011.

[137] ASTM Standard E 1545-11(2016), "Standard Test Method for Assignment of the Glass Transition Temperature by

Thermomechanical Analysis," ASTM International, West Conshohocken, PA, 2016.

[138] ASTM Standard E 1640-09, "Standard Test Method for Assignment of the Glass Transition Temperature by Dynamic Mechanical Analysis," ASTM International, West Conshohocken, PA, 2009.

[139] A. Rudin and P. Choi, "Mechanical Properties of Polymer Solids and Liquids," in *The Elements of Polymer Science & Engineering*, Third., Elsevier, Ed. Academic Press, 2013, pp. 149–229.

[140] D. W. van Krevelen and te Nijenhuis K., *Properties of polymers. Their correlation with chemical structure; their numerical estimation and prediction from additive group contributions*, Fourth. Elsevier B.V., 2009.

[141] X. Morelle, "Mechanical characterization and physics-based modeling of a highly-crosslinked epoxy resin," PhD Thesis. Université catholique de Louvain, 2015.

[142] J. K. Gillham, "Formation and Properties of Thermosetting and High Tg Polymeric Materials," *Polym. Eng. Sci.*, vol. 26, no. 20, pp. 1429–1433, 1986.

[143] European Standard EN ISO 527-1:1996, "Plastics - Determination of tensile properties. Part 1: General principles," Commité Européen de Normalisation, Brussels, 1996.

[144] T. Hobbiebrunken, B. Fiedler, M. Hojo, S. Ochiai, and K. Schulte, "Microscopic yielding of CF/epoxy composites and the effect on the formation of thermal residual stresses," *Compos. Sci. Technol.*, vol. 65, no. 10, pp. 1626–1635, 2005.

[145] X. P. Morelle, J. Chevalier, C. Bailly, T. Pardoen, and F. Lani, "Mechanical characterization and modeling of the deformation and failure of the highly crosslinked RTM6 epoxy resin," *Mech. Time-Dependent Mater.*, vol. 21, no. 3, pp. 419–454, 2017.

[146] L. E. Govaert, P. H. M. Timmermans, and W. A. M. Brekelmans, "The Influence of Intrinsic Strain Softening on Strain Localization in Polycarbonate: Modeling and Experimental Validation," *J. Eng. Mater. Technol.*, vol. 122, no. 2, pp. 177–185, 2000.

[147] Jatin, V. Sudarkodi, and S. Basu, "Investigations into the origins of plastic flow and strain hardening in amorphous glassy polymers," *Int.*

J. Plast., vol. 56, pp. 139–155, 2014.

[148] J. P. Jeandrau, "Analysis and design data for adhesively bonded joints," *Int. J. Adhes. Adhes.*, vol. 11, no. 2, pp. 71–79, 1991.

[149] J. P. Jeandrau, "Intrinsic mechanical characterization of structural adhesives," *Int. J. Adhes. Adhes.*, vol. 6, no. 4, pp. 229–231, 1986.

[150] A. J. Kinloch and R. J. Young, *Fracture Behaviour of Polymers*. Springer Science+Business Media Dordrecht, 1995.

[151] Z. P. Bažant and E.-P. Chen, "Scaling of Structural Failure," *Appl. Mech. Rev.*, vol. 50, no. 10, pp. 593–627, 1997.

[152] J. Chevalier, X. P. Morelle, C. Bailly, P. P. Camanho, T. Pardoen, and F. Lani, "Micro-mechanics based pressure dependent failure model for highly cross-linked epoxy resins," *Eng. Fract. Mech.*, vol. 158, pp. 1–12, 2016.

[153] J. Chevalier, X. P. Morelle, P. P. Camanho, F. Lani, and T. Pardoen, "On a unique fracture micromechanism for highly cross-linked epoxy resins," *J. Mech. Phys. Solids*, vol. 122, pp. 502–519, 2019.

[154] T. Hobbiebrunken, B. Fiedler, M. Hojo, and M. Tanaka, "Experimental determination of the true epoxy resin strength using micro-scaled specimens," *Compos. Part A Appl. Sci. Manuf.*, vol. 38, no. 3, pp. 814–818, 2007.

[155] J. Misumi, R. Ganesh, S. Sockalingam, and J. W. J. Gillespie, "Experimental characterization of tensile properties of epoxy resin by using micro-fiber specimens," *J. Reinf. Plast. Compos.*, vol. 35, no. 24, pp. 1792-1801., 2016.

[156] D. Roylance, *Mechanics of Materials*, First. John Wiley and Sons Ltd, 1996.

[157] R. Lakes, *Viscoelastic Materials*, First. Cambridge University Press, 2009.

[158] S. Deng, M. Hou, and L. Ye, "Temperature-dependent elastic moduli of epoxies measured by DMA and their correlations to mechanical testing data," *Polym. Test.*, vol. 26, pp. 803–813, 2007.

[159] R. Bailey and R. Hicks, "Behaviour of Perforated Plates under Plane Stress," *J. Mech. Eng. Sci.*, vol. 2, no. 2, pp. 143–165, 1960.

[160] W. Zhang, P. H. Taylor, and R. C. Darton, “Simple estimation of effective elastic constants for thin plates with regular perforations and an application to the vibration of distillation column trays,” *J. Strain Anal.*, vol. 52, no. 1, pp. 57–66, 2017.

[161] S. P. Timoshenko and J. N. Goodier, *Theory of Elasticity*, 3rd ed. .

[162] W. D. Pilkey, *FORMULAS FOR STRESS , STRAIN , AND STRUCTURAL MATRICES*, 2nd ed. Hoboken, New Jersey: John Wiley & Sons, Inc., 2005.

[163] W. J. O’Donnell and J. Porowski, “Yield Surfaces for Perforated Materials,” *J. Appl. Mech.*, vol. 40, pp. 263–270, 1973.

[164] H. Khatam and M.-J. Pindera, “Plastic deformation modes in perforated sheets and their relation to yield and limit surfaces,” *Int. J. Plast.*, vol. 27, no. 10, pp. 1537–1559, 2011.

[165] ASTM Standard A 240/A 240M, “Standard Specification for Chromium and Chromium-Nickel Stainless Steel Plate, Sheet, and Strip for Pressure Vessels and for General Applications,” ASTM International, West Conshohocken, PA, 2004.

[166] M. F. Ashby, *Materials Selection in Mechanical Design*, Fourth. Amsterdam: Elsevier Ltd., 2011.

[167] AK Steel, “316/316L Stainless Steel,” 2018. [Online]. Available: https://www.aksteel.com/sites/default/files/2018-11/316-316l-stainless.pdf. [Accessed: 09-Apr-2019].

[168] Acerinox, “Cr-Ni-Mo AUSTENITIC STAINLESS STEEL - ACX 240,” 2015. [Online]. Available: https://www.acerinox.com/opencms901/export/sites/acerinox/.content/galerias/galeria-descargas/galeria-documentos-producto/ACX240-low.pdf. [Accessed: 09-Apr-2019].

[169] Outokumpu Stainless, “Standard Cr-Ni-Mo Stainless Steels,” 2006. [Online]. Available: http://www.outokumpu-armetal.com/index.php?id=8. [Accessed: 09-Apr-2019].

[170] B. D. Cullity and S. R. Stock, *Elements of X-ray Diffraction*, Third. Upper Saddle River: Prentice-Hall, Inc., 2001.

[171] Bruker AXS GmbH, “DIFFRACplus LEPTOS 7 - User Manual.” Bruker AXS GmbH, 2009.

[172] Victor Hauk, *Structural and Residual Stress Analysis by Nondestructive Methods*. Amsterdam: Elsevier Science B.V., 1997.

[173] I. C. Noyan and J. B. Cohen, *Residual Stress - Measurement by Diffraction and Interpretation*. New York: Springer-Verlag, 1987.

[174] L. B. Freund, J. A. Floro, and E. Chason, "Extensions of the Stoney formula for substrate curvature to configurations with thin substrates or large deformations," *Appl. Phys. Lett.*, vol. 74, no. 14, pp. 1987–1989, 1999.

[175] D. E. Fahnline, C. B. Masters, and N. J. Salamon, "Thin film stress from nonspherical substrate bending measurements," *J. Vac. Sci. Technol. A*, vol. 9, no. 4, pp. 2483–2487, 1991.

[176] X. P. Morelle, F. Lani, M. A. Melchior, C. Bailly, and T. Pardoen, "The Elasto-Viscoplasticity and Fracture Behaviour of the RTM6 Structural Epoxy and Impact on the Response of Woven Composites," in *ECCM15 - 15th European Conference on Composite Materials*, 2012.

[177] S. B. Kumar, I. Sridhar, S. Sivashanker, and S. O. Osiyemi, "Mode-I adhesive fracture energy measurement with modified single-lap joint test geometry," *J. Adhes. Sci. Technol.*, vol. 20, no. 10, pp. 1109–1124, 2006.

[178] B. R. K. Blackman, A. J. Kinloch, M. Paraschi, and W. S. Teo, "Measuring the mode I adhesive fracture energy, GIC, of structural adhesive joints: the results of an international round-robin," *Int. J. Adhes. Adhes.*, vol. 23, no. 4, pp. 293–305, 2003.

[179] J. A. Nairn, "Energy release rate analysis for adhesive and laminate double cantilever beam specimens emphasizing the effect of residual stresses," *Int. J. Adhes. Adhes.*, vol. 20, pp. 59–74, 1999.

[180] L. F. Kawashita, A. J. Kinloch, D. R. Moore, and J. G. Williams, "The influence of bond line thickness and peel arm thickness on adhesive fracture toughness of rubber toughened epoxy-aluminium alloy laminates," *Int. J. Adhes. Adhes.*, vol. 28, no. 4–5, pp. 199–210, 2008.

[181] C. Z. Xia and J. W. Hutchinson, "Mode II fracture toughness of a brittle adhesive layer," *Int. J. Solids Struct.*, vol. 31, no. 8, pp. 1133–1148, 1994.

[182] F. G. A. Silva, J. J. L. Morais, N. Dourado, J. Xavier, F. A. M. Pereira,

and M. F. S. F. De Moura, “Determination of cohesive laws in wood bonded joints under mode II loading using the ENF test,” *Int. J. Adhes. Adhes.*, vol. 51, 2014.

[183] F. A. J. Leone, D. Girolamo, and C. G. Dávila, “Progressive Damage Analysis of Bonded Composite Joints,” Hampton, 2012.

[184] M. A. L. Silva, J. J. L. Morais, and M. F. S. F. de Moura, “Mode II wood fracture characterization using the ELS test,” *Eng. Fract. Mech.*, vol. 74, pp. 2133–2147, 2007.

[185] R. G. Hutchinson and J. W. Hutchinson, “Lifetime Assessment for Thermal Barrier Coatings: Tests for Measuring Mixed Mode Delamination Toughness,” *J. Am. Ceram. Soc.*, vol. 94, no. S1, pp. S85–S95, Jun. 2011.

[186] Y. Mi, M. A. Crisfield, G. A. O. Davies, and H.-B. Hellweg, “Progressive delamination using interface elements,” *J. Compos. Mater.*, vol. 32, no. 14, pp. 1246–1272, 1998.

[187] M. E. Tuttle, *Structural Analysis of Polymeric Composite Materials*, Second. Boca Raton: CRC Press Taylor & Francis Group, 2013.

[188] O. Allix, P. Ladevèze, and A. Corigliano, “Damage analysis of interlaminar fracture specimens,” *Compos. Struct.*, vol. 31, 1995.

[189] B. R. K. Blackman, H. Hadavinia, A. J. Kinloch, and J. G. Williams, “The use of a cohesive zone model to study the fracture of fibre composites and adhesively-bonded joints,” *Int. J. Fract.*, vol. 119, no. 1, pp. 25–46, 2003.

[190] Abaqus 6.9, “Defining the constitutive response of cohesive elements using a traction-separation description,” *Abaqus Analysis User’s Manual*. .

[191] P. H. Martiny, F. Lani, a. J. Kinloch, and T. Pardoen, “A maximum stress at a distance criterion for the prediction of crack propagation in adhesively-bonded joints,” *Eng. Fract. Mech.*, vol. 97, no. 1, pp. 105–135, Jan. 2012.

[192] I. Georgiou, S. Aramco, H. Hadavinia, A. Ivankovic, and A. J. Kinloch, “Cohesive zone models and the plastically deforming peel test,” *J. Adhes.*, vol. 79, pp. 239–265, 2003.

[193] T. a Bogetti, C. P. R. Hoppel, and W. H. Drysdale, “Three-Dimensional

Effective Property and Strength Prediction of Thick Laminated Composite Media." p. 96, 1995.

[194] J. N. Reddy, *Mechanics of laminated composite plates and shells - Theory and analysis*, 2nd ed. Boca Raton: CRC Press LLC, 2004.

[195] ASTM Standard E2550-11, "Standard Test Method for Thermal Stability by Thermogravimetry," ASTM International, West Conshohocken, PA, 2011.

[196] H. Czichos, T. Saito, and L. Smith, Eds., *Springer Handbook of Materials Measurement Methods*. Springer Science+Business Media, Inc., 2006.

[197] ASTM Standard E831-12, "Standard Test Method for Linear Thermal Expansion of Solid Materials by Thermomechanical Analysis," ASTM International, West Conshohocken, PA, 2012.

[198] E. Saldívar-Guerra and E. Vivaldo-Lima, Eds., *Handbook of Polymer Synthesis, Characterization, and Processing*, First. John Wiley & Sons, Inc., 2013.

[199] A. D. Mulliken and M. C. Boyce, "Mechanics of the rate-dependent elastic-plastic deformation of glassy polymers from low to high strain rates," *Int. J. Solids Struct.*, vol. 43, pp. 1331–1356, 2006.

[200] J. R. Davis, Ed., *Tensile Testing*, Second. Ohio: ASM International, 2004.

[201] H. B. Motra, J. Hildebrand, and A. Dimmig-osburg, "Assessment of strain measurement techniques to characterise mechanical properties of structural steel," *Eng. Sci. Technol. an Int. J.*, vol. 17, no. 4, pp. 260–269, 2014.

[202] N. McCormick and J. Lord, "Digital Image Correlation," *Mater. Today*, vol. 13, no. 12, pp. 52–54, 2010.

[203] R. C. Oats and Q. Dai, "Improved 2D Digital Image Correlation Method for Displacement and Deflection Measurements of Structural Beams," *Mod. Civ. Struct. Eng.*, vol. 1, no. 1, pp. 13–26, 2017.

[204] Y. H. Wang *et al.*, "Whole Field Sheet-Metal Tensile Test Using Digital Image Correlation," *Exp. Tech.*, no. March, 2010.

[205] D. Depuydt, K. Hendrickx, W. Biesmans, J. Ivens, and A. Willem Van Vuure, "Digital image correlation as a strain measurement technique for fibre tensile tests," *Compos. Part A*, vol. 99, pp. 76–83, 2017.

[206] K.-A. Kalteremidou, B. R. Murray, E. Tsangouri, D. G. Aggelis, D. Van Hemelrijck, and L. Pyl, "Multiaxial Damage Characterization of Carbon/Epoxy Angle-Ply Laminates under Static Tension by Combining In Situ Microscopy with Acoustic Emission," *Appl. Sci.*, vol. 8, no. 11, 2018.

[207] F. Hild, J.-N. Périé, and S. Roux, "Evaluating Damage with Digital Image Correlation: C. Applications to Composite Materials," in *Handbook of Damage Mechanics: Nano to Macro Scale for Materials and Structures*, G. Z. Voyiadjis and A. Shojaei, Eds. New York: Springer Science+Business Media, Inc., 2015, pp. 1301–1322.

[208] G. L. Golewski, "Measurement of fracture mechanics parameters of concrete containing fly ash thanks to use of Digital Image Correlation (DIC) method," *Measurement*, vol. 135, pp. 96–105, 2019.

[209] J. Abanto-Bueno and J. Lambros, "Investigation of crack growth in functionally graded materials using digital image correlation," *Eng. Fract. Mech.*, vol. 69, no. 14–16, pp. 1695–1711, 2002.

[210] L. Pyl, K.-A. Kalteremidou, and D. Van Hemelrijck, "Exploration of the design freedom of 3D printed continuous fibre-reinforced polymers in open-hole tensile strength tests," *Compos. Sci. Technol.*, vol. 171, pp. 135–151, 2019.

[211] European Standard EN ISO 527-2:1996 E, "Plastics - Determination of tensile properties. Part 2: Test conditions for moulding and extrusion plastics," Commité Européen de Normalisation, Brussels, 1996.

[212] ASTM Standard D 618-00, "Standard Practice for Conditioning Plastics for Testing," ASTM International, West Conshohocken, PA, 2000.

[213] ASTM Standard D 638-02a, "Standard Test Method for Tensile Properties of Plastics," ASTM International, West Conshohocken, PA, 2003.

[214] International Standard ISO 6892-1:2009(E), "Metallic materials - Tensile testing - Part 1: Method of test at room temperature," International Organization for Standardization, Geneva, 2009.

[215] H. Schreier, J.-J. Orteu, and M. A. Sutton, *Image Correlation for Shape, Motion and Deformation Measurements*. 2009.

[216] D. Lecompte *et al.*, "Quality assessment of speckle patterns for digital

image correlation," *Opt. Lasers Eng.*, vol. 44, no. 12, pp. 1132–1145, 2006.

[217] Correlated Solutions, "Application Note AN-1701 Speckle Pattern Fundamentals," Columbia, 2018.

[218] H. Sol, H. Hua, J. De Visscher, and W. P. De Wilde, "A mixed numerical/experimental technique for the nondestructive identification of the stiffness properties of fibre reinforced composite materials," *NDT&E Int.*, vol. 30, no. 2, pp. 85–91, 1997.

[219] T. Pottier, "Identification paramétrique par recalage de modèles éléments finis couplée à des mesures de champs cinématiques et thermiques," PhD Thesis. Université de Savoie, 2010.

[220] T. Lauwagie, "Vibration-Based Methods for the Identification of the Elastic Properties of Layered Materials," PhD Thesis. Katholieke Universiteit Leuven, 2005.

[221] H. Sol, "Identification of anisotropic plate rigidities using free vibration data," PhD Thesis. Vrije Universiteit Brussel, 1986.

[222] T. Lauwagie, H. Sol, G. Roebben, W. Heylen, and Y. Shi, "Validation of the Resonalyser method: an inverse method for material identification," in *Proceedings of ISMA 2002*, 2002.

[223] T. Lauwagie, H. Sol, G. Roebben, W. Heylen, Y. Shi, and O. Van Der Biest, "Mixed numerical - experimental identification of elastic properties of orthotropic metal plates," *NDT&E Int.*, vol. 36, pp. 487–495, 2003.

[224] T. Lauwagie, H. Sol, W. Heylen, and G. Roebben, "Determination of the in-plane elastic properties of the different layers of laminated plates by means of vibration testing and model updating," *J. Sound Vib.*, vol. 274, pp. 529–546, 2004.

[225] T. Lauwagie, K. Lambrinou, S. Patsias, W. Heylen, and J. Vleugels, "Resonant-based identification of the elastic properties of layered materials: Application to air-plasma sprayed thermal barrier coatings," *NDT&E Int.*, vol. 41, no. 2, pp. 88–97, 2008.

[226] T. Lauwagie, K. Lambrinou, H. Sol, and W. Heylen, "Resonant-based identification of the poisson's ratio of orthotropic materials," *Exp. Mech.*, vol. 50, no. 4, pp. 437–447, 2010.

[227] M. L. Sham and J. K. Kim, “Evolution of residual stresses in modified epoxy resins for electronic packaging applications,” *Compos. Part A Appl. Sci. Manuf.*, vol. 35, no. 5, pp. 537–546, 2004.

[228] P. S. Prevéy, “X-ray Diffraction Residual Stress Techniques,” in *Metals Handbook, Vol. 10*, American Society for Metals, 1986, pp. 380–392.

[229] E. Brinksmeier, J. T. Cammett, W. König, P. Leskovar, J. Peters, and H. K. Tönshoff, “Residual Stresses - Measurement and Causes in Machining Processes,” *CIRP Ann. - Manuf. Technol.*, vol. 31, no. 2, pp. 491–510, 1982.

[230] M. E. Fitzpatrick, A. T. Fry, P. Holdway, F. A. Kandil, J. Shackleton, and L. Suominen, “Determination of Residual Stresses by X-ray Diffraction - Issue 2,” Teddington, 2005.

[231] E. Macherauch and P. Müller, “Das sin 2 ψ-Verfahren der röntgenographischen Spannungsmessung,” *Zeitschrift für Angew. Math. und Phys.*, vol. 13, pp. 305–312, 1961.

[232] P. Van Houtte and L. De Buyser, “The Influence of Crystallographic Texture on Diffraction Measurements of Residual Stress,” *Acta Metall. Mater.*, vol. 41, no. 2, pp. 323–336, 1993.

[233] “GlobalPetrolPrices.” [Online]. Available: https://fr.globalpetrolprices.com/. [Accessed: 13-Jan-2020].